THE UNIVERSITY OF READING

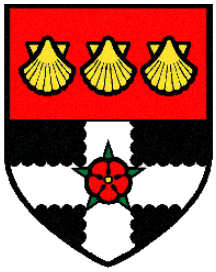

The Radiative Properties and Direct Effect of Southern African Biomass Burning Aerosols

Steven John Abel

A thesis submitted for the degree of Doctor of Philosophy

Department of Meteorology

October 2004

Declaration

I confirm that this is my own work and the use of all material from other sources has been properly and fully acknowledged.

Steven John Abel

Abstract

Aerosols perturb the climate system through the 'direct effect', whereby the scattering and absorption of radiation from aerosol particles is thought to partially offset the anthropogenic greenhouse warming. The impact of aerosols from biomass burning is poorly understood because the spatial and temporal distribution of the burden and optical properties are subject to large uncertainties. This thesis presents a detailed analysis of in-situ aircraft measurements of biomass burning aerosols from SAFARI 2000, and examines the direct effect of the smoke throughout the southern African region.

The microphysics, optical properties, and vertical structure of biomass burning aerosols are characterised in a fresh smoke plume and in the aged regional haze. A rapid increase in the single scattering albedo was observed in the first few hours subsequent to emission, suggesting that measurements taken near emission sources are of limited use when assessing the large-scale radiative effects of biomass smoke.

The current techniques used to retrieve aerosol optical depth from onboard the aircraft were compared, and a retrieval algorithm that has been developed to determine the aerosol columnar optical properties and size distribution from the measured down-welling sky radiance distribution, is shown to be in reasonable agreement with those measured in-situ.

A heavily polluted biomass burning aerosol layer was observed to exist above low-level stratocumulus clouds off the coast of Namibia and Angola. The aerosol is shown to exert a positive direct radiative forcing at the top of the atmosphere that can lead to significant biases in current spaceborne retrievals of cloud optical properties.

Finally, a multi-column radiation code is used to assess the direct radiative effect of biomass burning aerosols over southern Africa, revealing that the regional variability in the properties and vertical structure of biomass smoke and clouds, needs to be targeted by future observations and well represented in General Circulation Models.

Acknowledgements

I would like to thank my supervisors, Ellie Highwood and Jim Haywood, for their continual dedication and guidance throughout the past three years. Thanks also go to Marc Stringer for developing the multi-column radiation code and to Simon Osborne and Martin Glew for their assistance with the aircraft data. I would also like to thank NERC and the Met Office for providing the CASE studentship under which this research was undertaken.

A great deal of thanks goes to my family who have provided support and encouragement throughout my last six years at University. I would also like to thank my friends and housemates who were always keen to get out and make me forget about work, and to Anna who has managed to keep me smiling when things weren't going exactly as planned.

Contents

Chapter 1

Introduction

1.1 Motivation

The global mean surface temperature of the Earth has risen by 0.6 $\pm$ 0.2 K during the 20th century, and the rate of warming in the latter part of the 20th century appears to be unprecedented in the last millennium. There is a growing scientific consensus that much of the warming can be attributed to an increase in anthropogenic greenhouse gases (IPCC, 2001, p699). Climate models predict a further increase in the global mean surface temperature of 1.4 to 5.8 K by the year 2100, which would result in a rise in the global mean sea level of 0.09 to 0.88 metres due to the melting of ice caps and thermal expansion of the oceans, and an increased probability in the occurrence of extreme weather events such as intense precipitation (IPCC, 2001, p15-16). The economic, environmental, and social consequences of such rapid changes have led to an increased worldwide concern in the impact that mankind has on climate.

Atmospheric aerosols (solid or liquid sub-micron to micron sized particles) provide one of the largest uncertainties in our understanding of how human beings are continually altering climate. Aerosols act to modify the radiative balance of the climate system by absorbing and scattering radiation (the direct effect), and by altering the lifetime and radiative properties of clouds (the indirect effect). Both effects tend to cool the atmosphere on a global scale by increasing the planetary albedo, thereby suppressing the anthropogenic greenhouse ef-

fect. Quantifying the impact of aerosols on climate is problematic due to the complexity in their chemical, physical, and optical properties, their spatial and temporal variability in the atmosphere, and the difficulty in characterising their interaction with clouds. Further, distinguishing the effect of aerosols from anthropogenic emissions from those of natural origin is highly uncertain. The research in this thesis is focused on characterising the properties of aerosols from southern African biomass fire emissions, and assessing the direct radiative effect of the smoke on local and regional scales, both of which are poorly understood.

1.2 Climate change and radiative forcing

1.2.1 Natural variability and anthropogenic influence on the climate system

Significant long term trends in the state of the Earths climate system, termed 'climate change', is not a recent phenomenon. Over the past 400 thousand years, the Earth has experienced large shifts between ice ages and warmer interglacial periods (see figure 1.1 (a)). This is primarily the result of changes in the circulation of the atmosphere and ocean due to variations in the Earths orbit, thereby altering the spatial distribution of the incoming solar radiation which is the driving source of energy for the climate system. On shorter time-scales of the order of years to decades, changes in volcanic activity and the solar cycle have also acted to perturb the climate system. These natural perturbations to the climate system need to be considered when attributing climate change to anthropogenic activity.

The environment is continually affected by the activities of human beings. Of particular importance to the climate system, mankinds dependence upon fossil fuels in domestic and industrial usage, and the burning of biomass for domestic and agricultural purposes, produce copious amounts of greenhouse gases and aerosols which alter the chemical composition of the atmosphere. Since the industrial revolution (normally taken as 1750), there has been an sharp increase in the concentration of greenhouse gases. For example, the concentration of carbon dioxide has risen from close to 280 ppmv in 1800 to 367 ppmv in 1999 (+31 %) (IPCC, 2001, p187). The increased concentration of greenhouse gases

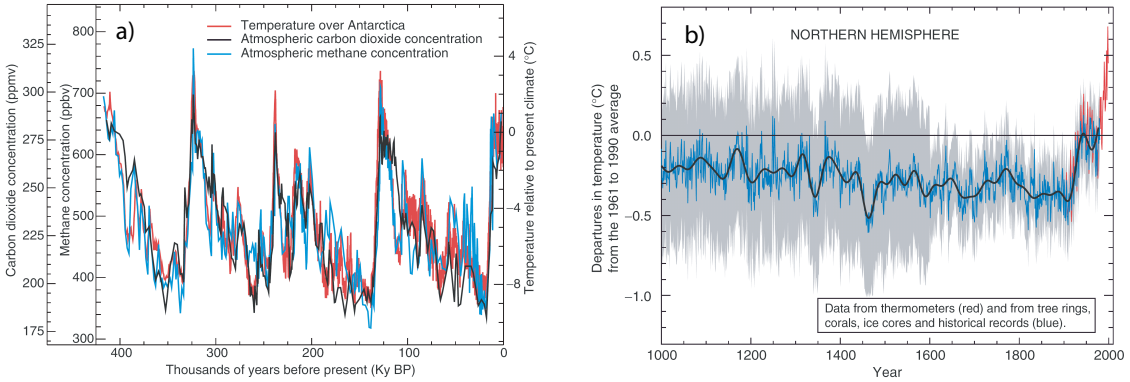

Figure 1.1: *a) The variation in temperature, carbon dioxide, and methane over the past 420 thousand years from the paleoclimate recored derived from ice core data collected at Vostok, Antarctica. Figure taken from IPCC (2001, p137). b) Variation in the annual mean surface temperature in the Northern hemisphere, over the last millennium. Figure taken from the summary for policy makers, IPCC (2001, p3).*

enhances the atmospheric opacity to longwave radiation, resulting in the absorption of terrestrial radiation and the re-emission of longwave radiation from higher altitudes within the atmosphere. Because the temperature tends to decrease with altitude in the troposphere, the radiative heat loss to space is reduced, thereby warming the surface and lower levels of the atmosphere. Figure 1.1 (b) shows a rapid increase in the global annual mean surface temperature in the past 100 years, which has been largely attributed to the enhanced anthropogenic greenhouse effect (IPCC, 2001, p10).

Anthropogenic aerosols are composed of a variety of aerosol types including water-soluble inorganic species (e.g. sulphate, nitrate, ammonium), organic condensed species, elemental or black carbon, and mineral dust. Natural types of aerosols include sea salt, marine sulphate compounds, dust, and particles from volcanic emissions. The influence of atmospheric aerosols are generally thought to somewhat offset the global warming, by reflecting a fraction of the incoming solar radiation back to space through direct interaction and modification of clouds. However, some aerosols such as those containing black carbon tend to directly absorb solar radiation, and can enhance the warming due to greenhouse gases on local scales. There is some evidence that the amount of aerosols in the atmosphere have increased in the past century (IPCC, 2001, p306), although there are few long term records. Monitoring of global aerosol amounts through current satellite observations should enable trends to be identified in the future.

Other anthropogenic influences include increases in tropospheric ozone due to chemical

reactions from precursor gases produced by biomass burning and industrial pollution and are thought to provide an additional warming. However, the depletion of the stratospheric ozone layer due to emissions of chlorofluorocarbons (CFCs), and changes in the physical and biological properties of the land surface due to urbanisation and human forestry and agricultural practices, are both thought to have exerted a cooling influence on the climate system.

1.2.2 The concept of radiative forcing

The concept of radiative forcing is used to assess the relative importance of the various natural and anthropogenic climate change mechanisms. It is a measure of the radiative impact on the surface-troposphere system that is induced by an external perturbation, such as an increase in anthropogenic aerosols, and is usually integrated over a specific time period. Radiative forcing is formally defined as the "change in the net (down minus up) irradiance (solar plus long-wave; in Wm^{-2}) at the tropopause after allowing for stratospheric temperatures to readjust to radiative equilibrium, but with surface and tropospheric temperatures and state held fixed at the unperturbed values" (IPCC, 2001, p353). A major benefit of radiative forcing, ΔF, is that it has been shown through General Circulation Model (GCM) simulations to be a reasonable indicator of the global annual mean change in surface temperature (ΔT_s) for different perturbations (e.g. solar or greenhouse gas forcing), once the climate system has reached equilibrium. The relation between ΔF and ΔT_s is described with the equation

$$\Delta T_s = \lambda_{T_s} \Delta F, \tag{1.1}$$

where λ_{T_s} is the climate sensitivity parameter. However, there is emerging evidence that the assumption of a constant λ_{T_s} may not hold true for all radiative forcing mechanisms (e.g. Hansen *et al.* (1997), Joshi *et al.* (2003), Cook and Highwood (2004)). For example, Cook and Highwood (2004) find that the value of λ_{T_s} is highly variable for aerosols depending on the degree of absorption of solar radiation, and that the sign of the ΔF may not even be a good indicator of the sign of the resultant ΔT_s. The instability of λ_{T_s}

was shown to result from varying strengths of climate feedback mechanisms, primarily the semi-direct aerosol effect (see section 1.3.4), and suggests that the direct radiative forcing for absorbing aerosols may be a poor indicator of surface temperature response. However, the mechanisms responsible for this non-linear response are poorly understood, and quantifying the magnitude of the variability in λ_{T_s} for different atmospheric aerosols may only be achieved with an improved representation of the radiative effects of aerosols (the manner in which aerosols alter the radiation budget of the atmosphere) in current GCMs.

1.3 Radiative effect of atmospheric aerosols

1.3.1 The direct aerosol effect

The direct aerosol effect describes the interaction of aerosol particles through both scattering and absorption of radiation. The scattering processes tend to reflect a fraction of the incoming solar radiation back to space, thereby cooling the atmosphere. In contrast, atmospheric absorption by aerosol particles (primarily black carbon) in the shortwave reduces the planetary albedo by converting the incoming solar radiation to heat. Both scattering and absorption act to reduce the irradiance incident at the surface, which may have important consequences to atmospheric circulation and the hydrological cycle (see section 1.3.4). In addition, interaction with longwave radiation can occur for large super-micron particles such as mineral dust (Highwood *et al.*, 2003), although the effect is negligible for the majority of anthropogenic aerosol constituents.

The direct radiative effect is poorly understood due to the large uncertainties in the spatial and temporal distribution in the column burden and optical properties of aerosols, combined with uncertainties in the implementation of aerosols into models, on which the majority of studies are based (Haywood and Boucher, 2000). The best estimate (rectangular bar) and estimated uncertainty (error bars) in the direct radiative forcing for the year 2000 relative to 1750 of anthropogenic sulphate, fossil fuel organic and black carbon, biomass burning, and mineral dust aerosols given by IPCC (2001) is shown in figure 1.2. By summing the best estimates of the individual aerosol components (mid point taken for mineral dust as no best estimate given), the total global mean direct radiative forcing due to anthropogenic

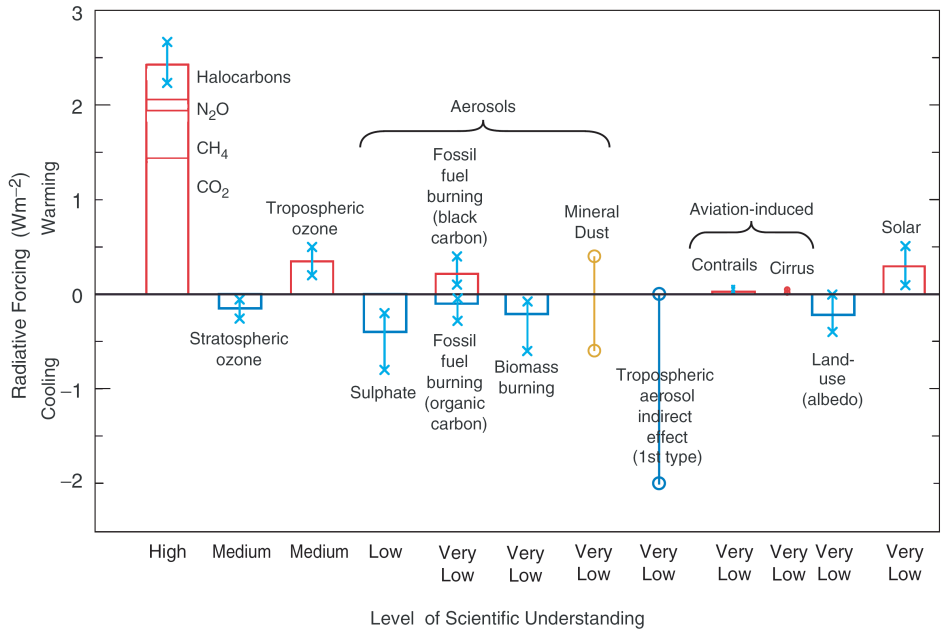

Figure 1.2: *The global annual mean radiative forcing of the climate system for the year 2000, relative to 1750 for the forcing mechanisms considered by IPCC (2001). Figure taken from the summary for policy makers, IPCC (2001, p8).*

aerosols is -0.4 Wm^{-2}, indicating that aerosols are likely to have a net cooling influence on the global climate system through their direct interaction with radiation. This can be compared to the positive radiative forcing of 2.43 Wm^{-2}, and thereby warming influence, that is attributed to greenhouse gases. However, the simple addition of the radiative forcings from different aerosol species is somewhat misleading. Because aerosol particles are highly inhomogeneous both spatially and temporally, the radiative effect of aerosols is often much more dramatic than that from greenhouse gases on local and regional scales.

1.3.2 Aerosol optical properties

The degree to which aerosols interact with electromagnetic radiation is governed by the particles extinction cross sectional area ($C_{e\lambda}$) and extinction efficiency ($Q_{e\lambda}$). These are dependent on the particle shape, size, complex refractive index (n), and the wavelength of the incident radiation (λ) . For spherical particles, the two are related through the equation

$$C_{e\lambda} = \pi r^2 Q_{e\lambda}, \tag{1.2}$$

where r is the particle radius. The scattering efficiency ($Q_{s\lambda}$) and absorption efficiency ($Q_{a\lambda}$) of the particle are defined in an analogous manner, such that $Q_{e\lambda} = Q_{s\lambda} + Q_{a\lambda}$.

If the aerosol size distribution and refractive index are known, Mie theory can be used with the assumption of spherical particles to calculate $Q_{e\lambda}$, $Q_{s\lambda}$, and $Q_{a\lambda}$, from which the specific extinction efficiency ($k_{e\lambda}$), the single scattering albedo ($\omega_{0\lambda}$), and the phase function ($P_\lambda(\phi)$) can be determined. These are the three bulk parameters that are commonly used to model the direct radiative effect of aerosols. The $k_{e\lambda}$ is defined as the extinction cross sectional area per unit mass of aerosol and is given by

$$k_{e\lambda} = \frac{3C_{e\lambda}}{4\pi\rho_{aer}r^3} = \frac{3Q_{e\lambda}}{4\rho_{aer}r}, \tag{1.3}$$

where ρ_{aer} is the density of the aerosol. In practice, the refractive index and density of aerosols are highly uncertain due to the variable nature in the chemical composition. For example, the reported density of black carbon ranges from 0.625 to 2.25 gcm^{-3}, and the complex refractive index, n, from 1.25-0.25i to 2.67-1.34i (Fuller *et al.*, 1999). In order to place constraints on the values of n used in Mie theory, detailed in-situ measurements of the aerosol scattering and absorption coefficients at specific wavelengths ($\sigma_{s\lambda}, \sigma_{a\lambda}$) are often used to infer optically equivalent values of n for a given ρ_{aer} (e.g. Abel *et al.* (2003), Haywood *et al.* (2003a)). $\sigma_{s\lambda}$ is given by

$$\sigma_{s\lambda} = \int_{r=rmin}^{r=rmax} N(r)C_{s\lambda}(r)dr, \tag{1.4}$$

where $N(r)$ is the size distribution of particles per unit volume. $\sigma_{a\lambda}$ is determined in an analogous manner.

The $\omega_{0\lambda}$ is defined as the ratio of scattering to total extinction, and is given by the equation

$$\omega_{0\lambda} = \frac{Q_{s\lambda}}{Q_{e\lambda}} = \frac{Q_{s\lambda}}{Q_{s\lambda} + Q_{a\lambda}}. \tag{1.5}$$

A $\omega_{0\lambda}$ of 1.0 implies that the aerosol scatters all radiation incident upon it, whereas a value

of 0.0 represents a purely absorbing aerosol. For atmospheric aerosols, values of $\omega_{0\lambda=0.55\mu m}$ may range from $\backsim$ 0.65 for urban or industrial aerosols that contain a lot of highly absorbing black carbon, to 1.0 for sulphate aerosols (WCP, 1986). The $\omega_{0\lambda}$ is critical in determining the sign of the direct radiative effect; both positive/negative ΔF can exist over regions of high/low surface albedos for $\omega_{0\lambda} < 1.0$ (Haywood and Shine, 1995).

The scattering phase function, $P_\lambda(\phi)$, describes the manner in which the aerosol particle scatters radiation as a function of λ, and scattering angle, ϕ. The forward scattering direction refers to scattering angles $0 < \phi < \pi/2$, whilst backward scattering refers to scattering angles $\pi/2 < \phi < \pi$. In modelling atmospheric radiative transfer with a two-stream radiation code, the asymmetry parameter, g_λ, is used to describe the asymmetricity of $P_\lambda(\phi)$. g_λ is defined as the mean value of the cosine of the scattering angle, using $P_\lambda(\phi)$ as a weighting function, and is given by

$$g_\lambda = \frac{\int_{-1}^{1} P_\lambda(\phi) cos(\phi) d(cos\phi)}{\int_{-1}^{1} P_\lambda(\phi) d(cos\phi)}. \tag{1.6}$$

A $g_\lambda > 0$ therefore represents a particle that primarily scatters radiation in the forward hemisphere, a value of 0 corresponds to radiation that is scattered isotropically, and a value < 0 corresponds to a particle that primarily scatters in the backward hemisphere. For atmospheric aerosols, g_λ tends to be positive and increases with particle size as more radiation is diffracted into the forward hemisphere from the edge of the particle. For example, at a $\lambda = 0.55\mu m$, values of 0.75 are typical for super-micron aerosols measured in Saharan dust plumes (Haywood *et al.*, 2003c), whereas values of 0.59 are more common in aerosols such as biomass smoke which show a dominance of submicron particles (Haywood *et al.*, 2003a).

As mentioned previously, Mie theory describes the scattering and absorption of radiation from spherical particles, whereas real particles in the atmosphere cover a wide range of morphologies. For example, black carbon is observed to exist in branched chain-like aggregates that are highly non-spherical (e.g. Johnson *et al.* (1991), Pósfai *et al.* (2003), Li *et al.* (2003)). Although there are numerical solutions available to treat the interaction of

electromagnetic waves with non-spherical particles (e.g. Mishchenko and Travis (1998)), determining the distribution of particle shapes in the atmosphere is highly problematic. As such, non-sphericity effects are often neglected when calculating the optical properties of aerosols and are treated as an additional uncertainty.

Further complications can arise when calculating the optical properties of aerosols that are hydrophilic. Hydrophilic aerosol species such as sulphates or sea salt particles tend to adsorb water with an increase in the atmospheric relative humidity, leading to an increase in the size and a change in the chemical composition of the aerosol particle. Consequently, the optical properties of the aerosol are altered. As water primarily scatters radiation at solar wavelengths, the addition of water tends to increase the $Q_{s\lambda}$ and hence the $k_{e\lambda}$ and $\omega_{0\lambda}$ of the aerosol particle. The increase in particle size also leads to a larger value of g_λ. The relative humidity dependence of aerosol scattering can be accounted for using empirical relations determined from humidograph measurements (e.g. Ten Brink *et al.* (2000), Magi and Hobbs (2003)).

The mixing state of the aerosol constituents is also required when modelling the optical parameters with Mie theory. An internal mixture describes an aerosol where the individual constituents such as sulphate and black carbon are aggregated with one another. In an external mixture, the components exist separately. Modelling results indicate that the absorption efficiency of black carbon is increased by a factor of 2 to 2.5 in an internal mixture with sulphate aerosols (Chylek *et al.*, 1995, Haywood and Shine, 1995), resulting in a lower $\omega_{0\lambda}$. However, the degree of internal mixing is largely dependent on the age of the particles, as processes such as coagulation, condensation, and water uptake occur as the aerosol is transported away from the primary source. It is therefore often difficult to characterise the exact mixing state of aerosol particles because the analysis of single particles is restricted to laboratory measurements using sophisticated instrumentation such as electron microscopes (e.g. Pósfai *et al.* (2003)), whereas in-situ field measurements tend to characterise bulk aerosol properties.

In addition to the aerosol optical properties, the direct radiative effect is dependent on the column burden of aerosol in the atmosphere. The aerosol optical depth (τ_λ) can be calculated by integrating the $k_{e\lambda}$ and the mass mixing ratio (m_r) of the aerosol, from the surface to the top of the atmosphere, using the equation

$$\tau_\lambda(z) = \int_{z=0}^{z=TOA} \rho k_{e\lambda} m_r sec(\theta) dz, \tag{1.7}$$

where θ is the solar zenith angle, ρ is the density of air, and z is the altitude. τ_λ is routinely measured from global satellite and ground based remote sensing, and therefore provides a useful constraint on global aerosol models (see section 1.4.1).

1.3.3 The indirect aerosol effect

Aerosols can also act as efficient cloud condensation nuclei (CCN), thereby altering the microphysics of cloud particles. Increasing the burden of anthropogenic aerosols can lead to an increase in the cloud droplet concentration, and therefore a decrease in the size of cloud droplets for a fixed amount of liquid water (Twomey, 1974). This in turn enhances the reflectivity of clouds, leading to an additional cooling effect on the climate system, and is termed the 'first indirect effect'. It is also proposed that the decrease in cloud droplet size acts to suppress the onset of precipitation, thereby increasing the liquid water amount and lifetime of clouds (Albrecht, 1989). This will also act to cool the climate system, and is termed the 'second indirect effect'.

Evidence for the first indirect effect exists from both remotely sensed and in-situ observations. Satellite inferences have shown a negative correlation between cloud droplet size and aerosol amount in regions influenced by anthropogenic aerosols (e.g. Kaufman and Fraser (1997), Sekiguchi *et al.* (2003), Quaas *et al.* (2004)). Further, in-situ aircraft measurements find the same correlation (e.g. Martin *et al.* (1994), Andreae *et al.* (2004)), and show that biomass burning aerosols can act to suppress the onset of precipitation, providing tentative evidence for the second indirect effect (Andreae *et al.*, 2004).

Modelling studies of the indirect radiative forcing of aerosols are subject to large uncertainties due to the lack of knowledge in exactly how aerosol particles interact with clouds. Current studies have used both empirical and mechanistic relationships to model the effect, resulting in a range in the global annual mean radiative forcing of 0 to -2 Wm^{-2} for the first effect, with the radiative perturbation from the second effect potentially exerting a similar

forcing in magnitude (IPCC, 2001).

1.3.4 Climate feedbacks associated with the radiative effect of aerosols

The direct scattering and absorption of solar radiation acts to reduce the surface irradiance and therefore cool the surface. The increase in cloud albedo and lifetime through the interaction of aerosols on cloud droplets will further enhance the surface cooling. The impact of the reduction in solar radiation at the surface is likely to reduce both the latent heat flux to the atmosphere through evaporation, and the sensible heat flux, therefore weakening the hydrological cycle. This has been identified in GCM studies that include the direct and indirect effect of sulphate aerosols (e.g. Roeckner *et al.* (1999)). Global model studies of the impact on the hydrological cycle for other aerosol types such as biomass smoke are yet to be performed.

Solar heating through the direct absorption of radiation by aerosol particles such as those containing black carbon will act to stabilise the boundary layer, reducing the convective potential and suppressing cloud formation. Further, if the aerosol exists in and around a cloud layer, the heating will increase the ability of the atmosphere to hold water vapour, and can lead to the 'burning-off' of clouds. The result is to reduce the cloud fraction and liquid water path, decreasing the planetary albedo and producing an additional warming on the climate system. This feedback is termed the 'semi-direct effect' (Hansen *et al.*, 1997). A negative correlation between the column burden of biomass smoke and the fraction of scattered cumulus clouds has been inferred from satellite measurements over South America (Koren *et al.*, 2004), providing observational evidence for the effect. The physical processes that govern the semi-direct effect have been investigated on local scales using large-eddy simulations (e.g. Johnson *et al.* (2004)), the results of which predict a reduction in cloud amount in the presence of partially absorbing aerosols. However, global simulations of the direct, indirect, and semi-direct radiative effect using transport models of carbonaceous and sulphate aerosols suggest that the warming resulting from the semi-direct effect is small in comparison to the cooling from the direct and indirect radiative effects (Lohmann and Feichter, 2001).

1.4 Improving the representation of aerosols in models

Current models are not able to determine the climatic impact of aerosols with sufficient accuracy due to the lack of knowledge in the spatial and temporal distribution of aerosol burden and optical properties, and the processes that govern aerosol-cloud interactions. However, regional and global scale models are the only tool in which both the present and future meteorological and climatic responses to anthropogenic aerosols can be determined.

To further develop climate models in order to improve the ability to assess the importance of aerosols on the climate system, long term monitoring of aerosols through remote sensing observations are required to characterise the means, variability, and trends in key aerosol properties. Further, intensive short term in-situ measurement campaigns are essential in order to validate the remote sensing retrievals, develop parameterisations for use in models, and through closure studies, characterise the radiative influence of aerosols.

1.4.1 Remote sensing

Global monitoring through satellite observations has allowed the spatial and temporal variability of aerosols to be characterised. Recent advances in spaceborne instruments designed to monitor the atmosphere, such as the Moderate Resolution Imaging Spectroradiometer (MODIS), can retrieve aerosol optical depth in cloud free regions over both land and ocean (Kaufman *et al.*, 1997, Tanré *et al.*, 1997). As an example, figure 1.3 shows the monthly mean aerosol optical depth for September (2000-2003 average) retrieved from the MODIS Terra satellite. With an a priori knowledge of aerosol sources, the plumes of biomass smoke over southern Africa and South America are evident. The signature of the Saharan dust plume off the West coast of Africa, and both anthropogenic and mineral dust aerosols over Asia are also clear. As such, satellites can provide a useful tool in the validation of global aerosol models (e.g. Kinne *et al.* (2003)).

Long-term observations of aerosols are also available from the Aerosol Robotic Network (AERONET) of ground based Sun-sky scanning radiometers (Holben *et al.*, 1998), comprising of $>$ 100 sites worldwide. The temporal variability in aerosol optical depth, and the column integrated size distribution and optical properties is retrieved from the measured so-

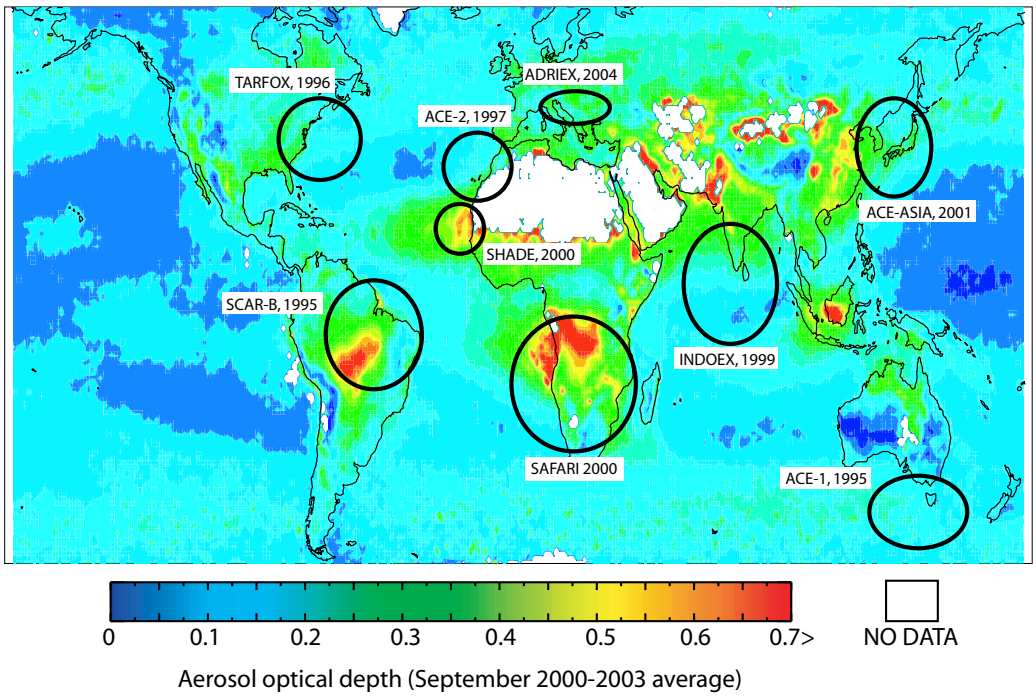

Figure 1.3: *Aerosol optical depth retrieved from the MODIS satellite at a wavelength of 0.55μm (September average). Retrievals are not made in the presence of clouds or areas of high surface reflectance as the aerosol signal cannot be accurately discerned in the measured radiances. This results in data gaps as evident in the figure. Also indicated are the approximate locations of several major field experiments.*

lar radiation, enabling a global database of aerosol characteristics to be compiled, thereby providing constraints on model simulations and satellite based retrievals of aerosols.

Whilst satellite and AERONET based measurements tend to retrieve column integrated quantities of aerosols, ground based lidars enable the vertical structure of tropospheric aerosols and clouds to be determined (e.g. Campbell *et al.* (2003)). Future spaceborne instruments such as the Cloud-Aerosol Lidar and Infrared Pathfinder Satellite Observations (CALIPSO) (Winker *et al.*, 2003) will enable the vertical structure to be characterised on global scales.

1.4.2 Field campaigns

The properties and radiative influence of aerosols from a variety of emission sources and meteorological conditions have been examined in detail in a series of recent field campaigns. These coordinated experiments combine detailed in-situ aircraft and ground based measurements with remote sensing observations and modelling work to reduce the large

uncertainty in current radiative forcing estimates. Figure 1.3 indicates the general location of several major campaigns; the series of Aerosol Characterisation Experiments, ACE-1 (Bates *et al.*, 1998), ACE-2 (Raes *et al.*, 2000), and ACE-ASIA (Huebert *et al.*, 2003), the Tropospheric Aerosol Radiative Forcing Observational Experiment (TARFOX) (Russell *et al.*, 1999), the Smoke, Clouds, and Radiation-Brazil (SCAR-B) experiment (Kaufman *et al.*, 1998), the Indian Ocean Experiment (INDOEX) (Ramanathan *et al.*, 2001b), the Saharan Dust Experiment (SHADE) (Tanré *et al.*, 2003), the Southern African Regional Science Initiative (SAFARI 2000) (Swap *et al.*, 2002a,b), and the Aerosol Direct Radiative Impact Experiment (ADRIEX).

1.5 Biomass burning aerosols

The burning of savanna and forests for agricultural and colonisation purposes, the burning of substances used for domestic fuel such as wood, peat, and dung, and the burning of agricultural waste produce copious quantities of aerosols (Crutzen and Andreae, 1990). The majority of the vegetation fires occur in the tropics during the dry season (e.g. Duncan *et al.* (2003)), from which the emissions may constitute up to 80% of those from global biomass burning (Cofer *et al.*, 1996). This can be seen by the large burdens of aerosol associated with biomass smoke over the southern African and South American regions in figure 1.3. Characterising the emissions, properties, and radiative effects of biomass smoke on both regional and global scales is therefore of vital importance in improving our understanding of the anthropogenic impact on the climate system.

1.5.1 The optical properties of biomass burning aerosols

Biomass burning aerosols contain a complex mixture of absorbing and scattering constituents, including black carbon, organic carbon, sulphates, and nitrates. There are large uncertainties in the optical properties of biomass smoke due to the variable nature in the exact composition of the aerosol. Values of the ω_0, k_e, and g of biomass burning aerosols from various published in-situ and remotely sensed measurements are compared in table 1.1. The optical properties are classified by region, and assigned as fresh or aged biomass

smoke where appropriate. Measurements taken directly over the fire, or in the smoke plume that is advected downwind from the fire are assigned as 'fresh', whereas aerosol that has dissipated in the atmosphere with age so that it becomes part of the regional haze is assigned as being 'aged'. The reported values of fresh and aged smoke from IPCC (2001) are also shown in table 1.1 and are also based on data from the literature. The uncertainty in the IPCC (2001) values are at least in part due to the regional variability in the optical properties.

Comparison of the ω_0 from the different regions show that the North American smoke tends to be less absorbing ($\omega_0 \backsim 0.92$) than the aged African biomass smoke ($\omega_0 \backsim 0.89$). The variation is likely dominated by changes in the characteristics of the fuel burnt and the combustion phase (flaming vs smouldering) of the fires in each region, of which the amount of highly absorbing black carbon per unit mass of smoke is sensitive (Dubovik *et al.*, 2002). A degree of confidence can be placed in the remotely sensed measurements as there is reasonable consistency with the reported values from in-situ data in these regions. In South America, values of $\backsim$0.84 for ω_0 are reported in Reid *et al.* (1998) and Ross *et al.* (1998) for aged smoke, whereas the more recent in-situ (Guyon *et al.* (2003)) and remotely sensed (Dubovik *et al.* (2002)) measurements suggest values closer to 0.91. The disparity between the reported values in South America requires further investigation, and should be the focus of future studies.

It can be seen that for both African and South American biomass smoke, the ω_0 tends to increase with age in the atmosphere, indicating that the aerosol particles are becoming less absorbing with age. The underlying physical mechanisms that are responsible for the change in ω_0 with age may include coagulation of particles, condensation of volatile species from the gaseous phase, uptake of water, and changes in the morphology of the aerosol particles and are examined in detail in chapter 2.

A typical value of g for biomass smoke is around 0.6, although the values listed in table 1.1 suggest that g increases as the aerosol ages in the atmosphere. This is primarily the result of a shift to larger particle sizes with age (e.g. Haywood *et al.* (2003a)). The AERONET remote sensing retrievals indicate some regional variability, with the smallest values associated with African smoke. This is indicative of smaller particles in African smoke, and may be the result of differences in the combustion phase, fire intensity, and fuel type of typical

Study	Comments	ω_0	k_e $[m^2g^{-1}]$	g
	IPCC			
IPCC (2001, p295)	• Aged regional haze	0.89±0.05	4.1±1.3$^{\#}$	0.63±0.16
	• Fresh biomass plumes	0.87±0.06	4.1±1.2$^{\#}$	0.63±0.12
	Africa			
Haywood *et al.* (2003a)	• In-situ aircraft measurements; aged	0.91±0.04	5.0±0.8	0.59±0.02
	• In-situ aircraft measurements; fresh	0.86	3.9	0.52
Formenti *et al.* (2003)	• In-situ aircraft measurements; aged	0.93±0.06	4.5-4.9$^{\#}$	
Magi *et al.* (2003)	• In-situ aircraft measurements; aged	0.89±0.03		
	• In-situ aircraft measurements; fresh	0.81±0.02		
Bergstrom *et al.* (2003)	• Retrieved from radiance measurements	0.84-0.88		
Dubovik *et al.* (2002)	• AERONET retrieval, λ=0.44/0.67μm	0.88/0.84		0.64/0.53
	South America			
Reid *et al.* (1998)	• In-situ aircraft measurements; aged	0.85±0.02	4.5±1.0	
	• In-situ aircraft measurements; fresh	0.79±0.05	4.1±0.8	
Ross *et al.* (1998)	• In-situ aircraft measurements; aged	0.82†	4.9†	
Guyon *et al.* (2003)	• In-situ measurements from 54m tower	0.91±0.02		
Dubovik *et al.* (2002)	• AERONET retrieval, λ=0.44/0.67μm	0.93/0.91‡		0.68/0.59‡
	North America			
Iziomon and Lohmann (2003)	• In-situ measurements from ARM site	0.91±0.03		
Dubovik *et al.* (2002)	• AERONET retrieval, λ=0.44/0.67μm	0.94/0.935		0.69/0.61

Table 1.1: *Optical properties of biomass burning aerosols from in-situ and remotely sensed measurements in Africa, South America, and North America. The values reported in IPCC (2001) are shown for comparison. A distinction between smoke in fresh plumes and aged regional hazes is made where appropriate. All values are at a λ=0.55μm, unless stated otherwise.* $^{\#}$*Calculated from reported ω_0 and k_s.* †*Calculated from reported fit to data.* ‡*Average of optical properties from Amazonian forest and South American cerrado smoke. Note that the reported accuracy of the AERONET retrieval is ±0.03 in ω_0 and ±0.02 in g (Dubovik* et al.*, 2000).*

fires in each region, combined with differences in the ambient relative humidity (Dubovik *et al.*, 2002). There is also the possibility that the AERONET site in Africa analysed by Dubovik *et al.* (2002) is situated closer to typical source regions than those in North and South America, which may result in a sampling of air masses that contain a greater fraction of fresh smoke with typically lower values of g.

The k_e of aged biomass smoke tends to lie between 4.5 and 5.0 m^2g^{-1}, with a lower value of $\backsim$4.0 m^2g^{-1} for fresh smoke. The transition to more optically active particles per unit mass of aerosol with age is the result of changes in the size distribution and chemical composition of the aerosol (Reid *et al.*, 1998). It is difficult to determine whether any regional variability exists due to the lack of reported values from in-situ measurements.

1.5.2 The direct radiative effect of biomass burning aerosols

A summary of the global annual mean ΔF from biomass smoke determined from various studies is given in table 1.2. Penner *et al.* (1992) and Hobbs *et al.* (1997) use simple 1-D box models similar to that of Chylek and Wong (1995) to calculate a ΔF of -0.8 and $\backsim$ -0.3 Wm^{-2} respectively. The two studies include different optical properties (see table 1.2) and global mean column burdens of aerosol (a factor of 2 larger in Penner *et al.* (1992)) in the model. A large degree of uncertainty exists in using 1-D box models to estimate a global ΔF, and they have been superseded by more detailed GCM simulations that account for the spatial and temporal distribution of smoke.

At the time of the third assessment report of the Intergovernmental Panel on Climate Change (IPCC, 2001), the more sophisticated studies using 3-D GCMs resulted in values of ΔF ranging from -0.14 Wm^{-2} (Penner *et al.*, 1998, Grant *et al.*, 1999) to -0.74 Wm^{-2} (Iacobellis *et al.*, 1999). Whilst Penner *et al.* (1998) and Grant *et al.* (1999) base the modelled optical properties on measured values, it can be seen in table 1.2 that the ω_0 and k_e used in the study of Iacobellis *et al.* (1999) are not representative of the optical properties of biomass burning aerosols (see table 1.1). The k_e used is approximately a factor of 2 higher than the measurements suggest, thereby leading to an unrealistically high aerosol optical depth in the model. Combined with the high ω_0 of 0.98 (absorption by black carbon was neglected), the unrealistic optical properties would act to overestimate the negative

Study	ω_0	k_e $[m^2g^{-1}]$	ΔF $[Wm^{-2}]$	Comments
Penner *et al.* (1992)	0.87	5.4	-0.8	• Simple 1-D box type model • Limited to cloud free conditions • Constant global column burden of aerosol
Hobbs *et al.* (1997)	0.80 to 0.84	3.4 to 4.1	-0.25 to -0.29	• Simple 1-D box type model • Optical properties from Brazilian biomass smoke • Limited to cloud free conditions • Constant global column burden of aerosol
Penner *et al.* (1998) and Grant *et al.* (1999)	0.76 to 0.80	3.4 to 6.5	-0.14 to -0.23	• Coupled GCM and chemical transport model • Optical properties modelled from two measured biomass smoke size distributions • Internal and external mixture of OC and BC
Iacobellis *et al.* (1999)	0.98 [a]	9.1 [a]	-0.74	• Coupled GCM and chemical transport model • Optical properties modelled from biomass smoke size distribution. Absorption by BC neglected • [a] $\lambda = 0.25 - 0.68\mu m$
Takemura *et al.* (2002)	0.85 to 0.90 [b]	4.6	-0.01	• Coupled GCM and chemical transport model • Modelled optical properties • External mixture of carbonaceous and sulphate (carbonaceous = internal mixture of OC and BC) • [b] $RH = variable$

Table 1.2: *The global and annual mean direct radiative forcing of biomass burning aerosols from various studies. The single scattering albedo ω_0 and specific extinction coefficient k_e are stated at a wavelength, $\lambda = 0.55\mu m$, and a relative humidity, $RH \leq 40\%$, unless stated otherwise. Organic carbon = OC. Black carbon = BC.*

radiative forcing of the biomass burning aerosol. However, it should be noted that almost a factor of 2 difference in the ΔF from the studies of Penner *et al.* (1998) and Grant *et al.* (1999) exists (-0.14 to -0.23 Wm^{-2}) when using size distributions measured in different regions to derive the aerosol optical properties included in the model. This suggests that the change in the optical properties of biomass smoke with age and region discussed in section 1.5.1 need to be quantified and incorporated into model simulations to accurately assess the direct effect.

Due to the large uncertainties involved in modelling the emissions and transport of biomass smoke from source regions, the variability in the measured optical properties, the uncertainty in the vertical structure of aerosol and cloud, and considering the scarcity of studies, IPCC (2001) assigned a best estimate of the ΔF of -0.2 Wm^{-2} with a factor of three uncertainty, thereby leading to a range of -0.07 to -0.6 Wm^{-2} (see figure 1.2).

A more recent GCM study calculated a global annual mean ΔF of -0.01 Wm^{-2} (Takemura

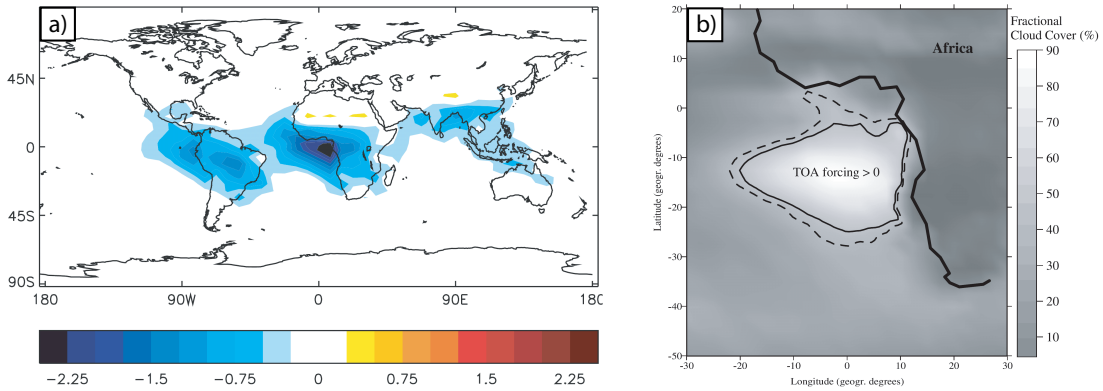

Figure 1.4: *a) The geographical distribution of annual mean radiative forcing (Wm^{-2}) from biomass burning aerosols (Penner* et al.*, 1998, Grant* et al.*, 1999); b) The predicted area of positive radiative forcing off the coast of southern Africa in September (Keil and Haywood, 2003).*

et al., 2002), a result which lies outside the range given by IPCC (2001). Further, it suggests that the net annual global direct radiative effect of biomass smoke is practically zero. To illustrate how even the sign of the radiative forcing of biomass smoke is uncertain, at least on regional scales, figure 1.4 (a) shows the geographical distribution of the annual mean ΔF of biomass smoke from the study of Penner *et al.* (1998) and Grant *et al.* (1999). The strongest regions of ΔF are evident over the main source regions, namely Africa, South America, and Indonesia. The ΔF is negative across the majority of the globe, although positive values of ΔF occur where the partially absorbing biomass burning aerosol exists above bright underlying surfaces such as the Saharan desert or snow in the Himalayas, where the probability that a photon will be absorbed by the smoke is greater due to increased surface-aerosol scattering (Haywood and Shine, 1995). However, aircraft measurements of the vertical structure of biomass smoke and clouds off the coast of Namibia show that the aerosol tended to be advected above bright low-level stratocumulus clouds, resulting in a large positive region of ΔF over the southern Atlantic Ocean as shown in figure 1.4 (b) (Keil and Haywood, 2003), a result that has been simulated in a recent regional GCM study (Myhre *et al.*, 2003). Further, the study of Takemura *et al.* (2002) also simulates this region of positive forcing, and is a major reason for why the global annual mean radiative forcing is less negative in comparison to the studies considered by IPCC (2001). This highlights the fact that the 3-D GCM simulations need to be able to model both aerosol and cloud fields well in order to model the direct radiative effect of aerosols, and brings into question the results from previous studies.

1.5.3 The indirect radiative effect of biomass burning aerosols

There have been very few global simulations of the indirect radiative forcing of biomass burning aerosols, with the study of Chuang *et al.* (2000) calculating a value of -1.16 Wm^{-2} for the first indirect effect. Lohmann *et al.* (2000) determine the sum of the first and second indirect effects of carbonaceous aerosols from biomass smoke and fossil fuel burning to be -0.9 Wm^{-2}, of which $\backsim 40\%$ is attributable to the first effect. Although a low degree of confidence can be placed in the exact value produced by the GCM simulations, the results suggest that the indirect aerosol effect of biomass smoke has a greater cooling influence on the atmosphere than the direct effect.

1.5.4 The Southern African Regional Science Initiative (SAFARI 2000)

Savanna fires in southern Africa are thought to be a major component of global biomass burning (Crutzen and Andreae, 1990), although the properties of the smoke aerosols, their transport in the atmosphere, and their radiative effect in this region were poorly understood prior to the SAFARI 2000 field campaign due to the lack of measurements. To address this, the influence of anthropogenic emissions on the surface and atmosphere in the southern African region were investigated during SAFARI 2000, with the most intensive measurements taken during the dry season when anthropogenic biomass burning is most prolific (August - September 2000) (Swap *et al.*, 2002a,b). The main objectives of the project as listed by Swap *et al.* (2002a) were to:

i) characterise, quantify and understand the processes driving biogenic, pyrogenic and anthropogenic emissions in southern Africa, with particular attention paid to atmospheric transport, chemical transformation and deposition.

ii) validate the remote sensing data, obtained from the Terra satellite, of terrestrial and atmospheric processes.

iii) study the influence of aerosol and trace gases on the radiation budget through their modification of the optical and microphysical properties of clouds.

The Met Office C-130 aircraft participated in the SAFARI 2000 campaign and was based

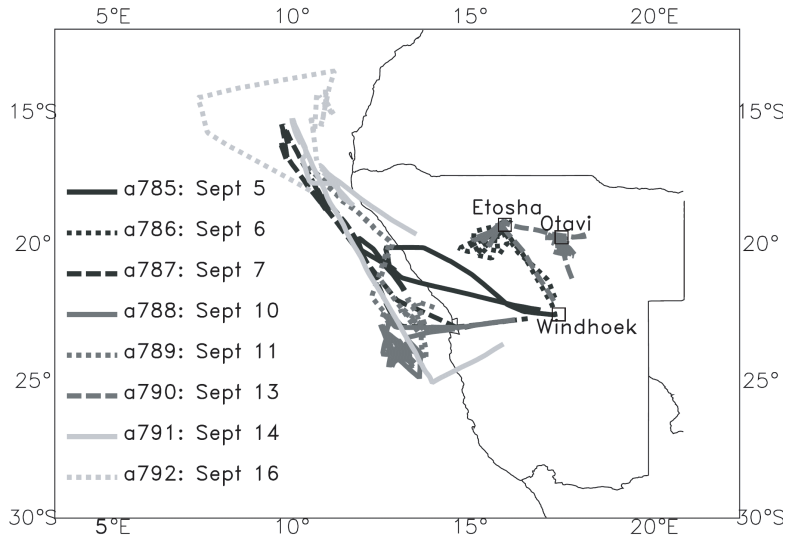

Figure 1.5: *A map showing the track of the C-130 aircraft for the eight flights performed during SAFARI 2000. Figure taken from Haywood* et al. *(2003a).*

in Windhoek, Namibia. From the 5th to 16th September 2000, 8 flights (shown in figure 1.5) designed to measure the optical properties, vertical structure, and radiative effects of biomass burning aerosols were performed. The majority of flights sampled air masses advected off the West coast of Africa, where radiative closure studies can be performed more easily than over land due to the fairly uniform sea surface. A flight over the AERONET site at Etosha Pan allowed validation of the Sun-sky scanning photometer retrieval to be made (see Haywood *et al.* (2003b) for details). Fresh biomass smoke was sampled over and downwind of a large anthropogenic fire at Otavi, allowing the effect of aging on the biomass smoke to be investigated. A further two transit flights to and from Ascension Island on the 2nd and 18th September 2000 were made, where biomass burning aerosol and stratocumulus clouds were studied.

A suite of instruments were employed onboard the C-130 aircraft to measure the chemical, physical, and optical properties of aerosols, both broadband irradiances and spectrally resolved radiances, and standard meteorological variables such as wind speed, temperature, and pressure. Data collected on the C-130 aircraft during the SAFARI 2000 campaign is used throughout this thesis and a description of the relevant instrumentation is given in appendix A.

1.6 Summary

A lack of modelling studies, combined with uncertainties in the spatial distribution and optical properties of biomass smoke, has led to a wide range of estimates in the global annual mean direct radiative forcing (-0.01 to -0.8 Wm^{-2}). Further, on regional scales even the sign of the direct radiative forcing is uncertain. Even larger uncertainties in the semi-direct and indirect aerosol effects of biomass smoke exist, of which the radiative forcing on regional and global scales is poorly constrained. It is therefore difficult to place a degree of confidence in the ability of current models to predict the influence of biomass burning aerosols on the climate system.

Long term monitoring of aerosols and aerosol radiative forcing from satellites and ground based remote sensing, in combination with detailed in-situ measurements of aerosol properties and vertical structure, have the potential to validate and therefore address some of the uncertainties in global aerosol models.

The properties and radiative influence of biomass burning aerosols were measured onboard the Met Office C-130 aircraft during the SAFARI 2000 field campaign. The collected data will improve our understanding of the climatic importance of biomass smoke in the southern African region, and determine the accuracy of current remote sensing retrievals of atmospheric constituents.

1.7 Thesis approach

The main aim of this thesis is to reduce the large uncertainties in the direct radiative effect of biomass burning aerosols, with a particular emphasis being placed on smoke in the southern African region, where vast quantities of biomass are burned by human beings on a yearly basis (Crutzen and Andreae, 1990).

In order to achieve this goal, a thorough analysis of the optical properties of southern African biomass smoke is performed from the measurements taken onboard the Met Office C-130 aircraft during the SAFARI 2000 field campaign. The evolution of the optical properties with age in the first few hours subsequent to emission are investigated in chapter

2, and those in the aged regional haze that pervades large areas of southern Africa characterised in chapter 3.

The direct radiative effect of the smoke advected over the Atlantic Ocean is then modelled on local scales under clear sky conditions in chapter 3. Analysis of the current methods used to retrieve the aerosol optical depth from onboard the aircraft is then made. The direct radiative effect of the biomass smoke overlying low-level clouds, a common feature off the western coast of Africa, is then considered in chapter 4. The impact of the overlying smoke on satellite retrievals of cloud optical properties that do not account for the radiative effect of aerosols is then explored.

The regional direct radiative impact of biomass burning aerosols is then treated using a multi-column radiative transfer code in chapter 5. By placing constraints on the spatial distribution of aerosols and clouds that are based on observations, the reliance on 3-D simulations of aerosols and clouds is negated, reducing one of the major uncertainties involved in determination of the direct radiative effect. The sensitivity of the direct radiative effect to variations in the model parameters, such as surface albedo, vertical structure, or aerosol optical properties is also investigated.

Chapter 2

Evolution of biomass burning aerosol properties with age

2.1 Introduction

There is a growing body of information on the initial emissions from biomass burning fires (e.g. Le Canut *et al.* (1996), Cofer *et al.* (1996), Ferek *et al.* (1998), Sinha *et al.* (2003)). Measurements within biomass burning smoke plumes in southern Africa indicate that there are rapid changes in both the gaseous and particulate chemistry as the plumes travel downwind from the source (Jost *et al.*, 2003, Yokelson *et al.*, 2003, Gao *et al.*, 2003, Hobbs *et al.*, 2003). For example, Gao *et al.* (2003) measure an order of magnitude increase in some organic and inorganic species within the first hour of emission, where the composition of the particulate matter in the plume undergoes significant changes (Pósfai *et al.*, 2003, Li *et al.*, 2003). Consequently, to assess the regional and global effects of smoke from biomass burning, an understanding of how the change in composition of the smoke affects the aerosols optical properties is required. Comparisons between freshly emitted biomass burning aerosol with aerosol that has aged over several days indicate that the change in the properties of the smoke has a large impact on the aerosols optical properties (Reid *et al.*, 1998). However, very little is known about the evolution of the optical properties on the much shorter time scales where the rapid changes in the composition of the smoke plume are observed.

Figure 2.1: *Photographs of the Otavi fire taken from the C-130 aircraft. Courtesy of the Met Office.*

This is the first study to analyse temporal measurements of the variation in the aerosol single scattering albedo with age in a fresh biomass burning plume. It is important to quantify this change as the variation in ω_0 can significantly affect the manner in which the aerosol interacts with radiation, and thereby influence the climate system.

This work in this chapter has been included in the paper Abel *et al.* (2003), which has been published in Geophysical Research Letters (see appendix C).

2.2 Otavi fire and aircraft flight pattern

Measurements of fresh biomass burning aerosol emitted from a large anthropogenic fire were made on the 13th September 2000 at Otavi in Namibia (flight a790). Figure 2.1 shows two photographs of the fire taken from the C-130 aircraft, in which the heavily polluted smoke plume is clearly visible. The burning had begun on agricultural land and had spread to the surrounding hillsides. As a result, the fuel consisted of a mixture of agricultural, savanna, and scrubland vegetation. There was a mixture of flaming and smouldering combustion occuring at the time that the aerosol was sampled. The burn scar of the fire is estimated to be approximately 5km^2 from visual observations made onboard the aircraft.

The aircraft performed a series of straight and level runs (SLRs) directly over the fire at altitudes ranging from 210 - 1,233 metres above ground level (AGL). This was followed by a raster pattern of cross plume transits at 1,233m (standard deviation = 17m) AGL to

Run number(s)	Time [GMT]	Altitude [m]	Type of run
R11 to R23	10:18:30 - 12:01:29	210 - 1,233	Cross plume transits at various altitudes directly over the fire.
R24 to R34	12:05:05 - 13:31:56	1,233	Cross plume transits at a constant altitude over and downwind of the fire.
P4	13:51:22 - 14:13:11	543 - 4,177	Vertical profile through the biomass plume (Start over fire and ascent made while aircraft flying downwind).

Table 2.1: *A brief summary of the runs in flight a790 that are used in this study. Local time= GMT + 2 hours.*

73km downwind of the source. The run numbers, altitudes, and time of runs are given in table 2.1. Figure 2.2 shows the series of cross plume transits over and downwind of the fire. The measurements of the aerosol number concentration, N_{tot}, made with the Passive Cavity Aerosol Spectrometer Probe 100X (PCASP) instrument are also contoured. Concentrations in excess of 100,000 cm^{-3} were measured directly over the fire. The cross indicates the general area of the burning and the two peaks in N_{tot} either side of the cross indicate the two areas of most intense burning. The number concentration is shown to spread out and decrease in magnitude as the plume becomes diluted with the background air downwind from the fire. After the series of cross plume transits, the aircraft was repositioned over the fire and a profile ascent was performed down the length of the plume to characterise the vertical structure of the aerosol.

The measurements taken across the series of cross plume transits at varying distances from the source enabled the characterisation of the biomass burning aerosols properties with age in the atmosphere. It should be noted that the experiment is not completely Lagrangian. For example, the aircraft sampled the plume at a distance of 73 km downwind of the source approximately 86 minutes after the final cross plume transit over the fire took place, whereas the time that it took the plume to travel that distance as estimated from the measured wind speeds is 143 minutes. Therefore, the aircraft sampled smoke downwind that is likely to have been emitted before the smoke was measured near the source. The assumption is made that any variability in the aerosol optical properties downwind is caused by aging processes in the smoke plume, and not by changes in the source characteristics.

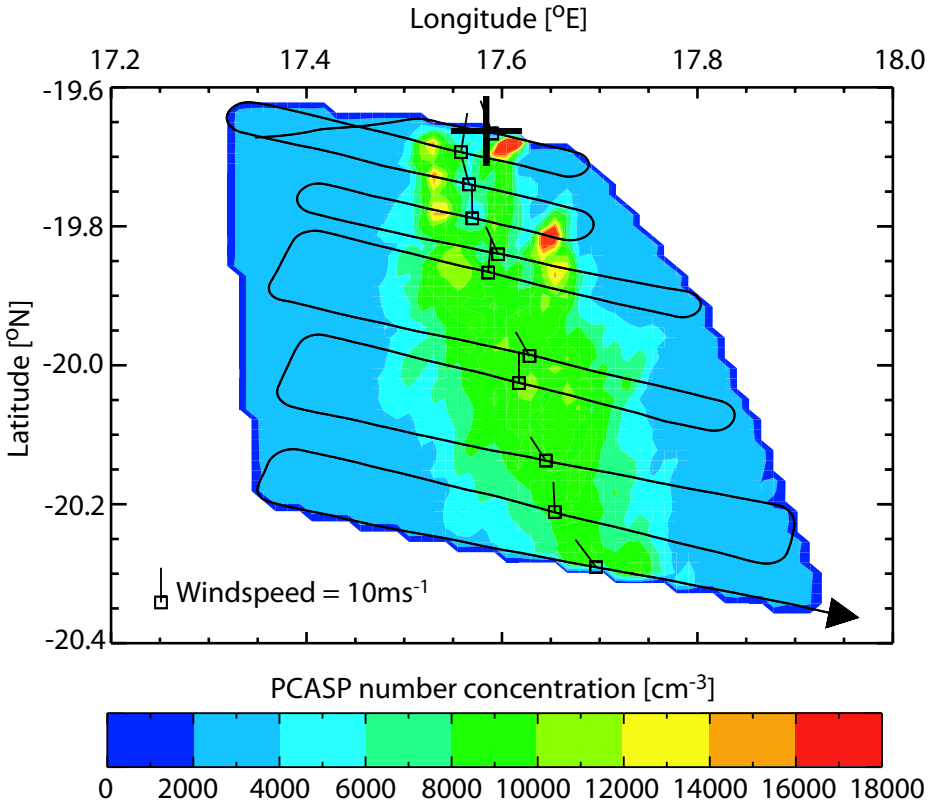

Figure 2.2: *The aircraft flight track over and downwind of the fire at Otavi (R24 - R34). The source region is marked with a cross. The measured PCASP number concentration has been interpolated between each cross plume transit. The mean wind speed and direction within the plume (PCASP concentration > 5000 cm^{-3}) is also indicated with wind barbs.*

2.3 Attenuation of solar radiation by the smoke

The main focus of this chapter is to study the effect of aging on the aerosols optical properties, and a more detailed examination of the radiative effect of the biomass smoke is given in subsequent chapters. However, a brief examination of the attenuation of the solar radiation directly over the Otavi fire is made. Figure 2.3 shows the measured down-welling flux (0.3 - 3.0 μm) from the Broad Band Radiometer (BBR) mounted on the top of the aircraft for the cross plume transit directly over the fire at 210 m AGL (R17). The two large peaks correspond to the areas where the most intense burning was taking place. The values of the down-welling irradiance either side of the peaks are representative of the more dilute background haze, and are typically around 300 Wm^{-2} larger. The significant reduction in the down-welling radiation directly over the fire indicates that a large amount of optically active particles were being emitted into the atmosphere.

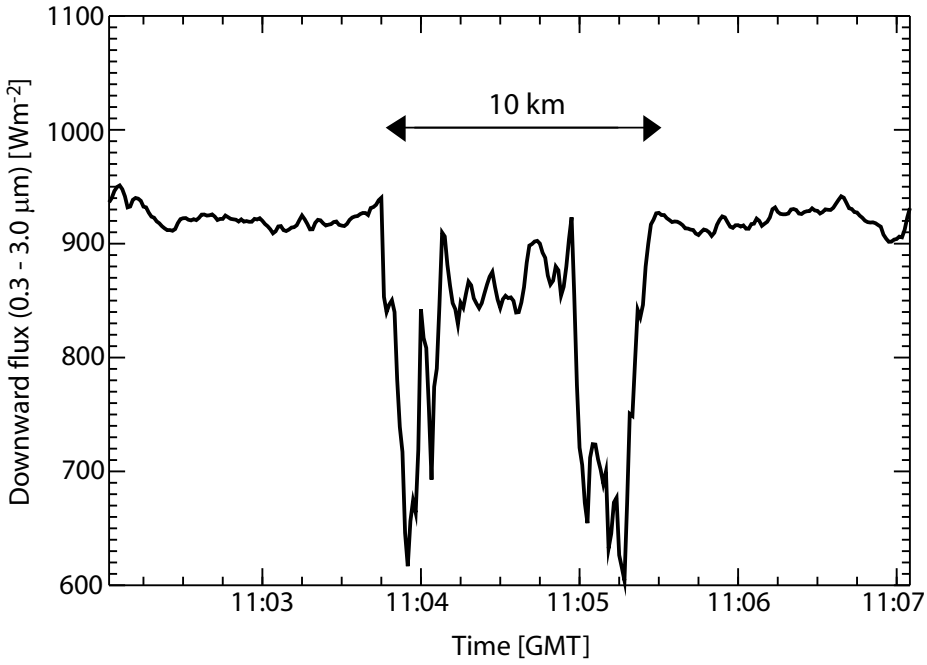

Figure 2.3: *Down-welling irradiance measured with the BBR (0.3 - 3.0 μm) at 210m AGL (R17). The large peaks are where the aircraft flew directly over the two main fires.*

2.4 Aerosol vertical structure

Figure 2.4 shows the vertical profiles of temperature (T) , dew point temperature (T_{dew}), relative humidity (RH), N_{tot}, and the nephelometer scattering coefficient at a wavelength of 0.55μm ($\sigma_{sca\lambda=0.55\mu m}$) measured during the profile ascent down the plume (P4). The temperature profile is very close to the dry adiabat up to $\backsim$ 3.5km AGL and the air in the plume is largely unsaturated. At the top of the profile there is the onset of a temperature inversion that capped the pollutants in the lower troposphere. The RH tended to increase with height and exceeds 100$\%$ at the top of the profile. This suggests that there may have been a tenuous layer of cloud at the top of the boundary layer as was observed visually from the aircraft, and that some cloud-aerosol interactions may occur. It is clear from figure 2.4 that the aerosol is relatively well mixed in the vertical from the surface to 4km AGL where the N_{tot} and $\sigma_{sca\lambda=0.55\mu m}$ fall off close to 0. However, there is a general decrease in both N_{tot} and $\sigma_{sca\lambda=0.55\mu m}$ with altitude. This may be because the main plume resided lower down in the boundary layer and the aerosol above it was more aged and therefore more dilute. Another possible reason is that during the ascent the aircraft flew down the length of the plume and so sampled aerosol that had become more diluted with the background air as the altitude of the aircraft increased. Similar well mixed profiles in the aged regional

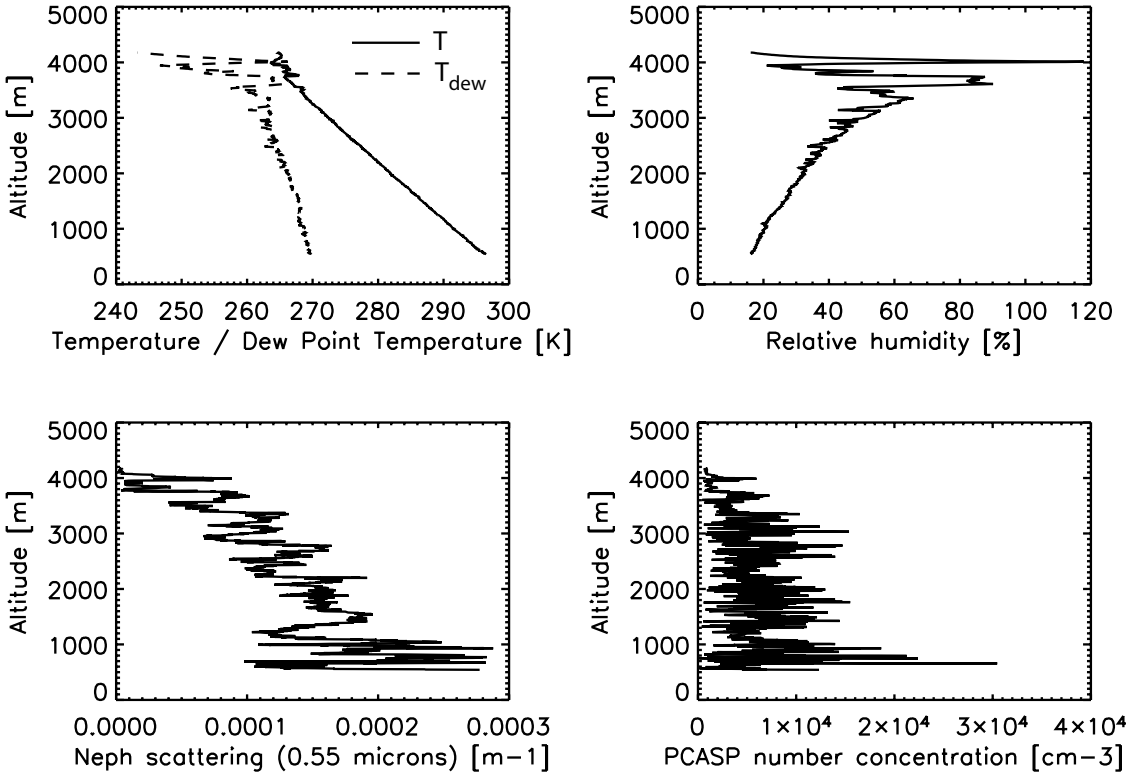

Figure 2.4: *Vertical profiles of temperature (T), dew point temperature (T_{dew}), relative humidity, nephelometer scattering coefficient at a wavelength of 0.55 μm, and the PCASP number concentration from the profile ascent P4. The corrections of Anderson and Ogren (1998) have been applied to the nephelometer data.*

haze were observed on the same day at Etosha Pan which is $\backsim$ 220km away from Otavi (Haywood *et al.*, 2003a,b).

Forward trajectories were run with the NOAA Air Resources Laboratory HYSPLIT model (available at http://www.arl.noaa.gov/ready.html) for air parcels originating at 19.66 °S, 17.57 °E at 13:00 GMT. This corresponds to the position of the fire at the time the aircraft was flying through the plume. The NCEP/NCAR reanalysis meteorological data were used as model input. Trajectories for parcels starting at 500, 1000, and 1500m AGL were modelled. Figure 2.5 shows the modelled trajectories. The trajectories show that the air parcels in the source region are initially advected in approximately a southerly direction. This is consistent with the observed direction that the plume travelled (see figure 2.2). The air parcels then pass over Botswana and South Africa before being advected over the Indian Ocean. The anticyclonic circulation is typical of the meteorology in southern Africa during the dry biomass burning season which tends to be dominated by a persistent high-pressure system (Garstang *et al.*, 1996). This tends to transport atmospheric pollutants over thou-

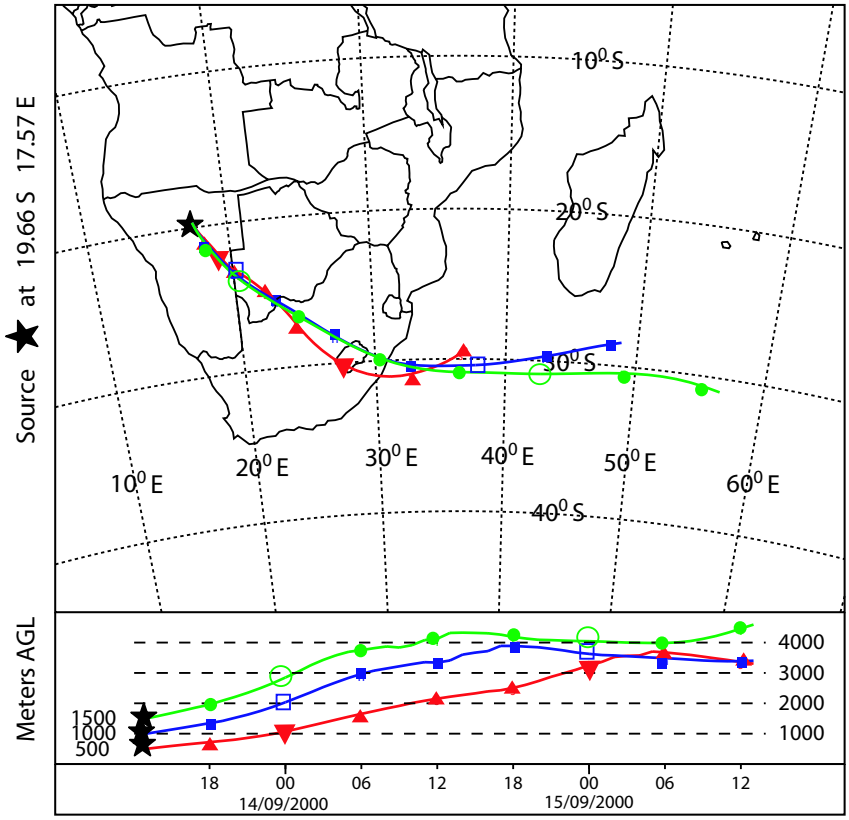

Figure 2.5: *48 hour forward trajectories for air parcels originating at 13:00 GMT on 13th September 2000 (19.66S, 17.57E) at altitudes of 500, 1000, and 1500 metres. Local time = GMT + 2 hours.*

sands of kilometres due to the lack of wet deposition. By the time the air parcels reach the ocean they are all at altitudes $>$ 3km AGL. Measurements of biomass burning aerosol during SAFARI 1992 and 2000 show that the aerosol is frequently observed to exist in elevated polluted layers over ocean regions (chapter 3, Tyson and D'Abreton (1998), Haywood *et al.* (2003a, 2004), Osborne *et al.* (2004)). This has important implications for the sign of the direct radiative forcing of the partially absorbing biomass burning aerosol as it can exist above low-level clouds (Keil and Haywood, 2003) and is investigated further in chapters 4 and 5.

2.5 Aerosol size distribution

Figure 2.6 shows the mean number and volume size distributions measured with the PCASP instrument for the 24 SLRs over and downwind of the fire. The size distributions are representative of the biomass burning aerosol in the plume ($N_{tot} > 5000cm^{-3}$) and are

normalised by the total number and volume concentrations to remove the effect of plume dilution. There is little variation in the size distributions from the SLRs in the plume, especially at particle sizes $< 0.2\ \mu m$ radius. Analyses of the change in the size distribution as the plume travels downwind suggests that there is perhaps a small decrease at particle sizes less than 0.1 μm radius, and a small increase in the number of particles between 0.1 and 0.2 μm radius with age, although it is difficult to determine whether this is significant. There is greater variability at particle sizes $> 0.2\ \mu m$ although no significant trend was evident in the distribution with age of the aerosol. This suggests that little particle growth in the accumulation mode of the aerosol occurs as the plume travels downwind. A typical example of the size distribution measured in the aged regional haze off the coast of Namibia and Angola (see chapter 3) is shown for comparison. The accumulation mode of the aged aerosol contains fewer particles with radii $< 0.1\ \mu m$ than the fresh aerosol but a greater number of particles with radii $> 0.1\ \mu m$. These results are consistent with those of Reid *et al.* (1998), who find only small changes in the size distribution between fresh ($<$ 4 minutes old) and young ($<$ 24 hours old) smoke, but much larger particles in the aged regional haze from Brazilian biomass burning. Reid *et al.* (1998) suggest that once the plume has dispersed into the regional haze, particle growth due to coagulation is a significant mechanism on timescales of a few days, although it is not a major mechanism in fresh smoke plumes.

2.6 Evolution of the aerosol single scattering albedo

The aerosol single scattering albedo is calculated over and downwind of the fire using two different methods; directly from the nephelometer and PSAP measurements, and retrieved using the measured PCASP size distribution with Mie scattering calculations. Mechanisms to explain the observed change in $\omega_{\mathbf{0}\lambda=\mathbf{0.55}\mu\mathbf{m}}$ with age are then investigated.

2.6.1 Derived from the PSAP and nephelometer measurements

The aerosol single scattering albedo at a wavelength of $0.55\mu m$, $\omega_{0\lambda=0.55\mu m}$, was calculated from the nephelometer measurements of the aerosol scattering coefficient, $\sigma_{sca\lambda=0.55\mu m}$, and the PSAP measurements of the aerosol absorption coefficient, $\sigma_{abs\lambda=0.567\mu m}$, for each cross

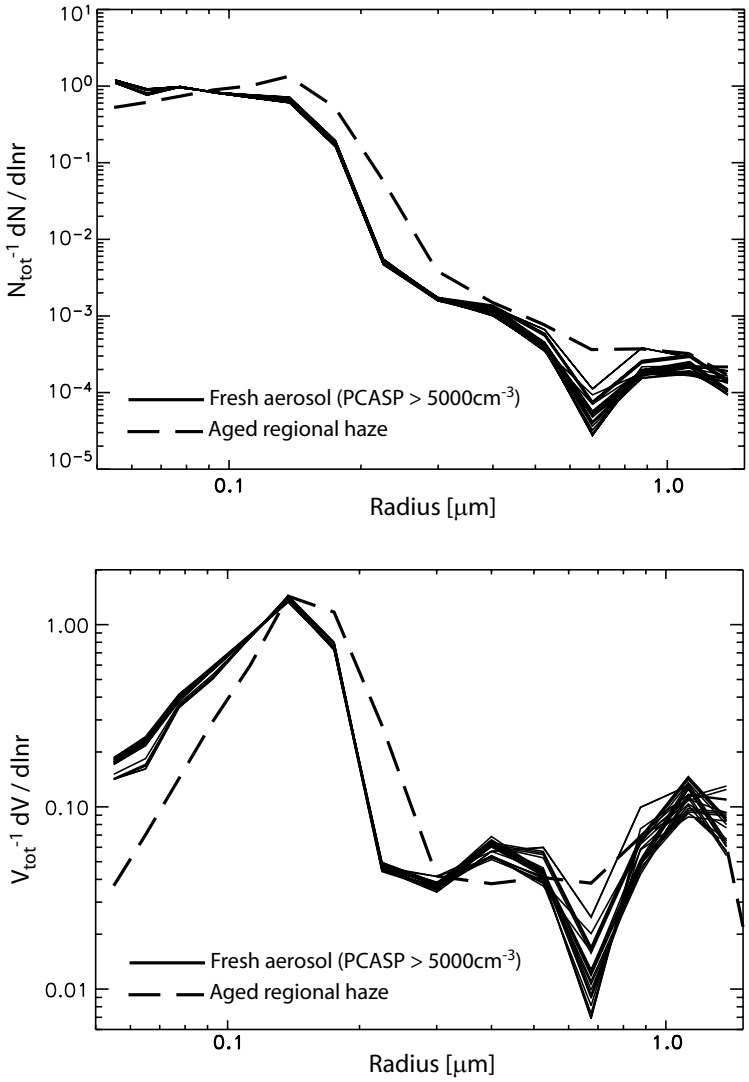

Figure 2.6: *Normalised PCASP number and volume size distributions for the 24 SLRs over and downwind of the fire. The size distributions are representative of the aerosol in the plume (PCASP concentration $>$ 5000cm^{-3}). A typical size distribution measured in the aged regional haze on the 14th September 2000 (see chapter 3) is shown for comparison.*

plume transit where $\sigma_{sca\lambda=0.55\mu m}$ exceeded 1x10^{-4} m^{-1}. This limit was the typical background value outside of the influence of the plume, and sharp peaks above this were evident when the aircraft entered the plume itself. The standard corrections described in appendix A were applied to the nephelometer and PSAP data respectively. The mean atmospheric relative humidity within the plume was 22.1 $\%$ (standard deviation = 0.7 $\%$). The effect of an increase in particle scattering on the nephelometer measurements due to water uptake by the aerosol is therefore negligible (Magi and Hobbs, 2003). However, due to the large values of $\sigma_{abs\lambda=0.567\mu m}$ measured in the heavily polluted plume, and the short time that the aircraft was in the plume for each cross plume transit ($<$4 minutes), the effect of saturation of the PSAP data and the different response time of the two instruments needs to be

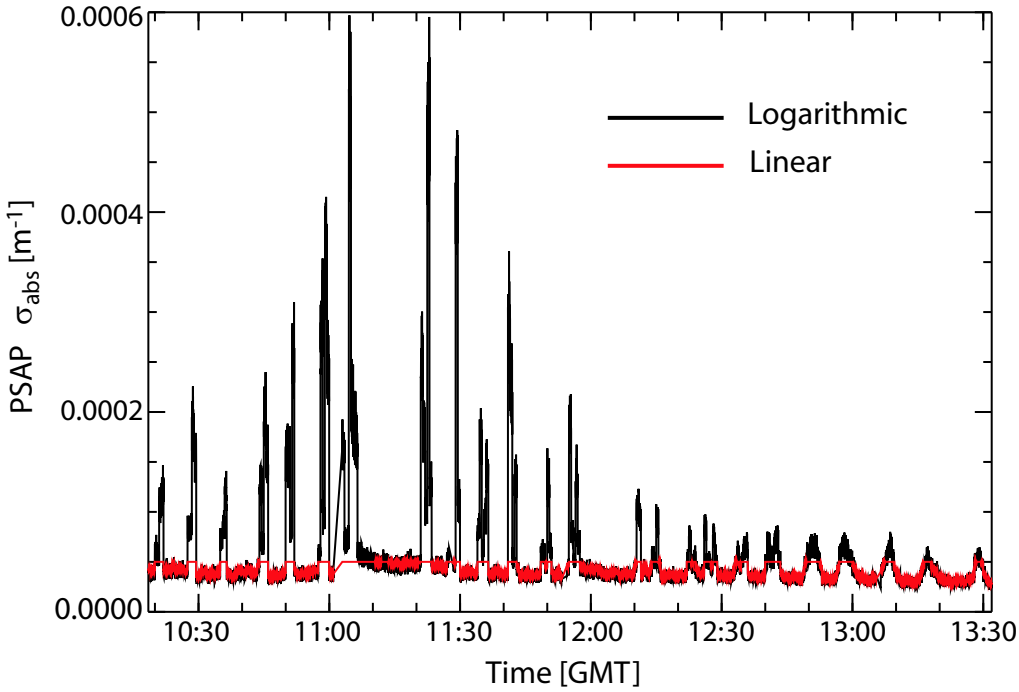

Figure 2.7: *Time series of the PSAP data over and downwind of the Otavi fire (R11-R34). Measurements from the linear and logarithmic signal outputs are shown. The linear output saturates at 50Mm^{-1}.*

considered and is described in more detail below.

Saturation; The PSAP instrument undergoes two different types of signal conditioning; linear and logarithmic. The linear output provides increased sensitivity at low $\sigma_{abs\lambda=0.567\mu m}$ while the logarithmic output provides a greater range and is used in aerosol plumes when $\sigma_{abs\lambda=0.567\mu m}$ is high. This can be demonstrated by considering figure 2.7, which shows a time series of the PSAP data covering the SLRs through the biomass plume (R11-R34). Measurements from both outputs are shown. There is a sharp increase in the absorption as the aircraft enters the plume and a sharp decrease as it exits. It is clear that the linear output saturates at 50 Mm^{-1} as the aircraft enters the plume. The measurements from the logarithmic output do not saturate and are used to calculate $\omega_{0\lambda=0.55\mu m}$ in this study. By comparing the two signal outputs outside of the influence of the plume (background values) it is clear that the logarithmic data produces noisier data than the linear processing. Therefore, the linear output should be used where $\sigma_{abs\lambda=0.567\mu m}$ is $<$50 Mm^{-1} e.g. in the aged regional haze.

Response time; The response time of the nephelometer is 1Hz compared to the PSAP instrument which integrates over a 30 second time period. Therefore the nephelometer

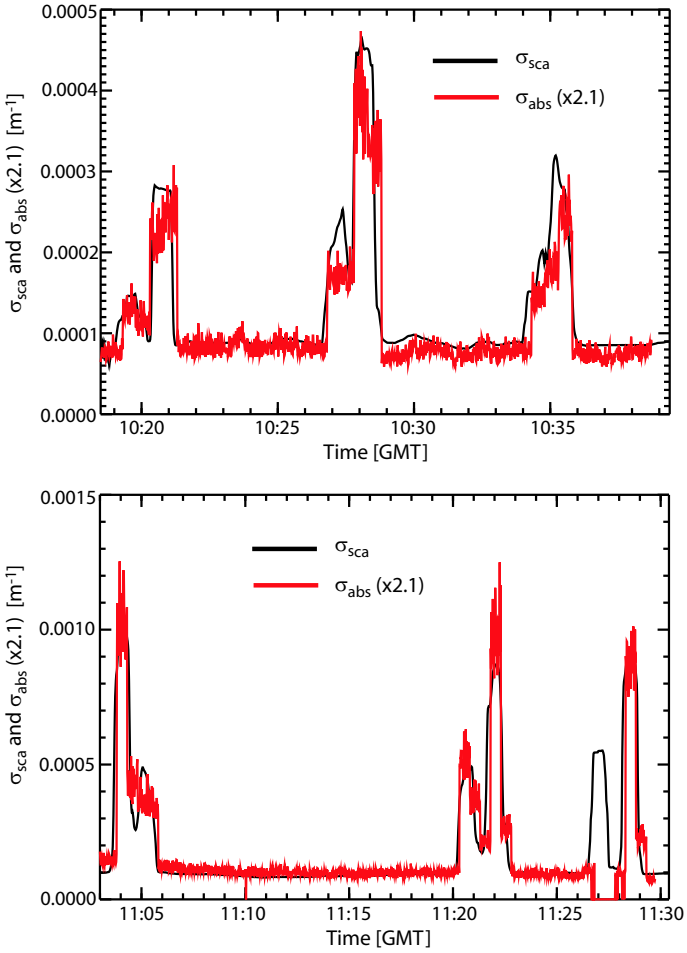

Figure 2.8: *Time series of the raw PSAP data (logarithmic output) for 6 cross plume transits (red). Also shown is the nephelometer data (black) which has been processed to replicate the longer response time of the PSAP. The standard corrections detailed in appendix A still need to be applied to the data. The PSAP data has been multiplied by 2.1 to approximately overlap the nephelometer data. At 11:27 GMT there is an increase in the nephelometer scattering but the PSAP data falls off to 0. Artifacts such as this were removed from the data set before the ω_0 calculation. It should be noted that the y-axis is different between the two plots in order to show the smaller peaks in the upper panel in more detail.*

data is smoothed to replicate the integration period of the PSAP data and shifted in time to account for the longer response time of the PSAP instrument. This processing is not typically applied in background aerosol (e.g. aged regional haze) because the aerosol tends to be more uniform over much larger spatial scales than in the fresh biomass plume studied here. Therefore the data in the background aerosol tends to be averaged over a longer time period (typically 30 minutes) and so the effect of the response time is negligible. Figure 2.8 show the processed nephelometer data and the logarithmic output from the PSAP from a series of runs through the plume. The PSAP data has been enhanced by a multiplicative factor to allow an easier comparison with the nephelometer data on the same figure. The

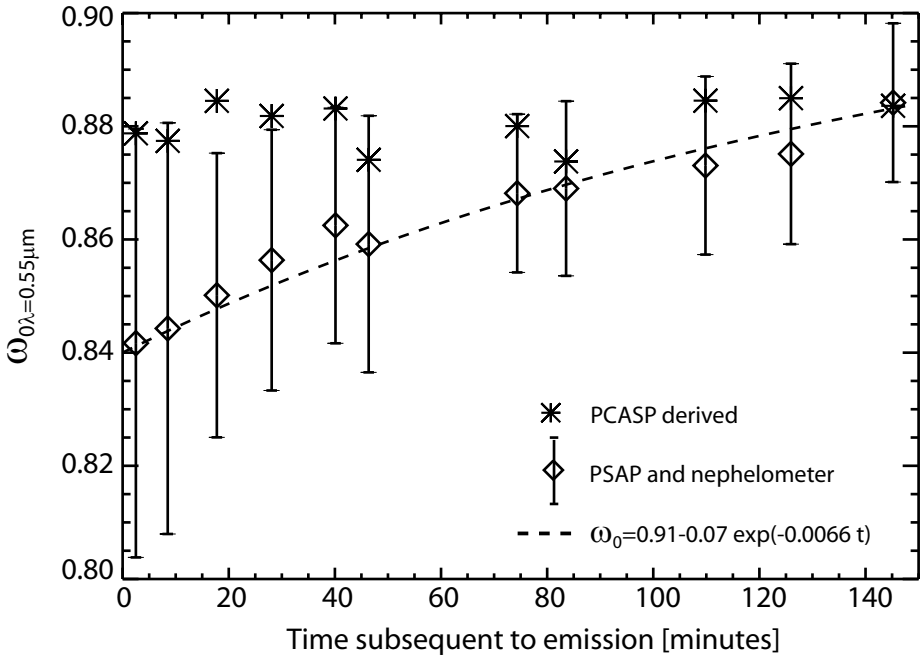

Figure 2.9: *Evolution of the aerosol single scattering albedo downwind of the fire. Diamonds represent the mean value for each cross plume transit measured with the PSAP and nephelometer. Error bars are the standard deviation from this mean. Values using the mean PCASP size distribution for each transit and Mie scattering calculations (n=1.54-0.0018i) are shown with an asterisk. An exponential fit to the data is shown with the dashed line.*

PSAP and processed nephelometer data are very well correlated with an evident increase as the aircraft enters the plume, and decreasing to the background values when it exits. The good correlation also indicates that no overloading of the PSAP filters occurs.

Figure 2.9 shows the evolution of $\omega_{0\lambda=0.55\mu m}$ as the plume travels downwind from the fire source. The $\omega_{0\lambda=0.55\mu m}$ calculation at the source combines measurements from four SLRs at various altitudes over the fire (765, 914, 1,057, 1,233 m AGL). The standard deviation about the mean $\omega_{0\lambda=0.55\mu m}$ is greatest at the source due to the large variability in the smoke plume directly above the fire. The time subsequent to emission is estimated from the measured wind speed and direction across each cross plume transit indicated on figure 2.2 and the aircraft Global Positioning System (GPS) data. The $\omega_{0\lambda=0.55\mu m}$ increases from 0.84 at source to 0.88 two and a half hours subsequent to emission, indicating that the aerosol is becoming less absorbing / more scattering with age. An exponential fit to the PSAP and nephelometer derived single scattering albedo of the form,

$$\omega_{0\lambda=0.55\mu m} = 0.91 - 0.07e^{-0.0066t}, \tag{2.1}$$

where t is the time subsequent to emission in minutes, suggests that it will take approximately 5 hours of aging in the atmosphere for the biomass burning aerosol $\omega_{0\lambda=0.55\mu m}$ to reach 0.90, typical of the aged regional haze measured off the coast of Namibia and Angola during SAFARI 2000 (Haywood *et al.*, 2003a). Reid *et al.* (1998) find a similar increase of 0.06 in $\omega_{0\lambda=0.55\mu m}$ with age from measurements in fresh ($<$ 4 minutes) and aged (2-4 days) biomass burning aerosol in Brazil. The results from the biomass smoke plume studied here indicate that a rapid transformation in $\omega_{0\lambda=0.55\mu m}$ occurs on timescales of less than a day.

2.6.2 Derived from the PCASP size distribution and Mie scattering calculations

$\omega_{0\lambda=0.55\mu m}$ was also calculated using the mean PCASP size distributions measured along each cross plume transit with Mie scattering calculations. The size distributions were constrained to the plume by restricting the analysis to measurements where the total number concentration exceeded 5000 cm^{-3} (see figure 2.6). A refractive index of 1.54 - 0.018i is used. This is the campaign mean refractive index for the aged regional haze (Haywood *et al.*, 2003a) and is in good agreement with AERONET retrieved values on the same day at Etosha Pan (Haywood *et al.*, 2003b), which is approximately 220 km West from the Otavi fire. The PCASP derived values of $\omega_{0\lambda=0.55\mu m}$ are shown in figure 2.9 and are higher than those derived from the nephelometer and PSAP measurements. There is little variation in the modelled $\omega_{0\lambda=0.55\mu m}$ as the aerosol ages, with a mean value of 0.88 and a standard deviation of 0.004. This constancy implies that the effective refractive index of the aged aerosol is not representative of the refractive index within the plume, especially at the source of the aerosol. Increasing the imaginary part of the refractive index to 0.025i decreases the $\omega_{0\lambda=0.55\mu m}$ at source to 0.84, which is consistent with the independent PSAP and nephelometer result. This suggests that in this case it is more important to constrain changes in the aerosol refractive index than the variation in the size distribution when determining $\omega_{0\lambda=0.55\mu m}$ within the plume. However, implicit in the Mie scattering calculations and the PCASP measurements is that the aerosol particles are spherical. The effect of non-spherical particles on the measured size distribution is unknown and requires additional investigation. However, the variation in particle morphology with age and the resulting effect on the aerosols optical properties is studied further in sections 2.6.3 and 2.6.4.

2.6.3 Model simulations of the black carbon morphology

Fresh biomass burning aerosol exists as an external mixture in the plume, consisting of quasi-spherical scattering components (organic and inorganic matter) and chain aggregates of black carbon (BC) (Pósfai *et al.*, 2003, Li *et al.*, 2003). Figure 2.10 shows transmission electron microscopy (TEM) images of biomass burning aerosol collected in a biomass plume by the University of Washington's CV-580 aircraft in the Timbavati Game Reserve during SAFARI 2000 (Hobbs *et al.*, 2003). The BC chain like structures emitted from the fire consist of aggregates of individual BC spherules. TEM images of BC from biomass burning aerosol from SAFARI 2000 show that the typical size of the individual BC spherules is in the range 0.01 - 0.025μm radius (Pósfai *et al.*, 2003). The lower end of the range is close the value of 0.0118μm reported for BC in WCP (1986). Pósfai *et al.* (2003) also observe the BC structures to have sizes ranging from a few attached spherules to micrometer sized branching aggregates such as that in figure 2.10 (b). As the aerosol ages in the atmosphere, the BC chain-like aggregates tend to collapse into densely packed clusters (Johnson *et al.*, 1991, Martins *et al.*, 1998a,b). This could be the result of cloud processing and water vapour interactions as suggested by Hallett *et al.* (1989), although low values of RH were observed in the Otavi smoke plume. Measurements of biomass burning aerosol in Brazil suggest that smoke particles that have resided in the atmosphere for more than 1 hour have collapsed sufficiently to be considered spherical (Martins *et al.*, 1998b). This time-scale is comparable to that where the $\omega_{0\lambda=0.55\mu m}$ is observed to increase rapidly with age from the fire at Otavi ($\backsim$ 2.5 hours). This raises the question;

Can the change in the BC morphology with age explain the measured change in ω_0?

To investigate the effect, the optical properties of the BC aggregates were modelled with a Mie scattering code based on the T-Matrix method (Mishchenko and Travis, 1998). The code[1] solves the Maxwell wave equations for an ensemble of non-overlapping clusters of spheres that are randomly orientated with respect to the incident radiation. Fuller *et al.* (1999) use the code to model linear chains of BC spherules with up to 10 individual BC spheres in the chain. The work of Fuller *et al.* (1999) is extended here to model the proper-

[1] code available at http://www.giss.nasa.gov/$\backsim$crmim; last accessed 01/09/04

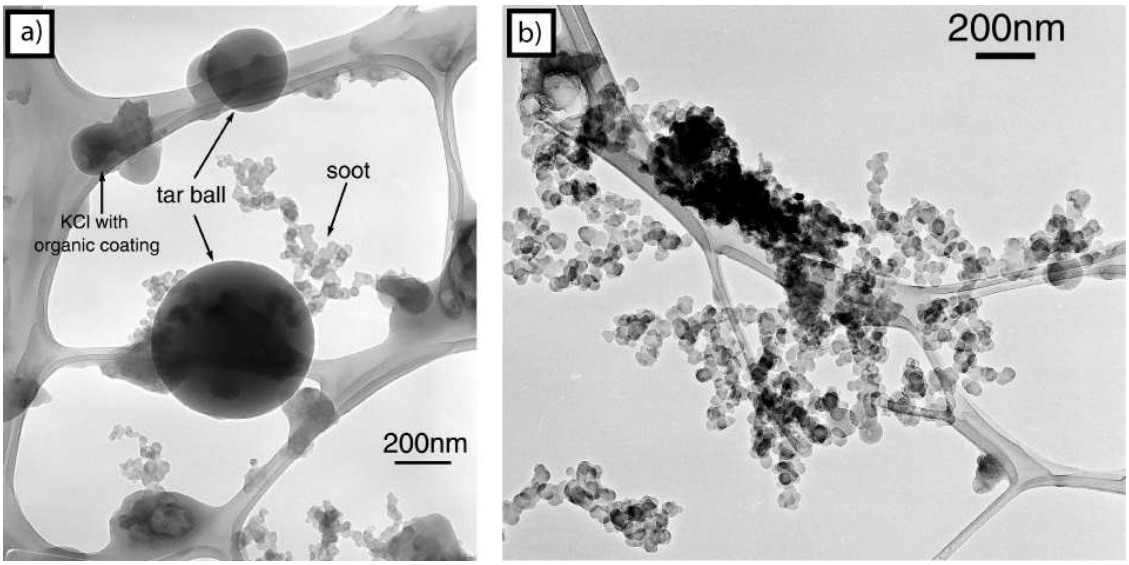

Figure 2.10: *TEM images of particles collected in a fresh biomass plume onboard the University of Washington's CV-580 aircraft in the Timbavati Game Reserve during SAFARI 2000. a) External mixture of BC (soot) aggregates, tar balls, and inorganic salts with an organic coating b) Micrometer sized BC aggregates estimated to have aged between 12 and 55 minutes subsequent to emission. Images courtesy of P. R. Buseck.*

ties of more realistic 3-D structures of BC chains and clusters observed in electron microscope (EM) images of particles emitted from biomass and fossil fuel burning (e.g. Johnson *et al.* (1991), Pósfai *et al.* (2003), Li *et al.* (2003), Martins *et al.* (1998a,b)). Figure 2.11 shows some examples of the BC structures that were modelled, consisting of both compact clusters associated with aged biomass burning aerosol and chain like aggregates more common in fresh aerosol, with the number of individual spherules, N, ranging from 1 (single sphere) to 251 spheres. To characterise the shapes of the modelled structures, a parameter called the asphericity, S, is defined, where

$$S = \frac{D_{max}}{D_{vol}} = \frac{D_{max}}{2(N({r_m}^3))^{1/3}}. \tag{2.2}$$

D_{max} is the maximum physical length of the structure over all orientations and r_m is the radius of each of the individual BC spherules. D_{vol} is the volume mean diameter of the shape i.e. the diameter that a sphere would have with the total volume of the individual BC spherules. Therefore, a value of S=1.0 corresponds to a sphere and as S becomes larger the shape becomes increasingly non-spherical. It can be seen from equation 2.2 that increasing r_m increases D_{vol}. However, D_{max} is increased by the same factor and so the asphericity is

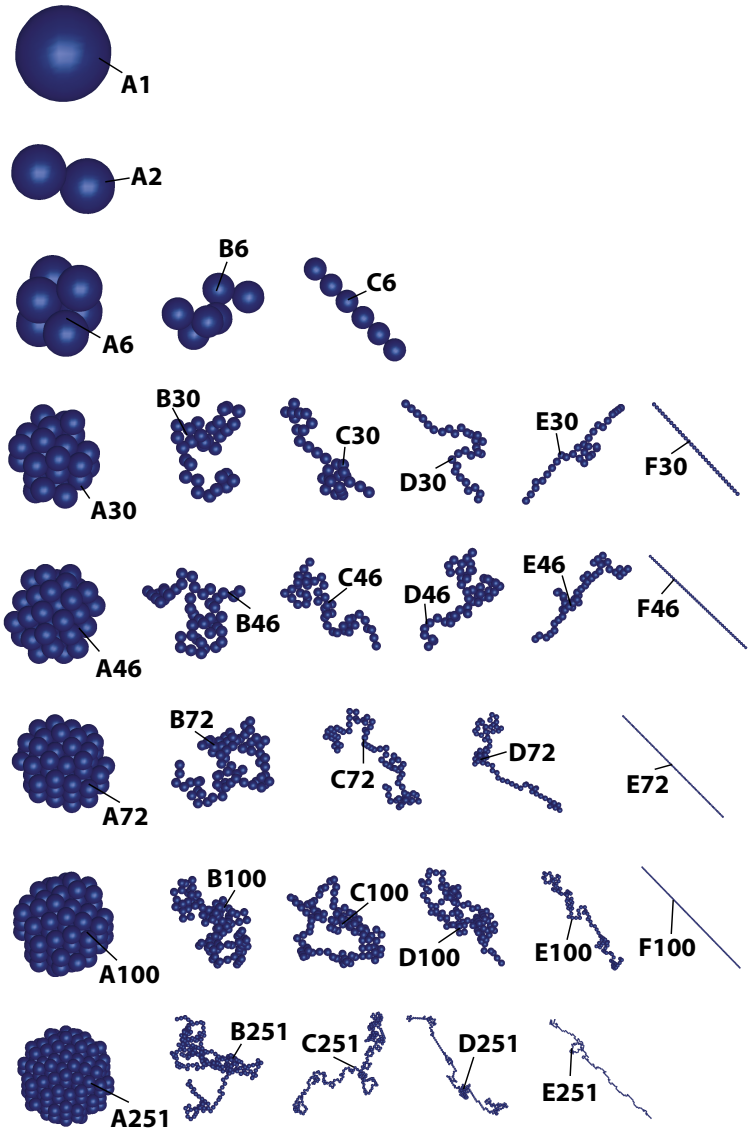

Figure 2.11: *Examples of the BC chains and clusters that were modelled. A FORTRAN code was written to generate the morphologies of quasi-random aggregates and clusters for input to the Mie code. The number of spheres and asphericity, S, of the above shapes are given in table 2.2.*

independent of r_m. This is useful when looking at the effect of changes in r_m for a given shape. Table 2.2 summarises the values of the asphericity for the structures in figure 2.11.

The optical properties were calculated with values of r_m of 0.0118 and 0.025μm, covering the approximate range of observed values (Pósfai *et al.*, 2003). Table 2.2 also lists the values of D_{max} for both values of r_m. It can be seen that the physical size of the modelled structures covers the few spherules to micrometer sized aggregates observed in TEM images from SAFARI 2000 (Pósfai *et al.*, 2003). The BC was assumed to have a refractive index , n_{abs}, of 1.75-0.44i WCP (1986). Figure 2.12 shows the modelled orientationally

Shape	N	S	D_{max} [μm] r_m=0.0118	D_{max} [μm] r_m=0.025	Shape	N	S	D_{max} [μm] r_m=0.0118	D_{max} [μm] r_m=0.025
A1	1	1.00	0.0236	0.0500	A72	72	1.31	0.1283	0.2717
A2	2	1.59	0.0472	0.1000	B72	72	2.97	0.2913	0.6172
A6	6	1.50	0.0645	0.1366	C72	72	4.35	0.4274	0.9055
B6	6	2.40	0.1027	0.2177	D72	72	5.70	0.5599	1.1862
C6	6	3.30	0.1416	0.3000	E72	72	17.31	1.6992	3.6000
A30	30	1.42	0.1042	0.2208	A100	100	1.32	0.1447	0.3066
B30	30	2.60	0.1906	0.4038	B100	100	2.85	0.3127	0.6625
C30	30	3.59	0.2632	0.5575	C100	100	3.26	0.3569	0.7561
D30	30	4.73	0.3469	0.7349	D100	100	4.34	0.4758	1.0081
E30	30	5.86	0.4297	0.9104	E100	100	7.32	0.8015	1.6980
F30	30	9.65	0.7080	1.5000	F100	100	21.54	2.3600	5.0000
A46	46	1.36	0.1150	0.2436	A251	251	1.24	0.1848	0.3916
B46	46	2.51	0.2120	0.4492	B251	251	4.38	0.6518	1.3810
C46	46	3.58	0.3031	0.6421	C251	251	6.73	1.0026	2.1241
D46	46	4.94	0.4177	0.8850	D251	251	9.23	1.3739	2.9108
E46	46	7.14	0.6037	1.2790	E251	251	17.71	2.6371	5.5870
F46	46	12.84	1.0856	2.3000					

Table 2.2: *A summary of the number of spheres, N, the asphericity, S, and the maximum physical length, D_{max}, of the BC chains and clusters in figure 2.11. D_{max} is shown with the radius of the individual BC spherules, r_m, at 0.0118 and 0.025μm.*

averaged $\omega_{0\lambda=0.55\mu m}$ as a function of asphericity for BC aggregates containing 6, 30, 46, 72, 100, and 251 individual BC spherules. It is clear that the modelled $\omega_{0\lambda=0.55\mu m}$ increases as the asphericity decreases for all values of N and r_m. As either N or r_m is increased for a given value of asphericity ω_0 is also increased, and is primarily the result of an increase in scattering efficiency with particle size. These two features suggest that:

i) As the BC chain-like aggregates collapse to densely packed clusters with age as observed in TEM images (Johnson *et al.*, 1991, Martins *et al.*, 1998a,b), the $\omega_{0\lambda=0.55\mu m}$ of the BC is increased.

ii) If coagulation was a dominant process in the plume then the particle would become larger and for a given asphericity ω_0 will also increase. However, as mentioned previously, Reid *et al.* (1998) suggest that only once the plume has dispersed into the regional haze does particle growth due to coagulation become a significant mechanism.

The $\omega_{0\lambda=0.55\mu m}$ for the modelled BC structures ranges from 0.011 (small chain-like aggregate) to 0.472 (large packed cluster). Measurements of the single scattering albedo of BC range from $<$ 0.10 to 0.30 (Fuller *et al.*, 1999), suggesting that the largest BC clusters modelled in this study may not have optical properties representative of the mean BC in the biomass burning aerosol. However, BC structures of this size were found to exist as

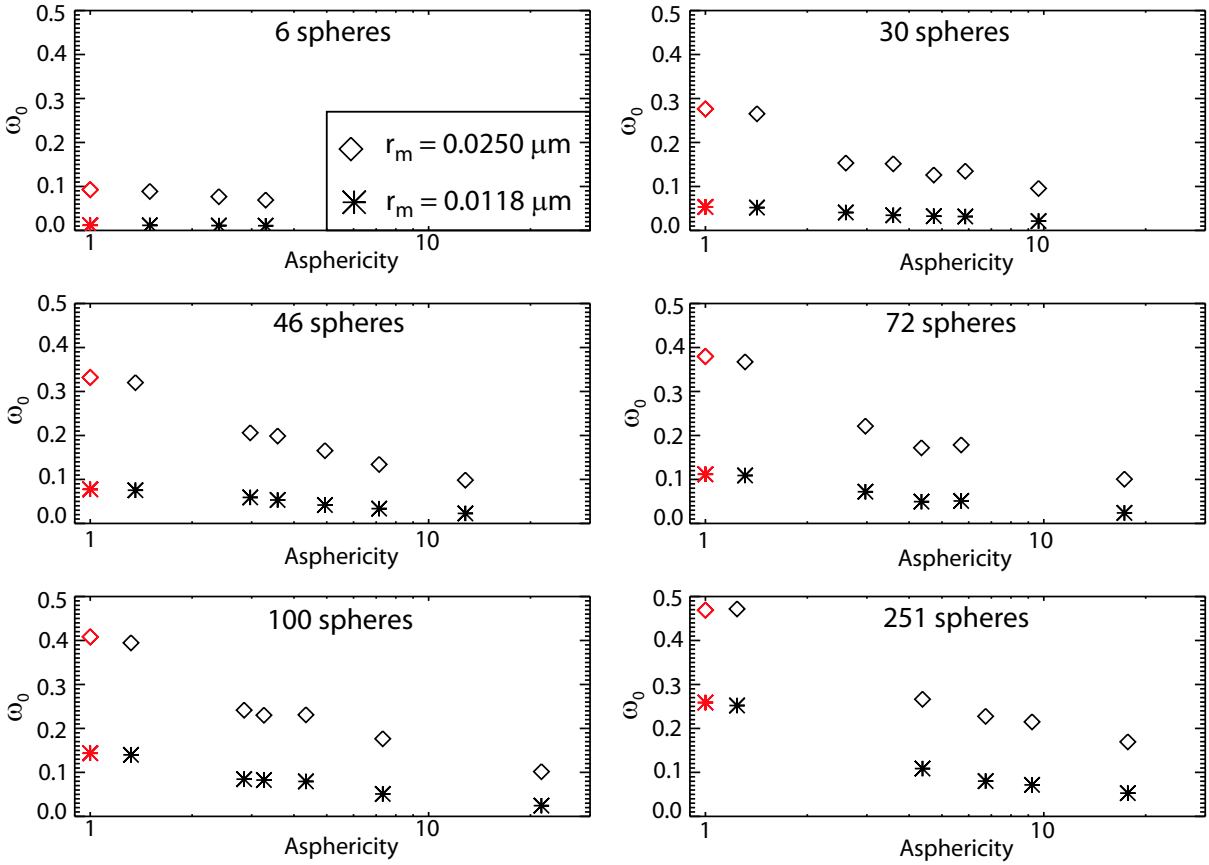

Figure 2.12: *Modelled orientationally averaged ω_0 at a wavelength of 0.55μm for the BC morphologies in figure 2.11 and table 2.2 as a function of their asphericity. The refractive index used is 1.75-0.44i. Results are shown with the radius of the individual BC spherules, r_m, set at 0.0118 and 0.025μm. The red data points (asphericity = 1.0) are for an individual sphere with the same volume of BC as the modelled structures.*

chain like aggregates in biomass plumes during SAFARI 2000 (Pósfai *et al.*, 2003, Li *et al.*, 2003) and may be expected to collapse to clusters of a similar size as modelled here. Also shown in figure 2.12 is the $\omega_{0\lambda=0.55\mu m}$ for a single sphere containing the same volume of BC as the modelled aggregates. The $\omega_{0\lambda=0.55\mu m}$ for the pure spheres is very similar to that of the densely packed clusters of individual BC spherules. This is to be expected as the clusters are quasi-spherical and implies that the assumption of spherical particles is valid in biomass burning aerosol that has aged sufficiently for the chain-like BC aggregates to have collapsed to densely packed clusters.

Although the $\omega_{0\lambda=0.55\mu m}$ of BC is shown to be sensitive to morphology, the modelled BC structures need to be mixed with the scattering components of the biomass burning aerosol to determine the impact on the bulk aerosol properties as measured by the instrumentation onboard the aircraft, and whether variations in the structure of BC can account for the rapid

change in $\omega_{0\lambda=0.55\mu m}$ measured downwind from the Otavi fire.

2.6.4 Mixing state of the aerosol

TEM analysis of particles within biomass plumes during SAFARI 2000 suggest that there are three main classes of particles; organic particles with inorganic inclusions, tar balls (primarily organic), and chain-like aggregates of BC (Pósfai *et al.*, 2003). Figure 2.10 (a) shows an example of these particle types. It is clear that the different particle types are externally mixed in the TEM image and this is a common feature of young biomass smoke (Pósfai *et al.*, 2003).

The optical properties of an external mixture of the BC aggregates with the other components of the biomass burning aerosol are calculated. The absorbing component of the aerosol is assumed to be the BC, whereas the tar balls and organic particles with inorganic inclusions are assumed to be non-absorbing. The scattering components were assumed to be spherical. This is a reasonable assumption as Pósfai *et al.* (2003) and figure 2.10 (a) show that tar balls are generally perfectly spherical and the organic structures with inorganic inclusions are typically quasi-spherical. The scattering components were modelled using Mie scattering calculations with a bi-modal log normal fit to the PCASP size distribution measured in the fresh aerosol and a refractive index, n_{sca}, of 1.53 - 0.00i at 0.55μm (Haywood *et al.*, 2003a), which results in a $\omega_{0\lambda=0.55\mu m}$ of 1.0. Assuming a density, ρ_{sca}, of 1.35 gcm^{-3} (Reid and Hobbs, 1998), the specific extinction coefficient of the scattering material, k_{esca}, is 3.64 m^{2}g^{-1}. The specific extinction coefficient of the BC structures modelled in section 2.6.3, k_{eBC}, ranges from 3.98 - 7.84 m^{2}g^{-1} assuming a density, ρ_{BC}, of 1.7 gcm^{-3} (Haywood *et al.*, 2003a). The single scattering albedo of the external mixture, ω_{0ext}, was then calculated using the equation,

$$\omega_{0ext} = \frac{k_{eBC}\rho_{BC}M_{BC}\omega_{0BC} + k_{esca}\rho_{sca}M_{sca}\omega_{0sca}}{k_{eBC}\rho_{BC}M_{BC} + k_{esca}\rho_{sca}M_{sca}}, \tag{2.3}$$

where M_{BC} and M_{sca} are the respective masses of the BC and scattering components. The M_{BC}/M_{tot} ratio was varied where M_{tot} is the total mass of the aerosol (M_{BC}+M_{sca}). Figure 2.13 shows how ω_{0ext} varies as a function of the M_{BC}/M_{tot} ratio for the different

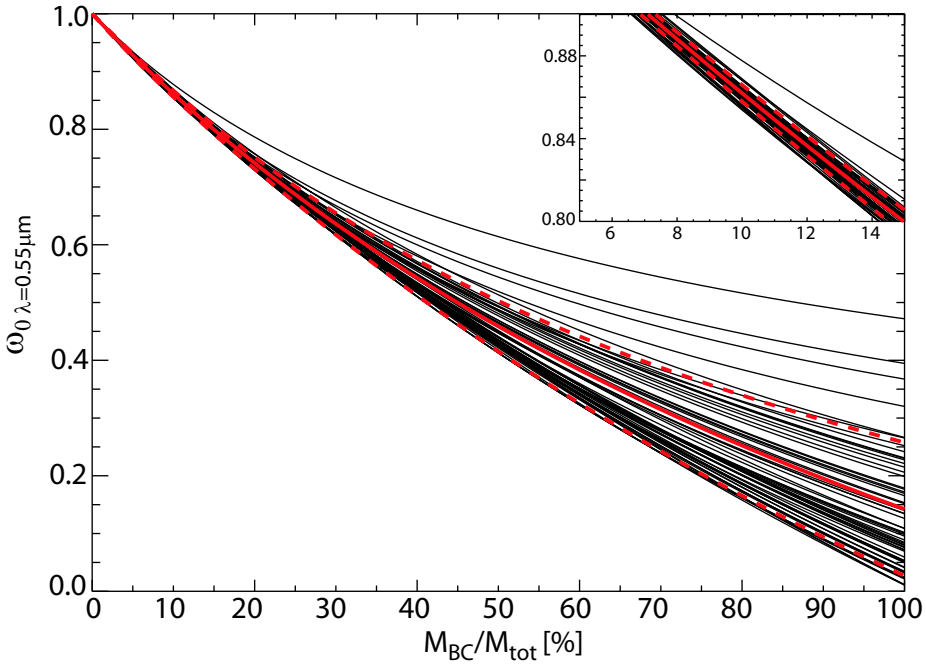

Figure 2.13: *Single scattering albedo at 0.55μm for an external mixture of the modelled BC structures in figure 2.12 and the scattering material modelled from the measured PCASP size distribution (black lines). The mean ω_{0ext} (solid red line) and standard deviation (red dashed lines) for the different BC morphologies is shown. A blow up of the region of interest is shown in the top right corner ($M_{BC}/Mtot$ = 5 to 15 $\%$, $\omega_{0\lambda=0.55\mu m}$ = 0.8 to 0.9).*

BC chain-like and cluster morphologies. It is clear that as M_{BC}/M_{tot} is increased the effect of the BC morphology on ω_{0ext} becomes more important i.e. the range in ω_{0ext} becomes larger. A M_{BC}/M_{tot} of 11.9 $\%$ results in a ω_{0ext} for the different BC structures of 0.84 $\pm$ 0.01, where the value of 0.84 is representative of the measured $\omega_{0\lambda=0.55\mu m}$ at source, and the error represents two standard deviations from the mean and encompasses 61 out of the 62 modelled BC structures. The variation in ω_{0ext} due to the different BC morphologies is smaller than the observed change in $\omega_{0\lambda=0.55\mu m}$ of 0.04 in two and a half hours of aging in the atmosphere. This suggests that the effect of BC morphology on the bulk aerosol optical properties is unlikely to be the dominant mechanism in explaining the measured change.

As the aerosol ages, the BC aggregates tend to become internally mixed with the scattering components, especially in the aged regional haze as a result of coagulation or condensation (Pósfai *et al.*, 2003, 2004). Martins *et al.* (1998a) show that the Maxwell-Garnet mixing rule adequately represents the internal mixture of BC clusters coated with scattering material, typical of particle structures observed in aged regional hazes in Brazil. The equation for the Maxwell-Garnet mixing rule is,

$$n_{eff}{}^2 = n_{sca}{}^2 \left(\frac{n_{BC}{}^2 + 2n_{sca}{}^2 + 2V_{BC}{}^2(n_{BC}{}^2 + n_{sca}{}^2)}{n_{BC}{}^2 + 2n_{sca}{}^2 - 2V_{BC}{}^2(n_{BC}{}^2 + n_{sca}{}^2)} \right), \tag{2.4}$$

where n_{eff} is the effective refractive index of the composite aerosol and V_{BC} is the volume fraction of BC given by,

$$V_{BC} = \frac{M_{BC}}{M_{tot}} \frac{\rho_{aer}}{\rho_{BC}}. \tag{2.5}$$

The mixing rule was used to model the mean M_{BC}/M_{tot} of the aged regional haze measured by the C-130 aircraft during SAFARI 2000 by constraining the values of the biomass burning aerosols n_{eff} equal to 1.54-0.018i (Haywood *et al.*, 2003a,b) and the density, ρ_{aer}, equal to 1.35 gcm^{-3} (Reid and Hobbs, 1998). The same assumptions for ρ_{BC}, n_{abs}, and n_{sca} used in the external mixture calculation were applied. This results in a M_{BC}/M_{tot} of 5.4$\%$ which is consistent with measurements using filter mass loadings collected onboard the aircraft from the aged regional haze (Formenti *et al.*, 2003, Haywood *et al.*, 2003a).

The calculations presented in this section suggest that;

i) the effect of the collapse of BC chain-like aggregates to more compact clusters within the first few hours subsequent to emission is unlikely to explain the large increase in the biomass burning aerosols $\omega_{0\lambda=0.55\mu m}$ within the plume.

ii) the M_{BC}/M_{tot} decreases from approximately 11.9$\%$ at source to 5.4$\%$ in the aged regional haze. Possible mechanisms for the decrease in the mass fraction of BC with age are discussed in section 2.7.

2.7 Summary and Discussion

Airborne measurements over and downwind of an agricultural fire show a rapid increase in $\omega_{0\lambda=0.55\mu m}$ from 0.84 at source to 0.88 two and a half hours subsequent to emission. An exponential fit to the measurements suggests that it will take approximately 5 hours for $\omega_{0\lambda=0.55\mu m}$ to reach 0.90, typical of aerosol in the aged regional haze (Haywood *et al.*,

2003a). The results presented use observations from a single biomass burning fire and may not be representative of the very large number of fires annually in southern Africa. For example, fuel type, fire intensity and the burning phase (predominantly flaming or smoldering combustion) have been shown to influence the composition of the aerosol e.g. (Le Canut *et al.*, 1996, Reid and Hobbs, 1998, Gao *et al.*, 2003, Pósfai *et al.*, 2003). However, Reid *et al.* (1998) find a similar increase of 0.06 in $\omega_{0\lambda=0.55\mu m}$ with age from measurements in fresh and aged smoke in Brazil. This increase has fundamental implications for climate modelling (see chapter 5), and could be combined with modelling efforts to better constrain the radiative effect of biomass burning aerosol on regional (and perhaps global) scales.

An attempt was made to obtain closure between the PSAP and nephelometer measured $\omega_{0\lambda=0.55\mu m}$ and Mie scattering calculations using the varying PCASP size distribution downwind and the fixed refractive index of aged regional haze. Large discrepancies were evident near the source and increasing the imaginary part of the refractive index was required to get consistency. This suggests that it is more important to constrain changes in the effective refractive index than the variation in the size distribution within the plume during the initial hours subsequent to emission.

Post combustion BC is emitted as chain-like structures of individual spherules that tend to collapse to densely packed clusters in the first few hours subsequent to emission (Martins *et al.*, 1998b). The Mie scattering properties of realistic chain-like and cluster morphologies observed in TEM images of BC from biomass burning aerosol were modelled. It was found that the $\omega_{0\lambda=0.55\mu m}$ of BC increases as the structures become more spherical. The clusters of individual spherules were found to have similar optical properties to spheres containing the same volume of BC. This implies that the spherical approximation commonly used for modelling the radiative effect of BC aerosols (e.g. Haywood and Shine (1997), Haywood *et al.* (1997), Sato *et al.* (2003)) is reasonably valid on global (and perhaps regional) scales.

Model results suggest that for $\omega_{0\lambda=0.55\mu m}$ to be consistent with measurements, the M_{BC}/M_{tot} decreases from approximately 12% at source to 5.4% in the aged regional haze. The effect of the change in BC morphology with age on the bulk aerosol absorption is found to be of secondary importance. Therefore, the change in $\omega_{0\lambda=0.55\mu m}$ is likely the result of an increase in the scattering efficiency of the aerosol with age. The small change in the measured PCASP size distribution downwind of the Otavi fire indicates little growth in the accumu-

lation mode aerosol particles with age in the plume, and is consistent with measurements of Brazilian smoke (Reid and Hobbs, 1998). Therefore, an increase in particle scattering through growth does not dominate. Rapid increases in particle size have been observed just above biomass fires where the concentrations of particles are orders of magnitude higher than in the plume that is advected downwind, thus coagulation processes are likely to be important immediately after emission (Hobbs, 2003), although less so over the time periods under investigation in this study. The formation of new scattering aerosol particles is therefore favoured as the process which increases $\omega_{0\lambda=0.55\mu m}$. The production of new particles can occur through the conversion of inorganic and semi-volatile organic species from the gaseous phase into the particulate phase (gas-particle conversion). Reid *et al.* (1998) observe an increase of 20 - 45$\%$ in aerosol mass concentration (inorganic plus organic) from fresh to aged biomass burning aerosol and estimate that between 50 - 75$\%$ of this increase is the result of condensation of volatile organics from the gas phase. Further, Hobbs *et al.* (2003) find that subsequent to removing the effect of plume dilution from a separate fire in southern Africa, the number of particles began to increase 10 minutes after emission. This is supported by Gao *et al.* (2003), who observe a rapid increase in some organic and inorganic species in the first 40 minutes of aging of the biomass smoke in the same fire studied by Hobbs (2003). TEM derived number concentrations of different particle types indicate a large increase in the number of tar balls (primarily OC) as the aerosol ages (Pósfai *et al.*, 2003). The spherical shape of the tar balls (see figure 2.10 a)) are indicative of a gas to particle type nucleation mechanism (Pósfai *et al.*, 2003).

Eatough *et al.* (2003) measure a decrease in the M_{BC} to fine particulate ($< 1.5\mu m$ diameter) mass between fresh and aged aerosol supporting the hypothesis that scattering material is condensing from the gas phase. In contrast, thermal optical transmission measurements from quartz filters collected onboard the C-130 aircraft suggest that the mass of elemental carbon to OC is smaller for fresh aerosol compared to the aged haze (Formenti *et al.*, 2003). However, the results are uncertain due to poor sampling statistics in the plume, and may also be biased by measurement artefacts that this technique suffers from in high intensity smoke plumes (Reid *et al.*, 2005). Kirchstetter *et al.* (2003) also find an increase in M_{BC}/M_{OC} with age but attribute this increase to the biomass burning aerosol mixing with air masses that are characterised by a higher M_{BC}/M_{OC} ratio (e.g. fossil fuel burning). The time scale for this large-scale mixing is likely to be significantly larger than measured

/ modelled here. Furthermore, the model simulations in this study assume that BC is the only significant absorbing component, whereas biomass burning aerosol is likely to contain amounts of absorbing coloured organic matter (Formenti *et al.*, 2003, Sato *et al.*, 2003, Pósfai *et al.*, 2004).

The apparent discrepancy between the results in this study and those from some of the filter measurements may be elucidated in future measurement campaigns utilising aerosol mass spectrometers. This would enable direct in-situ high temporal measurements of changes in the mass of organic and inorganic components in the biomass plume with age, something that is not possible with filter based methods.

Chapter 3

Aged Regional Haze: characterisation of properties and local direct radiative effect

3.1 Introduction

This chapter analyses aircraft measurements of biomass burning aerosol in the aged regional haze that pervades large areas of southern Africa throughout the biomass burning season. The work in chapter 2 showed that there is a rapid evolution of the optical properties of the smoke on time-scales of less than a day. However, due to a lack of wet deposition in the southern African region during the biomass burning season, the smoke can remain in the atmosphere for several weeks and can travel over large distances. For example, the C-130 aircraft detected biomass smoke at Ascension Island, some 2500 km off the coast of Angola (Haywood *et al.*, 2004). Furthermore, the monthly mean aerosol optical depth retrieved from the MODIS satellite shows significant amounts of biomass burning aerosol being transported thousands of kilometres from the source regions in September (see chapter 5 and Myhre *et al.* (2003)). It is therefore of vital importance to characterise the properties of the aged aerosol in order to model the radiative effect of biomass smoke on regional and global scales.

The UK Met Office C-130 aircraft sampled the aerosol physical and optical properties on six dedicated flights in the aged regional haze advected off the West coast of Namibia and Angola during SAFARI 2000 (Haywood *et al.*, 2003a). In-situ measurements of the aerosol in combination with a variety of remote sensing measurements including both broadband short-wave irradiances and spectrally resolved radiances were made. Osborne *et al.* (2004) present a detailed analyses of these measurements for two of the flights (a788 on 10th September 2000 and a789 on 11th September 2000). This chapter presents similar results for a CASE on the 14th September 2000 (flight a791), and also extends the analysis to include measurements from the short wave spectrometer (SWS).

The main aims of this chapter are to a) characterise the vertical structure of the aerosol off the coast of Namibia and Angola, b) characterise the physical and optical properties of the aged biomass burning aerosol, c) perform a detailed comparison of the current methods used to retrieve the aerosol optical depth from measurements made on-board the C-130 aircraft, d) to make recommendations of improvements in the measurements that are required to retrieve the optical depth more accurately for future campaigns, and e) validate the AERosol RObotic NETwork (AERONET) retrieval algorithm of the aerosol size distribution and optical properties (Dubovik and King, 2000) against in-situ measurements made onboard the aircraft.

3.2 Aircraft Flight Pattern

The aircraft performed a series of different manoeuvres during flight a791 to measure the aerosol physical and optical properties of the biomass burning aerosol in the aged regional haze, the vertical structure of the aerosol, and both the up and down-welling radiation. The flight pattern consisted of:

i) three profiles throughout the aerosol layer to characterise the vertical structure.

ii) a series of straight and level runs (SLRs) within the biomass burning aerosol layer to measure the physical and optical properties.

iii) SLRs above the aerosol layer to measure the up-welling broadband flux and the up-

welling radiances.

iv) SLRs below the biomass burning aerosol layer to measure the marine boundary layer (MBL) aerosol and both the down-welling and up-welling radiances. These were typically at an altitude of 33 metres above sea level (ASL).

v) a series of banked orbits below the aerosol layer (122 metres ASL) to measure the down-welling radiance as a function of scattering angle.

Table 3.1 summarises the run numbers, the time of the runs (local time = GMT+2 hours), and the relevant aerosol and radiation measurements that are used in this study. Figure 3.1 (a) shows the Global Positioning System (GPS) flight track of the aircraft for the region where the radiation measurements and vertical structure measurements are made, and figure 3.1 (b) shows a schematic of these runs.

3.3 Vertical structure

Figures 3.2 to 3.4 show the vertical profiles of temperature, dew point temperature, relative humidity (*RH*), PCASP number concentration (N_{tot}), and the nephelometer scattering at a wavelength of 0.55 μm ($\sigma_{sca\lambda=0.55\mu m}$) measured onboard the aircraft for the three profiles used in this study. All three vertical profiles show similar features, with the biomass burning aerosol plume existing in an elevated layer above the MBL. The biomass plume and MBL are separated by a clean air slot which is characterised by lower aerosol concentrations and scattering, and thus greater visibility than the air situated above and below them. Clean air slots were observed throughout the SAFARI 2000 campaign, both over land and oceanic regions, and are perhaps the result of air from the free troposphere being transported downward by large scale subsidence associated with the anticyclonic conditions prevelant over southern Africa in the dry season (Hobbs, 2003). A photograph of a clean air slot taken from the C-130 aircraft off the coast of Namibia and Angola is shown in figure 3.5.

Table 3.2 summarises the mean RH, N_{tot}, and $\sigma_{sca\lambda=0.55\mu m}$ in the MBL, clean air slot, and biomass burning aerosol layer for each of the three profiles. The RH was high in the MBL, with mean values ranging from 82 - 89 $\%$. Therefore, the sea salt particles in the MBL

Run number	Time [GMT]	Altitude	Type of run	Measurements
R2	07:24:45 - 08:09:45	FL120	SLR in biomass burning aerosol	Aerosol optical/physical properties
R3	08:17:55 - 08:47:35	FL080	SLR in biomass burning aerosol	Aerosol optical/physical properties
R4	08:53:30 - 09:23:30	FL100	SLR in biomass burning aerosol	Aerosol optical/physical properties
R12	13:27:15 - 13:47:15	FL170	SLR in biomass burning aerosol	Aerosol optical/physical properties
P9	11:17:34 - 11:40:01	15m - FL190	Profile ascent	Vertical structure
P10	12:02:02 - 12:18:08	FL190 - 15m	Profile descent	Vertical structure
O4-R11	12:59:53 - 13:22:55	122m - FL190	Profile ascent	Vertical structure
R10.1	12:27:54 - 12:37:54	33m	Low level SLR	MBL aerosol, Down/Up-welling radiances
R10.2	12:40:40 - 12:50:40	33m	Low level SLR	MBL aerosol, Down/Up-welling radiances
R8	11:41:20 - 11:46:30	FL190	High level SLR	Up-welling broadband flux and radiance
R9	11:47:55 - 11:57:55	FL190	High level SLR	Up-welling broadband flux and radiance
Orbits	12:51:41 - 12:59:53	122m	Low level banked orbits	Radiance (scattering angle)

Table 3.1: *A brief summary of the measurements made on the runs in flight a791 that are used in this study. Local time=GMT+2 hours. FL is the altitude in feet x 100.*

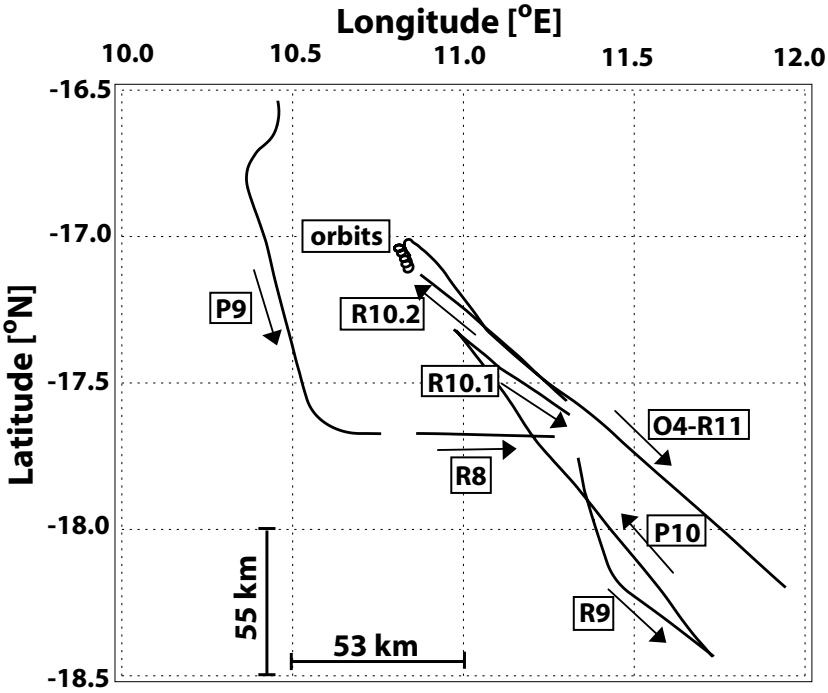

(a) Flight track

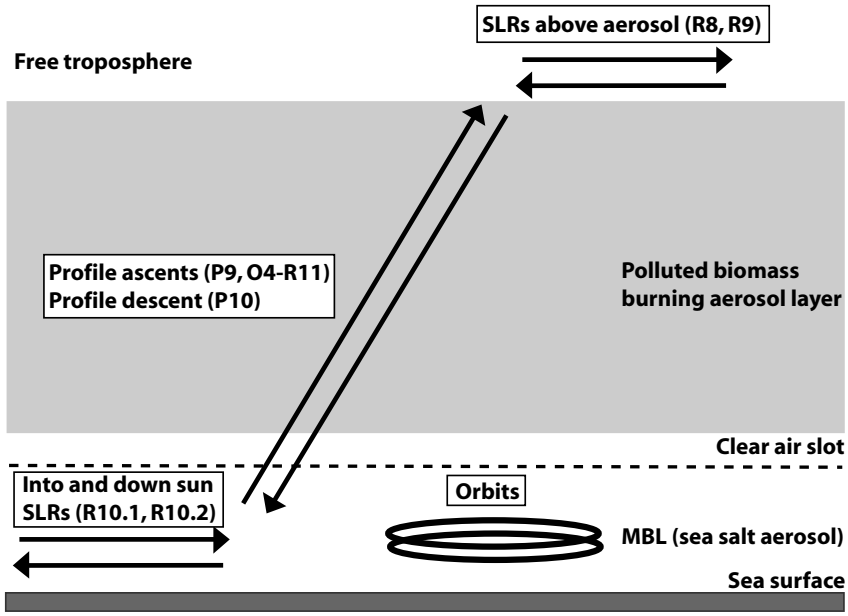

(b) Schematic of runs shown in (a)

Figure 3.1: *(a) Track of flight a791 on September 14th 2000 as determined from the Global Positioning System (GPS). The arrows indicate the direction of travel. Run numbers described in table 3.1 are shown. The straight level runs through the polluted biomass burning aerosol layer (R2,R3,R4,R12) are omitted for clarity. (b) Schematic of runs shown in (a)*

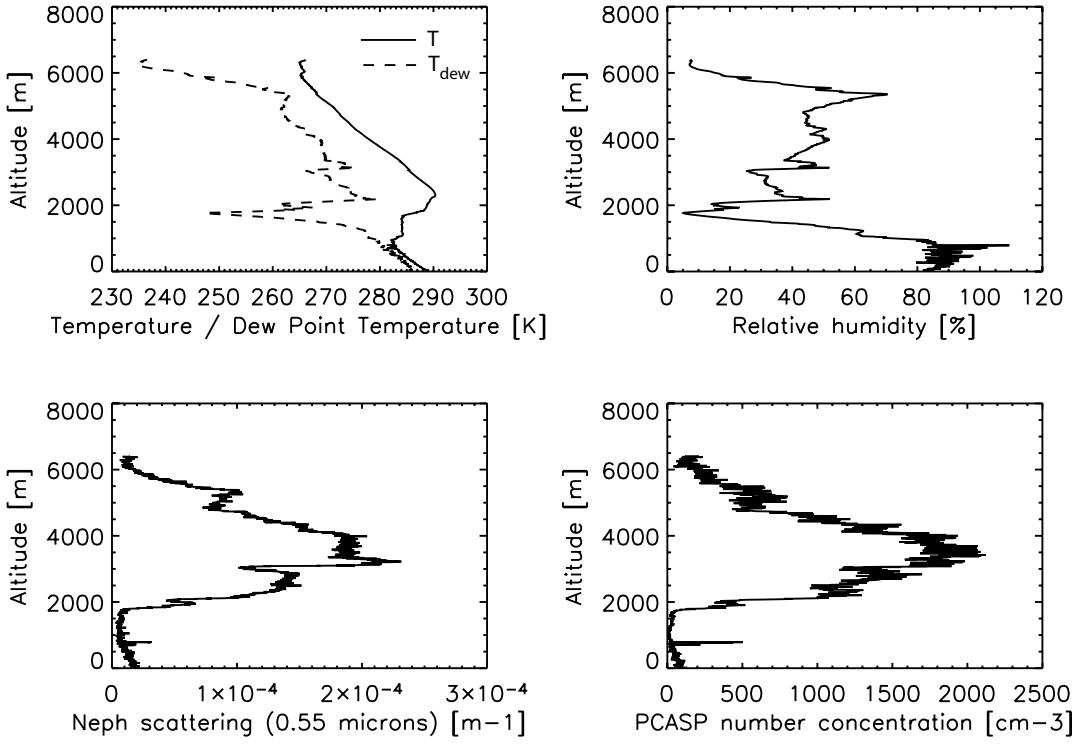

Figure 3.2: *Vertical profiles of temperature (T), dew point temperature (T_{dew}), relative humidity, nephelometer scattering at 0.55 μm, and PCASP number concentration from the profile ascent, P9. The corrections of Anderson and Ogren (1998) have been applied to the nephelometer data.*

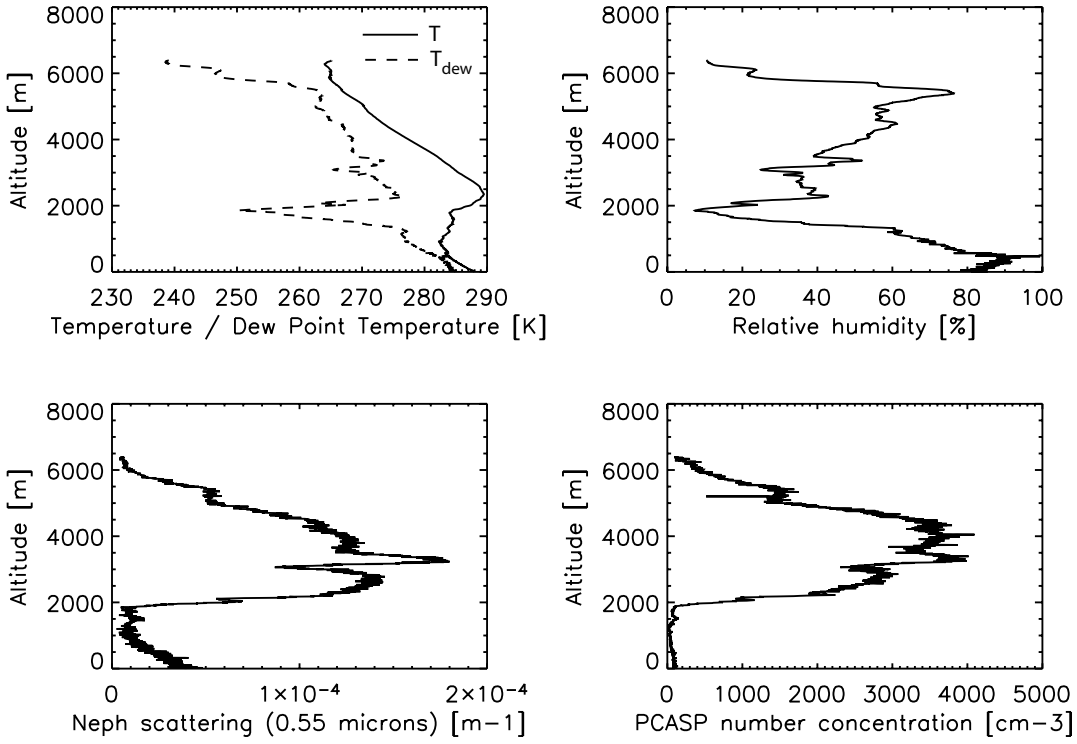

Figure 3.3: *As figure 3.2 but for the profile descent, P10.*

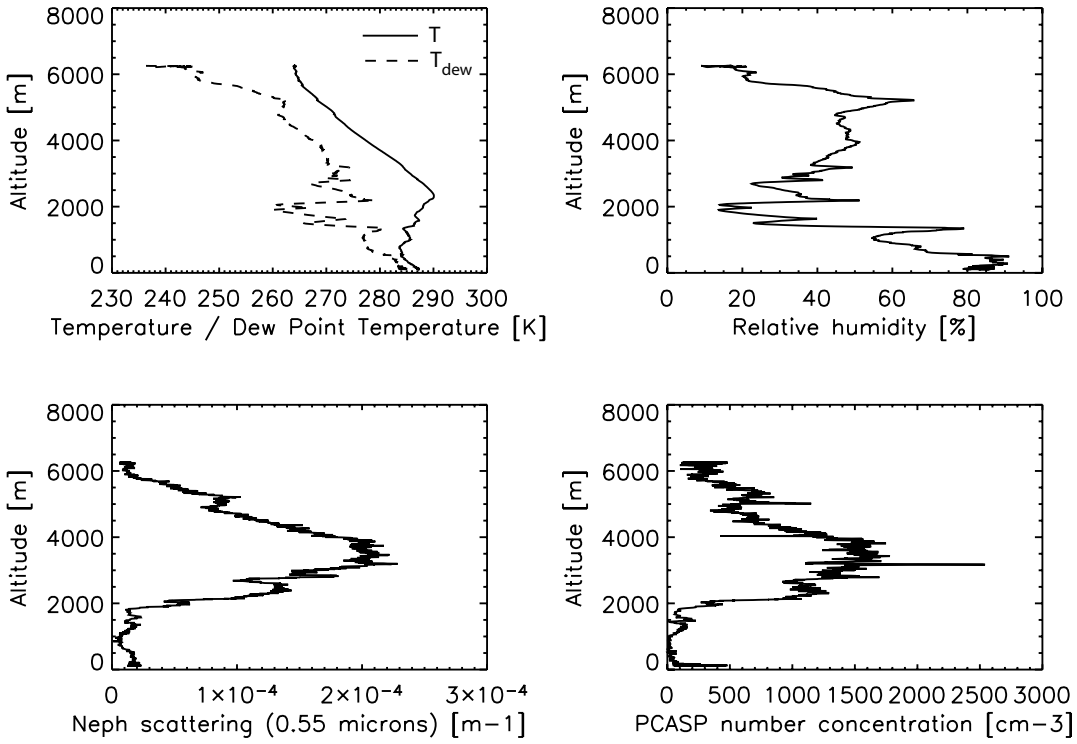

Figure 3.4: *As figure 3.2 but for the profile ascent, O4-R11.*

are likely to be deliquesced and can be considered spherical (Ten Brink *et al.*, 2000). The air is saturated at the top of the MBL (780 - 800 m) in P9 where the RH exceeds 100 $\%$. Thus, the formation of a shallow layer of stratocumulus cloud is likely. This is supported by the sharp peak in particle scattering and number concentration as the aircraft flew through the cloud. Low lying stratocumulus clouds were often observed below the biomass burning aerosol layers off the coast of Namibia and Angola throughout the SAFARI 2000 campaign (Keil and Haywood, 2003, Haywood *et al.*, 2004). The temperature inversions associated with the clean air slot which separates the cloud from the biomass plume is likely to inhibit mixing in the vertical, and therefore limit any indirect aerosol effects resulting from the biomass smoke increasing the cloud lifetime or reflectivity.

The mean N_{tot} ranged from (45 - 72) cm^{-3}, and the mean $\sigma_{sca\lambda=0.55\mu m}$ from (32 - 61) x 10^{-6}m^{-1} for the three profiles in the MBL. In the clean air slot, the mean values of N_{tot} drop off to (17 - 59) cm^{-3}, and the mean values of $\sigma_{sca\lambda=0.55\mu m}$ drop off to (7 - 9) x 10^{-6}m^{-1}. The largest values of N_{tot} and $\sigma_{sca\lambda=0.55\mu m}$ are observed in the heavily polluted biomass burning aerosol layer, with mean values from the three profiles ranging from (819 - 2370) cm^{-3} and (98 - 122) x 10^{-6}m^{-1} respectively, indicating that the majority of the optically active particles reside in the biomass smoke. The mean RH in the biomass burning aerosol

	MBL				Clean air slot				Biomass burning aerosol			
Run number	Altitude [m]	RH [%]	N_{tot} [cm^{-3}]	$\sigma_{sca\lambda=0.55\mu m}$ [x10^{-6}m^{-1}]	Altitude [m]	RH [%]	N_{tot} [cm^{-3}]	$\sigma_{sca\lambda=0.55\mu m}$ [x10^{-6}m^{-1}]	Altitude [m]	RH [%]	N_{tot} [cm^{-3}]	$\sigma_{sca\lambda=0.55\mu m}$ [x10^{-6}m^{-1}]
P9	0 - 800	89	60	14 (*32*)	800 - 1750	51	24	7	1750 - 6000	40	1055	119 (*122*)
P10	0 - 900	82	72	24 (*61*)	900 - 1850	43	59	9	1850 - 6000	46	2370	94 (*98*)
O4R11	0 - 600	85	45	17 (*39*)	600 - 1000	64	17	7	1000 - 5800	42	819	106 (*109*)

Table 3.2: *Summary of the mean relative humidity, RH, PCASP number concentration, N_{tot}, and nephelometer scattering, $\sigma_{sca\lambda=0.55\mu m}$, measured in the MBL, clear slot and biomass burning aerosol layer. The corrections of Anderson and Ogren (1998) have been applied to $\sigma_{sca\lambda=0.55\mu m}$. Further corrections to $\sigma_{sca\lambda=0.55\mu m}$ to account for particle growth with RH are given in italics by applying the growth curves of Ten Brink* et al. *(2000) for the MBL aerosol and Magi and Hobbs (2003) for the biomass burning aerosol.*

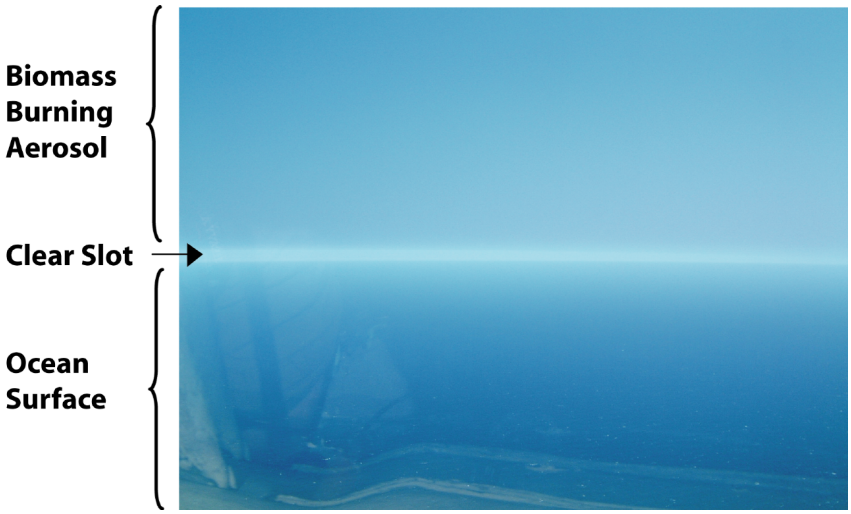

Figure 3.5: *Example of a clean air slot below the biomass burning aerosol layer. Photograph taken from the C-130 aircraft off the coast of Namibia/Angola. Courtesy of the Met Office.*

layer varied from 40 - 46 $\%$ between the profiles and the aerosol particles are unlikely to have adsorbed much water. However the RH is $> 60\%$ at the top of the plume and the adsorption of water onto the surface of the biomass burning aerosol particles may be important (Magi and Hobbs, 2003). This is investigated further in section 3.6.1. The top of the biomass burning aerosol layer can be seen by the sharp decrease in aerosol scattering and concentration at the hydrolapse (a rapid change in moisture with altitude). Above the hydrolapse is the clean free troposphere.

Backward trajectories were run with the NOAA Air Resources Laboratory HYSPLIT model (available at http://www.arl.noaa.gov/ready.html) for air parcels originating at 17.5°S, 11°E at 12:00 GMT on the 14th September 2000. This corresponds to the centre of the region where the aircraft was operating (see figure 3.1) and the start time of P10. The NCEP/NCAR reanalyses meteorological data was used as model input. Trajectories for parcels starting at altitudes of 500, 1500, and 4000 metres were modelled. These altitudes represent air from the MBL, clean air slot, and biomass burning aerosol layers respectively. Figure 3.6 shows that the air in the biomass burning aerosol layer had been advected from the North and had passed over Angola approximately 30 hours previously, implying that the biomass burning aerosol had aged in the atmosphere for more than a day. Trajectories from other altitudes in the biomass plume (3000 - 5000 metres) were found to have very similar backward trajectories to that at 4000 metres. The air parcel in the MBL had been advected from the South and had remained over the ocean for the previous 48 hours. In

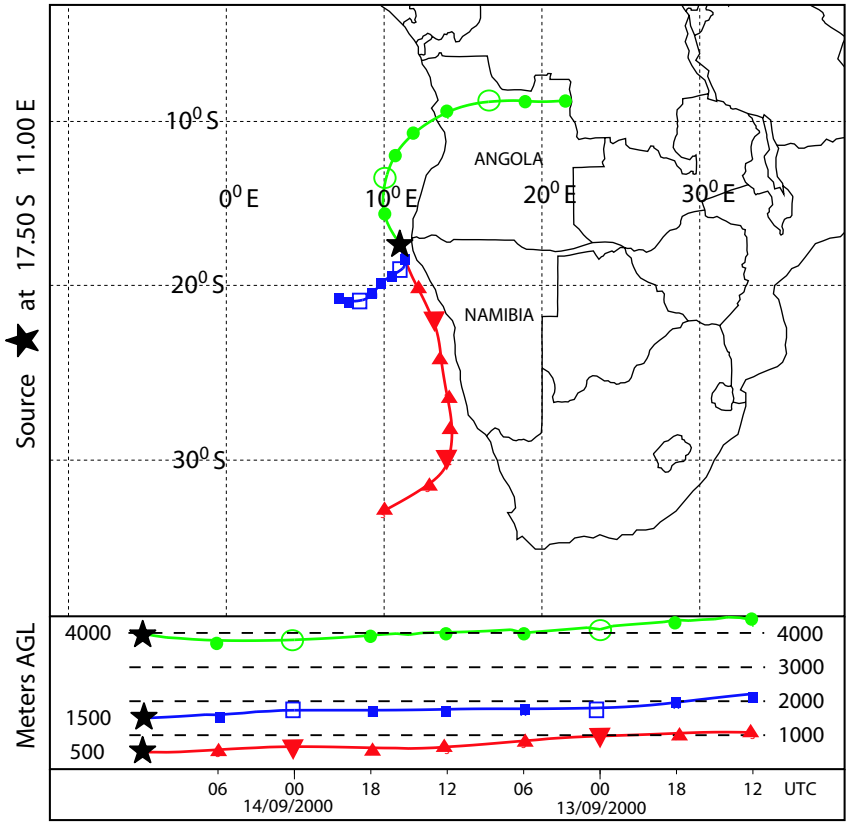

Figure 3.6: *Backward trajectories for air parcels originating at 12:00 GMT on 14th September 2000 (17.5° S, 11° E) at altitudes of 500m (MBL), 1500m (clean air slot) and 4000m (biomass burning aerosol).*

contrast, the air in the clear slot had been advected from the South West, and had travelled much shorter distances in the previous 48 hours compared to the air parcels in the MBL and biomass burning aerosol layers. Figure 3.7 shows the mean zonal and meridional winds from ERA-40 reanalysis data over the southern African region during September 2000. The winds are plotted at 1000 and 700 hPa, corresponding to air in the MBL and biomass burning aerosol layer respectively. The 1000 hPa wind field clearly shows a strong flow of air up the western coast of southern Africa that is associated with a predominant high pressure system in the south Atlantic. The 700 hPa wind field also indicates the presence of dominating anticyclonic conditions over the subcontinent at this level, resulting in a strong easterly flow off the coast of Namibia and Angola, and a westerly flow off the south eastern coast of Africa, both of which form the two main transport pathways of biomass burning aerosols away from southern Africa (e.g. Garstang *et al.* (1996)). The backward trajectories in the MBL and biomass burning aerosol layer in figure 3.6 are consistent with the typical meteorological situation identified in the ERA-40 data, suggesting that the case investigated in this chapter is not atypical.

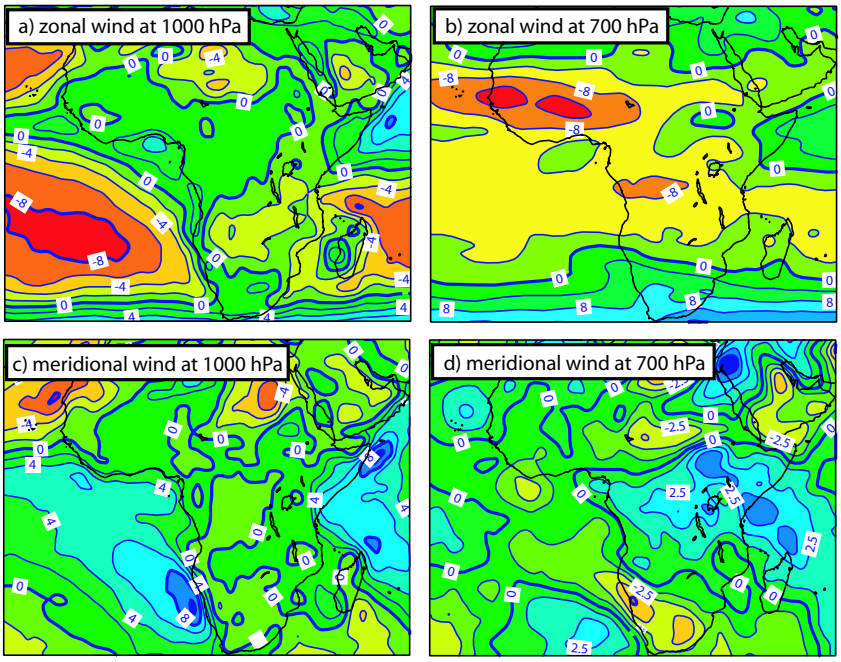

Figure 3.7: *September 2000 mean zonal and meridional winds over Africa at 1000 and 700 hPa at 12:00 UTC. Positive values indicate westerlies/southerlies. The ECMWF 40 year reanalysis data (ERA-40) is used (data available at http://data.ecmwf.int/data/d/era40_month/; last accessed 24/02/05.*

The trajectories indicate that the air in the clear slot trajectory had remained below 2500 metres in the previous 48 hours, suggesting that the feature of a clean unpolluted layer may persist for several days. This is further supported by soundings taken at Etosha National Park (Namibia) and Ascension Island (mid-Atlantic) during September and October 1992 (Swap *et al.*, 1996), shown in figure 3.8 a) and b). These temporally persistent stable layers that are associated with high level subsidence are likely to inhibit vertical transport and therefore create vertically stratified aerosol layers (e.g. Hobbs (2003)). Two stable layers are evident over Namibia in figure 3.8 a), with the lower layer typically existing at 4 - 6 km AGL. This is consistent with the location of the temperature inversion that capped the biomass burning aerosol in the fresh smoke plume studied in chapter 2 (see figure 2.4). Figure 3.8 b) also indicates the presence of two stable layers over oceanic regions. Although the base of the lower layer is at 2 - 3 km above sea level, this is likely to decrease to nearer 500 m to 1 km above the cold ocean water associated with the Benguela current off the coast of Namibia (Garstang *et al.*, 1996) where the aircraft measurements in this study were made. Thus, this clean air slots observed in figures 3.2 - 3.4 are likely to be associated with this lower stable layer, whereas the upper stable layer in figure 3.8 is associated with

the observed hydrolapse at the top of the biomass burning aerosol layer.

Building on the location of these persistent stable layers, the local meteorology, and the observed vertical profiles of biomass smoke, the schematic diagram in figure 3.8 c) illustrates how the aerosol can exist in elevated layers off the coast of Namibia and Angola. Aerosols emitted from the source regions become vertically mixed in the continental boundary layer and can be transported westwards by the dominating anticyclonic circulation pattern. The interior plateau of southern Africa is typically at an altitude $>$ 1 km above sea level, and the terrain falls gently towards the sea (Swap *et al.*, 1996) as illustrated in the schematic. Therefore, as the biomass plume is transported over the Atlantic Ocean, it can become trapped between the two stable layers shown in figure 3.8 b) and exist in an elevated plume above the MBL.

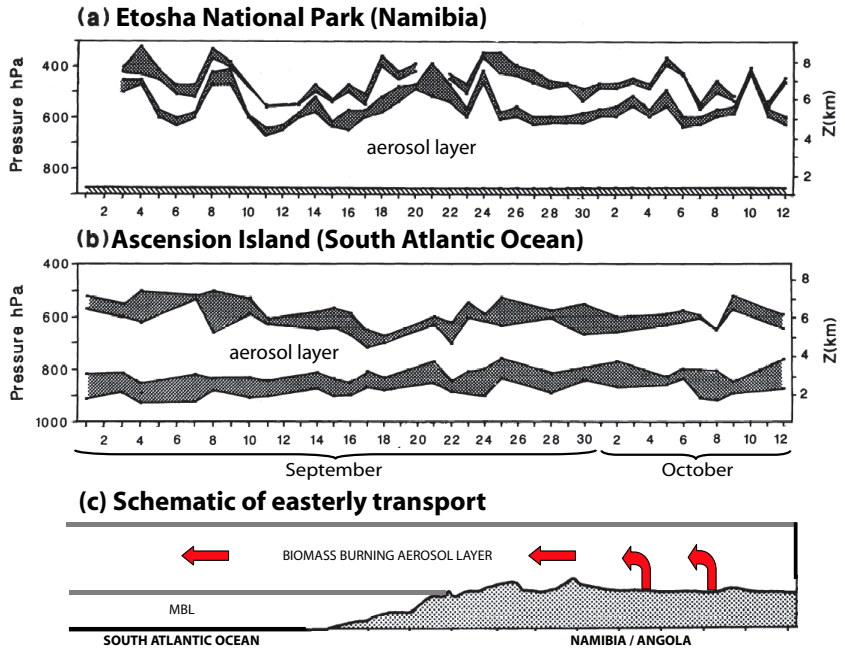

Figure 3.8: *Panels a) and b) show layers of absolute stability (environmental lapse rate $<$ wet adiabatic lapse rate) identified from daily soundings taken at Etosha National Park (Namibia) and Ascension Island (south Atlantic Ocean) from Sept 1st to Oct 12th 1992. The thickness of the stable layers is represented by the grey shading. Altitudes (Z) are above sea level. Also indicated are the likely locations of the biomass burning aerosol layers as identified from the vertical profiles shown in figures 2.4 and 3.3-3.4. Figure modified from Swap* et al. *(1996). A schematic diagram showing the transport of biomass smoke from the continent to the South Atlantic Ocean (red arrows) is shown in panel c).*

3.4 Aerosol size distributions

The aerosol size distributions were measured with a Passive Cavity Aerosol Spectrometer Probe (PCASP) and a Fast-Forward Scattering Spectrometer Probe (FFSSP). The PCASP counted particles in 15 discrete bins from 0.05 - 1.5 μm radius, and the FFSSP counted particles in a further 15 bins from 1 - 23 μm radius. The internal heaters of the PCASP were turned off to minimise evaporation of water or volatile compounds from the aerosol on sampling. This evaporation would tend to lead to an underestimation in the particle sizes. Corrections for the misclassification of sizes as a result of the aerosol absorption have not been considered as they have shown to have a minimal effect on the aerosol scattering and absorption (see Haywood *et al.* (2003a) and appendix A).

Figure 3.9 shows the measured size distributions for four SLRs through the biomass burning aerosol layer (R2, R3, R4, R12), each lasting between 20 and 45 minutes, and two SLRs of 10 minutes duration (R10.1, R10.2) in the MBL. The diamonds represent the mean from the PCASP and FFSSP data, and the error bars represent one standard deviation from the mean. The transition between the PCASP and FFSSP data is also indicated. There is a sharp decrease evident in the particle concentration in the 1-2 μm radius range where the PCASP and FFSSP bins overlap. The decrease from the PCASP to FFSSP data is typically 2-4 orders of magnitude for the biomass burning aerosol size distributions. This suggests that the FFSSP is unable to size the super micron particles in the aged regional haze effectively. One possible reason for the underestimation by the FFSSP is that the particles in the coarse mode are non-spherical. Haywood *et al.* (2003a) show that approximately 75 $\%$ of the biomass burning aerosols in the coarse mode are non-spherical, which could account for an under estimation of a factor of 4 in the particle count with the FFSSP if it only measured the spherical particles (25 $\%$). Therefore, the non-sphericity alone is not sufficient to explain the orders of magnitude decrease observed. Osborne *et al.* (2004) suggest that the inefficiency of the FFSSP to sample particles during SAFARI 2000 was due to low laser power or hardware rejection. As a result, the FFSSP data for the biomass burning aerosol are not used because of the large uncertainties involved. In order to include the coarse mode particles in the radiative transfer modelling in this work, three log-normal modes have been fitted to the average PCASP distribution from the 4 SLRs through the biomass plume, and are of the form,

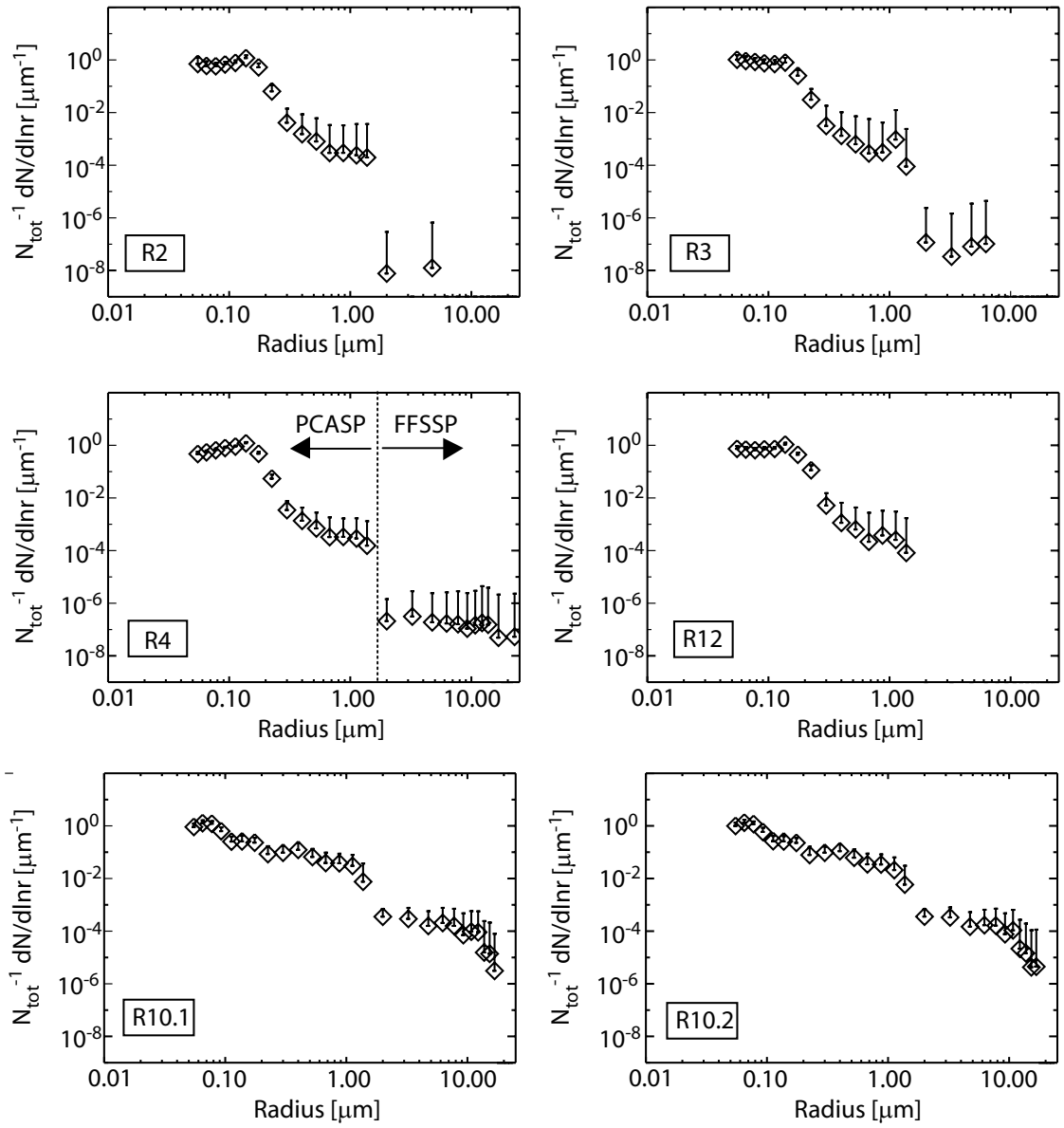

Figure 3.9: *The mean aerosol size distributions for six SLRs in the biomass burning aerosol layer (R2, R3, R4, R12) and in the MBL (R10.1, R10.2) measured with the PCASP and FFSSP. The error bars represent one standard deviation from the mean. The discontinuity between the PCASP and FFSSP data is indicated on the R4 plot.*

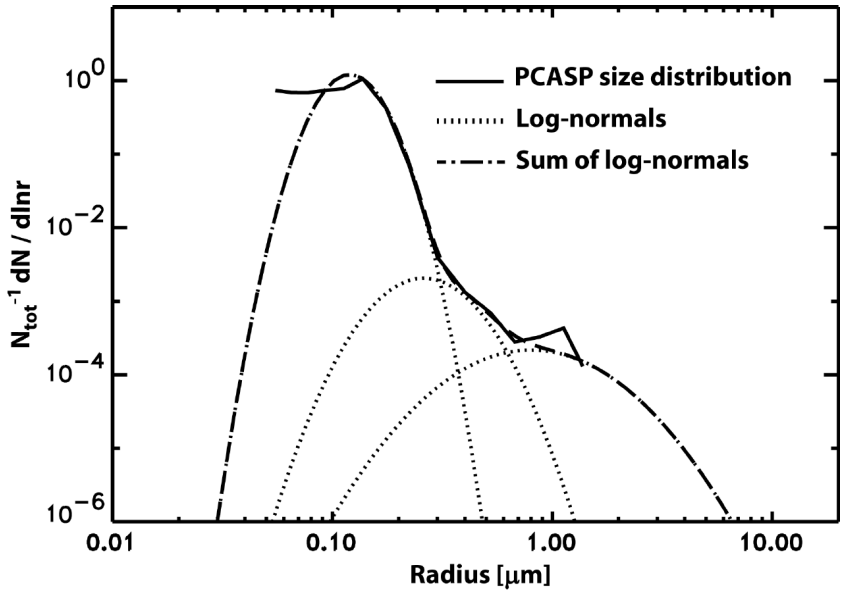

Figure 3.10: *The mean PCASP size distribution for biomass burning aerosol, averaged over runs R2, R3, R4, and R12. Three log-normals are fitted to the measured size distribution. The mean and standard deviation of the log-normals are given in table 3.4 along with the calculated optical properties.*

$$\frac{dN(r)}{dlnr} = \frac{N}{\sqrt{2\pi}} \frac{1}{ln\sigma} exp\left(\frac{-(lnr - lnr_n)^2}{2(ln\sigma)^2}\right), \tag{3.1}$$

where N is the number of particles, r is the particle radius, and r_n and σ are the geometric mean radius and standard deviation of the log-normal. Figure 3.10 shows the mean PCASP size distribution from the 4 SLRs and the three log-normals that are used to characterise the distribution. The measured ultra-fine particles ($r < 0.09\ \mu m$) are not represented by the log-normal fit as they are inactive in an optical sense (Haywood *et al.*, 2003a). Table 3.4 lists the parameters required to reproduce the three log-normals. The estimate of the error in σ is $\pm$ 0.1 for modes 1 and 2 that largely represent the accumulation mode particles, and $\pm$ 0.4 for mode 3 that represents the coarse mode particles. The larger uncertainty in mode 3 is due to the lack of data available to constrain the super-micron particles. The uncertainty in the r_n is $\pm$ 0.01 μm for the three modes (Haywood *et al.*, 2003a).

Figure 3.9 shows that the discrepancy between the PCASP and FFSSP data for the MBL aerosol (R10.1,R10.2) is much smaller than for the biomass burning aerosol. One possible reason to explain the better agreement is that the aerosol in the MBL is spherical (hydrated sea-salt), and so the FFSSP can size the coarse mode particles more accurately. Another

possibility is that due to the aerosol containing a large proportion of water, the refractive index is close to that of the calibration glass beads (see appendix A). The FFSSP sizing is considered to be reasonable in the MBL (Haywood *et al.*, 2003a) and so the PCASP and FFSSP data are used to model the optical properties of the MBL aerosol that are included in the radiative transfer model.

3.5 Aerosol optical properties

3.5.1 Optical properties derived from PCASP and FFSSP size distributions

The optical properties of the aerosol are derived from the measured size distributions in figure 3.9 and Mie scattering calculations. For the biomass burning aerosol only the PCASP data are used for the reasons outlined in section 3.4, whereas the PCASP and FFSSP data are used for the MBL aerosol. Figure 3.11 shows the wavelength dependent refractive indices used to model the aerosol optical properties. The refractive index of oceanic aerosol from WCP (1986) is used for the MBL aerosol (1.381 - 4.26e^{-9}i at 0.55μm) with a density of 1.00 g cm^{-3}. For the biomass burning aerosol, the wavelength dependent refractive index of Haywood *et al.* (2003a) is used (1.54 - 0.018*i* at 0.55μm) with a density of 1.35 g cm^{-3} (Reid and Hobbs, 1998). The assumed refractive index for the biomass burning aerosol is entirely consistent with that retrieved from ground based sun photometers during SAFARI 2000 for the wavelengths 0.44, 0.67, 0.87, and 1.02μm (Haywood *et al.*, 2003b).

Table 3.3 shows the calculated optical properties at 0.45, 0.55, and 0.70 μm for the four SLRs through the biomass plume and the SLR in the MBL. The asymmetry parameter, g, in the biomass burning aerosol layer is 0.60 $\pm$ 0.01, the single scattering albedo, ω_0 is 0.90 $\pm$ 0.01, and the mean specific extinction coefficient, k_e, is 4.6 m^{2}g^{-1} (variation= 4.1-4.9 m^{2}g^{-1}) at a wavelength of 0.55μm. The Mie calculations applied to the PCASP and FFSSP size distribution in the MBL result in a g of 0.77, a ω_0 of 1.0, and a k_e of 0.8 m^{2}g^{-1} at 0.55μm. The lower values of g and ω_0 in the biomass plume are indicative of smaller more absorbing particles compared to those found in the MBL.

Run	Altitude	Derived from PCASP											
		$N_{tot}[cm^{-3}]$	V_{frac}	g			ω_0			$k_e[m^2g^{-1}]$			
Number				$\lambda = 0.45$	$\lambda = 0.55$	$\lambda = 0.70$	$\lambda = 0.45$	$\lambda = 0.55$	$\lambda = 0.70$	$\lambda = 0.45$	$\lambda = 0.55$	$\lambda = 0.70$	
R2	FL120	1000 ± 342	1.09 x 10^{-20}	0.66	**0.61**	0.51	0.92	**0.91**	0.89	6.9	**4.6**	2.8	
R3	FL080	214 ± 157	8.66 x 10^{-21}	0.65	**0.59**	0.51	0.91	**0.89**	0.88	5.9	**4.1**	2.5	
R4	FL100	2003 ± 315	9.37 x 10^{-21}	0.65	**0.59**	0.50	0.91	**0.90**	0.88	6.5	**4.6**	2.8	
R12	FL170	723 ± 94	9.24 x 10^{-21}	0.66	**0.61**	0.53	0.91	**0.91**	0.89	6.7	**4.9**	3.0	
Mean	–	985	9.54 x 10^{-21}	0.66	**0.60**	0.51	0.91	**0.90**	0.89	6.5	**4.6**	2.8	
		Derived from PCASP and FFSSP											
R10	30 m	85 ± 18	4.64 x 10^{-19}	0.78	**0.77**	0.76	1.0	**1.0**	1.0	0.8	**0.8**	0.8	

Table 3.3: *The optical parameters derived from the measured size distributions and Mie scattering calculations. A refractive index at 0.55μm of 1.54 - 0.018i is used for the biomass burning aerosol (R2,R3,R4,R12) and 1.381 - 4.26e^{-9}i for the MBL aerosol (R10). FL is the altitude in feet x 100.*

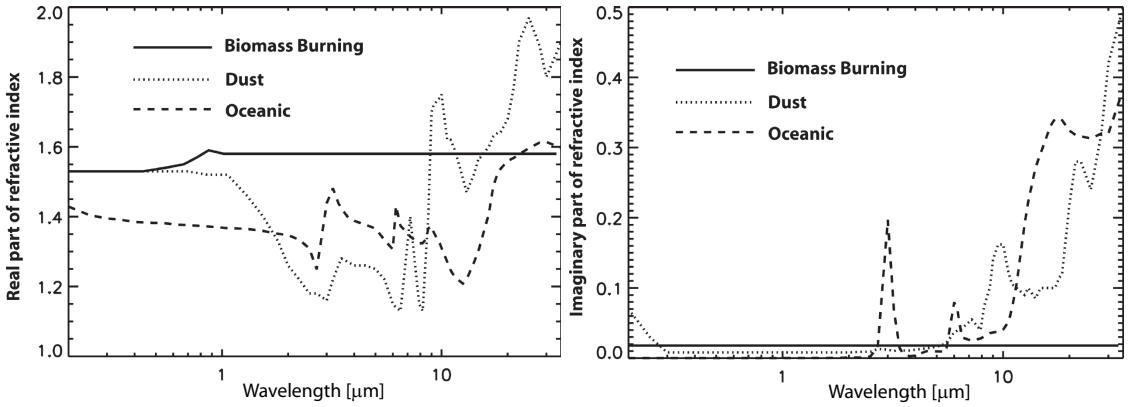

Figure 3.11: *The wavelength dependent real and imaginary parts of the refractive index used to model the aerosol optical properties.*

3.5.2 Optical properties derived from the log-normal fit to the PCASP size distribution

The Mie scattering calculations for the biomass burning aerosol are repeated with the log-normal fit to the PCASP size distribution to attempt to account for the effect of the coarse mode particles not measured with the PCASP instrument. For inclusion into the radiative transfer model in this study, the wavelength dependent refractive index in section 3.5.1 is used (1.54-0.018i at 0.55 μm) with a density of 1.35 g cm^{-3} (Reid and Hobbs, 1998) for both the accumulation (modes 1 + 2) and coarse (mode 3) particles. However, Haywood *et al.* (2003a) suggest that the coarse mode contains a significant amount of dust particles supported by filter measurements of the coarse fraction (Formenti *et al.*, 2003), and that a refractive index and density representing dust aerosols is more representative.

To ascertain the impact that the two different assumptions of refractive index and density of the coarse mode particles (mode 3 of the log-normal) have on the aerosol optical properties, Mie scattering calculations are performed for both cases. When modelling mode 3 as dust-like, a wavelength dependent refractive index of 1.53-0.008i at 0.55 μm (see figure 3.11), and a density of 2.65 g cm^{-3} is used (WCP, 1986). It should be noted that the uncertainty in the refractive index of soil dust aerosols is large, with studies indicating that the real part ranges from 1.6 to 1.54, and the imaginary part from 0.024 to 0.005 over the wavelength range 0.44 - 1.02 μm (Sato *et al.*, 2003). Further measurements would be required to determine a realistic refractive index of the coarse mode particles measured in the biomass burning plumes during SAFARI 2000.

Table 3.4 summarises the modelled optical properties at a wavelength of $0.55\mu m$, and figure 3.12 (a) shows the wavelength dependence of ω_0, g, and k_e for the external mixture using the two different assumptions for the coarse mode refractive index and density. At wavelengths less than $1\mu m$ the difference is $\leq 2\%$ in ω_0 and $\leq 1\%$ in g between the two different assumptions of the refractive index of mode 3. At wavelengths $> 1\mu m$ significant differences in ω_0 and g are evident. However, there is a sharp decrease in the k_e with increasing wavelength, with k_e being a factor of 9 smaller at $1\mu m$ compared to at $0.25\mu m$. As a result of the strong wavelength dependence in k_e, the differences in ω_0 and g in the near infra-red are likely to have a relatively minor impact on the radiative effect of the biomass burning aerosol (Haywood *et al.*, 2003a).

The $k_{e\lambda=0.55\mu m}$ derived from the log-normal fit to the PCASP size distribution is significantly less than that derived in section 3.5.1, which does not account for the large amount of aerosol mass residing in the coarse mode. Although the value derived from the log-normal fit is more representative of the aerosol in the atmosphere, it is shown to be highly uncertain (2.47 - 3.35 m^2g^{-1}) as a result of the assumption of the refractive index and density of mode 3. It is of vital importance to constrain the value of $k_{e\lambda=0.55\mu m}$ in future measurement campaigns by accurately measuring the coarse fraction in order to improve the analysis and validation of data from aerosol chemical transport models that tend to output spatial / temporal distributions of aerosol mass (e.g. Tegen *et al.* (1997)). It is not as important in the work presented in this thesis as the aerosol mass in the column can be varied in the radiative transfer model used until agreement with measured fluxes (this chapter) or aerosol optical depth measurements (chapter 5) is obtained.

3.5.3 Optical properties derived from the PSAP and nephelometer in SLRs

The single scattering albedo can be derived from the wavelength dependent nephelometer measurements of the aerosol scattering, $\sigma_{sca\lambda}$, [0.45,0.55,0.70μm], and the PSAP measurements of the aerosol absorption at $0.567\mu m$, $\sigma_{abs\lambda=0.567\mu m}$, allowing the calculation of $\omega_{0\lambda=0.55\mu m}$. $\omega_{0\lambda=0.45\mu m}$ and $\omega_{0\lambda=0.70\mu m}$ are estimated assuming a $1/\lambda$ dependence on the absorption in the biomass plume (Reid and Hobbs, 1998). The corrections discussed in

Mode	Aerosol type	Number fraction	$r_n \pm 0.01$ (μm)	σ $\pm$ 0.1 *	$k_{e\lambda=0.55\mu m}$ (m^2g^{-1})	$\omega_{0\lambda=0.55\mu m}$	$g_{\lambda=0.55\mu m}$
1	Biomass	0.9970	0.12	1.30	4.98	0.91	0.58
2	Biomass	0.0026	0.26	1.50	4.56	0.89	0.71
3	Biomass	0.0004	0.80	1.90	0.57	0.65	0.85
1+2	Biomass	N/A	N/A	N/A	4.97	0.91	0.59
1+2+3	**Biomass**	N/A	N/A	N/A	**3.35**	**0.89**	**0.59**
3	Dust	0.0004	0.80	1.90	0.29	0.77	0.81
1+2+3	Biomass + Dust	N/A	N/A	N/A	2.47	0.90	0.60

Table 3.4: *Log-normal parameters and optical properties of the 3 log-normal modes fitted to the measured PCASP size distribution in the biomass plume. The optical properties of the sum of the 3 modes are shown using the refractive index and density representative of the biomass burning aerosol (n=1.54-0.018i at 0.55μm, ρ_{aer}=1.35 gcm^{-3}) and soil-dust aerosol (n=1.53-0.008i at 0.55μm, ρ_{aer}=2.65 gcm^{-3}) for mode 3.*

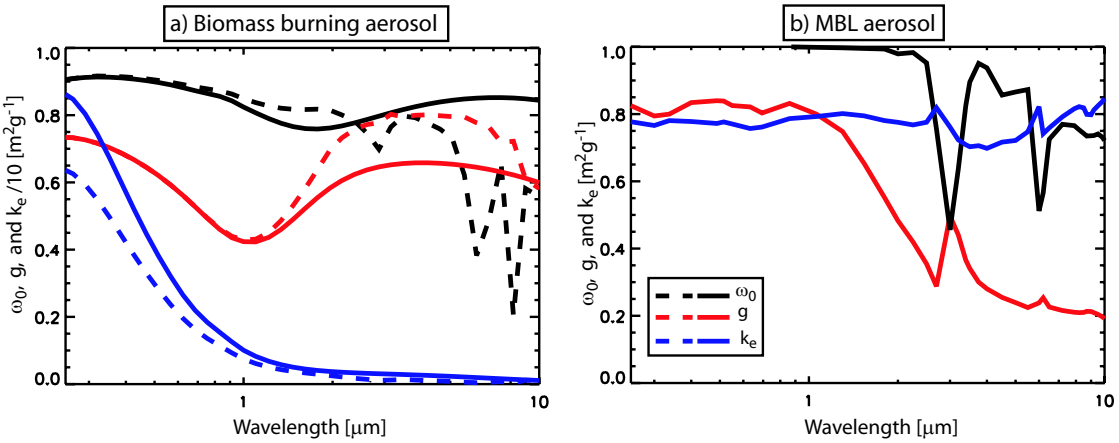

Figure 3.12: *The wavelength dependent optical properties derived from Mie calculations with a) the log-normal fit to the PCASP size distribution in the biomass plume using the refractive index of 1.54-0.018i at 0.55 μm and a density of 1.35 g cm^{-3} for all 3 modes (solid line), and using the same assumptions for modes 1 and 2 but using the refractive index of dust aerosol (1.53-0.008i at 0.55 μm) and a density of 2.65 g cm^{-3} for mode 3 (dashed line). b) PCASP and FFSSP MBL aerosol size distribution with the refractive index of oceanic aerosol (1.381-4,26e^{-9}i at 0.55 μm) and a density of 1.00 g cm^{-3}.*

appendix A are applied to the PSAP and nephelometer data before the $\omega_{0\lambda}$ calculation is made.

On sampling the aerosol, the nephelometer dries the aerosol to a degree. Therefore evaporation of water (and perhaps volatile organic species in the biomass plume) may occur, and the nephelometer measurements may not represent the ambient atmospheric aerosol. Figure 3.13 shows growth curves (the relative increase in $\sigma_{sca\lambda=0.55\mu m}$ with RH to that of dry aerosol) determined from humidograph measurements in biomass plumes off the coast of Namibia on the 11th and 13th September 2000 (Magi and Hobbs, 2003), and labora-

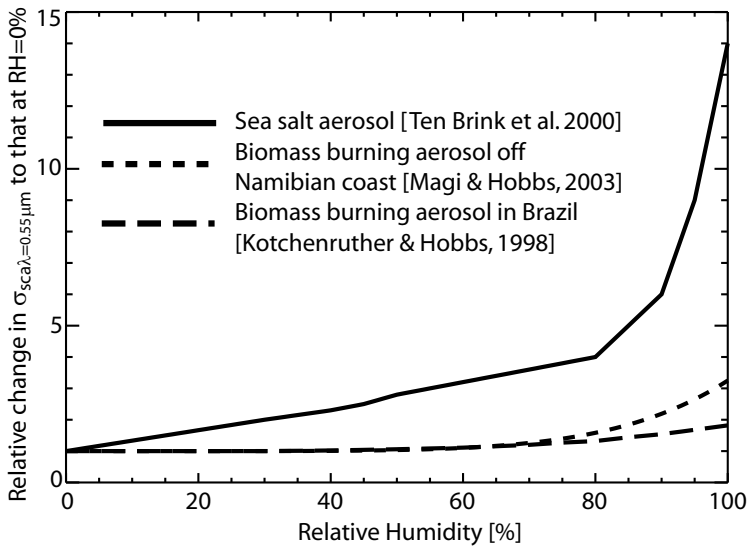

Figure 3.13: *Humidograph measurements at a wavelength of 0.55 μm. The measurements show the relative increase in aerosol scattering as a function of RH with respect to dry aerosol (RH=0$\%$).*

tory measurements of NaCl that is more representative of the sea salt aerosol in the MBL (Ten Brink *et al.*, 2000). Also shown for comparison is the growth curve for Brazilian biomass burning aerosol measured during the Smoke, Clouds and Radiation-Brazil field campaign (SCAR-B) (Kotchenruther and Hobbs, 1998).

The increase in scattering of the Brazilian and African biomass burning aerosol only becomes important at high atmospheric relative humidities. The mean RH in the SLRs throughout the biomass burning plume where the optical properties are calculated was 51, 34, 51, and 57 $\%$ for runs R2, R3, R4, and R12 respectively. The humidograph measurements of Magi and Hobbs (2003) suggest a negligible increase of less than a factor of 1.07 in $\sigma_{sca\lambda=0.55\mu m}$ at relative humidities $< 57\%$. This negates the need to account for the hygroscopic nature of the biomass burning aerosol in the ω_0 calculation during the SLRs (Haywood *et al.*, 2003a,b, Osborne *et al.*, 2004). For the MBL aerosol, the hygroscopic nature is not an issue in the ω_0 calculation because the MBL aerosol is purely scattering at $0.55\mu m$. However, the hygroscopic properties of the MBL aerosol are shown to be important when determining the aerosol optical depth from the nephelometer measurements in section 3.6.1.

Table 3.5 summarises the mean and standard deviation of ω_0 at 0.45, 0.55, and 0,70μm derived from the PSAP and nephelometer measurements for each of the SLRs. The $\omega_{0\lambda=0.55\mu m}$

Run Number	Altitude	RH [%]	Derived from nephelometer and PSAP			
			ω_0			
			$\lambda = 0.45$	$\lambda = 0.55$	$\lambda = 0.70$	σ
R2	FL120	51	0.88	**0.88**	0.85	$\pm$ 0.02
R3	FL080	34	0.90	**0.91**	0.91	$\pm$ 0.07
R4	FL100	51	0.85	**0.84**	0.81	$\pm$ 0.01
R12	FL170	57	0.93	**0.93**	0.92	$\pm$ 0.01
Mean biomass	–	–	0.89	**0.89**	0.87	$\pm$ 0.04 [a]
R10	30 m	82	1.0	**1.0**	1.0	$\pm$ 0.02

Table 3.5: *The wavelength dependent single scattering albedo derived from the nephelometer and PSAP for four SLRs within the biomass burning plume (R2,R3,R4,R12), and in the marine boundary layer (R10). R10 is the average of R10.1 and R10.2. σ represents one standard deviation from the mean value for each run. σ^a is the standard deviation of the mean ω_0.*

in the biomass plume was 0.89$\pm$0.04, where the error represents the standard deviation in $\omega_{0\lambda=0.55\mu m}$.

There is good agreement in the $\omega_{0\lambda=0.55\mu m}$ calculated from the various methods for flight a791. In the biomass burning aerosol layer, $\omega_{0\lambda=0.55\mu m}$ is 0.90 $\pm$ 0.01 derived from the PCASP size distributions, 0.89 from the log-normal fit to the PCASP measurements, and 0.89 $\pm$ 0.04 from the PSAP and nephelometer. The agreement between the PSAP and nephelometer derived values to those using Mie scattering calculations indicates that the assumed refractive index (1.54-0.018i at 0.55μm) is reasonable. The SAFARI 2000 campaign average $\omega_{0\lambda=0.55\mu m}$ in the aged regional haze was 0.91 $\pm$ 0.04 from the Met Office C-130 aircraft measurements (Haywood *et al.*, 2003a), and 0.89 $\pm$ 0.03 from the University of Washingtons CV-580 aircraft (Magi *et al.*, 2003). Therefore, the partially absorbing biomass burning aerosol studied in the plume here has a $\omega_{0\lambda=0.55\mu m}$ that is representative of the aged regional haze.

3.6 Aerosol optical depth retrieval

The aerosol optical depth at 0.55 μm ($\tau_{\lambda=0.55\mu m}$) can be calculated directly from measurements taken onboard the aircraft, or by a combination of aircraft measurements with radiative transfer modelling. The following seven retrieval methods are used to determine $\tau_{\lambda=0.55\mu m}$ for flight a791, of which several have been used in various other campaigns,

namely the Saharan Dust Experiment (SHADE) (Haywood *et al.*, 2003c) and the Tropospheric Aerosol Radiative Forcing Observational Experiment (TARFOX) (Francis *et al.*, 1999, Hignett *et al.*, 1999).

i) Integrating the aerosol extinction derived from the nephelometer and PSAP measurements in vertical profiles.

ii) Integrating the aerosol extinction derived from the PCASP size distribution and number concentration in vertical profiles.

iii) Modelling the measured up-welling BBR irradiances at high level above the aerosol layer.

iv) Modelling the magnitude and spectral dependence of the SWS measured up-welling radiances.

v) Modelling the magnitude and spectral dependence of the down-welling radiances measured with the Scanning Airborne Filter Radiometer (SAFIRE).

vi) Modelling the spectral dependence of the SAFIRE measurements of the down-welling radiance as a function of scattering angle.

vii) AERONET retrieval using SAFIRE measurements of the down-welling radiance as a function of scattering angle.

Radiative transfer model

The Edwards Slingo 1996 radiation code (Edwards and Slingo, 1996) is used to model the atmospheric radiative transfer for the optical depth calculation methods iii) - vi). The spectral resolution was set at 220 wave-bands encompassing the range 0.2 - 10 μm, with the majority of bands situated in the visible and near infra-red part of the spectrum. The solar constant at the top of the atmosphere was set at 1349.4 Wm^{-2}, which is representative of the insolation during SAFARI 2000. The vertical resolution of the model was set at 82 levels (56 levels from the surface to the top of the biomass burning aerosol layer at a resolution of 10mbar, and a 1km grid above the biomass burning aerosol). The aircraft measurements of temperature, O_3, and H_2O(g) from the profile descent (P10) were included in the model.

The tropical climatology of McClatchey *et al.* (1972) was used at altitudes greater than the maximum altitude of the measurements. The O_3 concentration was measured with a TECO 49 instrument that can measure mixing ratios over the range of 0 - 1000 ppbv with a sensitivity of ± 2 ppbv. The water vapour mass mixing ratio was derived from the measurements of the dew point temperature and total atmospheric pressure. Other greenhouse gases included in the model were nitrous oxide (N_2O), methane (CH_4), carbon dioxide (CO_2) and oxygen (O_2). The mixing ratio data for these gases was taken from Cofer *et al.* (1996) and IPCC (2001), and they were assumed to be well mixed throughout the atmosphere. Although biomass burning is a source of CH_4 and N_2O and in reality elevated levels will exist in the biomass plume, the impact on the short-wave radiation is negligible.

The biomass burning and MBL aerosol optical properties derived from the Mie scattering calculations shown in figure 3.12 are included in the model. For the biomass burning aerosol, a constant refractive index and density for all three log-normal modes is used (n=1.54-0.018i at 0.55μm, ρ_{aer}=1.35gcm^{-3}). As discussed in section 3.5.2 this leads to differences of $\leq 2\%$ in ω_0 and $\leq 1\%$ in g at $\lambda < 1.0\mu m$ compared to if the coarse mode particles are represented as being similar to soil dust. The shape of the vertical structure of the aerosol mass mixing ratio used is the same as the measured PCASP number concentration in the profile descent (P10). The aerosol optical depth in the MBL and biomass burning aerosol layer can then be varied by changing the magnitude of the mass mixing ratio of the MBL and biomass burning aerosol.

The aerosol optical depth at a single wavelength (τ_λ) can be calculated from Beers law using the formula,

$$\tau_\lambda = ln\left(\frac{S_{noaer\lambda}}{S_{aer\lambda}}\right) cos\theta_{szen}, \tag{3.2}$$

where θ_{szen} is the solar zenith angle, $S_{noaer\lambda}$ is the modelled direct flux at the surface with no aerosol in the column, and $S_{aer\lambda}$ is the direct flux at the surface including the effect of scattering and absorption by aerosol particles. The 2-stream version of the code with the Eddington approximation gives an adequate representation of $S_{noaer\lambda}$ and $S_{aer\lambda}$ at a single wavelength.

A 4-stream version of the code with the δ-Eddington approximation is used to model the broadband up-welling irradiances measured by the BBR in method iii). The δ-Eddington approximation is used as it gives a more accurate split between the direct and diffuse components of the scattered radiation. 21 moments of the aerosol phase function were used in the 4-stream version, and the ocean albedo was modelled using the broadband sea surface reflectance parameterisation of Glew *et al.* (2004), and the sea surface angular scattering parameterisation detailed by Thomas and Stamnes (1999).

A radiance version of the code is used to model the measured SWS and SAFIRE radiances in methods iv) to vi). 101 moments of the aerosol phase function are used to model the directional dependence of the scattered radiation more accurately, and the surface albedo is assumed to be Lambertian.

3.6.1 Integrating the aerosol extinction derived from the nephelometer and PSAP in vertical profiles

The aerosol optical depth can be calculated by integrating the aerosol extinction, σ_{ext} = σ_{sca} + σ_{abs}, with height, z, using the formula,

$$\tau_{\lambda=0.55\mu m} = \int \sigma_{ext\lambda=0.55\mu m}(z)dz. \tag{3.3}$$

The aerosol extinction is determined as a function of altitude for the three vertical profiles (P9, P10, O4R11) in both the MBL, clean air slot, and biomass smoke. The PSAP measurements of the aerosol absorption coefficient, σ_{abs}, in the vertical profiles are not used because they are deemed to be unreliable during aircraft ascents and descents. This is because the PSAP instrument is sensitive to changes in pressure, and during vertical profiles this can change quite rapidly over the integration time of the instrument (30 seconds). Therefore, the extinction is derived by combining the nephelometer measurements of σ_{sca} with the aerosol ω_0 as determined from the PSAP and nephelometer measurements in section 3.5.3 using,

$$\sigma_{ext\lambda=0.55\mu m}(z) = \frac{\sigma_{sca\lambda=0.55\mu m}(z)}{\omega_{0\lambda=0.55\mu m}}. \tag{3.4}$$

Because the nephelometer partially dries the aerosol on sampling, the relative humidity inside the nephelometer is typically lower than that of the ambient atmosphere (e.g. $\backsim 45\%$ at an atmospheric RH of 95% during flight a791). Table 3.2 shows the mean measured $\sigma_{sca\lambda=0.55\mu m}$ in the MBL and biomass plume for the three vertical profiles with and without a correction applied to the nephelometer data (see the growth curves of Magi and Hobbs (2003) and Ten Brink *et al.* (2000) in figure 3.13) to account for evaporation of water from the aerosol on sampling. For the MBL aerosol, the high RH together with the sharp increase in the sea salt aerosols size with RH leads to a large increase of 129%, 154%, and 129% in the mean $\sigma_{sca\lambda=0.55\mu m}$ for P9, P10, and O4R11 respectively when the RH correction is applied. The lower values of RH in the biomass burning aerosol layer and the much lesser dependence of $\sigma_{sca\lambda=0.55\mu m}$ with RH leads to small increases in the mean $\sigma_{sca\lambda=0.55\mu m}$ of 3%, 4%, and 3% for P9, P10, and O4R11 respectively. It is therefore important to account for this sampling bias in the MBL, where the aerosol optical properties are highly sensitive to the state of the atmosphere.

Table 3.6 compares the calculated column integrated $\tau_{\lambda=0.55\mu m}$, and the ratio of the MBL to biomass burning optical depth at $0.55\mu m$ ($\tau_{MBL}/\tau_{biomass}$) in the column for the three profiles, with and without the correction for an increase in particle scattering with RH applied to the nephelometer measurements in the biomass burning and MBL aerosol layers. The results show an increase in the column integrated $\tau_{\lambda=0.55\mu m}$ for the three vertical profiles of $\backsim$ 0.02 - 0.06 (5-13%), and in the $\tau_{MBL}/\tau_{biomass}$ ratio by more than a factor of 2 when the RH correction is applied. The large increase in the contribution of the MBL aerosol to the total column optical depth shows that it is most important to account for the evaporation of water on sampling the MBL aerosol. The corrected $\tau_{\lambda=0.55\mu m}$ ranges between 0.53$\pm$0.03 to 0.62$\pm$0.03 for the three profiles, and the $\tau_{MBL}/\tau_{biomass}$ ratio from 4.0$\pm$0.2% to 15.6$\pm$0.7%. The errors represent the uncertainty arising from the variation in $\omega_{0\lambda=0.55\mu m}$ measured with the PSAP and nephelometer (0.89$\pm$0.04) during the SLRs in the biomass plume. Thus, a contribution of 0.02 - 0.07 in the total $\tau_{\lambda=0.55\mu m}$ results from the inclusion of MBL aerosol in the calculation for the three profiles. The upper end of this range compares favourably with the background aerosol optical thickness of 0.05 to 0.07 over oceans

Run number	No correction applied		Correction applied	
	$\tau_{\lambda=0.55\mu m}$	$\tau_{MBL}/\tau_{biomass}$	$\tau_{\lambda=0.55\mu m}$	$\tau_{MBL}/\tau_{biomass}$
P9	0.59±0.03	3.0±0.2%	0.62±0.03	6.2±0.3%
P10	0.47±0.02	6.9±0.3%	0.53±0.03	15.6±0.7%
O4R11	0.59±0.03	1.9±0.1%	0.61±0.03	4.0±0.2%

Table 3.6: *Comparison of the derived optical depth at 0.55μm and the ratio of the MBL to biomass burning aerosol optical depth from integrating the aerosol extinction derived from the PSAP and nephelometer measurements. The errors are the result of the measured variation in the biomass burning $\omega_{0\lambda=0.55\mu m}$ from the SLRs. Results are shown with and without the correction for an increase in particle scattering with RH applied to the nephelometer measurements.*

determined from AERONET measurements (Kaufman *et al.*, 2001).

3.6.2 Integrating the PCASP number concentration

The average PCASP size distribution in the MBL and biomass burning aerosol layers for each of the three vertical profiles are combined with Mie scattering calculations to determine the extinction coefficient per particle, $\sigma_{extp\lambda=0.55\mu m}$ [m^{-1}]. The optical depth can then be calculated using,

$$\tau_{\lambda=0.55\mu m} = \int N_{tot}(z)\sigma_{extp\lambda=0.55\mu m}dz, \tag{3.5}$$

where N_{tot} is the PCASP number concentration and z is the altitude. The $\tau_{\lambda=0.55\mu m}$ calculated with this method for the three vertical profiles was 0.25 ($\tau_{MBL}/\tau_{biomass}$=7.1%), 0.58 ($\tau_{MBL}/\tau_{biomass}$=6.4%), and 0.19 ($\tau_{MBL}/\tau_{biomass}$=4.0%) for the profiles P9, P10, and O4R11 respectively. The $\tau_{\lambda=0.55\mu m}$ derived from the two profile ascents (P9 and O4R11) is a lot less than that derived from the profile descent (P10). This is possibly the result of the PCASP instrument under-sampling the N_{tot} in profile ascents. Table 3.2 shows that the mean N_{tot} in the biomass burning aerosol layer was 819 and 1055 cm^{-3} for the two profile ascents, compared to 2370 cm^{-3} in the profile descent. Haywood *et al.* (2003b) suggest that N_{tot} is highly sensitive to variations in the pitch of the aircraft as this alters the flow of air around the aircraft disrupting the isokinetic sampling of the wing mounted PCASP. The mean and standard deviation in the pitch of the aircraft was 6.6 $\pm$ 0.9° during P9 , 5.7 $\pm$ 2.4° during O4-R11, and 1.5 $\pm$ 0.8° during P10. The fact that the N_{tot} is so sensitive

to the aircraft pitch means that the $\tau_{\lambda=0.55\mu m}$ derived from this method is highly uncertain. However, more confidence can be placed in the $\tau_{\lambda=0.55\mu m}$ derived from the profile descent as it is within 10% of that derived in section 3.6.1, whereas the values derived from the ascents are approximately a factor of three smaller.

3.6.3 Measuring the up-welling irradiances at high level with the BBR

The aircraft measured the up-welling broadband irradiance (0.3-3.0 μm), F_{BBR}, above the heavily polluted biomass burning aerosol plume. Figure 3.14 shows the measured broadband irradiances for two separate SLRs (R8 and R9). The aircraft travelled approximately 43 km in R8 and 86 km in R9. The mean measured irradiance is 78.75 $\pm$ 1.59 Wm^{-2} and 78.58 $\pm$ 1.33 Wm^{-2} for R8 and R9 respectively, where the variability encompasses the maximum and minimum of the measurements and is the result of the variability in the aerosol below the aircraft.

The clear sky up-welling flux, F_{clear}, (i.e. the flux when no aerosol is present) was modelled at the aircraft flight level with the Edwards Slingo 96 radiation code. The mean value for R8 and R9 was 53.70 Wm^{-2}. The variation in F_{clear} as a result of the variation in solar zenith angle (θ_{szen} = 22.4 - 23.8 degrees) between R8 and R9 was negligible.

The direct radiative effect of the aerosol below the aircraft, ΔF is given by,

$$\Delta F = -(F_{BBR} - F_{clear}). \tag{3.6}$$

Therefore, by comparing the modelled clear-sky flux to the measurements, the column integrated ΔF can be diagnosed with no assumptions needed about the aerosol properties. The ΔF across R8 was -25.05 $\pm$ 1.59 Wm^{-2} and across R9 was -24.88 $\pm$ 1.33 Wm^{-2}.

The biomass burning aerosol plume and sea salt aerosol in the MBL are then included in the radiative transfer model. The ratio of the MBL aerosol optical depth to the biomass burning aerosol optical depth at 0.55 μm ($\tau_{MBL}/\tau_{biomass}$) is fixed at 16 $\%$. Although this represents the upper limit of that derived from the optical depth calculations from the nephelometer and PCASP methods (sections 3.6.1 and 3.6.2), it is shown in sections 3.6.5 - 3.6.6 to

produce a better representation of the measured down-welling radiances at low-level than using the mean value of 7%. Furthermore, the MBL $\tau_{\lambda=0.55\mu m}$ compares more favourably to the average measured maritime aerosol optical thickness over oceanic regions (Kaufman *et al.*, 2001) when a value of 16% is used.

The up-welling flux at the aircraft flight level is then modelled as a function of the total aerosol optical depth, $F_{aer}(\tau_{\lambda=0.55\mu m})$. The $\tau_{\lambda=0.55\mu m}$ across R8 and R9 is then determined when the modelled flux equals the measured flux (i.e. $F_{aer}(\tau_{\lambda=0.55\mu m}) = F_{BBR}$). This resulted in a $\tau_{\lambda=0.55\mu m}$ of 0.34 $\pm$ 0.02 for R8 and 0.33 $\pm$ 0.02 for R9. The maximum and minimum $\tau_{\lambda=0.55\mu m}$ and ΔF for R8 and R9 are indicated on figure 3.14. The corresponding normalised radiative impact of the biomass smoke (ΔF divided by $\tau_{\lambda=0.55\mu m}$) is $\backsim$ -75 Wm^{-2}, which is in reasonable agreement with the GCM modelling work of southern African biomass smoke of Myhre *et al.* (2003).

The BBR measurements of the up-welling irradiance are accurate to within 2% (Osborne *et al.*, 2004). This leads to an uncertainty in the ΔF of $\pm$ 2 Wm^{-2} and in $\tau_{\lambda=0.55\mu m}$ of $\pm$ 0.04.

3.6.4 Measuring the magnitude and spectral dependence of the up-welling radiance with the SWS

The aircraft measured the spectral dependence of the up-welling radiances in two SLRs, 33 metres above the sea surface (R10.1 and R10.2), and in two SLRs above the biomass plume (R8 and R9). The up-welling radiances are calculated with the measured biomass burning and MBL aerosol properties and vertical structure included in the model. The calculations require a degree of iteration in order to characterise both the spectral dependence of the surface albedo and the total aerosol amount in the column ($\tau_{MBL}/\tau_{biomass}$ fixed at 16%) until good agreement between the modelled and measured up-welling radiances at 0.55μm at both high and low-level is made. Implicit in the calculations is that the sea surface can be modelled using the Lambertian approximation and that the surface albedo and aerosol amount in the column does not change between the high and low-level runs. The iterative procedure used to model the radiances is as follows;

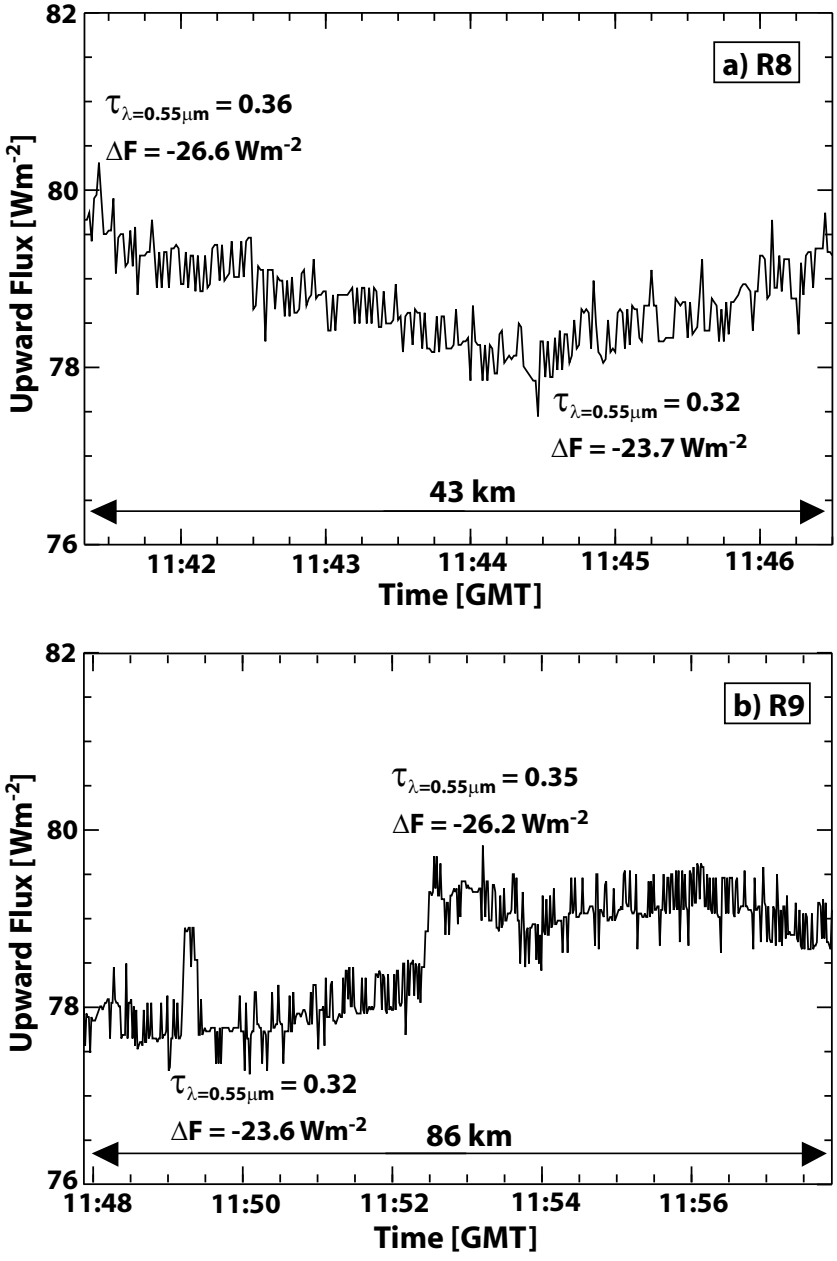

Figure 3.14: *Up-welling broadband irradiances (0.3 - 3.0 μm) measured with the Broad Band Radiometer (BBR) for two high level runs above the polluted biomass burning aerosol layer. The modelled up-welling flux in clear skies at the aircraft flight level is 53.7 Wm^{-2}. The direct radiative effect, ΔF, is calculated as the modelled clear sky flux - measured flux. The maximum and minimum ΔF and modelled optical depth, τ, are indicated.*

i) Estimate the aerosol mass loading.

ii) Estimate the value of the Lambertian surface reflectance.

iii) Model the up-welling radiance at low level and compare to the aircraft measurements.

iv) Adjust the surface reflectance to obtain agreement between the modelled and measured low level radiances.

v) Compare the modelled up-welling radiances at high level to the aircraft measurements.

vi) Adjust the aerosol mass loading to obtain agreement between the modelled and measured high level radiances.

vii) Repeat stages iii) to vi) until a match between the modelled and measured 0.55 μm radiance at both low and high level is obtained.

Figure 3.15 (a) shows the mean and standard deviation in the SWS measurements for the two low-level runs. The magnitude of the measurements from the down-Sun run (R10.1) is significantly less than those from the into-Sun run (R10.2) at all wavelengths. This is likely the result of the SWS instrument pointing into the shadow of the aircraft and therefore measuring a lower up-welling radiance due to the darker surface albedo, as schematically illustrated in figure 3.16. This is supported by analyses of aircraft measurements of the ocean bidirectional reflectance distribution function (BDRF) over the Atlantic Ocean, that suggest that the spectral albedo, $R_{s\lambda}$, ranges from 0.041 - 0.051 at a wavelength of 0.472 μm, and 0.026 - 0.035 at 0.682 μm (Gatebe *et al.*, 2004). The $R_{s\lambda}$ derived from the SWS measurements and the model calculations in this study was 0.019 and 0.041 at 0.472 μm, and 0.010 and 0.036 at 0.682 μm for R10.1 and R10.2 respectively. The values derived from R10.2 are in fairly good agreement with those of Gatebe *et al.* (2004), whereas the $R_{s\lambda}$ derived from R10.1 is much lower.

Figure 3.15 (b) shows the up-welling radiances measured at high-level above the aerosol layer (average of R8 and R9). The radiances at high level are modelled using the derived $R_{s\lambda}$ from the low-level runs. It is clear that when aerosol is not included in the model the radiances at high level cannot be simulated, and are significantly lower than the measurements at all wavelengths. When aerosol is included in the model using the $R_{s\lambda}$ derived for

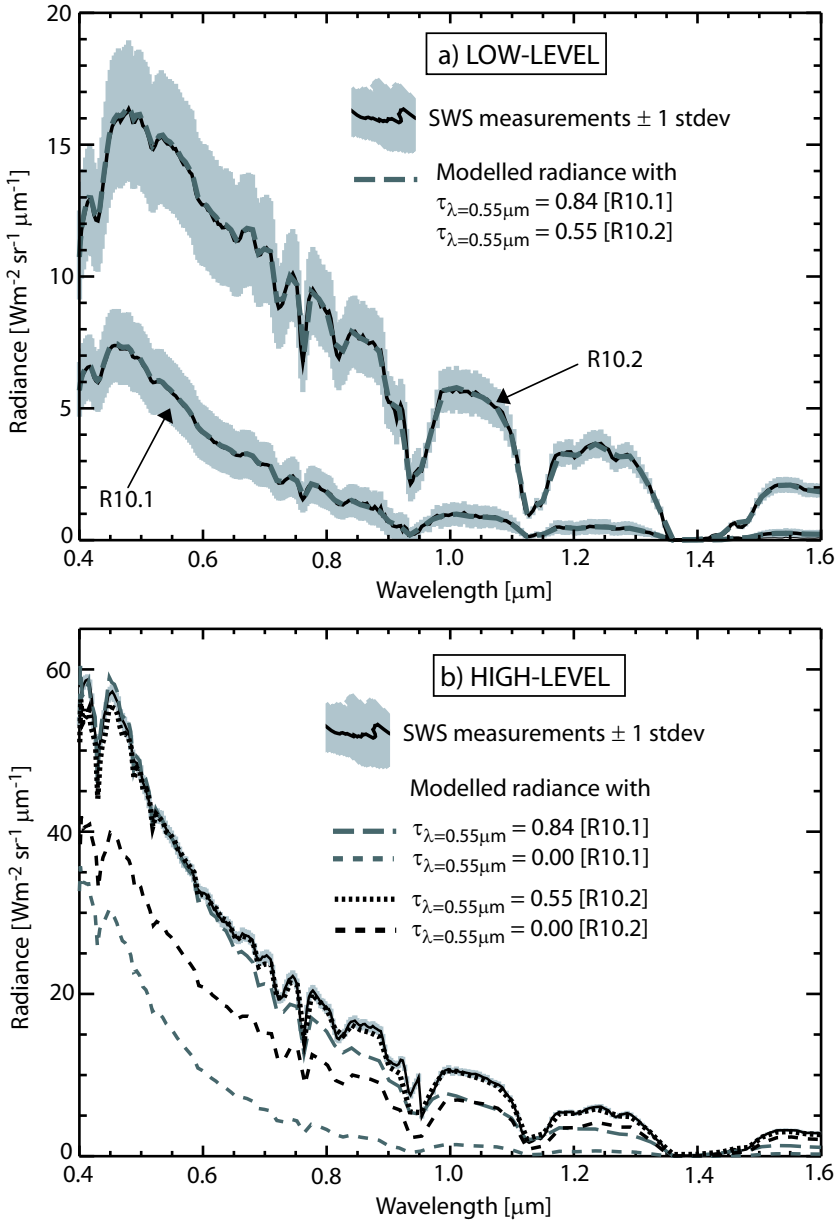

Figure 3.15: *a) Spectral measurements of the up-welling radiance at low-level (33 metres ASL) from the Short Wave Spectrometer (SWS) for R10.1 and R10.2. The magnitude of the measured radiance is lower in the down-sun run (R10.1) and is likely the result of the SWS field of view lying in the aircraft shadow (See figure 3.16). The dashed grey lines are the modelled radiances with a* $\tau_{\lambda=0.55\mu m}$ *of 0.84 for R10.1 and 0.55 for R10.2. It should be noted that the model surface reflectance is different for the two runs. b) The measured SWS radiances averaged over two high-level runs (R8 and R9). The modelled radiances with a* $\tau_{\lambda=0.55\mu m}$ *of 0.84 and 0.55 are shown, using the surface reflectance derived from R10.1 and R10.2 respectively. There is clearly better agreement with the measured radiances with a* $\tau_{\lambda=0.55\mu m}$ *of 0.55. The radiances at high level with no aerosol in the column are also shown for comparison.*

R10.1, a $\tau_{\lambda=0.55\mu m}$ of 0.84 is required to match the measurements at 0.55 μm. However at $\lambda > 0.6\mu m$ the agreement is poor, and the modelled radiances are again lower than the measurements. The retrieved $\tau_{\lambda=0.55\mu m}$ of 0.84 is also much higher than that derived from the other methods. This suggests that either the derived $R_{s\lambda}$ from R10.1 is not the same as that in the high level runs or that the aerosol properties in the model are not correct at $\lambda > 0.6\mu m$. When the up-welling radiances are modelled with aerosol included and the $R_{s\lambda}$ derived for R10.2, a $\tau_{\lambda=0.55\mu m}$ of 0.55 is needed to match the SWS measurements. This value is in better agreement with those derived from the other methods. Also, the modelled radiances are in good agreement with the measurements at all wavelengths. This suggests that the spectral dependence of aerosol properties included in the model are reasonable over the wavelength range 0.4 - 1.6 μm with a $\tau_{MBL}/\tau_{biomass}$ ratio of 16%, and that it is indeed the error in $R_{s\lambda}$ due to aircraft shadow contamination in R10.1 that leads to the large modelled value of $\tau_{\lambda=0.55\mu m}$.

It is clear that the value of the $\tau_{\lambda=0.55\mu m}$ retrieved from this method is very sensitive to the derived $R_{s\lambda}$, with $\tau_{\lambda=0.55\mu m}$ differing by >50% between the into-Sun and down-Sun runs. Although more confidence can be placed on the $R_{s\lambda}$ derived from the into-Sun run as aircraft shadow contamination was not as issue, there are still large uncertainties in modelling the up-welling radiances at high-level because the viewing geometry of the SWS instrument was different between the high and low level runs (i.e. the high-level runs were neither into or down-Sun). Therefore, if for example sun-glint (peak reflectance from the ocean surface) influenced the measured radiances at low-level, this would result in an unrealistic $R_{s\lambda}$ included in the model calculations of the high-level radiances where sun-glint may not have affected the measurements. An uncertainty of at least $\pm$ 10% in the $\tau_{\lambda=0.55\mu m}$ using the $R_{s\lambda}$ derived from the into-Sun run is estimated as a result of both errors in the surface properties included in the model, and the variability in the aerosol along the run (Haywood *et al.*, 2003b,c).

To reduce the uncertainties, either in-situ measurements, or an accurate model parameterisation of the sea surface BDRF would be required. Furthermore, the radiation code would need to be adapted to include a non-Lambertian surface. However, if an accurate representation of the surface is included in the model calculations the method will provide much more detailed spectral measurements of the aerosol optical depth than the other methods

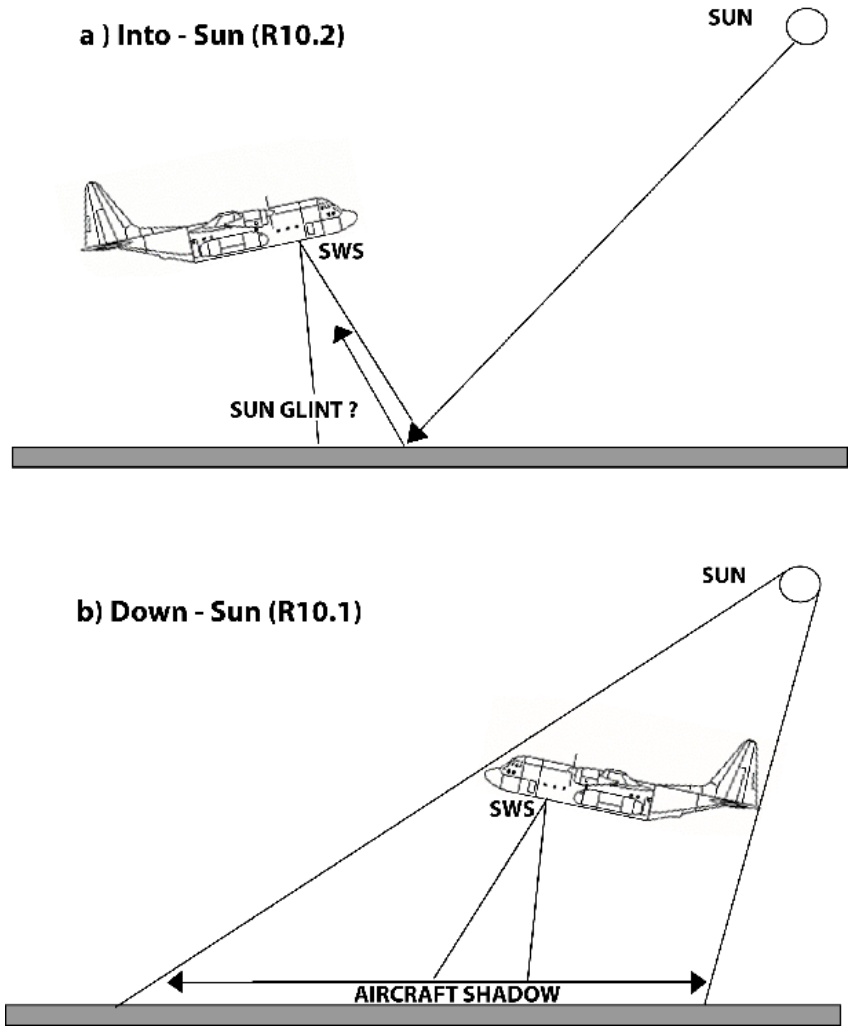

Figure 3.16: *Schematic diagram showing that the radiances measured by the Short Wave Spectrometer (SWS) in the (a) Into-Sun run may be influenced by sun glint off the sea surface. Measurements of the Bi Directional Reflectance Function (BDRF) of the sea surface would be needed to ascertain if this is the case. The swath of the SWS was pointing into the shadow of the aircraft on the down-sun run as illustrated in (b).*

considered in this study. It would also negate the need for a low-level run to characterise the surface, removing the uncertainty from the implicit assumption that the column amount of aerosol does not change between the low and high-level runs. The inclusion of a realistic surface BDRF into the Edwards Slingo radiation code is currently being explored at the Met Office.

3.6.5 Measuring the magnitude and spectral dependence of the down-welling radiance with SAFIRE

The aircraft flew below the biomass burning aerosol layer at an altitude of 33 m ASL and measured the down-welling zenith viewing radiances in seven wavelength channels with the SAFIRE instrument for an into-Sun (R10.2) and down-Sun run (R10.1). The mean and standard deviation measured radiance at 0.55μm was 174.5 $\pm$ 7.5 and 137.5 $\pm$ 2.7 Wm^{-2}sr$^{-1}\mu$m^{-1} for R10.1 and R10.2 respectively. The variation in the measurements suggests that there is some variability in the aerosol above the aircraft over the distance travelled in the two runs, 49 km for R10.1 and 66 km for R10.2.

The radiances at the SAFIRE wavelengths were then modelled with the inclusion of biomass burning and MBL aerosol in the column. Although the instrument was pointing directly upwards, the true viewing angle of the SAFIRE instrument was not exactly at zenith due to the pitch of the aircraft, which was 3.6 $\pm$ 0.4 $^\circ$ for R10.1 and 3.7 $\pm$ 0.4 $^\circ$ for R10.2 (see figure 3.16). Thus, the true viewing angle was θ_{szen} + θ_{pitch} for the into-Sun run and θ_{szen} - θ_{pitch} for the down-Sun run. The effect of the change in θ_{szen} was therefore required to model the radiances along each run and varied from 27.8 - 30.0° in R10.1 and from 30.4 - 31.7° in R10.2.

The $\tau_{MBL}/\tau_{biomass}$ ratio was initially set at 7 $\%$, which is representative of the mean value derived in sections 3.6.1 and 3.6.2. The $\tau_{\lambda=0.55\mu m}$ was then varied until a match was obtained with the mean measured radiances across each run at 0.55μm. Figure 3.17 (a) shows the modelled and measured radiances across both low-level runs. The slight downward slope in the modelled radiance with time is the result of the increasing θ_{szen}. The downward jump in the modelled and measured radiances between R10.1 and R10.2 is the result of the change in scattering angle relative to the Sun between the down and into-Sun runs. The modelling resulted in a $\tau_{\lambda=0.55\mu m}$ of 0.47 $\pm$ 0.03 for R10.1 and 0.47 $\pm$ 0.02 for R10.2. The error accounts for the variation in the measured radiance at 0.55 μm across each run and therefore represents the changes in the aerosol above the aircraft. A closer examination of figure 3.17 (a) reveals that there is good agreement between the model and measurements at 0.55 and 0.62 μm. The model calculation at 0.87 μm produces slightly higher radiances than the measurements, especially in R10.2. However, at all wavelengths larger than 0.87

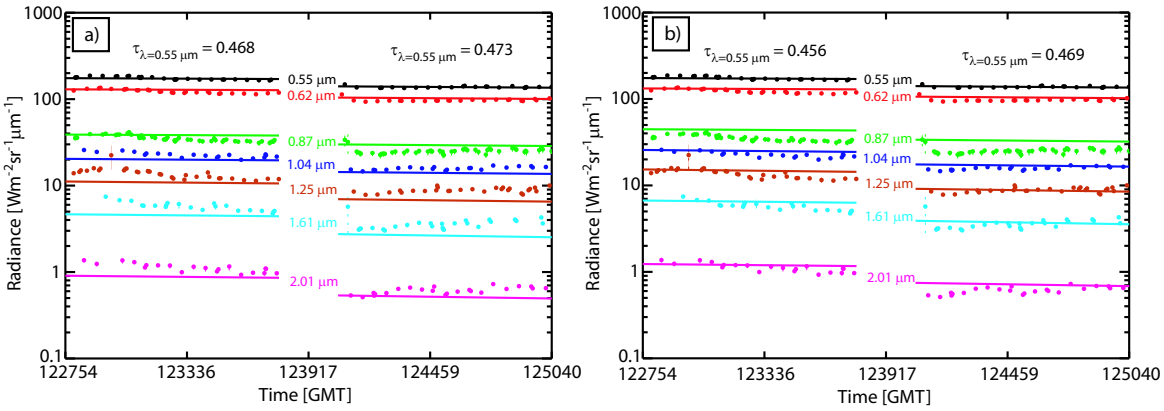

Figure 3.17: *The measured (filled circles) and modelled (straight lines) down-welling radiances at the SAFIRE wavelengths for the low-level runs (R10.1 followed by R10.2). The aerosol amount was varied in the column until agreement with the measurements was made at 0.55μm whilst holding the $\tau_{MBL}/\tau_{biomass}$ ratio held at a) 7$\%$, and b) 16$\%$.*

μm, the model underestimates the radiances. This is likely due to a mis-representation of the coarse mode particles in the model and can be explained when considering that maximum Mie scattering efficiency occurs when the wavelength of incident radiation is comparable to the particle size. Therefore, including more large coarse particles in the model will have the greatest impact on the down-welling radiances at the longer wavelengths.

By increasing the $\tau_{MBL}/\tau_{biomass}$ ratio to 16 $\%$, representative of the value calculated in the nephelometer calculation in the profile descent (P10) in section 3.6.1, the impact of the column integrated aerosol on the radiances in the near infra-red is enhanced. Figure 3.17 (b) shows the measured and the modelled radiances using a $\tau_{MBL}/\tau_{biomass}$ of 16 $\%$ with a $\tau_{\lambda=0.55\mu m}$ of 0.46 $\pm$ 0.03 for R10.1 and 0.47 $\pm$ 0.02 for R10.2. There is still good agreement at 0.55 and 0.62 μm. The modelled radiances at wavelengths between 0.87 and 2.01 μm are increased when the MBL aerosol amount is increased. This leads to a worse representation of the measured radiances at 0.87 μm compared to using a $\tau_{MBL}/\tau_{biomass}$ ratio of 7$\%$, although the agreement is improved at wavelengths between 1.04 and 2.01 μm. The effect of changing the relative amount of MBL aerosol in the column to that of the biomass burning aerosol on $\tau_{\lambda=0.55\mu m}$ is fairly small ($<$ 0.012). The down-welling radiances were found to be fairly insensitive to the assumed sea surface albedo. The radiometric calibration of the SAFIRE wavelength channels is estimated to lead to an absolute accuracy of 5 - 8 $\%$ in the measurements (Francis *et al.*, 1999). This leads to an uncertainty in $\tau_{\lambda=0.55\mu m}$ of approximately $\pm$ 0.04 - 0.07 from the mean value.

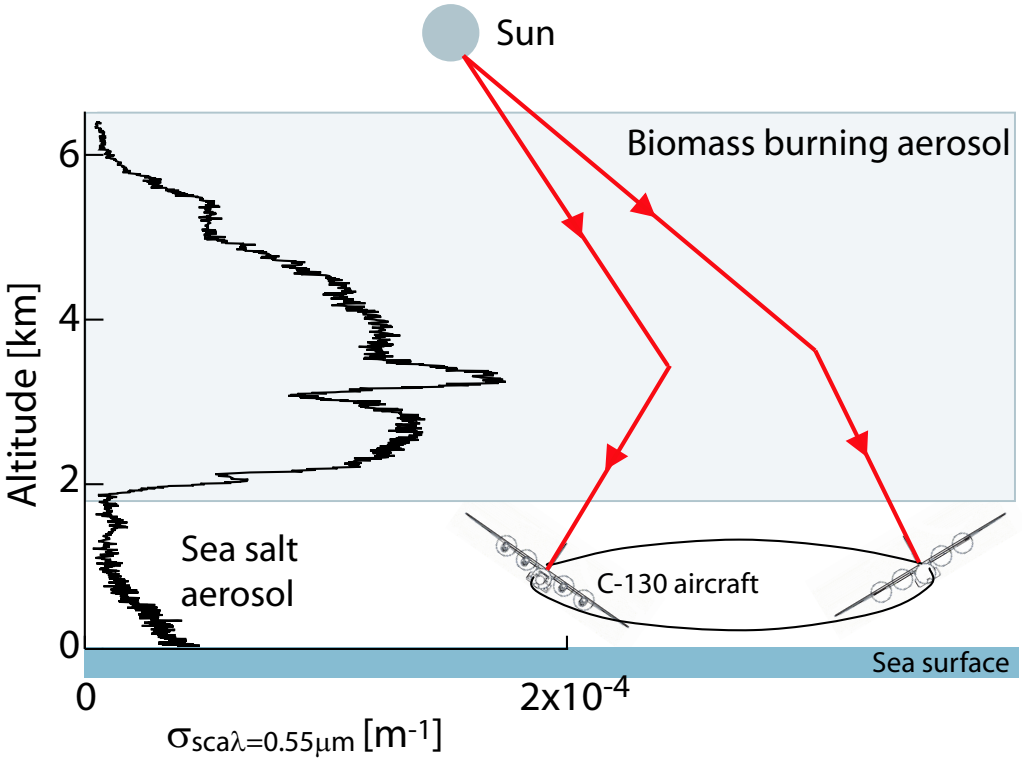

Figure 3.18: *Schematic diagram illustrating the aircraft orbit (typical diameter ∽2-3km) used to measure the down-welling sky-radiance distribution with the SAFIRE instrument. Also shown is the aerosol scattering coefficient, $\sigma_{sca\lambda=0.55\mu m}$, measured with the nephelometer during the profile descent, P10.*

3.6.6 Measuring the spectral dependence of the down-welling radiance as a function of scattering angle with SAFIRE

When the aircraft was flying in SLRs, the SAFIRE instrument was fixed in the zenith viewing position and so the measured radiances were for one scattering angle relative to the Sun (see section 3.6.5). The aircraft performed a series of 4 banked orbits at low level (118 metres ASL) below the biomass burning aerosol layer and was banked at an approximate angle of θ_{szen} = 32.6 ° as shown in figure 3.18. As the aircraft moved around the orbit (typical diameter of 2 - 3 km) the zenith viewing SAFIRE instrument measured radiances at the seven wavelengths as a function of scattering angle. The range of scattering angles observed in this method is approximately 0 to 2 x θ_{szen}. However, only measurements for scattering angles greater than 10 ° are considered to be reliable due to the calibration of the SAFIRE instrument when viewing a wide range of radiances (Haywood *et al.*, 2003b).

Figure 3.19 (a) compares the measured radiances as a function of scattering angle (filled

circles) to a model run (solid lines) with no aerosol in the column. It is clear that the magnitude and shape of the sky radiance distribution cannot be reproduced when no aerosol is included, with the modelled down-welling radiances being approximately 2-3 orders of magnitude too low. The biomass burning and MBL aerosols optical properties derived from the measured size distributions are then included in the model with the shape of the vertical structure measured during the aircraft profiles. The mass of aerosol in the column is then varied until the best agreement with the measured radiances at $0.55\mu m$ is made. Figure 3.19 (b) shows the model results using a $\tau_{MBL}/\tau_{biomass}$ of 7% with a $\tau_{\lambda=0.55\mu m}$ of 0.44. There is a significant improvement in the modelled radiances when the aerosol is included, although significant discrepancies still exist. The differences in the measured and modelled radiances may in part be attributed to the absolute accuracy of 5 - 8 $\%$ of the SAFIRE measurements (Francis *et al.*, 1999). However, at all wavelengths the shape of the modelled sky radiances is too flat, and at the longer wavelengths the magnitude of the modelled radiance is still too low. These features are indicative of a misrepresentation of the coarse mode particles which tend to scatter more radiation in the forward direction and are more efficient at scattering radiation at longer wavelengths compared to the smaller particles in the accumulation mode.

Increasing the amount of large MBL particles in the column so that the $\tau_{MBL}/\tau_{biomass}$ ratio is increased to 16% (figure 3.19 (c)) results in an excellent agreement at all scattering angles in the 0.55 and 0.62 μm channels with a $\tau_{\lambda=0.55\mu m}$ of 0.44. The agreement is much improved at all other wavelengths. However, there is still an underestimation in the magnitude of the sky-radiance at 2.01 μm. This implies that the modelled aerosol phase function from the Mie scattering calculations is not representative of the actual aerosol at the longer wavelengths. This is not a surprising result due to the large uncertainty in fitting the log-normal representing the coarse mode particles of the biomass burning aerosol to the measured PCASP size distribution. The PCASP instrument only measures particles up to 1.5 μm radius. The coarse mode particles in the biomass plume are also likely to be non-spherical (Haywood *et al.*, 2003b) and so standard Mie scattering calculations may not represent the aerosol phase function well. As mentioned in section 3.5.2 there is also a large uncertainty in the refractive index of the coarse mode particles which are likely to contain a significant fraction of dust-like particles. In this work the wavelength dependent refractive index of the coarse mode of the biomass burning aerosol is assumed to be the same

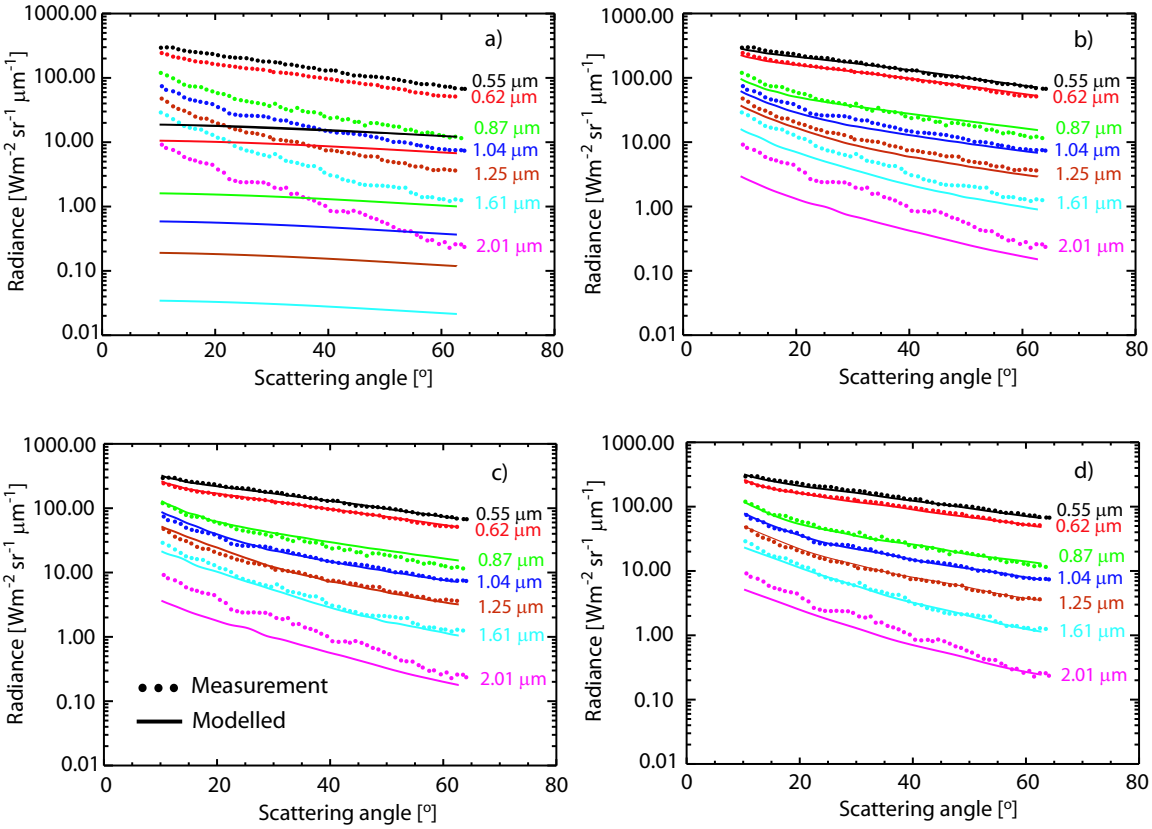

Figure 3.19: *The measured and modelled radiances as a function of scattering angle at the SAFIRE wavelengths. The modelled results are for a) no aerosol included in the model, b)* $\tau_{\lambda=0.55\mu m}$ *= 0.44 and the* $\tau_{MBL}/\tau_{biomass}$ *ratio = 7 %, c)* $\tau_{\lambda=0.55\mu m}$ *= 0.44 and the* $\tau_{MBL}/\tau_{biomass}$ *ratio = 16 %, d)* $\tau_{\lambda=0.55\mu m}$ *= 0.44 with the column size distribution and optical properties derived with the AERONET retrieval.*

as that of the accumulation mode particles, whose refractive index is better constrained. Osborne *et al.* (2004) present a similar analysis to that presented here for other CASE studies from SAFARI 2000 and use a refractive index more indicative of Saharan dust aerosol, although they still observe significant discrepancies at the longer wavelengths. The value of $\tau_{\lambda=0.55\mu m}$ derived here is in good agreement with the retrieval from the down-welling radiances measured in the SLRs with the same instrument. Accounting for the uncertainty in the magnitude of the measured radiances leads to an error of $\pm$ 0.05 in $\tau_{\lambda=0.55\mu m}$.

3.6.7 AERONET retrieval from SAFIRE measurements in section 3.6.6

The AERONET retrieval algorithm is designed to simultaneously retrieve the aerosol size distribution, complex refractive index, and single scattering albedo derived from spectral almucantar measurements of the sky radiance and the optical depth obtained by ground-based

Sun-sky photometers (Dubovik and King, 2000, Dubovik *et al.*, 2000). It is currently applied to a globally distributed network of ground-based radiometers. It is therefore important to validate the retrieval algorithm against detailed in-situ measurements, as AERONET measurements are often used to validate both satellite measurements (Hsu *et al.*, 1999, Chu *et al.*, 2002, Remer *et al.*, 2002a, Ichoku *et al.*, 2003), and outputs from chemical transport models (Tegen *et al.*, 1997, Sato *et al.*, 2003).

The retrieval has been validated through a comparison of in-situ aircraft measurements of the retrieved quantities with those obtained with a co-located AERONET site (Haywood *et al.*, 2003b). Because the AERONET sites are predominantly situated on land this type of validation is generally restricted to continental aerosol. However, the inversion algorithm can also use the sky radiance data measured with the SAFIRE instrument during the banked orbits, thereby enabling the testing of the retrieval over oceanic regions. Because the aerosol optical depth is a quantity that we are trying to retrieve, an a-priori knowledge of the effective refractive index of the aerosol in the column is required to invert the measured radiances to the aerosol size distribution, optical properties, and optical depth (compared to AERONET sites that measure the τ_λ independently and use as input to the retrieval). The wavelength dependent refractive index used for the biomass burning aerosol in this study (see figure 3.11) is used as the a-priori as the majority of the aerosol in the column resides in the biomass plume. The retrieval uses the a-priori to constrain the output refractive index, which is more representative of the MBL and biomass aerosol above the aircraft.

The inversion algorithm was run using the measured SAFIRE radiances as input. The run was then repeated with the measured radiances varied by $\pm 8\%$, which represents the maximum expected error in the measurements (Francis *et al.*, 1999). Figure 3.20 shows the retrieved column integrated size distribution and wavelength dependent optical depth, single scattering albedo, and real and imaginary parts of the refractive index. The retrieved $\tau_{\lambda=0.55\mu m}$ is 0.44$\pm$0.05, where the error represents the sensitivity to uncertainties in the magnitude of the measured sky-radiances. An additional uncertainty of +0.01 should be included to account for the MBL aerosol below the aircraft. The optical depth falls off rapidly with wavelength, to a value of 0.07$\pm$0.01 at 2.01μm, and has a corresponding Angstrom parameter of 1.47 over the measured wavelength range. The Angstrom parameter was calculated from a linear fit of lnτ versus lnλ for the retrieval at the SAFIRE wavelengths. The

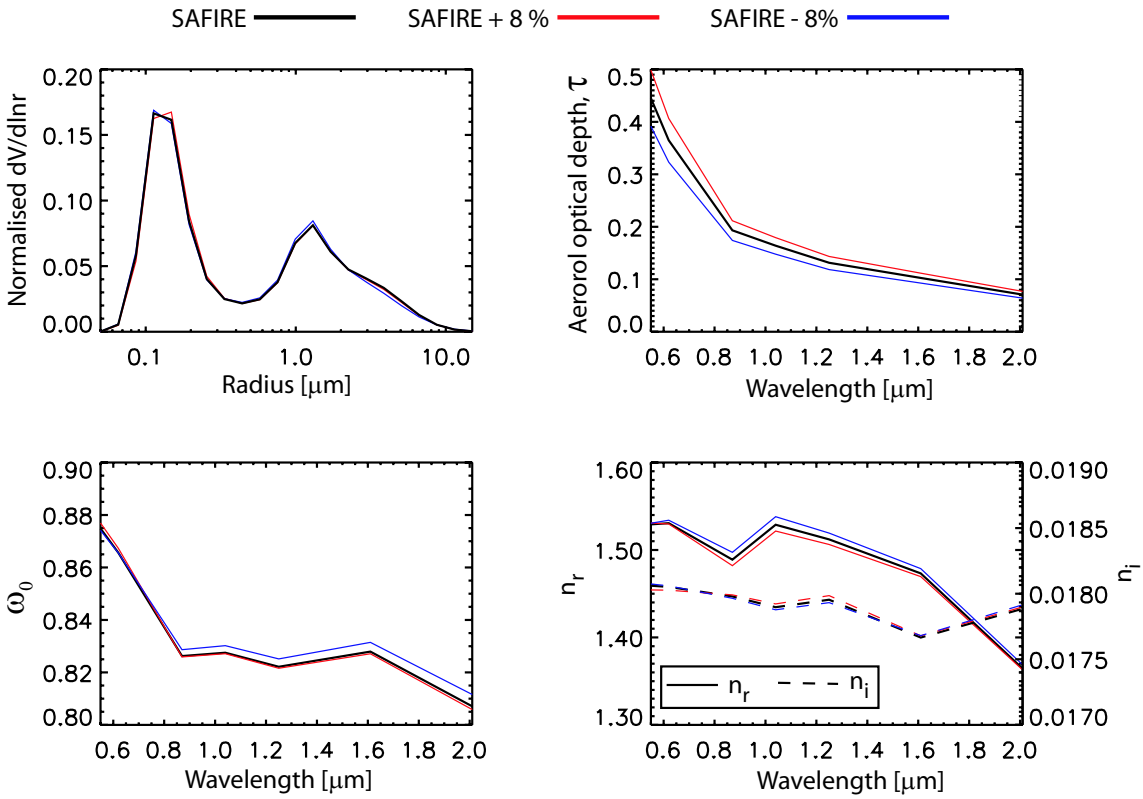

Figure 3.20: *The columnar aerosol size distribution, optical depth, single scattering albedo, real (n_r) and imaginary (n_i) refractive indices calculated with the AERONET retrieval algorithm and the SAFIRE radiances. The retrieval is repeated with the measured SAFIRE radiances varied by $\pm 8\%$ which represents the uncertainty in the measurements.*

value of 1.47 indicates that the aerosol in the column is dominated by the smoke particles in the accumulation mode. The retrieved $\omega_{0\lambda=0.55\mu m}$ is 0.88. This is in agreement with the value of 0.89$\pm$0.04 derived from the PSAP and nephelometer measurements within the biomass plume, although it should be noted that the MBL aerosol ($\omega_{0\lambda=0.55\mu m}$ =1.0) above the aircraft will also be included in the retrieval. The retrieved real part of the refractive index tends to fall off with increasing wavelength (1.53 - 1.36 across the SAFIRE wavelengths), whereas the imaginary part is relatively constant at $0.018\pm0.0005i$. The retrieved aerosol size distribution is fairly insensitive to the uncertainties in the SAFIRE measurements, although there are slight changes in the peak of the accumulation mode.

Figure 3.21 compares the in-situ measurements of the biomass burning aerosol size distribution to the AERONET retrieval. The in-situ measurements have been re-gridded onto the output sizes of the retrieval. There is a reasonably good agreement in the modal size of the accumulation mode, with the measured peak at $0.15\mu m$ and the retrieved peak at $0.11\mu m$, although the retrieved distribution is broader. For the retrieval using the SAFIRE radiances

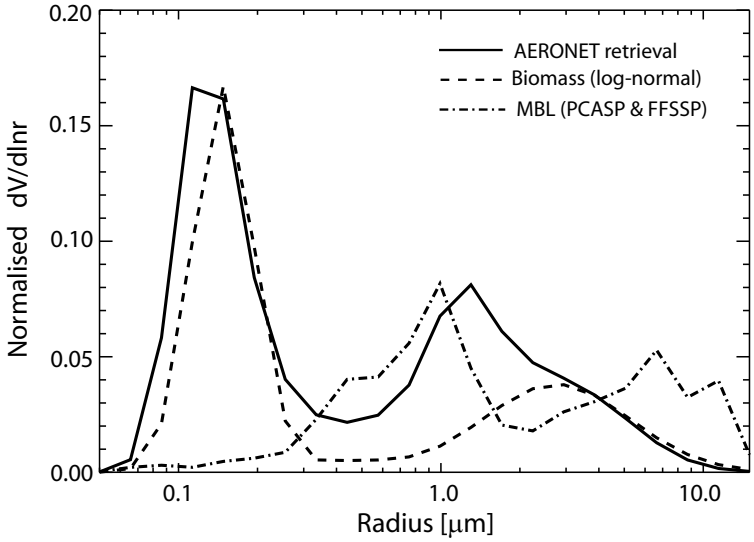

Figure 3.21: *Comparison of the particle size distribution measured in-situ and retrieved with the AERONET algorithm. The in-situ size distribution for biomass burning and MBL aerosol are those included in the radiative transfer model.*

(+8%) the peak in the accumulation mode is the same as the in-situ measurements. The measured distribution for the MBL aerosol peaks at around $1\mu m$, with a secondary peak at approximately $7\mu m$, whereas the coarse mode of the biomass burning aerosol peaks at around $3\mu m$. The AERONET retrieved coarse mode peaks at 1.3 μm which is very similar to the MBL aerosol. The influence of the coarse mode biomass particles and perhaps the secondary peak in the MBL aerosol can be seen in the extended tail of the retrieved size distribution to larger sizes.

The AERONET retrieved size distribution and optical properties are then inserted into the Edwards Slingo 1996 radiation code in a uniform layer above the aircraft flight level and the radiances modelled. Figure 3.19 (d) compares the measured radiances to those modelled using a column $\tau_{\lambda=0.55\mu m}$ of 0.44. There is excellent agreement between the measured and modelled radiances at wavelengths from 0.55 - $1.61\mu m$, although the modelled radiance at $2.01\mu m$ is lower than the measurements. Good agreement would be expected as the aerosol properties inserted in the model are themselves retrieved from the measurements. The discrepancies at $2.01\mu m$ may be the result of the non-spherical particles in the coarse mode of the biomass burning aerosol (the retrieval assumes spherical particles), and a lack of measurements at scattering angles less than 10°. Information at scattering angles less than 10° would provide further information on the scattering of the coarse mode particles, and therefore perhaps improve the retrieval at the longer wavelengths. However, it does in-

dicate that in this case where there are two distinct layers of aerosol comprising of different aerosol types in the column, the sky-radiance distribution can be well represented with a column average of the aerosol properties.

The inversion algorithm could easily be modified to accept the measured radiances from the SWS instrument, that has a much finer spectral resolution than the SAFIRE instrument. If the SWS instrument was mounted on the aircraft so that it could measure the down-welling sky radiance during banked orbits (as with the SAFIRE instrument during SAFARI 2000), or mounted so that it could scan the down-welling radiances as a function of scattering angle as the aircraft flies in SLRs, then this would provide excellent constraints on the retrieved size distribution and optical properties with the AERONET algorithm.

3.7 Summary and discussion

The physical and optical properties of biomass burning aerosol in the aged regional haze were measured on September 14th 2000 off the coast of Namibia and Angola. Model trajectories indicate that the aerosol had aged in the atmosphere for at least 30 hours, and so the results are more representative of the aerosol that pervades large areas of southern Africa during the dry biomass burning season than the fresh aerosol studied in chapter 2.

Vertical profiles made during aircraft ascents and descents show that the biomass burning aerosol layer exists in an elevated polluted layer above the MBL. The two distinct layers are separated by a clean air slot that is characterised by low aerosol concentrations and scattering, and thus high visibility. There is evidence of a thin layer of cloud capping the MBL in one of the profiles. The temperature inversions associated with the clean air slot inhibits mixing in the vertical and therefore minimises cloud-aerosol interactions.

Direct measurements of the aerosol scattering and absorption in the biomass plume resulted in a $\omega_{0\lambda=0.55\mu m}$ of 0.89$\pm$0.04 which is entirely consistent with the value of 0.90$\pm$0.01 derived from the measured PCASP size distribution and Mie scattering theory. It is also in good agreement with the average $\omega_{0\lambda=0.55\mu m}$ value of 0.91$\pm$0.04 (Haywood *et al.*, 2003a), and 0.89$\pm$0.03 (Magi *et al.*, 2003) measured in aged regional hazes during the SAFARI 2000 campaign. To include the aerosol into the radiative transfer model a series of three

log-normals were fitted to the mean PCASP size distribution to account for the coarse mode particles that were not measured with the PCASP instrument. Mie calculations were performed to determine the wavelength dependent optical properties, and resulted in a $\omega_{0\lambda=0.55\mu m}$ of 0.89. However, the uncertainty in the optical properties of the particles in the coarse mode is large due to i) uncertainties in the log-normal fit, ii) non-spherical particles that are not accurately represented by standard Mie scattering calculations and iii) uncertainties in the assumed refractive index of the coarse particles.

Seven different methods were used to calculate the $\tau_{\lambda=0.55\mu m}$ in the column and the results are summarised in table 3.7. The $\tau_{\lambda=0.55\mu m}$ calculated from the different methods varied widely, ranging from 0.19 to 0.84. However, the lowest value arises from the integration of the aerosol extinction derived from the PCASP instrument during profile ascents, and is likely the result of under-sampling of the aerosol number concentration due to the aircraft pitch. The value derived from the profile descent is in much better agreement with those derived from the other methods, and is consistent with the value derived from the nephelometer and PSAP measurements in the same profile. The upper limit is the result of modelling the up-welling spectrally dependent radiances measured with the SWS instrument with a derived surface albedo that is unrealistic due to shadow contamination from the aircraft. Using a more realistic surface albedo resulted in consistency with other methods. Detailed in-situ measurements of the surface BDRF would be required to reduce the uncertainties in this technique.

A relatively low value of 0.33-0.34$\pm$0.06 was calculated when modelling the BBR up-welling fluxes at high level. Osborne *et al.* (2004) obtain similar low values of $\tau_{\lambda=0.55\mu m}$ with the BBR method and suggest that the irradiance pyranometers may have become coated with a significant amount of aerosol during the flight, and thus affect the measurements.

There is good agreement (within the uncertainties of each method) between the $\tau_{\lambda=0.55\mu m}$ derived from the SAFIRE radiances in both SLRs and orbits, the AERONET retrieval algorithm, the SWS radiances, and integrating the aerosol extinction from the nephelometer and PSAP during the profile descent (the profile ascents resulted in a higher $\tau_{\lambda=0.55\mu m}$), with values ranging from 0.44$\pm$0.06 to 0.55$\pm$0.06. The radiometric measurements both above the biomass plume and at low-level show variations in $\tau_{\lambda=0.55\mu m}$ of up to $\pm$ 0.03 on spatial

Optical depth retrieval	Run number	$\tau_{\lambda=0.55\mu m}$
i) Integrating extinction derived	P9	0.62±0.03
from the nephelometer and PSAP	P10	0.53±0.03
	O4R11	0.61±0.03
ii) Integrating extinction derived	P9	0.25 [a]
from the PCASP	P10	0.58
	O4R11	0.19 [a]
iii) Modelling the measured	R8	0.34±0.06
up-welling BBR irradiance	R9	0.33±0.06
iv) Modelling the measured	R10.1;(R8/R9)	0.84 [b]
up-welling SWS radiance	R10.2;(R8/R9)	0.55±0.06
v) Modelling the measured	R10.1	0.46±0.10
down-welling SAFIRE radiance	R10.2	0.47±0.09
vi) Modelling the SAFIRE radiance as a function of scattering angle	orbits	0.44±0.05
vii) As vi) but using AERONET retrieval	orbits	0.44±0.06 [c]

Table 3.7: *Summary of the $\tau_{\lambda=0.55\mu m}$ derived from the different methods. The error in method i) arises from the uncertainty in ω_0 used to derive the aerosol extinction. The error in methods iii) and v) is the result of instrument precision and the variation in the aerosol along the run. The error in method iv) is the result of the variation in the aerosol along the run and the uncertainty in the sea surface reflectance. The error in methods vi) and vii) is due to uncertainties in the magnitude of the measured radiances. [a] low values likely the result of under-sampling of N_{tot} during profile ascents. [b] high value due to aircraft shadow contamination in the up-welling radiances. [c] includes an additional uncertainty of 0.01 to account for the MBL aerosol below the aircraft.*

scales as low as 43km. Therefore, the variation in $\tau_{\lambda=0.55\mu m}$ between the different methods can be in part attributed to the variability of the aerosol in the area where the measurements were taken ($\backsim$150 - 200km^2).

Modelling the measured sky-radiance distribution from the aircraft orbits is considered to be the most accurate method as it has previously been validated against ground based sun-photometer measurements (Haywood *et al.*, 2003b). The method is also sensitive to the wavelength dependent aerosol optical properties included in the model and can therefore give insight into any potential errors in the in-situ aircraft measurements, such as a mis-representation of the coarse mode particles. Future measurement campaigns should concentrate on measuring the sky-radiance as a function of scattering angle when attempting to retrieve $\tau_{\lambda=0.55\mu m}$. This should be combined with SLRs at various altitudes in the

aerosol layer(s) to identify any layered structure in the aerosol optical properties, and deep vertical profiles from the surface to the clean free troposphere to characterise the relevant amount of aerosol as a function of altitude.

The AERONET retrieval of the column integrated aerosol size distribution and optical properties were shown to be in reasonable agreement with the in-situ aircraft measurements. Future measurement campaigns should continue to aim at validating the AERONET retrieval algorithm for different aerosol types. If the SWS instrument was mounted on the aircraft in a manner to measure the sky-radiance distribution, this would provide much more detailed spectral measurements than the SAFIRE instrument used in this study, providing excellent constraints for input into the algorithm. Of particular importance to radiative forcing studies is that the measured sky-radiance distribution was accurately modelled using the column integrated aerosol properties, even though there were two distinct atmospheric layers consisting of different types of aerosol (MBL and biomass burning). Therefore, the long-term global distribution of AERONET measurements could and should be used to improve global simulations of aerosol properties and the direct aerosol radiative effect, at least in clear skies. However, chapters 4 and 5 show that in the presence of clouds, the direct effect of partially absorbing aerosols such as biomass smoke is highly sensitive to the vertical structure, thus column integrated optical properties may not be appropriate. Furthermore, the aerosol semi-direct and indirect radiative effects are likely to be most sensitive to the aerosol properties in and around cloud layers.

Chapter 4

The effect of overlying biomass burning aerosol layers on remote sensing retrievals of cloud optical properties

4.1 Introduction

A semi-permanent layer of marine stratocumulus exists off the coast of Namibia and Angola (see figure 4.1), and is the result of cool upwelling ocean water associated with coastal currents and the presence of synoptic scale high-level subsidence (Slingo *et al.*, 1982). As the aged biomass burning aerosol is advected over these oceanic regions, it tends to exist in elevated polluted layers above the cloud, which is separated by a clean air slot thus inhibiting aerosol-cloud interactions (see chapter 3). However, the presence of the partially absorbing aerosol above the highly reflective cloud leads to a reduction in the outgoing flux at the top of the atmosphere (Keil and Haywood (2003) and chapter 5). Haywood *et al.* (2004) present theoretical calculations showing that the Moderate Resolution Imaging Spectrometer (MODIS) and Advanced Very High Resolution Radiometer (AVHRR) satellite retrievals of water cloud optical depth, τ_{cloud}, and cloud particle effective radius, r_e, are subject to potential biases as a direct result of the overlying aerosol which is not accounted for in the retrieval. This chapter investigates whether the bias in r_e is indeed evident in the MODIS retrievals.

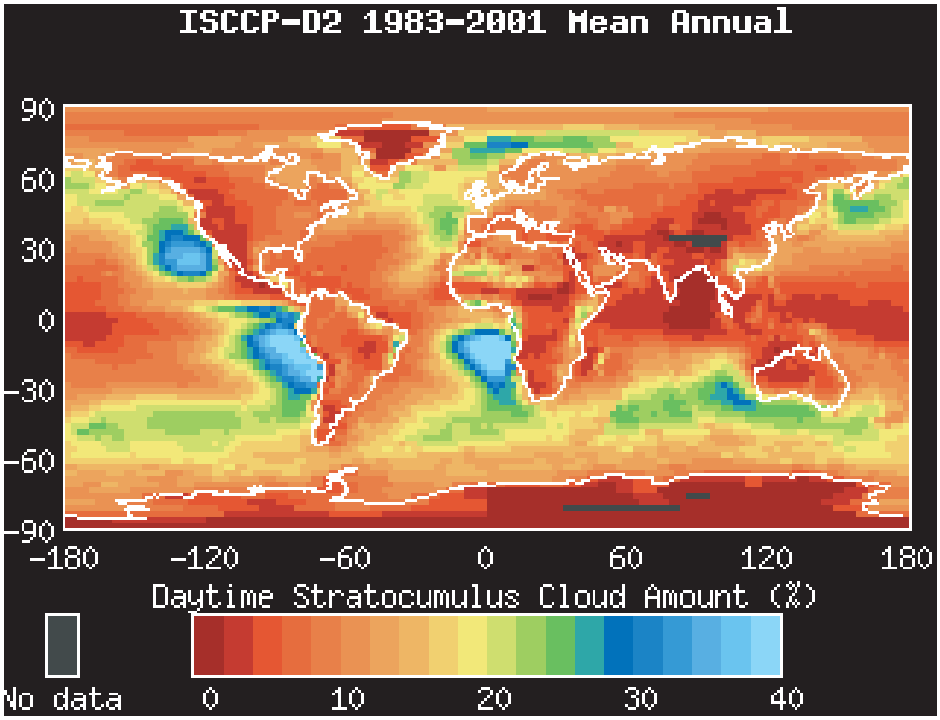

Figure 4.1: *Annual mean (1983-2001) global daytime stratocumulus cloud fraction from the International Satellite Cloud Climatology Project (ISCCP) D2 data set. Stratocumulus is defined as having a cloud optical depth of 3.6 - 23, and a cloud top pressure exceeding 680 hPa. The semi-permanent stratocumulus cloud sheet off the West coast of southern Africa is evident, with annual mean daytime cloud fractions* $\geq 40\%$*. The figure is available at http://isccp.giss.nasa.gov.*

Section 4.2 gives a description of the underlying principles used to retrieve cloud optical properties from satellite platforms. Section 4.3 outlines the theoretical calculations of Haywood *et al.* (2004), and section 4.4 examines the MODIS pixel level data to determine whether the theoretical biases are evident in the satellite retrieval algorithms. Section 4.5 summarises this works findings.

The work in this chapter is included in the paper Haywood *et al.* (2004) which has been published in the Quarterly Journal of the Royal Meteorological Society (see appendix D).

4.2 Satellite retrievals of cloud optical properties

The manner in which clouds interact with radiation depends primarily on the cloud optical depth, τ_{cloud}, droplet single scattering albedo, ω_0, and the droplet phase function (primarily the asymmetry factor, g). As with aerosols, each of these parameters are dependent on

the particle size distribution and wavelength dependent refractive index. However, Slingo and Schrecker (1982) show that the exact nature of the size distribution is not critical, and that the radiative parameters can be determined from the cloud particle effective radius, r_e, given by,

$$r_e = \frac{\int_0^\infty r^3 n(r) dr}{\int_0^\infty r^2 n(r) dr}, \tag{4.1}$$

where $n(r)$ is the droplet size distribution function, and r is the radius. Therefore, remote sensing retrievals of cloud properties are designed to retrieve global distributions of τ_{cloud} and r_e, both of which are required to model the radiative impact of clouds on climate (e.g. Slingo (1989)).

The AVHRR and MODIS satellite retrieval algorithms compare measurements of the up-welling top of the atmosphere (TOA) radiances/reflectances from two channels (one visible, one near infra-red) to look-up tables based on extensive radiative transfer calculations for a range of τ_{cloud} and r_e until a best fit is obtained (e.g. Han *et al.* (1994), Platnick and Valero (1995), King *et al.* (1998, 2003)). The underlying principle of this technique is that the up-welling TOA radiance in a non-absorbing band in the visible wavelength region ($\backsim< 1\mu m$) is primarily a function of τ_{cloud}, and largely independent of r_e because cloud droplet absorption (1-ω_0) is negligible for all particles sizes (see figure 4.2). It should be noted that there is a small dependence on r_e as illustrated in figure 4.3 (a), which results from slight increases in the g with particle size, thus reducing the probability that a photon will be scattered back out of the cloud top.

In a water (or ice) absorbing band in the near infrared ($\backsim\geq 2.5\mu m$), the up-welling TOA radiance is primarily a function of r_e because droplet absorption becomes important, and increases significantly with particle size. Therefore, as the cloud droplet size increases, there is a greater chance that a photon will be absorbed as it passes through the cloud, reducing the amount of photons exiting the cloud and reaching the TOA. This is illustrated in figure 4.3 (b), where the cloud reflectance in the near infra-red is reduced as the r_e increases. At τ_{cloud} values $> 4 - 7$, the radiance at $3.7\mu m$ is independent of τ_{cloud} for a

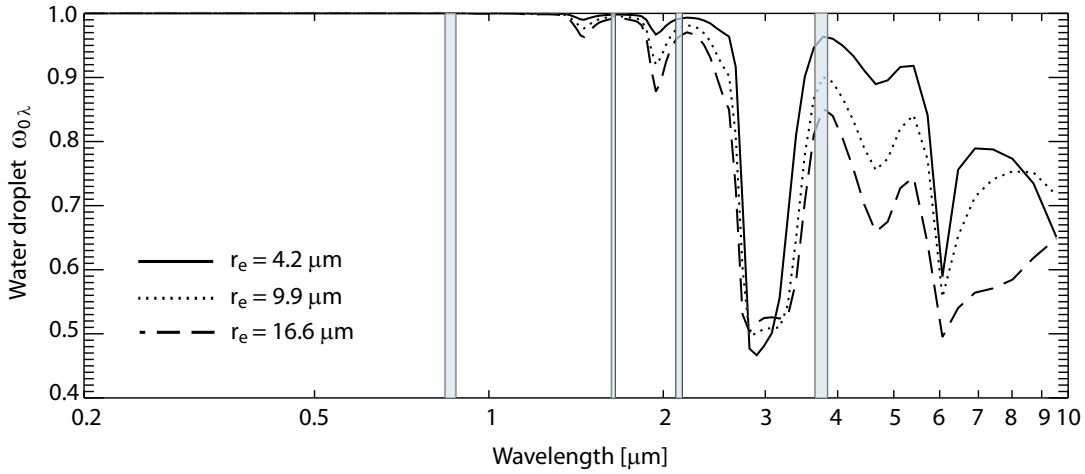

Figure 4.2: *Water droplet $\omega_{0\lambda}$ as a function of wavelength for selected values of r_e. The refractive index of Hale and Querry (1973) is used to 2μm, thereafter Palmer and Williams (1974). Results apply to log-normal distributions with a mode radius and r_e of the St2, Sc2, and analytic size distributions in Slingo and Schrecker (1982). The location and bandwidth of the MODIS wavebands used to retrieve cloud optical properties over ocean are also indicated.*

given r_e (for realistic values of r_e i.e. $> 4\mu m$).

At intermediate wavelengths (1-2.5μm), the TOA radiance is a function of both τ_{cloud} and r_e. By combining a measurement from the visible and near infra-red wavelengths, both τ_{cloud} and r_e can be inferred. The calculations that form the basis of the look-up tables include the effects of Rayleigh scattering, gaseous absorption, solar zenith angle and the viewing geometry of the satellite. However, the effect of aerosols are neglected due to the large uncertainties in the spatial and temporal distribution of aerosol optical properties and vertical structure.

AVHRR retrieval; The AVHRR algorithm employs the non-absorbing 0.63μm band in conjunction with the water absorbing 3.7μm band to determine τ_{cloud} and r_e (Han *et al.*, 1994, Platnick and Valero, 1995). The measured radiances are included in the International Satellite Cloud Climatology Project (ISCCP) analysis of cloud properties (Rossow and Schiffer, 1991).

MODIS retrieval; The MODIS algorithm uses the non-absorbing band at 0.86μm over ocean and 0.65μm over land. Different non-absorbing bands are used over ocean and land to minimise the contribution of the underlying surface reflectance to that measured at the TOA. These are combined with water absorbing bands at 1.63, 2.13, and 3.7μm

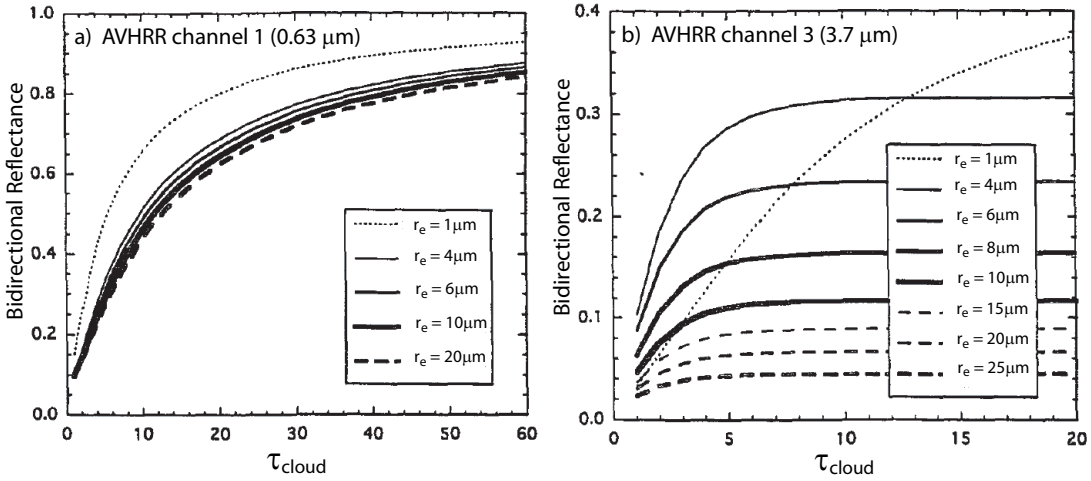

Figure 4.3: *Bidirectional reflectance for various r_e as a function of τ_{cloud} for the a) non-absorbing (0.63μm) and b) water absorbing (3.7μm) wavelengths used in the AVHRR retrieval of cloud properties. The same features would be evident in up-welling TOA radiances. Figure modified from Platnick and Valero (1995).*

to produce three retrievals of τ_{cloud} and r_e (King *et al.*, 2003, Platnick *et al.*, 2003). The MODIS Level-2 MOD06 cloud product includes daily τ_{cloud} and r_e values derived from the default 0.86/2.13μm radiance pairs at a spatial resolution of 1km. Haywood *et al.* (2004) adopt the nomenclature of $r_{e1.63}$, $r_{e2.13}$, and $r_{e3.7}$, to represent the cloud effective particle radius derived from the 0.86/1.63, 0.86/2.13, and 0.86/3.7μm radiance pairs. In addition to the $r_{e2.13}$, the particle sizes from the retrievals that use the 1.63 and 3.7 μm bands are reported as differences from the default value, e.g. $r_{e1.63}$-$r_{e2.13}$, and $r_{e3.7}$-$r_{e2.13}$. However, the difference in τ_{cloud} resulting from the three retrievals is small (Platnick *et al.*, 2003) and so only the default retrieval is reported. The Level-3 MOD08 product contains daily, eight day, and monthly aggregated global 1x1 degree grids of the data from the Level-2 1km 0.86/2.13μm retrieval.

4.3 Theoretical calculations

An overview of the theoretical calculations detailed in Haywood *et al.* (2004) that form the basis for the work in this chapter are given in this section.

The radiance version of the Edwards Slingo radiation code (Edwards and Slingo, 1996) was used to model the up-welling radiances at the top of the atmosphere at the wavelengths

	$\lambda = 0.55\mu m$	$\lambda = 0.63\mu m$	$\lambda = 0.86\mu m$	$\lambda = 1.63\mu m$	$\lambda = 2.13\mu m$	$\lambda = 3.7\mu m$
τ_λ	0.5	0.39	0.35	0.05	0.04	0.02

Table 4.1: *Wavelength dependent aerosol optical depth (τ_λ) included in the radiative transfer model. Values listed are at 0.55μm and the wavelengths used in the AVHRR and MODIS (over ocean) satellite retrievals of cloud properties.*

0.63, 0.86, 1.63, 2.13, and 3.7μm, corresponding to those used in the AVHRR and MODIS retrieval algorithms of cloud properties. A sea surface temperature of 287K and cloud top temperature of 300K was used for the radiative transfer calculation at 3.7μm, and was typical of the C-130 aircraft measurements during SAFARI 2000. The contribution by thermal emission to the TOA radiances at the other wavelengths is negligible. Calculations were performed using a SZA of 30° and a nadir viewing angle. The surface albedo was assumed to be Lambertian and have a constant value of 0.05 at all wavelengths. The biomass burning aerosol was included in the model between 500 and 900 hPa with a $\tau_{\lambda=0.55\mu m}$ of 0.5. The optical properties of the biomass burning aerosol had similar wavelength dependence to the aged biomass burning aerosol detailed in chapter 3, and were such that $\omega_{0\lambda=0.55\mu m}$ = 0.91 and τ_λ decreased rapidly with wavelength as indicated in table 4.1. The cloud was inserted between 950 and 980 hPa and the liquid water content varied so that τ_{cloud} ranged from 4 - 20, and r_e from 4 - 20μm.

Analyses of the monthly mean $\tau_{\lambda=0.55\mu m}$ from the MODIS satellite in chapter 5 show that values of $\tau_{\lambda=0.55\mu m} \geq 0.5$ are common over the Namibian cloud sheet during the month of September. Further, the analysis of different techniques to derive the aerosol $\tau_{\lambda=0.55\mu m}$ from aircraft measurements in chapter 3 resulted in a mean $\tau_{\lambda=0.55\mu m}$ of 0.41 for the biomass smoke component for flight a791. A similar analysis for flights a788 and a789 is presented in Osborne *et al.* (2004). Although the $\tau_{\lambda=0.55\mu m}$ reported for these two flights is typically lower than flight a791, values as large as 0.34 and 0.40 were retrieved for the biomass smoke, with the most reliable technique for deriving $\tau_{\lambda=0.55\mu m}$ (modelling down-welling radiances in banked orbits) resulting in values at the top end of this scale. Therefore, the inclusion of aerosol with a $\tau_{\lambda=0.55\mu m}$ = 0.5 is representative of the situation over the Namibian cloud sheet during the dry burning season.

AVHRR retrieval; Figure 4.4 (a) shows the calculated radiance at 0.63μm versus that at 3.7μm for the range of cloud properties modelled. The black lines show the model calculations excluding aerosol, which are representative of the look-up table used in the

satellite retrieval, and the white lines include the overlying biomass burning aerosol. The inclusion of the partially absorbing aerosol leads to a significant reduction in the TOA up-welling radiance at 0.63μm, such that for a τ_{cloud} of 10 the look-up table would be retrieving a value of 8 (point A), and for a τ_{cloud} of 20 a value of 14 would be retrieved (point B). The error becomes larger as τ_{cloud} increases as a direct result of the cloud reflecting more photons back through the absorbing aerosol layer. At 3.7μm the aerosol optical depth is only 0.02, and so the change in the up-welling TOA radiance at 3.7μm when including aerosol is slight. The effect of including the aerosol leads to a general overestimation in the retrieved r_e of $< 2\mu m$, with the most noticeable error for clouds with large τ_{cloud} and r_e.

MODIS retrieval; Figures 4.4 (b) to (d) show the modelled TOA up-welling radiances for the three radiance pairs used to determine the cloud properties which are subsequently reported in the Level-2 MOD06 cloud product. The result of including the aerosol on the retrieval using the 0.86/3.7μm radiance pair is similar to the AVHRR retrieval, with figure 4.4 (b) indicating that the retrieval algorithm would return a τ_{cloud} of 10 for a real value of 12 (point A), and a τ_{cloud} of 14 for a real value of 18 (point B). The error in r_e again does not exceed 2μm. Figure 4.4 (c) shows the results from the default 0.86/2.13μm radiance pair. The underestimation in τ_{cloud} is again evident with points A and B showing the same errors as those from the 0.86/3.7μm radiance pair. The errors in r_e are fairly minor and do not exceed -1μm in the parameter space tested. The results from the 0.86/1.63μm radiance pair in figure 4.4 (d) again show similar errors in τ_{cloud}. However, marked differences in the retrieved r_e are apparent between the cases where aerosol is included/excluded in the calculations. Point A indicates that the look-up table used in the retrieval would return a τ_{cloud} of 10 and a r_e of 7μm for a real of τ_{cloud} of 12 and a r_e of 10μm. Furthermore, point B shows that a τ_{cloud} of $\sim$9 and a r_e of $\sim$5μm would be returned for a real of τ_{cloud} of 10 and a r_e of 10μm. This fairly large underestimation in r_e in the presence of an overlying biomass burning aerosol layer results from a large reduction in the radiance at 0.86μm (aerosol τ = 0.39) which shifts all points to the left, whereas the aerosol effect at 1.63μm is small (aerosol τ = 0.05). However, because the up-welling 1.63μm TOA radiance is sensitive to changes in both cloud droplet size and cloud optical depth, as points move to the left of the look-up table the retrieval returns a lower r_e.

Over land the non-absorbing wavelength band used is centred at 0.65μm where the aerosol

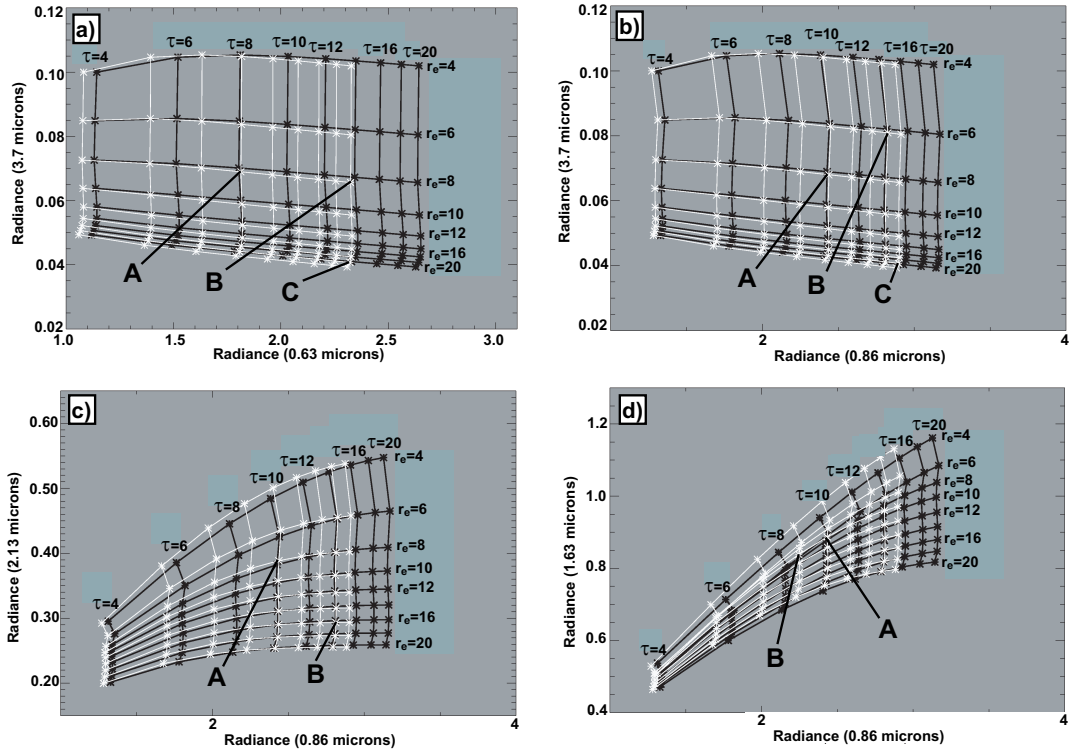

Figure 4.4: *Modelled radiances as used in (a) the AVHRR, and (b,c,d) the MODIS retrievals of τ_{cloud} (τ in figure) and r_e from Haywood* et al. *(2004). The default MODIS retrieval uses the 0.86/2.13μm radiance pairs. The black (white) lines show results excluding (including) the overlying biomass burning aerosol. A solar zenith angle of 30° and a Lambertian surface reflectance of 0.05 is used in the calculations.*

optical depth is greater compared to at 0.86μm which is used over ocean and in the above calculations. This implies that over land regions even larger errors in the retrieved τ_{cloud} and r_e are likely where a partially absorbing biomass burning aerosol layer exists above low level cloud.

4.4 Results

The theoretical calculations of Haywood *et al.* (2004) have shown that for the range of cloud and biomass burning aerosol properties modelled, the MODIS and AVHRR satellite retrievals may be subject to systematic low biases as large as 30% in τ_{cloud}, and of up to 5μm in $r_{e1.63}$ as a result of not accounting for aerosol scattering and absorption. Because the MODIS MOD06 cloud product only reports τ_{cloud} from the default 0.86/2.13 μm radiance pair, it is not possible to look for evidence of an aerosol effect on cloud optical depth. However, by analysing the wavelength dependence in the reported values of $r_{e1.63}$, $r_{e2.13}$,

and $r_{e3.7}$, the following question can be explored;

Is there evidence of an aerosol related bias in r_e in the MODIS cloud product?

4.4.1 Vertical structure of r_e

To address this question, the impact that the vertical structure of cloud droplet size has on the MODIS retrieval of r_e needs to be considered. Since water droplet absorption at $1.63\mu m < 2.13\mu m < 3.7\mu m$ (see figure 4.2), the retrievals at the shorter wavelengths will probe deeper into the cloud due to the increase in the path length of the photon. A degree of vertical sampling of r_e with the three MODIS retrievals is therefore possible. Aircraft measurements of marine stratocumulus clouds show that they tend to be close to adiabatic in nature (liquid water content increases linearly with height) and that the water droplet r_e is greater at the cloud top compared to at the cloud base (Slingo *et al.*, 1982, Garrett and Hobbs, 1995, Keil and Haywood, 2003). Therefore, the droplet size retrievals of $r_{e1.63} < r_{e2.13} < r_{e3.7}$ in the absence of any aerosol effect.

The magnitude of this effect, termed 'parcel theory', on the MODIS satellite retrieval is modelled by Platnick (2000). For adiabatic clouds the differences are fairly small, with $r_{e1.63} - r_{e2.13}$ values $<$ -0.6 μm and $r_{e3.7} - r_{e2.13} <$ +0.9 μm for the τ_{cloud} range of 5 to 15. For modelled clouds that are subadiabatic at mid levels, the maximum differences increased to $<$ -1.0 μm and $<$ +1.6 μm in $r_{e1.63} - r_{e2.13}$ and $r_{e3.7} - r_{e2.13}$ respectively. This is a result of a larger gradient in r_e near the cloud top in the modelled subadiabatic cloud in comparison with the adiabatic cloud.

Platnick *et al.* (2003) analyse a data granule from the MODIS MOD06 cloud product off the coast of Peru and Chile (18th July 2001, 15:30 UTC), where extensive marine stratocumulus boundary layer clouds were evident. For the liquid water cloud, the $r_{e1.63} - r_{e2.13}$ effective radius difference is generally within -1μm, although values $>$ -2.5μm are apparent in the broken stratocumulus region. In contrast, the $r_{e3.7} - r_{e2.13}$ differences are typically within +1μm. These are in general agreement with the theoretical calculations of Platnick (2000), and can thus be explained by the vertical structure of cloud droplet size as there is unlikely to be significant amounts of absorbing aerosol present.

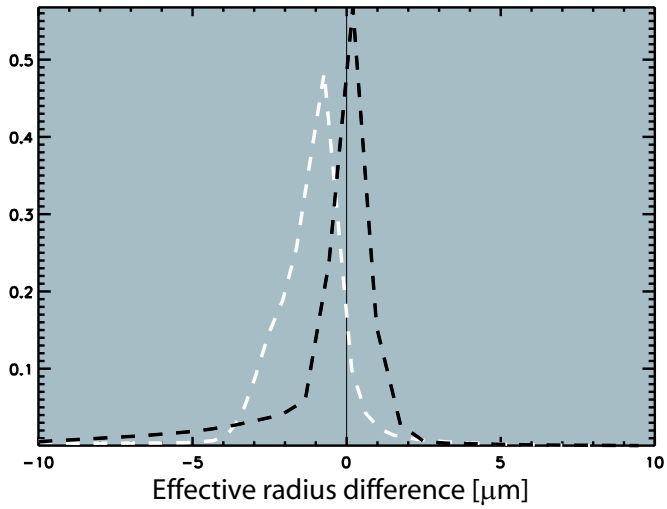

Figure 4.5: *Probability density functions of* $r_{e1.63} - r_{e2.13}$ *(white dashed) and* $r_{e3.7} - r_{e2.13}$ *(black dashed) for the MODIS granule analysed by Platnick* et al. *(2003) off the coast of Peru on the 18th July 2001.*

The same data granule is analysed further in this study by constructing probability density functions (pdfs) of the $r_{e1.63} - r_{e2.13}$ and $r_{e3.7} - r_{e2.13}$. The pdfs are constrained by τ_{cloud} values between 5 and 25 and over oceanic regions in order to be consistent with the statistical analysis of the southern African cases in section 4.4.4. Figure 4.5 shows the two pdfs. A slight positive bias is evident in the $r_{e3.7} - r_{e2.13}$, with the modal peak at +0.20 μm. A larger negative shift (modal peak of -0.73 μm) in the $r_{e1.63} - r_{e2.13}$ is clear, with differences of $>$ -2.5 μm accounting for 14$\%$ of the data.

The presented differences in the r_e in non absorbing aerosol influenced regions need to be borne in mind when assessing whether a bias is evident in the MODIS cloud retrieval of r_e off the coast of Namibia due to the presence of an overlying biomass plume.

4.4.2 SAFARI 2000 case studies

The MODIS 1 km resolution MOD06 Level2 data is analysed for six individual cases off the coast of southern Africa, on the 5th, 7th, 10th, 11th, 14th, and 16th September 2000. The locations of the MODIS granules in the analysis are shown in figure 4.6 (a), and were concurrent with the C-130 aircraft flights (a785, a787, a788, a789, a791, and a792). Biomass burning aerosol was observed to exist in elevated polluted layers above the MBL in all six cases, with the semi-permanent stratocumulus cloud sheet measured

during SAFARI 2000 existing at levels below the smoke (Haywood *et al.*, 2004). Thus, if significant amounts of biomass smoke exist in the granule, identifying whether a theoretical bias in the MODIS cloud product is possible.

Figure 4.6 (b) shows the MODIS quick-look, real-colour composites of the granules that are investigated. For all six cases, the images show extensive marine stratocumulus clouds off the coast of Africa. Land based clouds are evident in some of the images, the extent of which varies between cases. Areas of the sea surface where specular reflection (sun-glint) is large can be visually identified in the images by the darker appearing regions over ocean. Biomass smoke can be identified by the hazy conditions in the images in regions free of cloud. The biomass smoke and sun-glint is more difficult to distinguish visually in cloudy conditions.

4.4.3 Identifying aerosol influenced data

A knowledge of the spatial location of the biomass smoke corresponding to the MODIS data analysed is required in order to detect the effect of the aerosol on the retrieved cloud properties. Although the MODIS Level2 MOD04 aerosol product reports $\tau_{\lambda=0.55\mu m}$, the retrieval is limited to clear skies (Tanré *et al.*, 1997, Kaufman *et al.*, 1997). Analysis of the MODIS optical depth data for the six cases showed that very few retrievals were made due to the large amounts of cloud present in the granules. Therefore, the Total Ozone Mapping Spectrometer (TOMS) Aerosol Index (AI) data[1] is used to detect the presence of the overlying absorbing aerosol layer. The TOMS AI has previously been used to characterise the temporal and spatial distributions of absorbing tropospheric aerosols in other studies (e.g. Hsu *et al.* (1996), Herman *et al.* (1997), Hsu *et al.* (2003)).

The AI is a measure of the wavelength dependent change in the Rayleigh scattered radiance as a result of aerosol absorption and scattering, and is defined so that positive values generally correspond to absorbing aerosols and negative values to a conservative scattering aerosol. However, when the aerosol resides near the Earths surface ($<$1.5 km), the TOMS AI can be negative for partially absorbing aerosol at low optical depths (Hsu *et al.*, 1999).

[1] available at http://toms.gsfc.nasa.gov/aerosols/aerosols.html; last accessed 18/05/04.

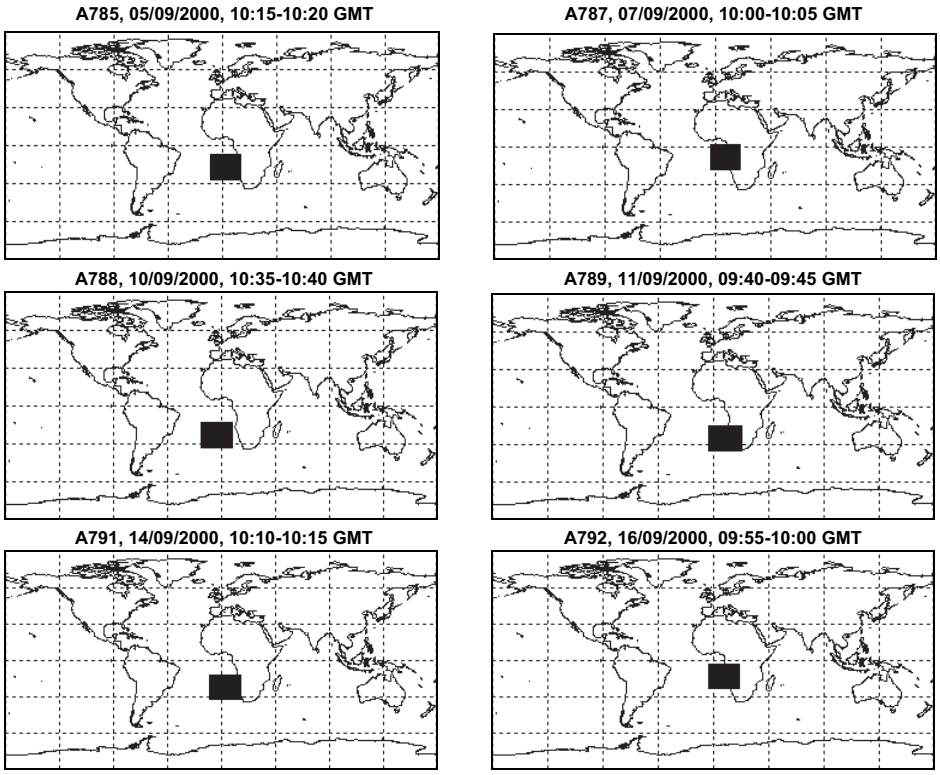

(a) The locations of the MODIS granules concurrent with the C-130 flights that are used in the analysis

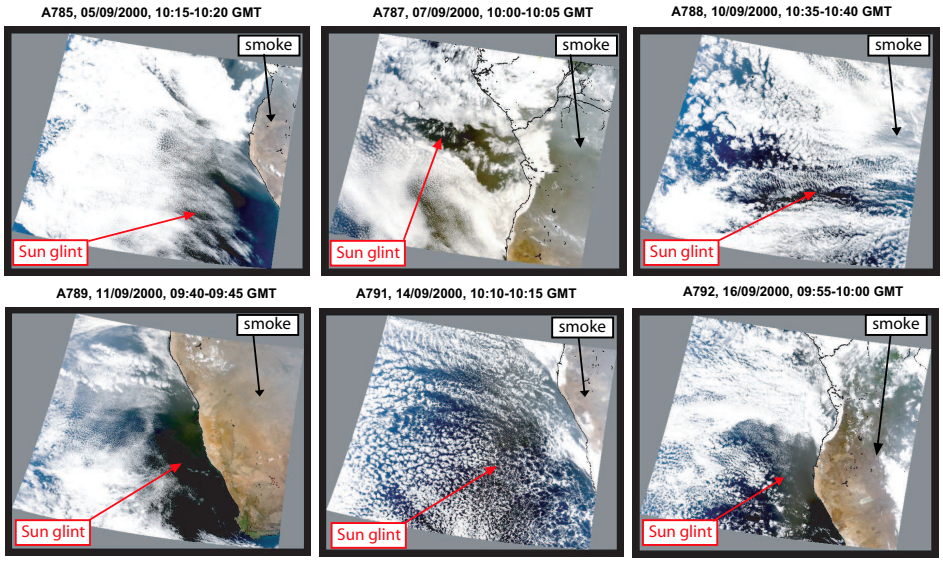

(b) Quick-look images of the MODIS granules analysed. Areas where biomass burning aerosols and sun-glint are visually apparent are indicated.

Figure 4.6: *The MODIS Level2 data granules for the six SAFARI 2000 cases.*

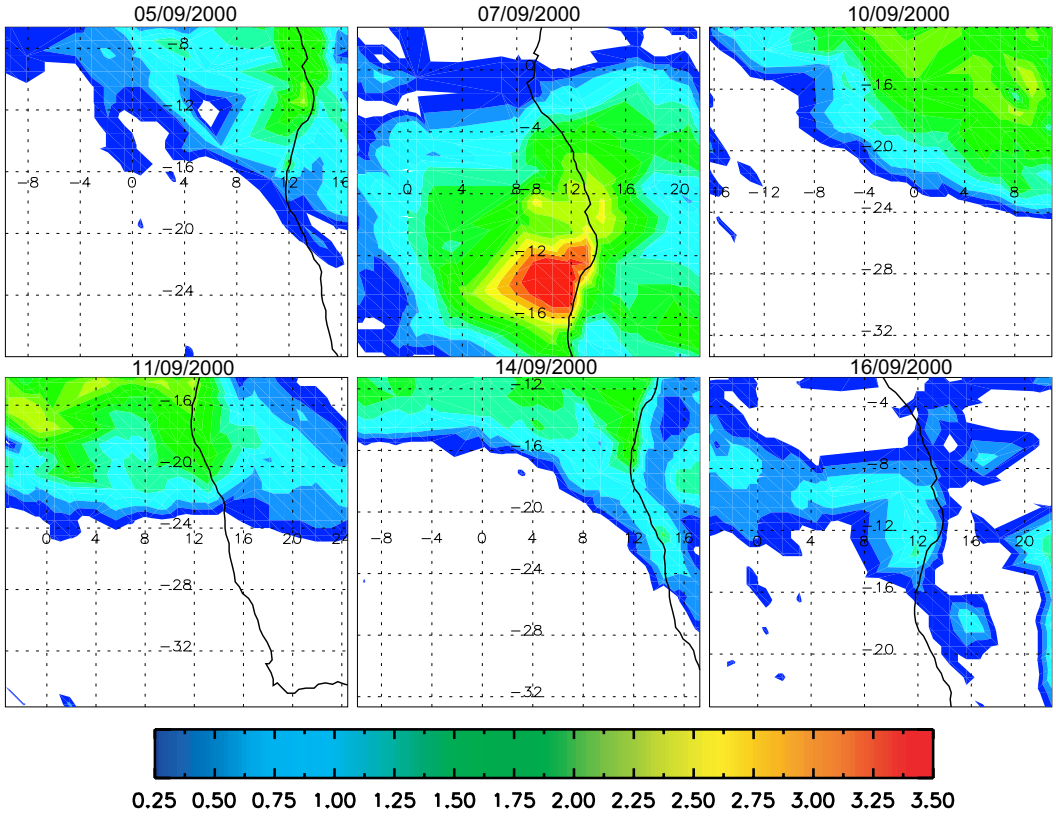

Figure 4.7: *TOMS AI corresponding to the locations of the MODIS granules in figure 4.6. The data has been linearly interpolated to regions not covered by the swath of the TOMS instrument.*

The vertical profiles measured onboard the C-130 aircraft show that the majority of the biomass smoke exists at altitudes of ∼1.5-6 km (see chapter 3 and Haywood *et al.* (2004)) in the region of interest, and so positive values of the TOMS AI can be used to identify the spatial distribution of the aerosol.

A comparison of the TOMS AI to ground based sun photometer measurements of aerosol optical thickness during the biomass burning season over southern Africa reveals an approximate linear relationship between the two ($\tau_{\lambda=0.38\mu m} \backsim 0.8\text{x}AI$) (Hsu *et al.*, 1999). By considering the wavelength dependence of the biomass smoke optical properties (see chapter 3), this corresponds to $\tau_{\lambda=0.55\mu m} \backsim 0.4\text{x}AI$ (Haywood *et al.*, 2004). However, the comparison is likely biased to measurements taken near source regions, where the aerosol $\omega_{0\lambda=0.55\mu m}$ is likely to be lower than in the aged regional haze (Abel *et al.*, 2003). Therefore, the exact relation may not hold true for the aerosol advected off the coast of Namibia and Angola, although larger values of AI will generally correspond to larger values of $\tau_{\lambda=0.55\mu m}$.

Figure 4.7 shows the Total Ozone Mapping Spectrometer (TOMS) Aerosol Index (AI) data for the MODIS granules analysed. The data has been linearly interpolated to 'data-missing' regions that result from gaps between the swath of the TOMS instrument on successive orbits. On the 5th, 10th, 11th, and 14th September, a clear North-South gradient is evident in the TOMS AI, with values greater than 1.25 in all cases ($\tau_{\lambda=0.55\mu m}$ exceeds $\backsim$ 0.5) to the North. The southern areas of the granules are comparatively free of biomass smoke. On the 7th September it is clear that biomass smoke influences the whole region, with values of TOMS AI in excess of 3.5 ($\tau_{\lambda=0.55\mu m}$ exceeds $\backsim$ 1.4). For the case on the 16th September the TOMS AI is more patchy, and a low confidence is placed in the interpolation of the TOMS AI to data missing regions due to the relative lack of data.

4.4.4 Analysis of MODIS data

A detailed analysis is presented for the two cases on the 7th and 10th September 2000. The other four cases are less ideal due to a lack of aerosol influenced pixels, excessive sun-glint, sub-pixel cloudiness, or other cloud types that are not consistent with the theoretical analysis, although the results are discussed in brief subsequently.

Qualitative analysis

7th September 2000 ; Figure 4.8 (a) and (b) show the quick-look image and the TOMS AI for the case on the 7th September. Figure 4.8 (c) and (d) show the MODIS retrieval of τ_{cloud} and r_e using the default 0.86/2.13 μm radiance pair. The area of sun-glint is readily identifiable by the sharp transition to regions where cloud is observed to exist in the quick look image, although a retrieval is not made due to additional constraints placed on the cloud-mask (Platnick *et al.*, 2003). This results in the screening out of optically thin clouds in areas where the effect of sun-glint on the measured TOA reflectances is significant. The majority of the stratocumulus cloud sheet shows $6 < \tau_{cloud} < 14$, and $5 < r_{e2.13} < 15$. This is in general agreement with values measured onboard the C-130 aircraft off the coast of Angola, at a latitude of $\backsim$ 15-17°S (Keil and Haywood, 2003). Higher values of τ_{cloud} and r_e are evident to the North of the data granule, particularly over land regions. This is indicative of deep convective cells with ice particles (maximum $r_{e2.13}$ for water droplets is

$30\mu m$ in the retrieval (Platnick *et al.*, 2003)).

The effective radius difference, $r_{e3.7} - r_{e2.13}$ is shown in figure 4.8 (e), with the majority of the region showing values $\leq 1\mu m$ (green colours). This is in agreement with the theoretical calculations which show that the biomass smoke has a small impact on the retrieval using the $3.7\mu m$ waveband. Positive and negative values to the North of the region are apparent and are associated with the deep convective ice clouds that were not considered in the theoretical calculations. Figure 4.8 (f) shows the $r_{e1.63} - r_{e2.13}$, with a negative bias (blue colours) evident across the majority of the region. Biases of -2 to -4 μm are common (mid blue colours) over the low-level stratocumulus, with values in excess of -5 μm (deep blue colour) also apparent over large areas. This bias is consistent with the theoretical calculations of biomass burning aerosol overlying cloud, and is larger than that attributed to parcel theory in the South American case where there is little or no absorbing aerosol present.

10th September 2000 ; Figure 4.9 (a) and (b) shows the quick look image and TOMS AI for the case on the 10th September. The sharp gradient in the TOMS AI between the polluted area to the North-East, and the more pristine air to the South, allows the impact of the biomass smoke to be examined in both aerosol and non-aerosol influenced pixels within the same MODIS data granule. Typical values of τ_{cloud} and $r_{e2.13}$ (figures 4.9 (c) and (d)) are in the range, $6 < \tau_{cloud} < 16$, and $5 < re_{2.13} < 15$ for stratocumulus clouds. Higher values of both τ_{cloud} and $r_{e2.13}$ are evident in the bottom left of the granule ($\backsim$ 29°S,12°E), and are again indicative of ice clouds.

The $r_{e3.7}$-$r_{e2.13}$ effective radius difference is shown in figure 4.9 (e). Predominantly green colours are evident across the granule corresponding to a bias of $\leq 1\mu m$, as with the 7th September case. By examination of the TOMS AI and the $r_{e1.63}$-$r_{e2.13}$ (figure 4.9 (f)), a typical bias in the range of -2 to -5 μm (blue colours) is evident to the North-East of the granule where the partially absorbing aerosol overlies the low-level stratocumulus cloud. In the regions free of both biomass smoke and ice clouds to the South of the granule, the bias is significantly reduced, and is generally within 1 μm (green colours). The spatial correlation between the TOMS AI and the low bias in the $r_{e1.63}$ provides evidence for the effect of overlying biomass smoke on the MODIS cloud retrieval off the coast of southern Africa predicted by theory. Further, it shows that the biomass burning aerosol produces a

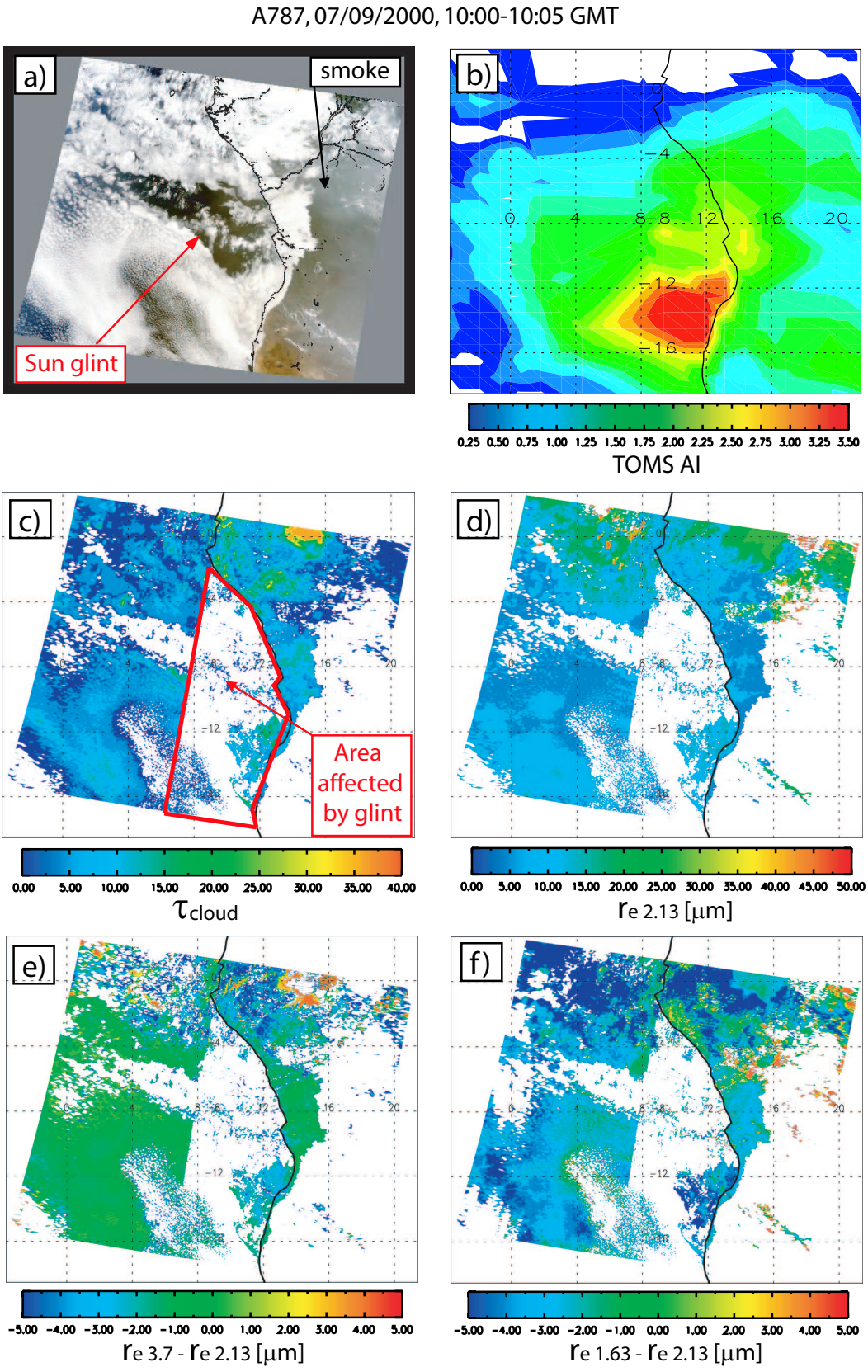

Figure 4.8: *7th September 2000; a) MODIS quick-look image. Obvious sun glint regions and biomass smoke is indicated in clear-sky areas; b) TOMS AI; c) MODIS* τ_{cloud}*. The area where sun glint influences the retrieval is indicated; d) MODIS default* $r_{e2.13}$ *[*μm*]; e)* $r_{e3.7}$*-*$r_{e2.13}$ *[*μm*]; f)* $r_{e1.63}$*-*$r_{e2.13}$ *[*μm*].*

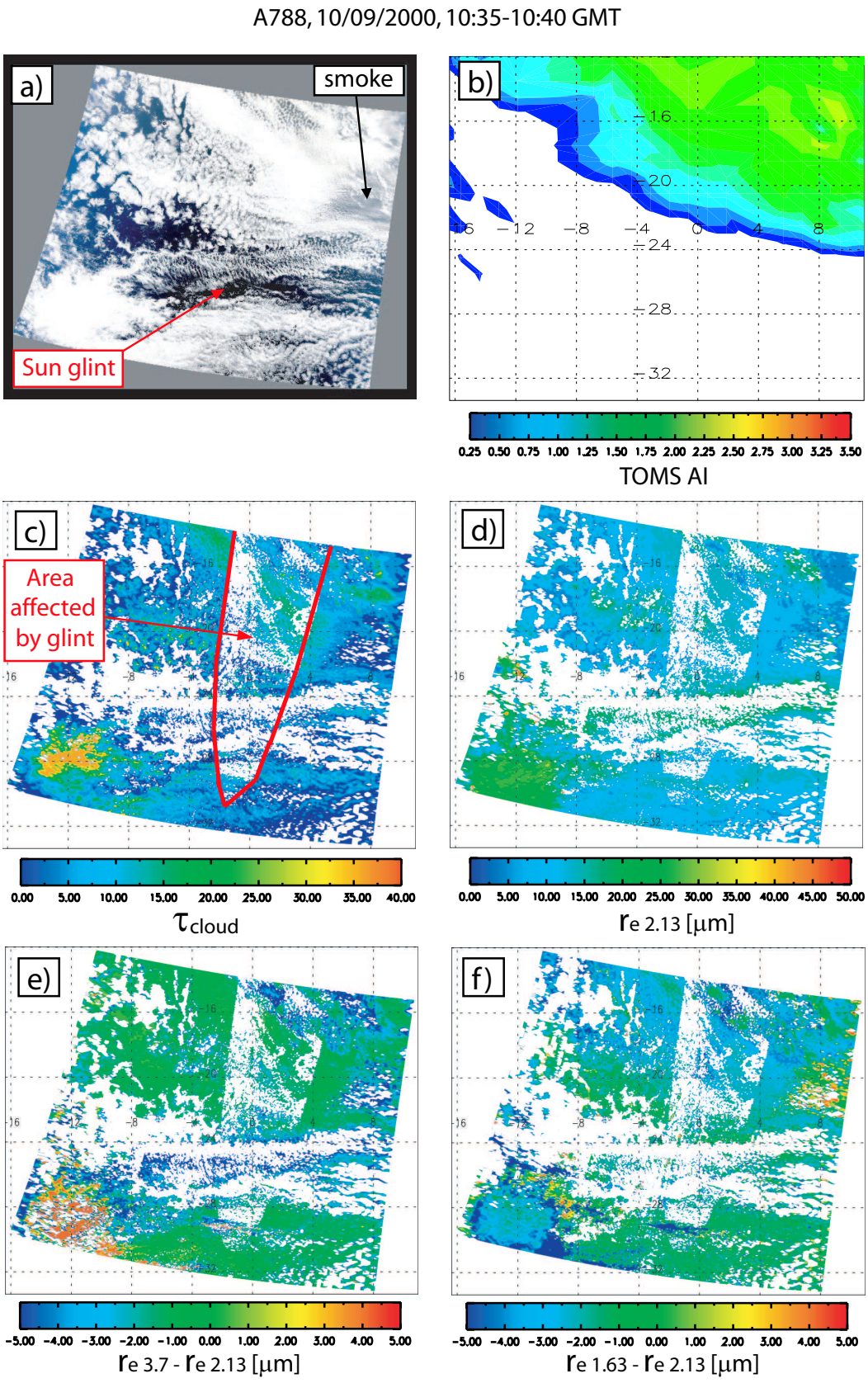

Figure 4.9: *As figure 4.8 but for the case on the 10th September 2000.*

noticeable effect on the 1.63 μm reflectance above that resulting from parcel theory in the non-aerosol influenced pixels.

Other SAFARI 2000 cases ; The 7th and 10th September cases show that the most significant bias is apparent in retrieval of cloud droplet size using the 1.63 μm reflectance. Therefore,a brief discussion of the $r_{e1.63} - r_{e2.13}$ for the less ideal cases (5th, 11th, 14th, and 16th September 2000) shown in figure 4.10 is given. Also contoured in figure 4.10 is the TOMS AI to assist with the visual identification of aerosol influenced pixels. It is clear that the number of pixels in which a retrieval is not made (white areas) is far greater for the less ideal cases than on the 7th and 10th September 2000, and so the statistical certainty of any biases is reduced.

The case on the 5th September shows a small bias across the whole region (-1 to -2 μm). There is perhaps evidence of a more negative bias in aerosol influenced pixels around the coastal areas where the TOMS AI, and thus τ_λ, is the greatest. However, the large amount of sun-glint removes the majority of the pixels influenced by aerosol making it difficult to visually identify the bias predicted in the theoretical calculations.

On the 11th September, a negative bias to the North associated with the biomass smoke exists, and reaches values in excess of -5 μm. In the aerosol free regions, the data is noisy and is the result of deep convective clouds ($\tau_{cloud} \backsim 25$). This makes it difficult to ascertain if any bias in non-aerosol influenced pixels for clouds that are consistent with those modelled exists.

Broken stratocumulus clouds are persistent across the granule for the case on the 14th September, and the cloud amount is low leading to poor statistics.

The uncertainty in the interpolation of the TOMS AI as a result of the large amount of 'data-missing' regions on the 16th September makes it problematic when looking for a bias in aerosol influenced pixels. Therefore, although large biases up to -5 μm in the $r_{e1.63}$ retrieval are apparent, it is difficult to determine whether these pixels are influenced by biomass smoke.

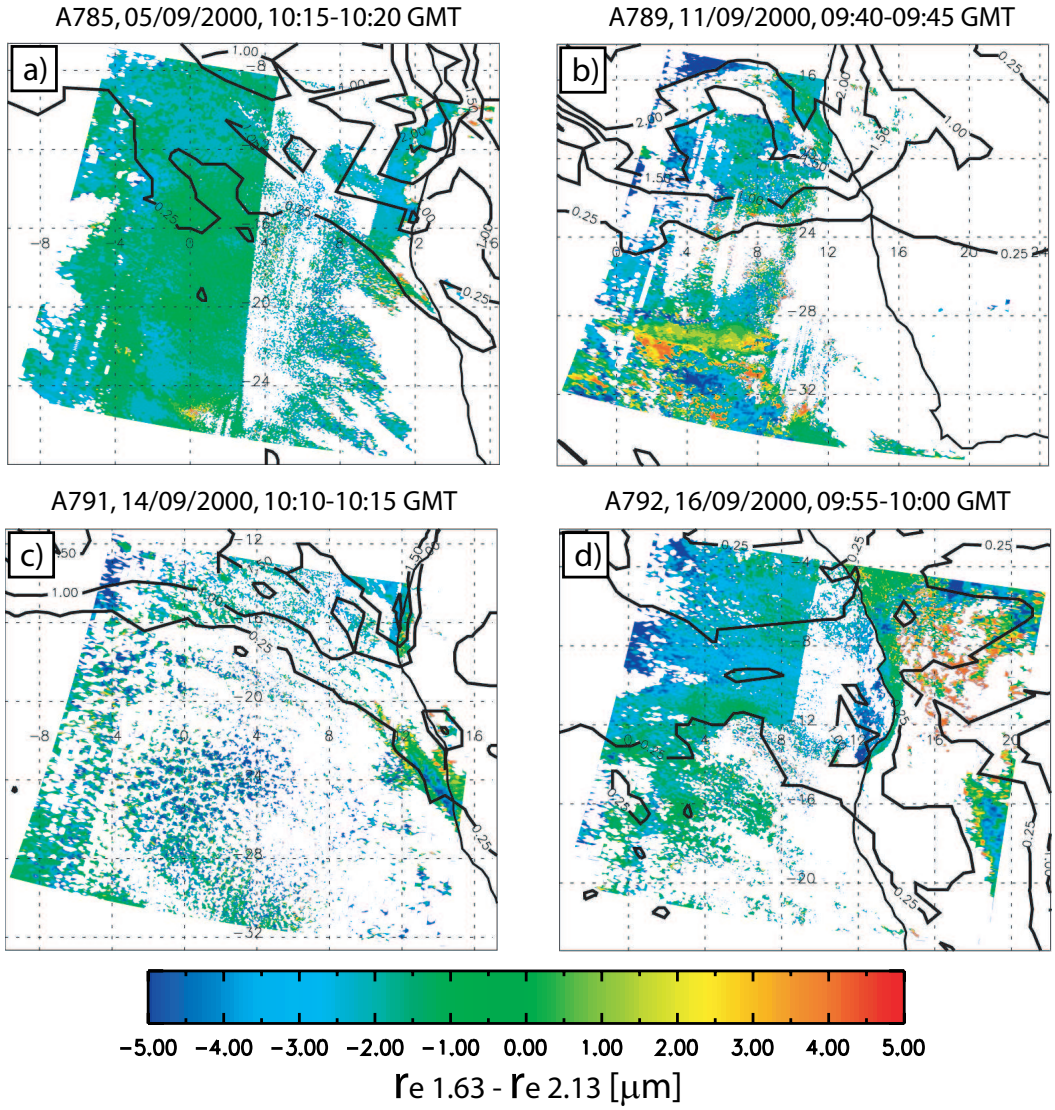

Figure 4.10: $r_{e1.63}$-$r_{e2.13}$ *[μm] for the cases on the a) 5th September, b) 11th September, c) 14th September, and d) 16th September. Also contoured (thick black lines) is the TOMS AI, shown in more detail in figure 4.7.*

Statistical analysis

Probability density functions (pdfs) of $r_{e1.63}$-$r_{e2.13}$ and $r_{e3.7}$-$r_{e2.13}$ were constructed in both aerosol and non-aerosol influenced regions in order to determine the magnitude of the aerosol effect on the MODIS cloud retrieval that is evident in the spatial analysis presented in figures 4.8 to 4.10. In determining the pdfs the following three conditions are applied;

i) $5 < \tau_{cloud} < 25$; This removes low τ_{cloud} values that are likely to include sub pixel cloudiness regions e.g. the pixel is classed as overcast in the cloud retrieval although clear regions on the sub pixel scale will reduce the TOA up-welling radiance leading to a low bias in

τ_{cloud} (Platnick *et al.*, 2003). High τ_{cloud} values are screened out to remove large convective clouds that whilst important, are not considered in the theoretical calculations of Haywood *et al.* (2004). Furthermore, the range of τ_{cloud} considered is broadly consistent with the theoretical calculations (τ_{cloud}=4 - 20) and the ISCCP classification of stratocumulus clouds (τ_{cloud}=3.6 - 23).

ii) *Pixels over land areas are screened out*; Aircraft measurements over land show that the biomass burning aerosol tended to be well-mixed throughout the boundary layer (see chapter 2, Haywood *et al.* (2003a), Magi *et al.* (2003)). Furthermore, the vertical profile at Otavi in chapter 2 showed evidence of cloud at the top of the boundary layer. It is therefore uncertain if significant amounts of biomass burning aerosol exist in elevated layers above low level cloud over land areas.

iii) *TOMS Aerosol Index*; A pixel is defined as being influenced by the biomass burning aerosol if the TOMS AI $\geq$ 0.25. For values of AI $\leq$ 0 the pixel is classed as being non-aerosol influenced. To remove the effects of any misclassification of aerosol and non-aerosol pixels around the edges of the biomass plume, intermediate values of the TOMS AI ($0 <$ AI < 0.25) are classed as being indeterminate. This misclassification may arise due to advection of aerosol between the time of the TOMS and MODIS satellite overpass, or as a result of the coarser spatial resolution of the TOMS data.

Once again, the cases on the 7th and 10th September 2000 are discussed in detail, results from the less ideal cases are summarised in table 4.2. Figure 4.11 shows the aerosol and non-aerosol pdfs for the cases on the 7th and 10th September 2000. Biomass burning aerosol was persistent across the whole granule analysed on the 7th September as has been identified by the TOMS AI, thus the pdfs contained no non-aerosol influenced pixels, approximately 735,000 aerosol influenced pixels, and 20,000 indeterminate pixels with the above screening procedure applied. A large negative bias in the aerosol influenced $r_{e1.63} - r_{e2.13}$ pdf is evident, with a peak at -2.78μm (54$\%$ of pixels $>$ -2.5μm). This shift is much more significant than that which can be attributed to parcel theory, with the results in section 4.4.1 indicating a low bias of -0.73μm (14$\%$ of pixels $>$ -2.5μm) in the case off the coast of South America. This additional negative bias in the aerosol influenced pdf is entirely consistent with the theoretical calculations of the $r_{e1.63}$ retrieval in the presence of an overlying biomass plume. The aerosol influenced $r_{e3.7} - r_{e2.13}$ pdf has a modal peak

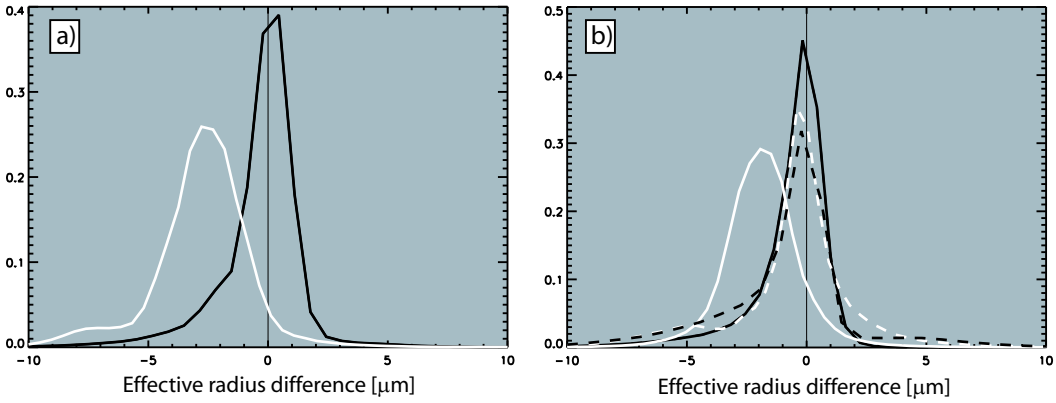

Figure 4.11: *Probability density functions of* $r_{e1.63} - r_{e2.13}$ *(white) and* $r_{e3.7} - r_{e2.13}$ *(black) for the MODIS granules off the coast of Namibia on a) 7th September 2000; b) 10th September 2000. Solid lines represent pdfs for aerosol influenced and dashed lines for non-aerosol influenced pixels.*

at +0.45μm, a result that perhaps indicates a slightly more positive bias than the value of +0.20μm in the South American case.

The strong North to South gradient in the biomass smoke on the 10th September allowed both aerosol and non-aerosol pdfs to be constructed, with approximately 705,000 aerosol, 490,000 non-aerosol, and 115,000 indeterminate pixels being assigned. There is no statistical difference in the modal peak of the $r_{e3.7} - r_{e2.13}$ aerosol (-0.17μm) and non-aerosol (-0.22μm) pdfs. However, the modal peak in the aerosol $r_{e1.63} - r_{e2.13}$ pdf is -1.93μm (32$\%$ of pixels $>$ -2.5μm), and -0.40μm (16$\%$ of pixels $>$ -2.5μm) in the non-aerosol influenced pdf. Thus, by delineating the MODIS pixels that are influenced by the overlying biomass plume from the aerosol-free pixels, the negative bias in the $r_{e1.63}$ retrieval is apparent.

The TOMS AI (and thus $\tau_{\lambda=0.55\mu m}$) in typically lower on the 10th September than the 7th September. This would act to reduce the probability that a photon will be absorbed by the overlying aerosol layer. Therefore, the negative bias in the $r_{e1.63}$ retrieval would be expected to be less on the 10th September, as is evident in both the modal peak and in the percentage of pixels with a bias in excess of -2.5 μm in the aerosol influenced pdfs.

Table 4.2 summarises the modal peak in the aerosol and non-aerosol pdfs for the other four cases concurrent with the C-130 flights. The $r_{e3.7} - r_{e2.13}$ pdfs show a small negative bias in the non-aerosol influenced pixels, with the aerosol pixels being more positive or negative. With the exception of the case on the 14th September where there is significant amounts of broken stratocumulus, the peak in the $r_{e1.63} - r_{e2.13}$ pdf in non-aerosol regions is negative,

			Mode of pdf (μm)						
			aerosol		non-aerosol		Approximate number of pixels x1000		
Region	Flight	Date	$r_{e1.63} - r_{e2.13}$	$r_{e3.7} - r_{e2.13}$	$r_{e1.63} - r_{e2.13}$	$r_{e3.7} - r_{e2.13}$	aerosol	indeterminate	non-aerosol
southern Africa	A785	05/09/00	-1.14	-0.15	-0.58	-0.31	425	450	460
southern Africa	A787	07/09/00	-2.78	+0.45	N/A	N/A	735	20	0
southern Africa	A788	10/09/00	-1.93	-0.17	-0.40	-0.22	705	115	490
southern Africa	A789	11/09/00	-1.02	-1.04	-0.04	-0.62	130	55	295
southern Africa	A791	14/09/00	-1.68	-1.40	+0.74	-0.86	185	85	330
southern Africa	A792	16/09/00	-1.32	+0.25	-0.10	-0.32	380	180	140
South America	N/A	18/07/01	N/A	N/A	-0.73	+0.20	N/A	N/A	1120

Table 4.2: *Modal effective radius difference from the constructed pdfs relating to aerosol and non-aerosol influenced pixels for* $r_{e1.63} - r_{e2.13}$ *and* $r_{e3.7} - r_{e2.13}$*. A summary of the approximate number of 1km cloud data pixels that were classed as aerosol, non-aerosol, or indeterminate are also tabulated. Results are shown for the six cases off the coast of Namibia, and for the granule analysed by Platnick* et al. *(2003) off the coast of Peru and Chile.*

in agreement with parcel theory. Broken stratocumulus clouds have been shown to produce spurious results in the MODIS data (Platnick *et al.*, 2003). The results for $r_{e1.63} - r_{e2.13}$ pdfs are always more negative in aerosol influenced regions when compared to the non-aerosol influenced regions, in agreement with the potential low bias predicted in the theoretical calculations. Further, for all six cases the bias in $r_{e1.63} - r_{e2.13}$ in aerosol influenced pixels is greater than that observed in the granule off the coast of South America, where little absorbing aerosol is present.

4.5 Summary and discussion

The theoretical calculations of Haywood *et al.* (2004) show that a potential low bias of up to 30$\%$ in the MODIS and AVHRR retrievals of τ_{cloud} may occur when biomass burning aerosol ($\tau_{\lambda=0.55\mu m}$ = 0.5) overlies low-level cloud. Furthermore, low biases as large as -5μm may occur in the MODIS retrieval of r_e that uses the 1.63μm reflectance.

Both the MODIS and AVHRR τ_{cloud} (and AVHRR r_e) products are only reported from the retrieval that uses the default radiance pairs. Thus, additional independent information would be required such as detailed in-situ aircraft measurements co-ordinated with the satellite overpass to determine whether a bias is present. However, the MODIS r_e is reported in the MOD06 cloud product for all three retrievals, allowing the identification of any wavelength dependent biases to be examined.

Previous analyses of the MODIS MOD06 cloud product off the coast of South America have shown that that $r_{e1.63} < r_{e2.13} < r_{e3.7}$ in regions where there is little or no partially absorbing aerosol (Platnick *et al.*, 2003), a result that is consistent with the photons at shorter wavelengths penetrating deeper into the cloud where the cloud effective radius is typically smaller (Platnick, 2000). A statistical analysis of the same data granule in this study revealed a modal bias in $r_{e1.63} - r_{e2.13}$ of -0.73 μm, with 14 $\%$ of the pixels having a negative bias $>$-2.5μm. Thus, the effect of aerosols on remote sensing retrievals of r_e must be considered in addition to this effect.

The C-130 aircraft measurements from SAFARI 2000 off the coast of Namibia and Angola show that biomass smoke existed in an elevated polluted layer above the MBL, and that

the semi-permanent stratocumulus cloud sheet is separated from the overlying aerosol by a clean air slot, thus minimising cloud-aerosol interactions (see chapter 3). By analysing MODIS granules that are concurrent with the observations, it is shown that

i) spatial distributions of negative biases in $r_{e1.63} - r_{e2.13}$ exist that appear to be correlated with absorbing biomass burning aerosol as identified from the TOMS AI.

ii) a modal bias in $r_{e1.63} - r_{e2.13}$ as large as -2.78 μm, with 54% of pixels $>$-2.5μm in aerosol influenced regions, a result that is larger than that attributed to parcel theory.

iii) a more negative bias in $r_{e1.63} - r_{e2.13}$ in aerosol influenced pixels compared to non-aerosol influenced pixels.

This under estimation in $r_{e1.63}$ observed in the MODIS data in regions influenced by biomass smoke is entirely consistent with the theoretical calculations. The result suggests that a simultaneous low bias in τ_{cloud} from spaceborne retrievals that are based on measuring the cloud top reflectance is likely. Furthermore, in identifying cloud modification by aerosol particles (the indirect aerosol effect) from satellite observations of cloud optical properties in the presence of a surrounding aerosol, studies need to account for the reduction in the r_e due to any overlying partially absorbing aerosol if the 1.63μm reflectance is used. The impact of the potential low bias in the MODIS τ_{cloud} and r_e on the modelled direct radiative effect of southern African biomass burning aerosols is investigated in chapter 5.

Biomass burning aerosols are likely to overlay low-level clouds in other regions of the world. Similar biases in satellite retrievals of cloud optical properties as over the Namibian cloud sheet may therefore be apparent. For example, Hsu *et al.* (2003) find that the impact of smoke aerosols from burning activities in Southeast Asia significantly reduced the outgoing solar irradiance at the TOA by as much as 100Wm^{-2} during March 2000 (a positive radiative forcing), and that the reduction in spectral reflectivity of clouds due to the overlying smoke is similar to the theoretical calculations of (Haywood *et al.*, 2004). Further, other partially absorbing aerosols such as Saharan dust are observed to be transported in elevated polluted layers (Tanré *et al.*, 2003) and may therefore exert similar biases.

Satellite based retrievals of clouds potentially contain valuable information on the properties of any overlying partially absorbing aerosol. In particular, the magnitude of the bias

in the MODIS $r_{e1.63}$ and τ_{cloud} is primarily sensitive to the τ_λ and $\omega_{0\lambda}$ of the aerosol. An increase in the aerosol absorption (1-$\omega_{0\lambda}$) or in the τ_λ will enhance any bias evident in the retrieval. By combining the 1.63μm reflectance with that from other MODIS wavebands in the spectral range 0.4-0.75 μm (MODIS has 11 bands in this range) and building up detailed look-up tables based on radiative transfer calculations that include both aerosol and cloud models, retrievals of aerosols above cloud may be possible. In practice, this may be difficult due to the temporal and spatial variability of the aerosol and cloud vertical structure and optical properties. However, additional information from future spaceborne instruments, such as the Cloud Aerosol Lidar and Infrared Pathfinder Satellite Observations (CALIPSO) (Winker *et al.*, 2003) satellite which is due to fly in formation with the MODIS Aqua satellite, has the potential to provide such information.

Chapter 5

Modelling the regional direct radiative effect of southern African biomass burning aerosol

5.1 Introduction

Previous attempts to model the direct radiative effect of biomass burning aerosol on regional and global scales have either used detailed in-situ measurements to determine the forcing on a local scale and then estimated a large scale impact (e.g. Penner *et al.* (1992), Chylek and Wong (1995), Hobbs *et al.* (1997)), or have used modelled distributions of aerosols in sophisticated general circulation models (GCMs) (e.g. Penner *et al.* (1998), Grant *et al.* (1999), Iacobellis *et al.* (1999), Takemura *et al.* (2002), Myhre *et al.* (2003)). The conversion to a large scale forcing using the former method is inherently uncertain, whereas the uncertainties in the burden, optical properties, and vertical structure of aerosol included in different models with the latter method is large. The impact of these uncertainties are highlighted by the wide range of estimates in the global annual mean direct radiative effect of biomass smoke determined from the GCM studies, with values ranging from -0.74 Wm^{-2} (Iacobellis *et al.*, 1999) to -0.01 Wm^{-2} (Takemura *et al.*, 2002). These uncertainties need to be addressed before a degree of confidence can be placed in the GCM model results.

In this work a multi-column radiation code is used to calculate the direct radiative effect of biomass burning aerosols over the southern African region. The aerosol optical properties, and the aerosol and cloud vertical structure are constrained by the airborne measurements presented in chapters 2 and 3. Satellite and GCM data are used to estimate the horizontal distribution of aerosol. Satellite retrieved fields of clouds and land surface albedo are also incorporated into the model. Sensitivity tests, such as ”What impact does the potential error in the MODIS retrieval of cloud optical depth and effective droplet radius presented in chapter 4 have on the direct aerosol effect?” are then performed, in order to assess the most important parameters that need to be targeted by future measurement studies and captured in the more detailed GCMs.

Section 5.2 describes the experimental set-up and gives a description of the model, with the results from the model calculations presented in section 5.3. A comparison with other studies and concluding remarks is given in section 5.4.

5.2 Experimental setup

5.2.1 Multi-column radiative transfer model

The single-column 2-stream version of the Edwards Slingo 1996 radiation code (Edwards and Slingo, 1996) was reconfigured to an independent multi-column version. Whilst the spectral file used in the single-column version is retained to maintain the codes flexibility, the user can now prescribe 3-D fields of any radiatively active gaseous absorbers, aerosols, and clouds. A 2-D surface pressure and Lambertian albedo/emissivity field can also be included. The model can be run over the whole of the Earths surface or the user can specify a box with a set longitude and latitude range. The horizontal resolution can then be specified by the user. The vertical resolution of the model is specified in the same manner as the single-column version. The user can specify the start/end time and date and the time-step required for each call to the radiation code. The incoming insolation at the top of the atmosphere (TOA) and solar zenith angle (SZA) used to calculate the fluxes at each time-step are determined using the scheme employed in the Met Office Unified model (Ingram *et al.*, 1997). The output model fluxes are then averaged over the total number of

time-steps.

For this study the long-wave effect of the biomass burning aerosol is neglected and is likely to be small due to the strong wavelength dependence of the aerosol extinction coefficient in the biomass smoke (see chapter 3). For the short-wave calculations the spectral resolution was set at 220 wave-bands in the wavelength range 0.2-10μm with the majority of wave bands situated in the visible and near infra-red part of the spectrum. The vertical resolution of the model was set at 33 levels. The vertical profiles of temperature, pressure, and gaseous absorbers were held constant at every grid box. The tropical climatology of McClatchey *et al.* (1972) was used for temperature, O_3, and H_2O(g). Other greenhouse gases included in the model were N_2O, CH_4, CO_2, and O_2. The mixing ratio data for these gases were taken from Cofer *et al.* (1996) and IPCC (2001) and were assumed to be well mixed throughout the atmosphere. The distribution of biomass burning aerosol, cloud, and surface albedo included in the model is discussed in subsequent sections.

5.2.2 Horizontal distribution of aerosol

The horizontal distribution of biomass burning aerosol over southern Africa is estimated from two independent sources; i) General circulation model calculations that utilise transport models of various aerosol species (Tegen *et al.*, 1997); ii) the MODIS satellite retrieval of aerosol optical depth (Kaufman *et al.*, 1997, Tanré *et al.*, 1997, Ichoku *et al.*, 2003).

Model estimate of aerosol optical depth

To simulate the spatial distribution of biomass burning smoke over southern Africa the GCM model results of Tegen *et al.* (1997) are used[1]. The data consists of a global distribution of monthly mean averaged $\tau_{\lambda=0.55\mu m}$ at a horizontal resolution of 4x5° for several aerosol species based on transport models of soil dust (Tegen and Fung, 1995), sea salt (Tegen *et al.*, 1997), sulphate (Chin *et al.*, 1996), and organic and black carbon (Liousse *et al.*, 1996) aerosols. Implicit in the GCM calculations is that the individual aerosol species are externally mixed. Therefore the total column integrated optical depth is given by the sum of the optical depths from the individual aerosol components.

[1] data available at http://gacp.giss.nasa.gov/transport/; last accessed 29/06/04

For the transport of the carbonaceous aerosol (OC+BC) the GCM generates climatological meteorology and uses monthly averaged emission rates. The emission inventories used characterise aerosols emitted from natural sources (e.g. direct emission of OC from plants), fossil fuel burning, domestic fires (e.g. wood/charcoal/dung), agricultural fires (e.g. wheat/corn/rice), and savanna and forest burning. Removal of aerosol from the atmosphere due to both dry and wet deposition is parameterised in the GCM. For this study the contribution by biomass burning aerosols to the carbonaceous component over southern Africa during the dry season are assumed to dominate over emissions from natural and fossil fuel sources allowing the spatial distribution of the biomass smoke to be determined.

A climatology of ground based observations from the AERONET sun photometer network (Holben *et al.*, 1998) over southern Africa is compiled to assess the accuracy of the the GCM calculations. The cloud screened, calibrated and manually inspected Level 2.0 AERONET data[2] covering the time period of June 1995 - September 2003 is used. A daily averaged τ_λ is initially compiled at each sun-photometer site and then the monthly mean computed. Only days where at least three individual measurements are available are included in the climatology. This process resulted in a total of 4857 daily and 268 monthly averaged values covering the 22 AERONET stations that had data available in the observation period considered, the location of which are indicated in figure 5.1. Table 5.1 summarises the observational statistics for each month. A more detailed overview of the climatology at each AERONET station is given in appendix B. It is clear that August and September contain the greatest number of observations. This is a result of some temporary stations only taking measurements during the intensive SAFARI 2000 field campaign. The spatial distribution of observations is poorest for April with only 6 stations included in the climatology.

To allow for a direct comparison with the GCM results the AERONET data is interpolated to $0.55\mu m$ from the reported wavelengths of 0.34, 0.38, 0.44, 0.50, 0.67, 0.87, and $1.02\mu m$. This was achieved using a quadratic fit of form $y = a + bx + cx^2 + dx^3$. For all months and stations the coefficient of determination (R^2) for the fit was > 0.95. Figure 5.2 shows a comparison of the total column integrated optical depth from the six AERONET stations that have data for at least 11 months of the year with the GCM data in the grid

[2]data available at http://aeronet.gsfc.nasa.gov/; last accessed 29/06/04

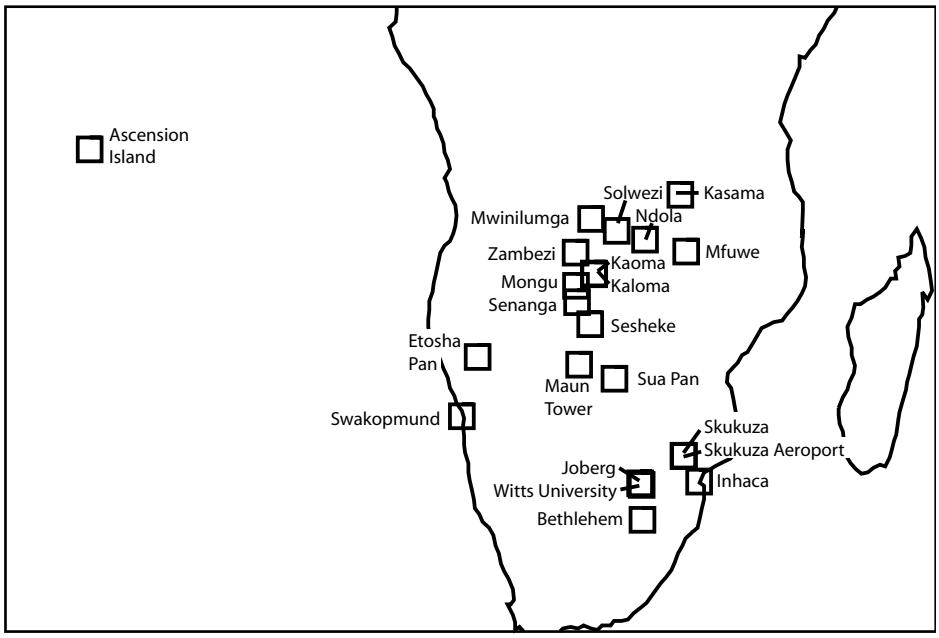

Figure 5.1: *AERONET Sun-photometer stations in southern Africa that are used to build up a climatology of monthly mean aerosol optical depth. Appendix B summarises the monthly* $\tau_{\lambda=0.55\mu m}$ *and observational statistics for each station.*

	Jan	Feb	Mar	Apr	May	Jun	Jul	Aug	Sep	Oct	Nov	Dec
Stations	7	8	7	6	8	13	11	18	20	13	10	9
Months	16	18	17	14	17	23	22	34	36	27	25	19
Days	281	258	260	287	373	445	435	685	706	461	367	299
Factor	2.7	3.1	2.5	2.2	1.3	0.9	1.1	1.8	2.5	3.4	1.8	2.2

Table 5.1: *Summary of the number of sun-photometer stations, months, and days in the observation period June 1995 - September 2003 included in the AERONET climatology for each month of the year. Also shown is the factor that the total aerosol optical depth in the GCM of Tegen* et al. *(1997) needs to be increased to obtain a reasonable agreement with AERONET measurements.*

box co-incident with each sun-photometer site. The sun-photometer data at Ascension Island, some 2500km off the coast of southern Africa has a peak in August indicating that significant amounts of biomass burning aerosol are transported large distances over the southern Atlantic Ocean during the dry season as was measured onboard the C-130 aircraft during SAFARI 2000 (Haywood *et al.*, 2004). The other stations on the southern African continent show large increases in $\tau_{\lambda=0.55\mu m}$ from the background values for the period of August to October when biomass burning is prevalent. It is clear that the GCM results severely under predict the $\tau_{\lambda=0.55\mu m}$ at all stations, especially in the dry season. This is consistent with the analysis of Remer *et al.* (2002a) and Kinne *et al.* (2003), who find that the same GCM model under estimates biomass burning aerosol optical depth over southern Africa. The discrepancy between the GCM and observations may be due to errors in

the model source strength or transport of aerosols. For example, the source inventory of carbonaceous aerosols used in the GCM (Liousse *et al.*, 1996) contains an annual global value of 45 Tg yr^{-1} of organic matter and 5 Tg yr^{-1} of BC produced by biomass burning, whereas the study of Scholes and Andreae (2000) predict values of 80 and 9 Tg yr^{-1}. It also appears that the model initiates the biomass burning season too early (May - June) whereas the observations suggest it occurs closer to July. This is likely to result from the seasonality in biomass burning fires in the source inventory (Liousse *et al.*, 1996), which imposes a similar pattern in the GCM calculated aerosol optical depth.

In order to quantify the underestimation in the model optical depth, a correction factor specific to each month is derived from a linear fit of the GCM $\tau_{\lambda=0.55\mu m}$ to that measured at the AERONET stations using all of the data in the climatology. Table 5.1 lists the correction factors for each month. The model appears to predict the column integrated optical depth to within $\pm 10\%$ in the months of June and July, although this may be due to the early initiation of the biomass burning cycle. During the burning season the model under predicts the $\tau_{\lambda=0.55\mu m}$ by a factor of 1.8 to 3.4, with the largest error in September and October. Figure 5.2 also includes the GCM data multiplied by the derived correction factors and the MODIS satellite data for September. The improvement in the model data with respect to the AERONET and satellite observations in both the magnitude and the seasonal cycle of the $\tau_{\lambda=0.55\mu m}$ is evident, suggesting that the correction factors are realistic.

However, to model the radiative impact of the biomass smoke alone, the fraction of aerosol in the column that is attributed to the background aerosol needs to be removed. Following the methodology of Remer *et al.* (2002a), it is assumed that the GCM of Tegen *et al.* (1997) models the background aerosol components (sea salt + soil dust + sulphate) well in the dry season and that the underestimation in the column integrated optical depth is entirely due to the model producing low amounts of biomass burning aerosol. To compensate for the underestimation of the biomass burning aerosol $\tau_{\lambda=0.55\mu m}$ in September the smoke component in the GCM data is boosted by a factor of 4.4 to reach agreement with the AERONET climatology. This translates to a mean and standard deviation column fraction of biomass smoke of $84 \pm 12\%$. The derived column fraction is in agreement with the C-130 aircraft measurements over the south Atlantic (see chapter 3 and Osborne *et al.* (2004)). However, the assumption that the background aerosol is modelled well in the GCM is highly uncer-

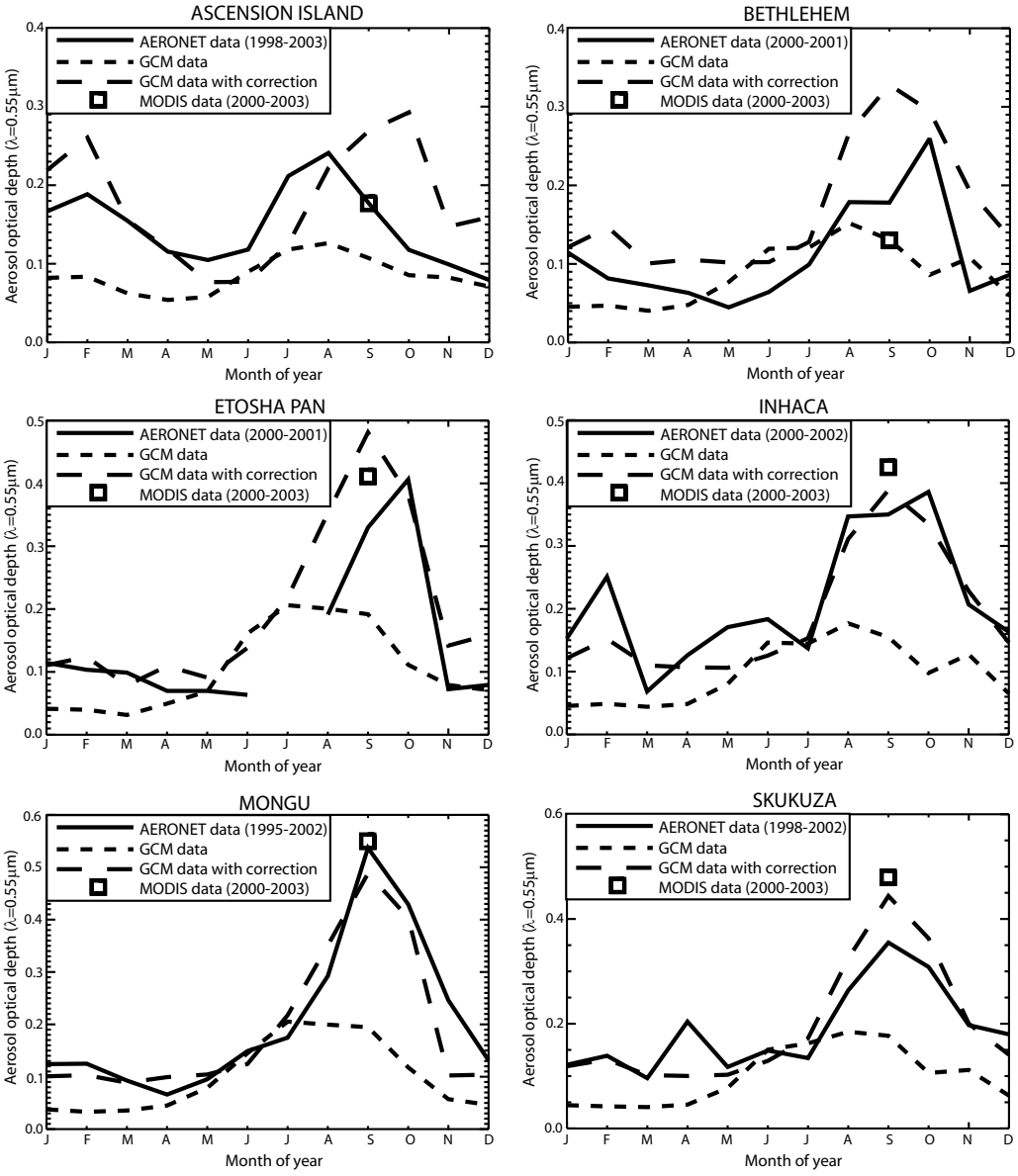

Figure 5.2: *Comparison of the monthly mean column integrated aerosol optical depth at 0.55μm from the GCM of Tegen* et al. *(1997) with values measured at 6 AERONET sites. The years where the AERONET data was obtained is indicated on the individual plots. Also shown is the monthly mean value with a correction factor applied to the GCM data derived from a linear fit to the AERONET measurements (see table 5.1), and the mean MODIS aerosol optical depth for September (2000-2003 average) co-incident with the AERONET site.*

tain, especially when the GCM also underestimates the $\tau_{\lambda=0.55\mu m}$ in months where biomass burning is uncommon (e.g. by a factor of 3.1 in February). Until global aerosol models can adequately reproduce observed distributions of aerosol, estimating the column contribution of aerosol by type is problematic.

MODIS retrieval of aerosol optical depth

The monthly mean column integrated aerosol optical depth for September (2000-2003 average) retrieved with the MODIS instrument onboard the Terra satellite and reported in the MOD08 Level-3 global atmospheric product[3] at a wavelength of $0.55\mu m$ is also used to estimate the spatial distribution of the biomass burning aerosol. The monthly aerosol product results from an average of the daily Level-2 MOD04 10x10 km resolution aerosol product aggregated to a spatial resolution of 1x1° (King *et al.*, 2003). A brief overview of the retrieval algorithm is now given.

The underlying assumption in the MODIS aerosol retrieval is that the up-welling reflectance measured at the TOA is given by the sum of the surface and atmospheric components in the solar wavelength range. The atmospheric component of reflectance contains information about both molecular scattering, clouds, and aerosols. For the aerosol retrieval, cloud pixels are screened out using the MODIS cloud mask (Platnick *et al.*, 2003) and aerosol properties are determined only in clear skies. To remove the surface contribution, different procedures are then applied when retrieving aerosol properties over land and ocean as a result of the more complex characteristics of the land surface reflectance. Over ocean the surface contribution to the TOA reflectance is relatively small and is parameterised in the operational retrieval algorithm (Ichoku *et al.*, 2003). Over land the surface reflectance is estimated using the $2.13\mu m$ channel which is largely transparent to anthropogenic aerosol (large coarse mode particles are likely to degrade the accuracy). This is then used to estimate the surface reflectance in other channels. However, the empirical relation used to estimate the surface reflectance at other wavelengths is only applicable to dark dense vegetation or dark soils (Kaufman *et al.*, 1997) and aerosol retrievals over bright surfaces such as deserts are not made.

Once the surface characteristics are determined the retrieval then uses look-up tables based

[3]data available at http://daac.gsfc.nasa.gov/MODIS/; last accessed 25/04/04

on detailed radiative transfer calculations that include variable τ_λ, SZA, satellite viewing angles, and various aerosol models to obtain agreement between the measured and modelled reflectances. Nine aerosol models are used in the ocean algorithm (4 fine modes, 5 coarse modes) and are not restricted to geographical location (Tanré *et al.*, 1997), whereas the operational land algorithm contains only 3 aerosol models (2 fine modes, 1 coarse mode), of which an a-priori assumption of any fine mode contribution is determined solely on geographical location and season (Kaufman *et al.*, 1997). During the biomass burning season over southern Africa, the aerosol model used assumes a fine fraction ω_0 of 0.90. This is in agreement with the C-130 aircraft measurements taken in the aged regional haze but significantly higher than the measurements taken near source regions (Abel *et al.*, 2003). The lower ω_0 near source regions is likely to lead to an underestimation in the MODIS retrieved optical depth in southern Africa (Ichoku *et al.*, 2003). However, the prelaunch estimates for the retrieval accuracy of $\Delta\tau = \pm 0.05 \pm 0.05\tau$ at a wavelength of $0.55\mu m$ over ocean (Tanré *et al.*, 1997) and $\Delta\tau_\lambda = \pm 0.05 \pm 0.20\tau_\lambda$ over land (Kaufman *et al.*, 1997) have been shown to be reasonable (Chu *et al.*, 2002, Remer *et al.*, 2002b).

In constructing the 4 year average MODIS $\tau_{\lambda=0.55\mu m}$ distribution for this study, the data were linearly interpolated to 'data-missing' regions over land where the surface reflectance is too high for the retrieval algorithm. The data were then aggregated to the same resolution as the GCM and multiplied by the biomass smoke column fraction of 84% derived from the GCM distribution. As discussed previously, estimating the contribution of biomass smoke is highly problematic and the errors associated with the value of 84% need to be treated as an additional uncertainty in the presented model calculations.

Comparison of the GCM and MODIS aerosol optical depth

Figure 5.3 shows the spatial distribution of the monthly mean $\tau_{\lambda=0.55\mu m}$ for September from the a) uncorrected OC+BC component in the GCM results of Tegen *et al.* (1997); b) the OC+BC component boosted by the correction factor of 4.4 derived from the comparison with the AERONET climatology; c) the MODIS total column integrated value; d) the MODIS data multiplied by 84% to estimate the biomass burning aerosol component and aggregated to the GCM resolution. The transition between the ocean and land retrievals of aerosol in the monthly mean MODIS data is reasonably consistent even though significant differences exist between the retrieval algorithms over land and ocean.

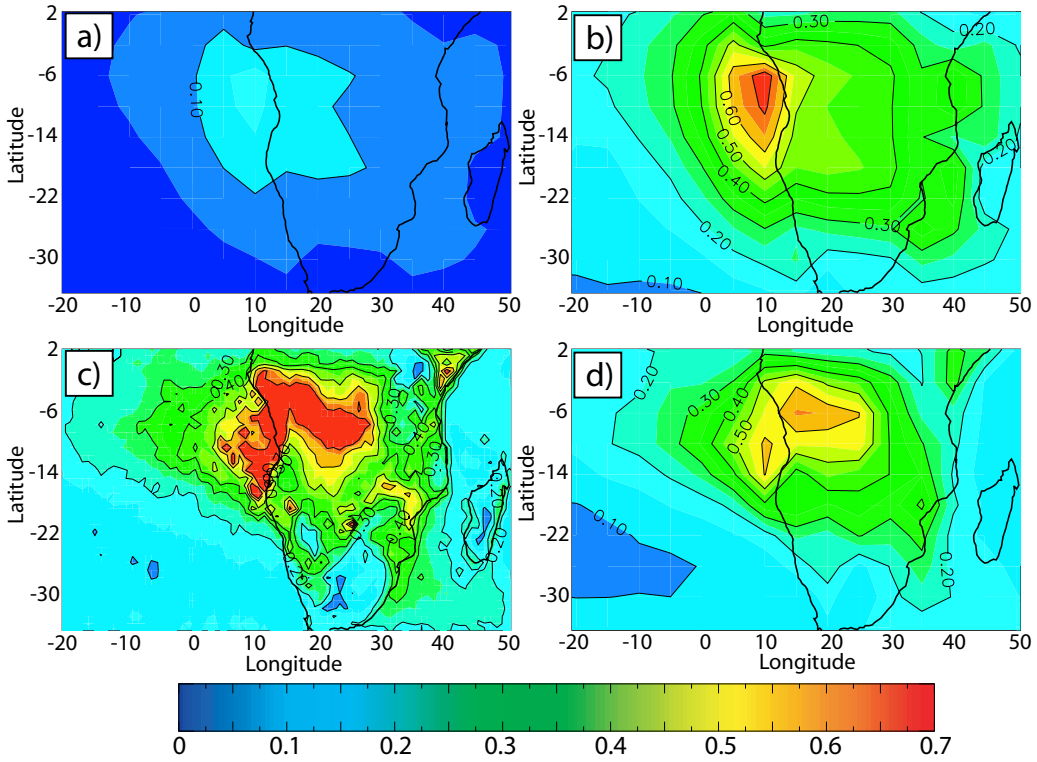

Figure 5.3: *Monthly mean aerosol optical depth for September at a wavelength of 0.55μm for a) OC+BC component in the GCM; b) OC+BC component in GCM increased by a factor of 4.4 as derived from comparison with AERONET measurements; c) MODIS total column (2000-2003 average); d) MODIS data aggregated to the GCM resolution and x 0.84 to estimate the biomass burning aerosol fraction. The MODIS data is linearly interpolated to missing data regions over arid land areas where the surface reflectance exceeds the threshold value required for the aerosol retrieval.*

The under estimation of the aerosol optical depth in the uncorrected GCM data is evident with values over southern Africa being significantly lower than in the MODIS satellite retrieval. Correcting the GCM data with the factor derived from the AERONET climatology brings the spatial pattern into much better agreement with the MODIS distribution. In the region of outflow off the coast of Namibia and Angola from the southern African anticyclone, a North-South gradient in aerosol optical depth is evident in both the GCM and MODIS derived climatologies, and is consistent with that shown for the individual cases studied in chapter 4 (see figure 4.7). However, whereas there is a single peak off the western coast of southern Africa in the model data, the MODIS data has a secondary peak inland. Over oceanic regions the corrected GCM distribution tends to produce higher values of aerosol optical depth than the remotely sensed data, especially off the eastern coast of Africa. The higher values may be the result of the compiled AERONET climatology being biased to locations over land (only a single site out of the 22 was over oceanic

regions), and so the derived correction factor of 4.4 is perhaps more representative of sites closer to the source regions. The sensitivity of the radiative forcing of the biomass burning aerosol over southern Africa to the two spatial distributions of smoke (figures 5.3 b) and d)) is examined in section 5.3.1.

5.2.3 Aerosol optical properties

The aerosol optical properties in both fresh biomass burning plumes and in the aged regional haze have been discussed in chapters 2 and 3 respectively. To include the aerosol in the multi-column radiative transfer model the wavelength dependent properties derived from three log-normals fitted to the measured PCASP size distribution and suitable refractive indices are used. In this study the aged regional haze is modelled with the size distribution measured on flight a791 (see chapter 3) and a refractive index of 1.54-0.018i at a wavelength of 0.55μm, which results in a $\omega_{0\lambda=0.55\mu m}$ of 0.89. For the fresh aerosol the log-normal fit to the size distribution measured in the Otavi plume of Haywood *et al.* (2003a) is used with a refractive index of 1.54-0.024i at a wavelength of 0.55μm for all three modes, which results in a $\omega_{0\lambda=0.55\mu m}$ of 0.84. This is in agreement with the direct measurements of aerosol scattering and absorption directly over the fire (Abel *et al.*, 2003). The effect of hygroscopic growth is neglected as the effect on the optical properties is minimal (Magi and Hobbs, 2003) and so the measured quasi-dry aerosol optical properties are used.

To identify the most active regions of burning over southern Africa the multi-year active fire dataset derived from the Visible and Infrared Scanner (VIRS) instrument on the Tropical Rainfall Measuring Mission (TRMM) satellite is used[4]. The strong emission of mid infra-red radiation from fires is exploited to detect a fire from the VIRS instrument and a detailed description of the retrieval algorithm and performance is given in Giglio *et al.* (2003). Figure 5.4 shows the mean fire counts for southern Africa in September (1998-2002 average). It is clear that the majority of fire activity in September occurs in a band between latitudes of -2 and -18 degrees North, although the East coast of southern Africa

[4]data available at http://daac.gsfc.nasa.gov/CAMPAIGN_DOCS/hydrology/TRMM_VIRS_Fire.shtml; last accessed 25/04/04

undergoes significant burning at latitudes below this. Also indicated in figure 5.4 are the GCM grid boxes where the total fire count exceeds 500, indicating the areas where biomass burning is most prevalent and the optical properties of fresh biomass burning aerosol are likely to dominate over the aged regional haze and should be included in the multi-column radiative transfer model. Abel *et al.* (2003) show a rapid evolution of the aerosol properties as the plume travels away from the fire source and by the time the aerosol is advected away from the burning region the optical properties measured in the aged regional haze will be more suitable. This is supported by AERONET measurements of ω_0 from SAFARI 2000 that show values of 0.84 to 0.85 in the areas where local biomass burning is common, with higher values in areas away from the source regions (Eck *et al.*, 2003). It should be noted that the threshold of 500 fires in a grid box to define the areas with greatest fire activity and thus where fresh aerosol properties are used is somewhat arbitrary, especially since the fire count data used is likely to underestimate the total number of fires (Giglio *et al.*, 2003). However the sensitivity of the direct radiative effect over southern Africa to variations in the threshold value is investigated in section 5.3.3.

5.2.4 Horizontal distribution of cloud

Monthly mean data from the MODIS Terra satellite is employed to include cloud into the multi-column radiative transfer model using the MOD08 Level-3 global atmospheric product[5]. The monthly mean value results from an average of the daily Level-2 MOD06 cloud products discussed in chapter 4 aggregated to a spatial resolution of 1x1° (King *et al.*, 2003, Platnick *et al.*, 2003). Figure 5.5 shows the horizontal distribution and histograms of the water cloud τ_{cloud} and r_e derived from the default 0.86/2.13μm (ocean) and 0.65/2.13μm (land) radiance pairs for September (2000-2003 mean). Also shown are the water and ice cloud fractions over the southern African region. It should be noted that the water cloud τ_{cloud} and r_e are averaged over data points where the water cloud fraction is greater than 0%.

The spatial distribution of the water cloud τ_{cloud} (figure 5.5 (a)) shows values ranging from approximately 6-13 off the coast of Namibia and Angola in September, where values of

[5]data available at http://daac.gsfc.nasa.gov/MODIS/; last accessed 25/04/04

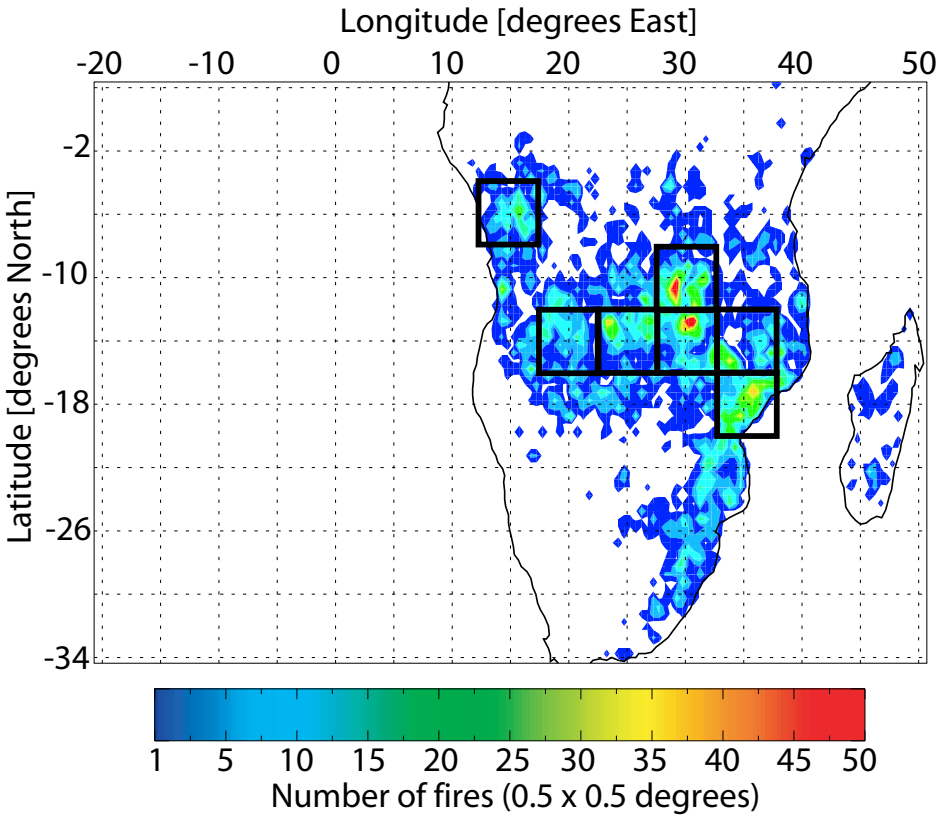

Figure 5.4: *Fire pixels for September (1998-2002 average) retrieved from the Visible and Infrared Scanner (VIRS) instrument onboard the Tropical Rainfall Measuring Mission (TRMM) satellite. The data has been corrected for multiple satellite overpasses and missing observations (Giglio* et al.*, 2003). The black squares show the grid boxes used in the modelling work in this study where the most frequent burning occurs (total fire counts* $\geq$ *500).*

τ_{cloud} ranging from 1-12 were inferred from the C-130 aircraft measurements of cloud liquid water path and r_e (Haywood *et al.*, 2004). Higher values occur when cloud forms over land. The histogram reveals a peak value of 8 (mean=9, σ=3) over the whole of the southern African region.

The histogram of water cloud r_e (figure 5.5 (b)) peaks at 13μm (mean=14μm, σ=3μm). This value is somewhat higher than that measured on the C-130 aircraft during SAFARI 2000, with Keil and Haywood (2003) reporting a cloud top r_e of 7.4$\pm$3.6μm, 7.4$\pm$3.1μm, and 7.8$\pm$1.1μm for three flights off the coast Namibia and Angola. It is also larger than the value of 10μm used for low-level clouds in the Oslo GCM when modelling the radiative effect of biomass burning aerosols during SAFARI 2000 (Myhre *et al.*, 2003). Therefore the cloud included in the modelling work in this study is generally less reflective than the work of Myhre *et al.* (2003) as a result of the larger water droplet size.

The water cloud fraction (figure 5.5 (c)) histogram peaks at 38% (mean=41%, σ=21%), although much larger values in excess of $\backsim 60-70\%$ can be seen off the coast of Namibia and Angola where a semi-permanent startocumulus cloud sheet is present. Furthermore, it is clear from the spatial distribution plot that the majority of the land mass in southern Africa is persistently cloud free during September, with the exception being near some coastal areas.

The ice cloud fraction (figure 5.5 (d)) shows a very different distribution to the water cloud. The histogram peaks at 0% (mean=8%, σ=10%). It is clear from the spatial distribution that ice cloud is uncommon over the majority of the southern African region in September. For the purpose of this study ice clouds are not included in the multi-column radiative transfer code. The presence of high ice clouds would act to reduce the magnitude of the direct radiative effect of any underlying biomass burning aerosol.

The theoretical calculations of Haywood *et al.* (2004) discussed in chapter 4 suggest that the MODIS retrieval of τ_{cloud} is subject to low biases of up to 30% in the presence of an overlying biomass burning aerosol layer with a $\tau_{\lambda=0.55\mu m}$ of 0.5. A value of 0.5 is not uncommon off the coast of Namibia and Angola during September (see section 5.2.2). A potential low bias in r_e of several microns was also evident, although the effect is likely to be $< 1\mu m$ in the default 0.86/2.13μm retrieval used in the monthly mean data product. The sensitivity in the radiative impact of the biomass burning aerosol to the potential low bias in τ_{cloud} and r_e in the MODIS cloud retrievals is explored in section 5.3.4.

The effect of the diurnal variation of cloud amount and optical properties in the southern African region in September is also investigated. The majority of this work uses a four year mean cloud field derived from the Terra satellite, the orbit of which passes from North to South across the equator in the morning. The cloud field included in the model is therefore biased towards clouds present during the morning. The recent addition of the MODIS Aqua satellite with an orbit that overpasses the equator from South to North in the afternoon will dramatically increase the ability to monitor the daily variability of the atmosphere. Figure 5.6 shows the percentage change from the Terra (morning overpass) to Aqua (afternoon overpass) data of τ_{cloud}, r_e, and water cloud fraction for September (2002-2003 average). A positive value represents an increase during the day whilst a negative value represents a decrease. It is clear that the τ_{cloud} and cloud fraction tends to decrease over oceanic regions

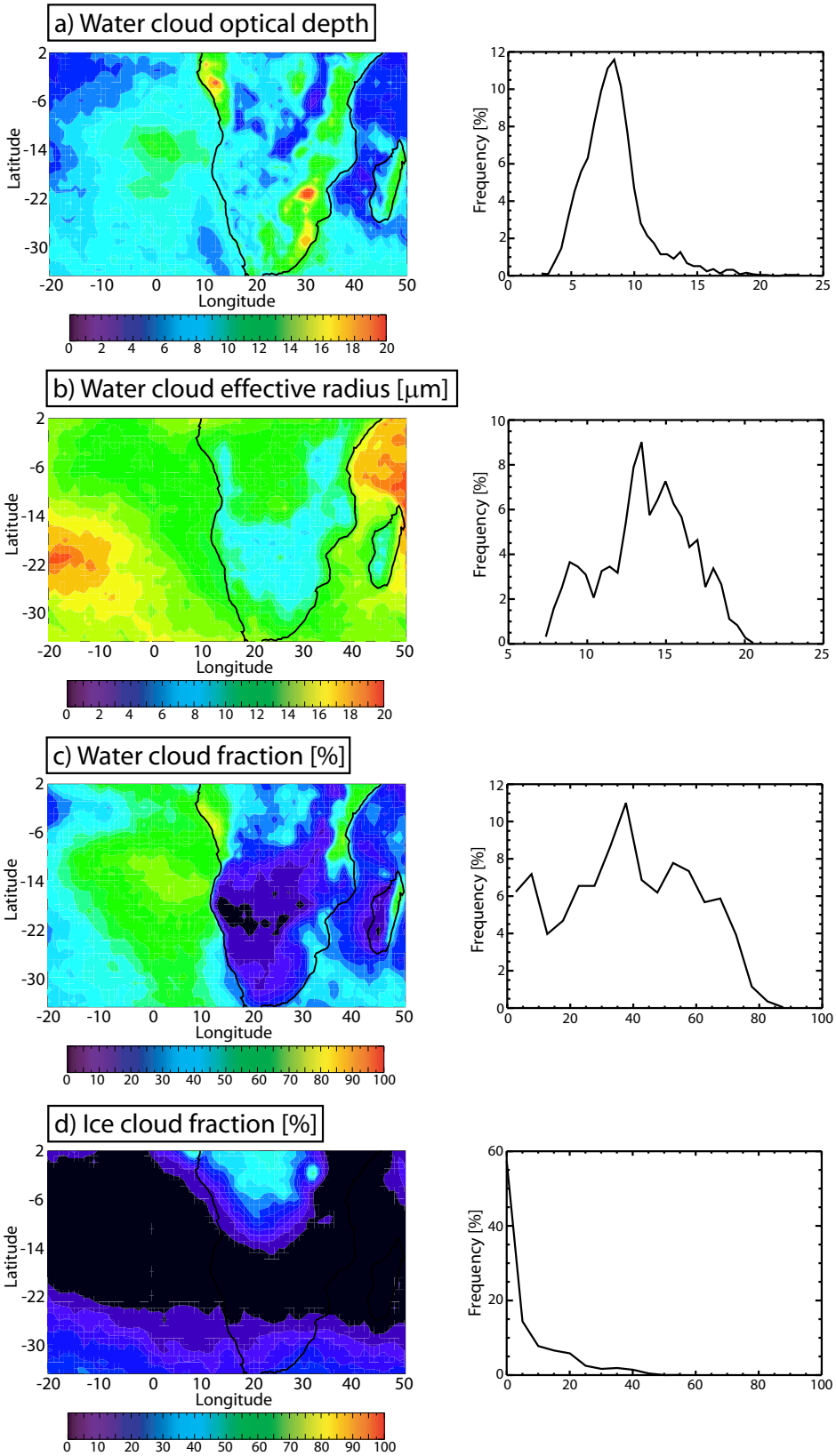

Figure 5.5: *MODIS Terra cloud products over southern Africa at 1x1° resolution for September (2000-2003 average). The spatial distribution and histograms are shown for a) water cloud optical depth; b) water cloud droplet effective radius [μm]; c) water cloud fraction [%]; d) ice cloud fraction [%]. The cloud optical depth and effective particle radius are averaged over data points where the water cloud fraction is greater than 0%.*

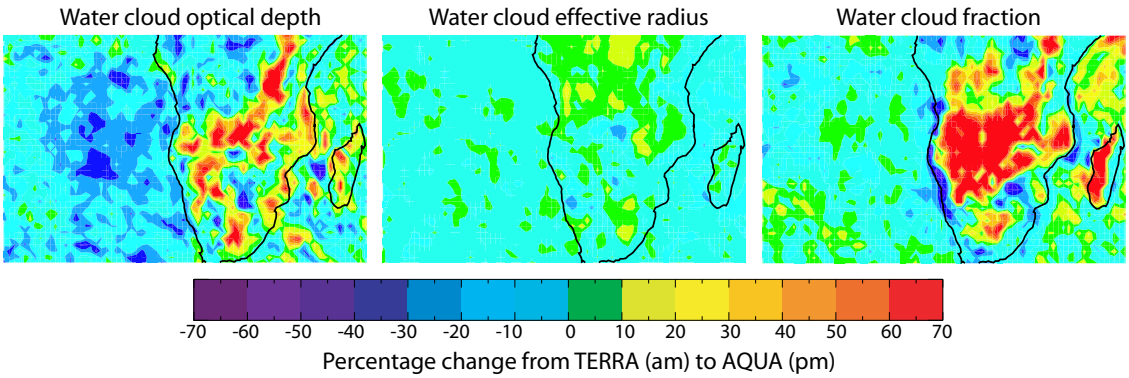

Figure 5.6: *The diurnal cycle of water cloud properties from the MODIS Terra (morning) and Aqua (afternoon) measurements in September (2002-2003 average). Positive values indicate an increase from morning to afternoon and negative values a decrease.*

during the day. This decrease is consistent with visual observations of the stratocumulus cloud sheet off the coast of Namibia and Angola from the C-130 aircraft during SAFARI 2000. It is also in agreement with ship based observations of marine stratiform clouds (Rozendaal *et al.*, 1995) and is likely a result of the increase in solar heating during the day tending to 'burn-off' the low-level cloud (e.g. Johnson *et al.* (2004)). Over land regions increases in the τ_{cloud} and cloud fraction during the day are evident. This is possibly the result of an increase in convective activity. Differences between the Terra and Aqua measurements of r_e are fairly small over both land and oceanic regions. To test the impact of the cloud diurnal cycle on the radiative forcing, model runs are also performed using the two year mean cloud field derived form the Aqua satellite in section 5.3.4.

5.2.5 Water cloud optical properties

The Edwards-Slingo 1996 radiation code adopts the parameterisation of Slingo and Schrecker (1982) to determine the optical properties of cloud droplets as a function of τ_{cloud} and r_e in order to negate the need of computationally expensive Mie theory. The parameterisation is of the form;

$$\tau_{cloud\lambda} = LWP\left(a_\lambda + \frac{b_\lambda}{r_e}\right) \tag{5.1}$$

$$\omega_{0\lambda} = 1 - (c_\lambda + d_\lambda r_e) \tag{5.2}$$

$$g_\lambda = e_\lambda + f_\lambda r_e \tag{5.3}$$

where LWP is the cloud liquid water path and a_λ, b_λ, c_λ, d_λ, e_λ, and f_λ are fitting parameters as a function of wavelength derived from a least squares fit to Mie scattering calculations for water droplets covering a range of realistic size distributions. For the purpose of this study, Mie scattering calculations for stratiform water droplets were performed using log-normal distributions with the modal radius and r_e of the eight drop size distributions detailed in Slingo and Schrecker (1982) and the refractive index of Hale and Querry (1973) to $2\mu m$, thereafter that of Palmer and Williams (1974). The fitting parameters were then calculated for the 220 wavebands used in the radiation code.

The inclusion of cloud at each grid box in the model requires the cloud liquid water mass (LWM), r_e, and cloud fraction at each model level. The r_e and cloud fraction in this study are simply taken from the monthly mean MODIS data discussed in section 5.2.4. The LWM is calculated by initially deriving the LWP from the monthly mean τ_{cloud} retrieved from the MODIS satellite using equation 5.1 with values of a_λ and b_λ at $0.65\mu m$ over land and $0.86\mu m$ over oceanic regions to correspond with the wavelengths used in the MODIS retrieval (see chapter 4). The LWM is then calculated from the LWP using,

$$LWP = \int_i LWM_i \frac{dP_i}{g}, \tag{5.4}$$

where dP is the pressure interval for model level i, and g is the acceleration due to gravity.

5.2.6 Vertical distribution of aerosol and cloud

The vertical profiles of biomass burning aerosol measured on the C-130 aircraft during SAFARI 2000 show that the aerosol tended to be well mixed in the continental boundary layer over land ($<$ 4.5 km AGL) due to strong dry convection (chapter 2 and Haywood *et al.* (2003a,b)), whereas over oceanic regions the aerosol existed in an elevated polluted layer (1.5 - 5.5 km ASL) above a shallow marine boundary layer (chapter 3, Keil and Haywood (2003), Haywood *et al.* (2004)). Similar vertical structures of biomass burning aerosol

over land and oceanic regions have been measured with other instrument platforms in the southern African region (Anderson *et al.*, 1996, Kaufman *et al.*, 2003, Magi *et al.*, 2003, Schmid *et al.*, 2003). Furthermore, the Oslo CTM reproduced similar vertical profiles of biomass smoke for September 2000 (Myhre *et al.*, 2003).

In this study the cloud is only included in one model level at each grid box, although this level can change depending on whether the cloud is over land or ocean. The justification for using one grid box in the vertical is that it is the quantity of the aerosol above the top level of the cloud that is important in accurate determination of the direct effect. Aerosol within or below cloud exerts a radiative forcing that is close to negligible (Haywood and Shine, 1997). Therefore the exact details of the underlying cloud are not relevant although it is recognised that these factors may be important in determining the indirect and semi-direct aerosol effects. The C-130 aircraft measurements show that over oceanic regions the low-level cloud tends to form at the top of the MBL below the elevated biomass plume (chapter 3 and Haywood *et al.* (2004)). Over land the cloud was observed to form at the top of the continental boundary layer (J Haywood, personal communication 2004). Figure 5.7 shows the vertical structure of aerosol and cloud included in the multi-column radiative transfer model. The land vertical profile is used at grid points where more than 50% of the area within the relevant grid box is situated over land. Aerosol particles and cloud droplets are assumed to be externally mixed when they exist in the same model layer and changes in the aerosol optical properties with adsorption of water or any aerosol indirect effect on the cloud properties is neglected.

In section 5.3.5 the impact of changing the vertical profile on the direct radiative effect of the biomass smoke is investigated.

5.2.7 Surface albedo

Determination of the magnitude and sign of the aerosol radiative effect on climate is highly sensitive to the prescribed surface albedo (e.g. Haywood and Shine (1995), Ross *et al.* (1998), Myhre *et al.* (2003)). A large number of GCMs currently adopt a land cover classification scheme for the parameterisation of the surface albedo which in turn requires an accurate representation of the soil and vegetation system (e.g. Sellers *et al.* (1996)). How-

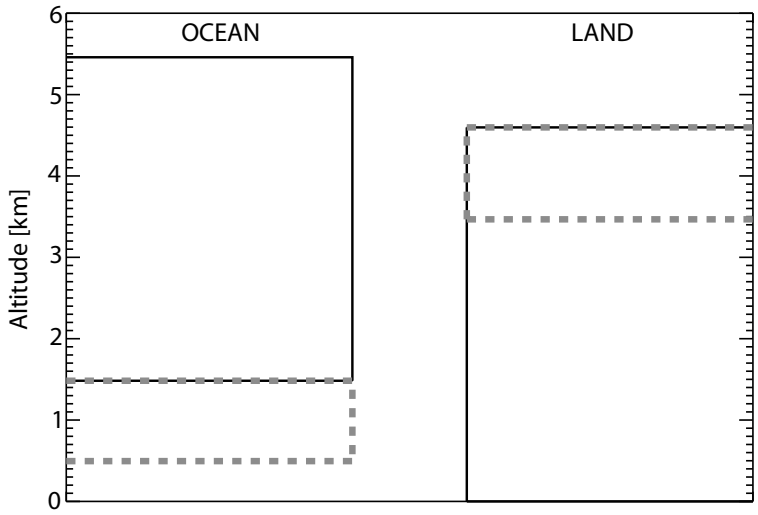

Figure 5.7: *Vertical profile of the biomass burning aerosol (solid line) and cloud (dashed line) included in the model over oceanic and land regions. The vertical profiles are based on the in-situ aircraft measurements detailed in chapters 2 and 3.*

ever, recent advances in satellite based retrievals allow a long term consistent global and high spatial resolution data set of surface albedo to be derived. In this study, the sensitivity of the direct radiative effect of southern African biomass burning aerosol to the surface albedo derived from the AVHRR and MODIS satellites is investigated.

Both the AVHRR and MODIS satellites follow a similar methodology to convert the measured clear-sky up-welling reflectances at the top of the atmosphere to a land surface albedo. The method involves converting the measured directional reflectances to a hemispheric albedo by utilising models of the land bidirectional reflectance functions (BDRF), an atmospheric correction to account for aerosol and water vapour effects, and a narrow to broadband spectral conversion.

The current operational MODIS surface albedo algorithm is discussed in detail in Jin *et al.* (2003a,b). The retrieval outputs seven spectral narrowband albedos (λ =470, 555, 648, 858, 1240, and 2130 nm) and three broadband albedos, one in the visible (0.3-0.7μm), one in the near infra-red (0.7-5.0μm), and one covering both the visible and near infra-red range (0.3-5.0μm). Furthermore, both black-sky and white-sky albedos are reported at each spectral resolution. The black-sky albedo refers to the case where the surface is only illuminated by the direct component of the radiation whereas the illuminating radiation field in the white-sky albedo represents the diffuse component. These are both intrinsic albedos that depend on the reflectance properties of the surface. The actual albedo that occurs in nature is a

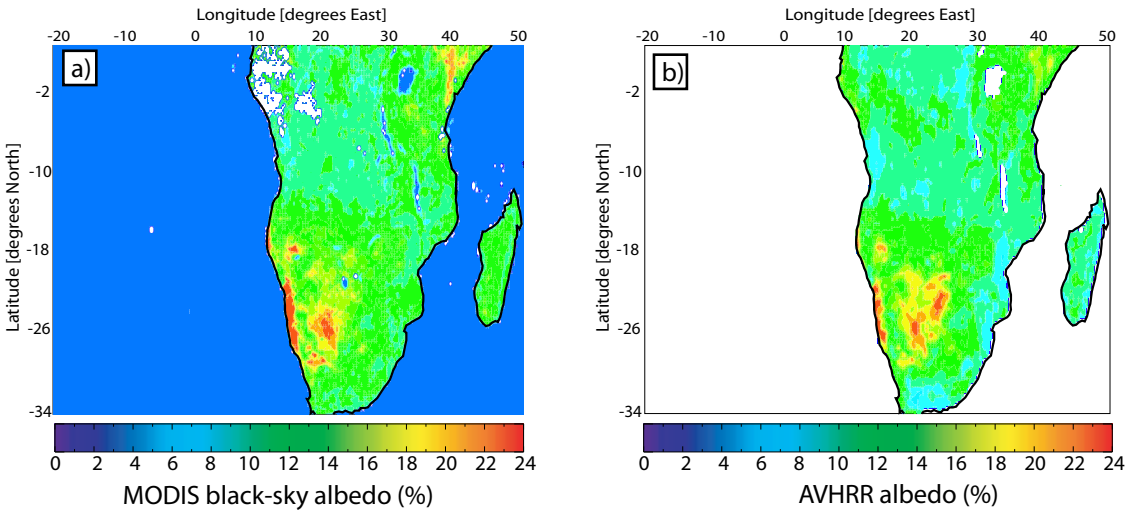

Figure 5.8: *a) MODIS black-sky albedo at 0.25° resolution for the period 14th - 29th September 2001 and b) AVHRR albedo at 0.25° resolution for September averaged over a five year period (1985-1987,1989-1990). White pixels in both data sets represent missing data values.*

combination of the two and is dependent on the atmospheric illumination conditions. At the time of this study a long term data set of the MODIS surface albedo product was not available and so the 0.25° resolution MOD43 16 day average product[6] covering the period from the 14th - 29th September 2001 is used. However, inclusion of the MODIS data into the multi-column radiative transfer model allows the effect that the increase in spectral complexity of the surface has on the radiative impact of the biomass burning aerosols to be investigated.

A detailed description of the AVHRR retrieval is given by Gutman *et al.* (1995) and Csiszar and Gutman (1999). The data set used[7] in this study reports five year averaged values (September 1985-1987,1989-1990), and contains the direct component of the albedo (similar to the MODIS black-sky albedo) in a broadband covering the spectral range 0.35-3.0μm at a resolution of 0.25°. A comparison with the MODIS broadband albedo will give insight into the effect that differences in the two retrievals, and perhaps changes in the surface albedo with time have on the radiative transfer calculations.

Figure 5.8 compares the broadband MODIS black-sky albedo over the southern African region to the broadband AVHRR albedo. Similar spatial patterns in the different retrievals

[6]data available at http://edcdaac.ugs.gov/; last accessed 02/06/04

[7]data available at http://islscp2.sesda.com/ISLSCP2_1/html_pages/groups/veg.html; last accessed 02/06/04

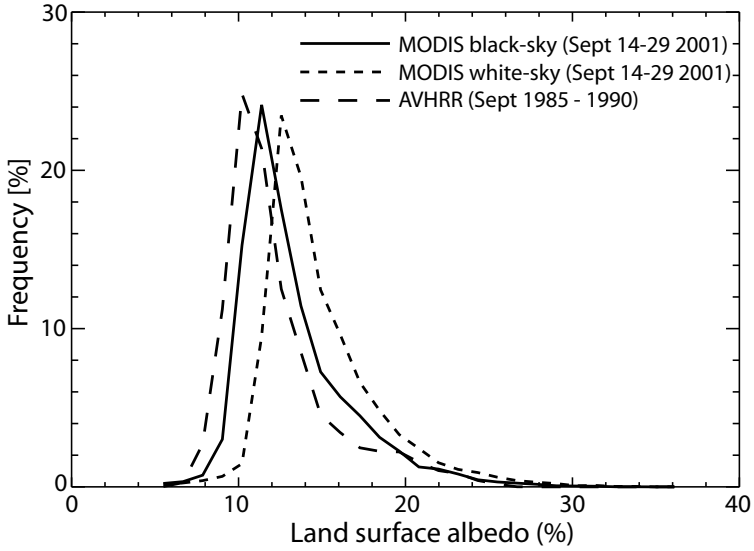

Figure 5.9: *Histograms of land surface albedo at 0.25° resolution for southern Africa for the MODIS black and white-sky, and AVHRR albedo retrievals. The bin size in the histogram is 1.2%.*

of the direct component of the land surface albedo are evident. However, significant differences in the two retrievals can be seen by examination of the histograms in figure 5.9, with the albedo from the MODIS retrieval being larger in general. This is consistent with the results of Jin *et al.* (2003b), who compare the two albedos over the whole globe and attribute the difference to i) the direct component of the albedo generally being higher as the solar altitude increases due to the reflectance properties of the surface (the MODIS black-sky albedo is normalised to local-solar noon whereas the AVHRR albedo is normalised to an overhead Sun); ii) a possible residual aerosol effect in the AVHRR data due to an underestimation of the aerosol amount in the retrievals atmospheric correction procedure; iii) a change in the land cover from the historical AVHRR data-set to the more recent MODIS observations. Differences may also arise from the broadband retrievals of the two satellites covering different spectral ranges. The possible explanations are not investigated here, rather it is the resulting uncertainty in the modelled direct radiative effect to the different satellite retrievals of surface albedo that is of interest.

It is also clear in figure 5.9 that the MODIS white-sky albedo (isotropic illumination) $>$ MODIS black-sky albedo (direct illumination). The higher albedo results from an increase in the path length of a photon through the atmosphere and therefore a greater probability of multiple surface-atmosphere scattering with isotropic illumination compared to direct illumination at local solar noon.

Figure 5.10 shows the different spectral complexities available in the MODIS retrieval for a grid box that is spatially coincident with low level runs performed by the C-130 aircraft during SAFARI 2000 (flight a790, see chapter 2). The seven spectral narrowband retrievals show that there is an increase in the land surface albedo with wavelength to $\backsim 2\mu m$, highlighting the strong spectral dependence of the land surface reflectance. A 220 band spectral albedo is constructed at each grid box by performing a quadratic fit to the seven spectral measurements in the wavelength range 0.47-2.13μm. Outside of the wavelength range covered by the retrieval the albedo is extrapolated at a fixed value. Also indicated are the three different broadband retrievals. In section 5.3.6 the effect of including either the broadband (0.3-5.0μm), the visible and near infra-red broadbands, or a 220 band spectral albedo to the radiative forcing of the biomass smoke is explored.

The average broadband albedo (0.3-3.0μm) across the MODIS grid box determined from the measured up and down welling BBR irradiances onboard the C-130 aircraft is also shown in figure 5.10 for comparison. The C-130 measurement of 17$\%$ is in reasonable agreement with the MODIS white-sky (0.3-5.0μm) albedo of 15$\%$, although it should be stressed that the measured values are from the previous year. However, this type of comparison highlights the fact that in-situ aircraft measurements of land surface albedo can and should be used for validation studies of satellite based retrievals.

In the multi-column radiative transfer model both diffuse and direct components of surface albedo can be included. The ratio of the downwelling direct/diffuse radiation to the total downwelling radiation at the surface in the model is used to weight the individual direct/diffuse albedo components respectively. The inclusion of cloud or aerosol in the atmospheric column will therefore increase the relative weighting of the diffuse albedo. It should be noted that for the AVHRR albedo only a single direct broadband retrieval is available and so the diffuse component is set equal to the direct component. Interpolation to data missing regions in the MODIS data-set over land due to non clear sky conditions is performed before inclusion into the model. Over oceanic regions the surface albedo is set equal to 4$\%$ at all wavelengths in both data sets and is in agreement with the C-130 aircraft broadband measurements of Glew *et al.* (2004) for the relevant monthly mean solar altitude over southern Africa. The strong SZA dependence of the sea surface reflectance is not accounted for in this study.

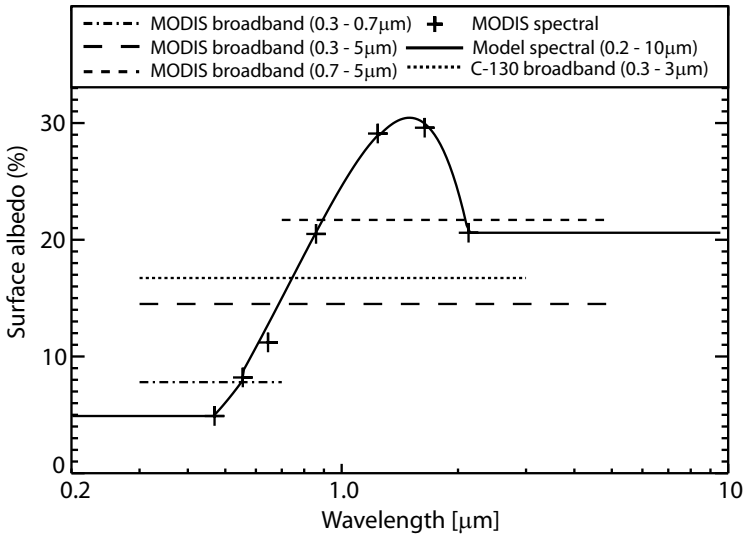

Figure 5.10: *MODIS white-sky albedo as a function of wavelength for September 14th-29th 2001 for the 0.25° grid box centred at -19.625°N, 17.375°E. Shown are the three broadband retrievals at 0.3-0.7μm, 0.7-5μm, 0.3-5μm, and the spectral dependent albedo derived from seven of the MODIS wavebands. Also indicated is the spectral albedo included in the model using least squares fitting with a quadratic of the form y=a+bx+cx^2 to the spectral measurements at $\lambda = 0.47-2.13\mu m$, and extrapolated at a constant wavelength outside of this range. The measured albedo from the C-130 aircraft spatially coincident with the MODIS data (13th September 2000) is shown for comparison.*

5.3 Results

Base case calculations were performed with both the MODIS and GCM derived distributions of aerosol optical depth. Each model run included the fresh aerosol optical properties ($\omega_{0\lambda=0.55\mu m}$=0.84) at the GCM grid boxes where the total number of fire counts $\geq$500 and aged regional haze optical properties ($\omega_{0\lambda=0.55\mu m}$=0.89) elsewhere, MODIS broadband (0.3-5.0μm) direct and diffuse albedo, MODIS water cloud properties and spatial distribution from the Terra satellite, and the vertical profile measured onboard the C-130 aircraft over land and oceanic regions. The input parameters were then varied from the base case and the sensitivity of the radiative forcing to each parameter determined, where the radiative forcing is defined as the instantaneous change in the net irradiance caused by the direct aerosol effect.

The horizontal resolution of the model was set at the resolution of the GCM aerosol data (4x5°). The finer resolution of the other data sets were aggregated to the coarser resolution of the GCM for the majority of model runs. This allowed a direct comparison of the results

from both of the aerosol distributions. However, calculations were also performed using the MODIS data-set at a resolution of 1x1°, increasing the number of columns over the southern African region from 150 to $\backsim$ 3000.

For the majority of the work in this study a monthly time-step was selected. Therefore, for each model run the SZA and incoming TOA insolation is averaged over the whole month at each grid box and the radiation code called once. Sensitivity tests were performed by selecting a daily time-step (30 calls to the radiation code) to test the impact of variations in the daily mean SZA and insolation during the month of September, and using an hourly time-step for the middle day in September (24 calls to the radiation code) to test the sensitivity to the daily SZA variation not accounted for in the monthly time-step.

5.3.1 Base case; sensitivity to aerosol spatial distribution

Figure 5.11 shows the radiative forcing at the top of atmosphere (ΔF_{TOA}) for model runs with clouds not included (clear-sky) and with the inclusion of clouds (whole-sky) over the southern African region using the base case with the MODIS (1x1° and 4x5°) and GCM (4x5°) derived horizontal distributions of biomass burning aerosol. The clear-sky ΔF_{TOA} is negative everywhere and the spatial pattern is similar to the aerosol optical depth distribution included in the model, with the exception over the semi-arid regions to the South where the higher surface reflectance reduces the net outgoing flux at the TOA compared to areas with a lower surface albedo. The whole-sky model runs show a positive ΔF_{TOA} off the coast of Namibia and Angola where the partially absorbing aerosol overlies low-level cloud and is negative elsewhere. The region of positive forcing is in agreement with that predicted from the calculations of Keil and Haywood (2003). Also shown in figure 5.11 is the whole-sky radiative forcing at the surface ($\Delta F_{surface}$) with large negative values evident over the whole of the southern African region.

Table 5.2 shows the average ΔF_{TOA} and $\Delta F_{surface}$ diagnosed from the different spatial distributions of biomass smoke across the whole region, land pixels only, and sea pixels only. The average regional clear-sky ΔF_{TOA} ranged from -9.0 to -10.8 Wm^{-2}, and the $\Delta F_{surface}$ from -20.5 to -24.3 Wm^{-2} for the different aerosol distributions. In the absence of clouds the radiative impact at the surface is $\backsim$ 2.3 times greater compared to at the TOA

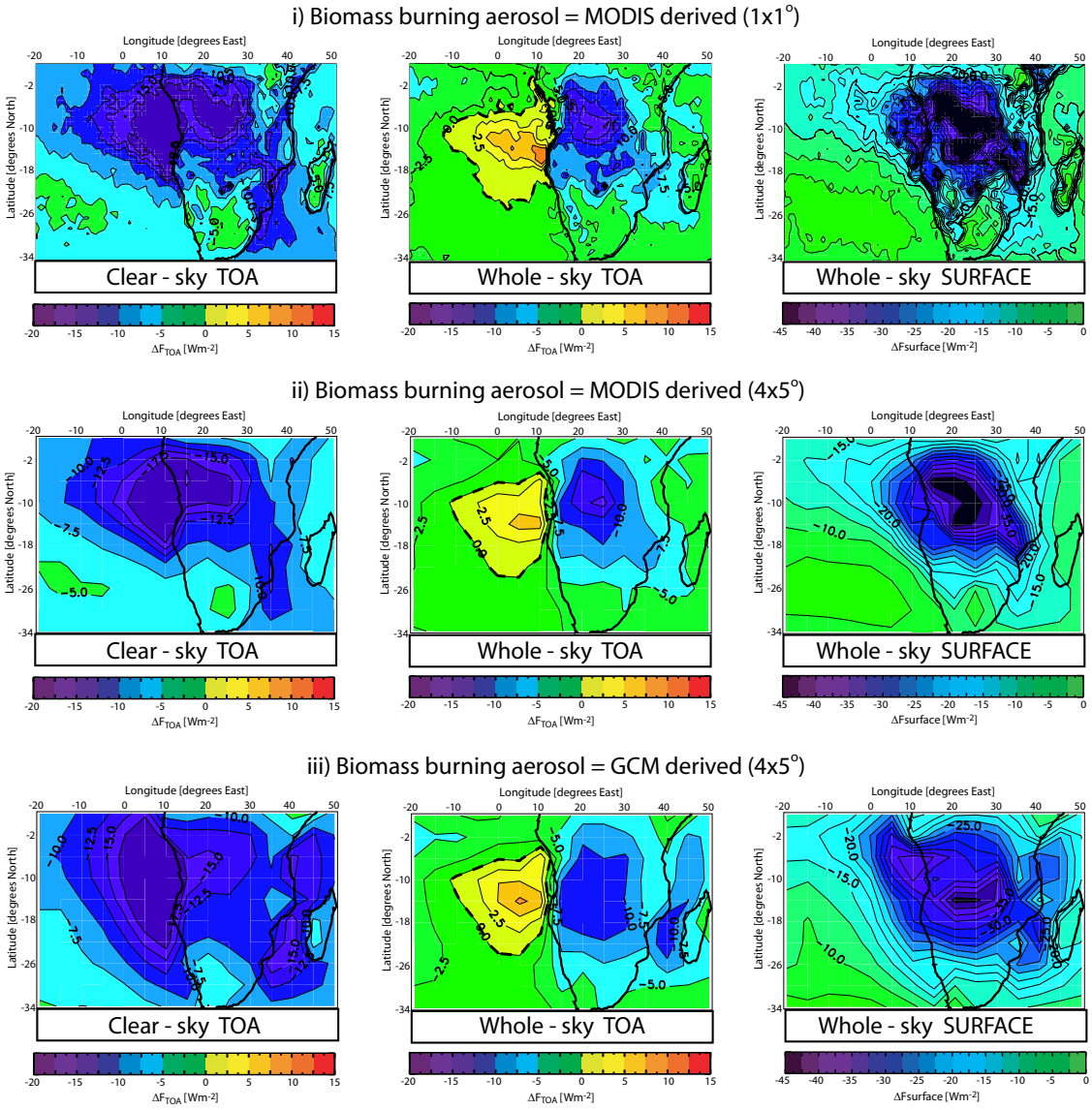

Figure 5.11: *Radiative impact over the southern African region using the base case (see text for details) with the biomass burning aerosol spatial distribution derived i) from the MODIS satellite at a resolution of 1x1°, ii) as i) but aggregated to a resolution of 4x5°, and iii) from the corrected model results of Tegen* et al. *(1997) at 4x5°. Panels show a) ΔF_{TOA} under clear-sky conditions; b) ΔF_{TOA} with clouds included (whole-sky); c) $\Delta F_{surface}$ with clouds included (whole-sky). The dashed line indicates the transition between positive and negative radiative forcing. The colour scale changes between the ΔF_{TOA} and $\Delta F_{surface}$ plots.*

over the region, and is typical of other studies over southern Africa (Ichoku *et al.*, 2003) and the Indian Ocean (Satheesh and Ramanathan, 2000). The strength of the mean clear-sky ΔF_{TOA} over land is greater than that over the sea with the MODIS aerosol field, and less with the GCM derived distribution. However, the MODIS and GCM averaged results are in good agreement over the land. The impact of the biomass smoke over the sea is perhaps over estimated with the GCM distribution, which contained higher values of aerosol optical depth than the remotely sensed data, particularly off the eastern coast of southern Africa (see figure 5.3).

The averaged regional ΔF_{TOA} for whole-sky conditions ranges from -3.5 to -4.2 Wm^{-2}, and the $\Delta F_{surface}$ from -15.7 to -18.6 Wm^{-2} depending on the aerosol distribution used, with the strongest radiative impact from the GCM derived optical depth. This is again due to the excess aerosol over oceanic regions in the GCM distribution. The magnitude of the regional forcing is $\backsim$ 4.4 times greater at the surface compared to the TOA. This is a direct consequence of the large amount of solar radiation absorbed by the aerosol in the atmosphere which is given by ΔF_{TOA} - $\Delta F_{surface}$, resulting in average values of 12.1 and 14.4 Wm^{-2} for the two cases. This is similar to the value of 14$\pm$3 Wm^{-2} reported for the Indian Ocean region during the dry season where large amounts of partially absorbing aerosol are persistent in a heavily polluted haze layer (Ramanathan *et al.*, 2001a). By comparing the clear-sky to the whole-sky runs it is clear that clouds reduce the direct radiative impact of biomass burning aerosol in the southern African region during September by a factor of $\backsim$ 2.5 at the TOA and $\backsim$ 1.3 at the surface. However, the effect is more significant over the sea due to the increased presence of clouds (factor of $\backsim$ 4.6 at the TOA and 1.4 at the surface).

Model runs were also performed using the uncorrected GCM aerosol distribution. This resulted in a large weakening of the modelled radiative forcing as a result of the large under estimation in the amount of aerosol. The impact was to reduce the average whole-sky ΔF_{TOA} to -1.1 Wm^{-2} and the $\Delta F_{surface}$ to -4.5 Wm^{-2}, corresponding to changes from the base case of -74$\%$ and -76$\%$ for the TOA and surface forcings respectively. This highlights the large potential errors that more detailed GCM calculations will make if the characterisation of aerosol emissions and transport are incorrect.

The effect of reducing the MODIS spatial distribution from 1x1° to 4x5° has a very small

Aerosol distribution	*Clear-sky* ΔF_{TOA}				*Clear-sky* $\Delta F_{surface}$			
	ΔF_{reg}	Range	ΔF_{land}	ΔF_{sea}	ΔF_{reg}	Range	ΔF_{land}	ΔF_{sea}
MODIS x 84% 1x1°	-9.0	-2 to -34	-9.7	-8.6	-20.6	-5 to -75	-27.6	-17.0
MODIS x 84% 4x5°	-9.0	-4 to -26	-10.0	-8.5	-20.5	-9 to -65	-27.5	-16.9
GCM x 4.3778 4x5°	-10.8	-4 to -29	-10.0	-11.3	-24.3	-10 to -64	-27.5	-22.6

Aerosol distribution	*Whole-sky* ΔF_{TOA}				*Whole-sky* $\Delta F_{surface}$			
	ΔF_{reg}	Range	ΔF_{land}	ΔF_{sea}	ΔF_{reg}	Range	ΔF_{land}	ΔF_{sea}
MODIS x 84% 1x1°	-3.5	11 to -18	-6.8	-1.8	-15.7	-5 to -55	-23.2	-11.8
MODIS x 84% 4x5°	-3.6	6 to -16	-7.0	-1.8	-15.7	-6 to -45	-23.1	-11.8
GCM x 4.3778 4x5°	-4.2	8 to -12	-7.2	-2.5	-18.6	-7 to -44	-23.4	-16.0

Table 5.2: *September monthly mean surface and top of atmosphere direct radiative effect [Wm^{-2}] averaged over the southern African region (ΔF_{reg}), land only (ΔF_{land}), and ocean only (ΔF_{sea}). The maximum to minimum range [Wm^{-2}] in the forcing over the whole region (Range) is also included. Clear-sky and whole-sky results are shown for model runs including the spatial distribution of biomass smoke derived from the MODIS satellite at 1x1° and 4x5° resolution and from the GCM data at 4x5° resolution.*

impact on the average radiative forcing (+3% at the TOA and $<1\%$ at the surface). Because the impact of the higher resolution runs does not improve the calculation of the mean forcing across the region, the following whole-sky sensitivity runs are all performed at a resolution of 4x5° to reduce the computational time.

Tables 5.3 and 5.4 summarise the average, minimum, maximum, and the percentage change from the base case in the radiative impact of the aerosol at the TOA and surface from the various model runs using the MODIS and GCM optical depth distributions respectively, whilst figures 5.12 and 5.13 show the spatial distribution of the ΔF_{TOA} and $\Delta F_{surface}$ for a selection of model runs using the MODIS aerosol distribution. Identical features are evident in the ΔF_{TOA} and $\Delta F_{surface}$ to changes in the model input with the GCM aerosol distribution.

5.3.2 Sensitivity to model time step

The sensitivity of the radiative forcing to daily variations in SZA and the TOA insolation was examined by selecting a daily time step in the model for the base case setup. This resulted in negligible changes in the radiative forcing of $< 1\%$ at both the TOA and surface.

Haywood and Shine (1997) show that the magnitude of the direct aerosol effect has a high dependence on variations in solar altitude. Running the model for the middle day in September and selecting an hourly time-step allows the sensitivity to daily variations in the SZA to be explored. Figure 5.12 and 5.13 b) show that accounting for the change in SZA resulted in a weaker radiative impact over the region at the TOA and surface when compared to the base case (figures 5.12 and 5.13 a)). The average difference in the regional ΔF_{TOA} and $\Delta F_{surface}$ from the base case was -14$\%$ and -9$\%$ respectively. The reduction in both the maximum and minimum values at the TOA indicated in tables 5.3 and 5.4 shows that the weakening occurs for regions of both positive and negative radiative forcing, although the effect is most significant in the land pixels. Whilst this result shows that the magnitude of the radiative impact of the biomass smoke will be over estimated when choosing a monthly mean SZA instead of accounting for the daily variation, the aim of this study is to test the sensitivity to model inputs of aerosol, cloud, and surface reflectance. It is therefore not an exact value that is required, rather the difference resulting from perturbing the model inputs. Therefore the systematic bias that results from the assumption of a monthly mean SZA is treated as an additional uncertainty in the absolute values.

5.3.3 Sensitivity to aerosol optical properties

To assess the sensitivity in the radiative impact of the smoke from including one aerosol type in the model (fresh or aged) instead of identifying regions of persistent burning and including two types as in the base case, model runs were performed with the aerosol optical properties measured at the source and in the aged regional haze prescribed to the whole region.

The ΔF_{TOA} and $\Delta F_{surface}$ averaged over the whole region were found to be highly sensitive to the aerosol properties, with differences of $\backsim$50$\%$ at the TOA and $\backsim$25$\%$ at the surface between the fresh and aged aerosol only runs. However, the aged aerosol case had differences of $< \pm 3\%$ at both the TOA and surface when compared to the base case. The largest difference from the more detailed base case arises from the assumption of fresh aerosol everywhere. Figure 5.12 d) shows that the inclusion of the fresh aerosol at all grid boxes results in a larger region of positive ΔF_{TOA} over the southern Atlantic Ocean due to

the presence of a more absorbing aerosol overlying the highly reflective cloud layer when compared to the base case. This results in a significant weakening in the magnitude of the net regional impact of the biomass smoke at the TOA ($\backsim$ 100 $\%$ over ocean and 20 $\%$ over land). In contrast the excess absorption of the aerosol acts to further reduce the flux reaching the Earth's surface and therefore strengthens $\Delta F_{surface}$ when compared to the base case as shown in figure 5.13 d).

The sensitivity to variations in the threshold value required to assign fresh aerosol properties to a grid box based on satellite fire counts is reduced to 300 from the base case of 500. This increases the surface area of the southern African region covered by fresh biomass smoke in the model from approximately 5 to 9 $\%$ and results in a small weakening in the land ΔF_{TOA} by 3$\%$. This suggests that the added complexity of including both fresh aerosol where burning is prevalent, and aged aerosol properties elsewhere does not significantly improve the estimation of ΔF_{TOA} and $\Delta F_{surface}$ on a regional scale compared to when using aged properties everywhere (3 - 5$\%$ depending on the threshold value).

5.3.4 Sensitivity to cloud optical depth and optical properties

The effect of the potential low bias in the MODIS satellite τ_{cloud} and r_e retrievals as a direct result of the overlying biomass plume is considered. Whilst the theoretical calculations of Haywood *et al.* (2004) suggest that the bias in the r_e from the default MODIS retrieval used in this study is $<$-1 μm, the analysis of the MODIS cloud product in chapter 4 presented evidence that a modal low bias as large as -3μm is evident off the coast of southern Africa in the presence of an overlying biomass burning aerosol layer when using the retrieval based on the 0.86 and 1.63 μm radiance pairs. To assess the impact that any underestimation in the cloud droplet size has on the radiative forcing of the biomass smoke, model runs were performed with the r_e increased by 1 to 3 μm across the whole region, thus representing the possible uncertainty in r_e from the default 0.86/2.13 μm and the 0.86/1.63 μm retrieval. The theoretical calculations also indicate that a potential low bias of up to 30$\%$ in τ_{cloud} may occur in the default retrieval as a direct result of the partially absorbing biomass smoke. To test the sensitivity to the uncertainty in τ_{cloud}, runs are carried out by correcting the MODIS data for a 10$\%$ (τ_{cloud}/0.9) and a 30$\%$ (τ_{cloud}/0.7) underestimation in cloud optical thickness

across the whole region.

Increasing the r_e of the MODIS data decreases the cloud reflectivity. Hence, the radiative impact of the aerosol over land increases as more solar radiation passes through the cloud to the underlying aerosol, and over oceanic regions the positive forcing decreases due to a smaller probability of multiple scattering between the aerosol and cloud. The impact on the radiative forcing to the uncertainties in r_e is only significant over the ocean, due to the greater cloud coverage than over land in the dry season (see figure 5.5). The ocean averaged ΔF_{TOA} is strengthened by 3 to 10$\%$, whereas over land the changes are $\leq$1$\%$ for an increase in r_e of 1 to 3 μm. Changes in the $\Delta F_{surface}$ are $\leq$1$\%$ over both land and sea.

An increase in τ_{cloud} leads to a greater probability of a photon being scattered back out of the cloud top, and so the impact on the forcing is of the opposite sign to an increase in r_e. Figure 5.12 f) shows that the positive region of ΔF_{TOA} over the southern Atlantic Ocean expands significantly compared to the base case with the MODIS τ_{cloud}/0.7 inserted into the model. The net effect is to decrease the average regional ΔF_{TOA} by 7 to 25 $\%$ when compensating for a 10 to 30 $\%$ low bias in cloud optical thickness, although the impact is more important over oceanic regions with a decrease of $\backsim$ 60$\%$. The sensitivity at the surface is less, with regional changes ranging from -1 to -5 $\%$. The potential low bias in τ_{cloud} in the MODIS satellite retrieval could lead to a significant overestimation of the direct radiative effect over the southern African region in this study.

The effect of the diurnal cycle of clouds on the radiative effect of the biomass smoke is investigated by replacing the water cloud spatial distribution and optical properties derived from the MODIS Terra satellite (morning overpass) used in the majority of this study with those derived from the MODIS Aqua satellite (afternoon overpass). Figure 5.12 g) shows that the general reduction in both cloud cover and τ_{cloud} over oceanic regions results in a reduction in the positive ΔF_{TOA} of the overlying biomass smoke, strengthening the ocean only averaged ΔF_{TOA} by 42$\%$. Over land regions the ΔF_{TOA} becomes slightly weaker by 2$\%$ due to an increase in cloud at the top of the biomass burning aerosol layer. The impact of the cloud diurnal cycle is clearly weaker than over oceanic regions due to the lower cloud fraction. The net effect is an increase of 13 to 15$\%$ in the ΔF_{TOA}, and of 2$\%$ in the $\Delta F_{surface}$ across the southern African region using the MODIS and GCM aerosol distributions.

5.3.5 Sensitivity to the vertical structure of aerosol and cloud

The sensitivity to the vertical structure was examined by performing calculations with both the oceanic profile (aerosol above cloud level) and the land profile (aerosol in and below cloud level) applied to the whole region.

The average land ΔF_{TOA} decreased by 40 to 45 $\%$ with application of the oceanic vertical structure for the two aerosol distributions included in the model. Figure 5.12 h) shows that this is the result of the region of positive forcing off the West coast of southern Africa extending into land regions around the coast where cloud is prevalent. The magnitude of the forcing is also weakened further inland where the cloud amount is not large enough to result in a positive ΔF_{TOA}.

Substituting the vertical profile measured over land to the whole region resulted in an increase in the ΔF_{TOA} of 143 to 160 $\%$ over the oceanic regions. It can be seen in figure 5.12 i) that the presence of cloud at the top of the aerosol layer eliminates all of the areas of positive ΔF_{TOA}, and so the impact of the biomass burning aerosol is to increase the outgoing flux at the TOA throughout the southern African region.

In contrast, the $\Delta F_{surface}$ is not sensitive to the vertical profile, with differences from the base case of $\leq 1\%$ for both oceanic and land profiles. This is because the down-welling flux at the surface is mainly sensitive to the transmission of the overlying atmosphere which is largely independent on the vertical structure, whereas the fluxes at the TOA are sensitive to the radiation incident on the aerosol layer and the underlying reflectance. These in turn are highly dependent on the aerosol and cloud profile.

5.3.6 Sensitivity to the land surface albedo

The inclusion of the AVHRR broad-band land surface albedo (figure 5.12 j)) resulted in a strengthening of the land averaged ΔF_{TOA} by 4% when compared to the MODIS broad-band albedo used in the base case, and is the result of a lower probability of multiple surface-aerosol scattering due to the less reflective surface leading to less aerosol absorption. Changes of $<1\%$ in the radiative impact were evident at the surface. It should be

noted that small differences between the ocean averaged ΔF_{TOA} and the $\Delta F_{surface}$ occur when using different land surface albedos in the model because of the grid box averaging around the coastline.

Application of the more detailed spectrally varying albedo (220 bands) derived from the polynomial fit to the seven wavelengths in the MODIS satellite retrieval resulted in a larger strengthening of the land ΔF_{TOA} and the $\Delta F_{surface}$ by 13 to 14 $\%$ and 3% respectively. This increase is a direct result of the high spectral dependence of the aerosol optical properties. Because the land surface albedo tends to be lower in the visible wavelength range (where the aerosol extinction coefficient is the largest) than at longer wavelengths, the surface is effectively less reflective than in the broad-band retrieval and therefore leads to less aerosol absorption in the atmosphere and a greater outgoing flux at the TOA (see figure 5.12 k)). The inclusion of the MODIS visible and near infra-red broadband albedo resulted in small differences of $<3\%$ in the land ΔF_{TOA} compared to using the more detailed 220 band version.

Aerosol spatial distribution = MODIS														
Difference from base case[a]	Top of atmosphere							Surface						
	ΔF_{reg}	$\delta_{reg}(\%)$	Range$_{reg}$	ΔF_{land}	$\delta_{land}(\%)$	ΔF_{sea}	$\delta_{sea}(\%)$	ΔF_{reg}	$\delta_{reg}(\%)$	Range$_{reg}$	ΔF_{land}	$\delta_{land}(\%)$	ΔF_{sea}	$\delta_{sea}(\%)$
None	**-3.6**	*N/A*	**6.1 to -16.0**	**-7.0**	*N/A*	**-1.8**	*N/A*	**-15.7**	*N/A*	**-6.4 to -44.9**	**-23.1**	*N/A*	**-11.8**	*N/A*
Model time step														
Daily	-3.6	< 1	6.1 to -16.0	-7.0	< 1	-1.8	< 1	-15.7	< 1	-6.4 to -44.9	-23.1	< 1	-11.8	< 1
24 hour (mid September)	-3.1	*-14*	5.1 to -13.1	-5.8	*-17*	-1.7	*-8*	-14.4	*-8*	-5.9 to -43.5	-21.1	*-9*	-10.8	*-8*
Aerosol optical properties														
ω_0=0.89 everywhere	-3.7	*+3*	6.1 to -16.0	-7.3	*+4*	-1.8	*0*	-15.4	*-2*	-6.4 to -44.9	-22.1	*-4*	-11.8	*0*
ω_0=0.84 everywhere	-2.0	*-46*	14.4 to -13.2	-5.8	*-18*	0.0	*-103*	-19.3	*+23*	-8.1 to -55.6	-27.7	+20	-14.9	*+26*
ω_0=0.84 (fire counts>300)	-3.6	*-2*	6.1 to -14.5	-6.8	*-3*	-1.8	*0*	-16.0	*+2*	-6.4 to -54.4	-23.9	*+3*	-11.8	*0*
Cloud optical properties														
Cloud r_{eff} + 1μm everywhere	-3.7	*+1*	5.8 to -16.0	-7.0	< 1	-1.9	+3	-15.8	*<1*	-6.4 to -45.0	-23.2	< 1	-11.8	< 1
Cloud r_{eff} + 3μm everywhere	-3.8	*+4*	5.4 to -16.0	-7.1	*+1*	-2.0	*+10*	-15.8	*+1*	-6.4 to -45.2	-23.2	< 1	-11.9	*+1*
Cloud τ/0.9 everywhere	-3.4	*-7*	7.5 to -15.9	-6.9	*-1*	-1.5	*-18*	-15.5	*-1*	-6.2 to -44.5	-22.9	*-1*	-11.6	*-2*
Cloud τ/0.7 everywhere	-2.8	*-23*	10.7 to -15.6	-6.7	*-5*	-0.7	*-60*	-15.0	*-5*	-5.9 to -43.6	-22.5	*-3*	-11.0	*-7*
Cloud diurnal cycle														
AQUA cloud field	-4.1	*+13*	2.6 to -13.9	-6.9	*-2*	-2.6	*+43*	-16.0	*+2*	-6.9 to -45.7	-22.9	*-1*	-12.4	*+5*
Vertical structure														
Aerosol and cloud land profile	-5.4	*+50*	-2.4 to -16.0	-7.0	*0*	-4.6	*+160*	-15.7	*<1*	-6.3 to -44.9	-23.1	*0*	-11.8	< 1
Aerosol and cloud oceanic profile	-2.5	*-30*	13.4 to -13.8	-3.9	*-45*	-1.8	*0*	-15.6	*-1*	-6.4 to -44.5	-22.9	*-1*	-11.8	*0*
Surface albedo														
AVHRR broadband surface albedo	-3.7	*+3*	6.1 to -16.0	-7.3	*+4*	-1.9	*+1*	-15.8	*<1*	-6.4 to -44.7	-23.3	*+1*	-11.8	< 1
MODIS spectral surface albedo	-4.0	*+9*	6.0 to -17.6	-8.0	*+13*	-1.9	*+1*	-16.0	*+2*	-6.4 to -46.1	-23.8	*+3*	-11.8	< 1
MODIS VIS and NIR albedo	-4.0	*+11*	6.0 to -18.2	-8.1	*+16*	-1.9	*+1*	-16.0	*+2*	-6.4 to -46.7	-23.9	*+4*	-11.8	< 1

Table 5.3: *Surface and top of atmosphere direct radiative effect [Wm^{-2}] for the series of model runs described in the text. Averaged regional (ΔF_{reg}), land (ΔF_{land}), and oceanic (ΔF_{sea}) values for September are presented. The percentage change from the base case ($\delta_{reg/land/sea}$) and the range in the regional average (Range$_{reg}$) are also shown.* [a] *base case uses MODIS aerosol optical depth distribution x 0.84, fresh aerosol properties (ω_0=0.84) where TRMM fire counts> 500, aged aerosol (ω_0=0.89) everywhere else, MODIS spatial distribution of water cloud optical depth, effective radius and cloud fraction, MODIS broadband surface albedo, cloud and aerosol vertical profile measured onboard the C-130 aircraft over land and ocean.*

Aerosol spatial distribution = GCM														
Difference from base case[a]	Top of atmosphere							Surface						
	ΔF_{reg}	$\delta_{reg}(\%)$	Range$_{reg}$	ΔF_{land}	$\delta_{land}(\%)$	ΔF_{sea}	$\delta_{sea}(\%)$	ΔF_{reg}	$\delta_{reg}(\%)$	Range$_{reg}$	ΔF_{land}	$\delta_{land}(\%)$	ΔF_{sea}	$\delta_{sea}(\%)$
None	**-4.2**	*N/A*	**8.1 to -12.4**	**-7.2**	*N/A*	**-2.5**	*N/A*	**-18.6**	*N/A*	**-6.7 to -43.6**	**-23.4**	*N/A*	**-16.0**	*N/A*
Model time step														
Daily	-4.2	< 1	8.1 to -12.4	-7.2	< 1	-2.5	< 1	-18.6	< 1	-6.7 to -43.6	-23.4	< 1	-16.0	< 1
24 hour (mid September)	-3.6	*-14*	7.0 to -10.8	-6.0	*-18*	-2.3	*-9*	-17.0	*-9*	-6.1 to -39.1	-21.3	*-9*	-14.6	*-8*
Aerosol optical properties														
ω_0=0.89 everywhere	-4.3	*+2*	8.1 to -13.3	-7.5	*+3*	-2.5	*0*	-18.2	*-2*	-6.7 to -39.1	-22.5	*-4*	-16.0	*0*
ω_0=0.84 everywhere	-2.1	*-50*	16.5 to -11.1	-6.0	*-18*	0.0	*-99*	-22.8	*+23*	-8.4 to -49.0	-28.1	*+20*	-20.0	*+25*
ω_0=0.84 (fire counts>300)	-4.1	*-2*	8.1 to -12.4	-7.0	*-3*	-2.5	*0*	-18.8	*+1*	-6.7 to -43.6	-24.2	*+3*	-16.0	*0*
Cloud optical properties														
Cloud r_{eff} + 1μm everywhere	-4.2	*+1*	7.8 to -12.5	-7.3	< 1	-2.6	*+3*	-18.6	*<1*	-6.7 to -43.6	-23.5	< 1	-16.0	< 1
Cloud r_{eff} + 3μm everywhere	-4.3	*+4*	7.3 to -12.6	-7.3	*+1*	-2.8	*+10*	-18.7	*<1*	-6.7 to -43.7	-23.5	< 1	-16.1	*+1*
Cloud τ/0.9 everywhere	-3.9	*-8*	9.5 to -12.3	-7.2	*-1*	-2.1	*-17*	-18.3	*-1*	-6.5 to -43.5	-23.2	*-1*	-15.7	*-2*
Cloud τ/0.7 everywhere	-3.1	*-25*	12.6 to -12.1	-6.9	*-4*	-1.1	*-57*	-17.7	*-5*	-6.3 to -43.2	-22.8	*-3*	-14.9	*-7*
Cloud diurnal cycle														
AQUA cloud field	-4.8	*+15*	3.5 to -12.9	-7.1	*-2*	-3.6	*+41*	-18.9	*+2*	-7.3 to -42.6	-23.2	*-1*	-16.7	*+5*
Vertical structure														
Aerosol and cloud land profile	-6.5	*+57*	-2.1 to -14.0	-7.2	*0*	-6.2	*+143*	-18.6	*<1*	-6.4 to -43.6	-23.4	*0*	-16.0	< 1
Aerosol and cloud oceanic profile	-3.2	*-24*	11.4 to -12.4	-4.4	*-40*	-2.5	*0*	-18.5	*<1*	-6.7 to -43.5	-23.2	*-1*	-16.0	*0*
Surface albedo														
AVHRR broadband surface albedo	-4.3	*+3*	8.1 to -12.9	-7.5	*+4*	-2.6	*+1*	-18.6	*<1*	-6.7 to -44.4	-23.6	*+1*	-16.0	< 1
MODIS spectral surface albedo	-4.5	*+9*	8.1 to -13.8	-8.2	*+14*	-2.6	*+1*	-18.8	*+1*	-6.7 to -45.0	-24.1	*+3*	-6.0	< 1
MODIS VIS and NIR albedo	-4.6	*+10*	8.1 to -14.2	-8.4	*+16*	-2.6	*+1*	-18.9	*+2*	-6.7 to -45.6	-24.3	*+4*	-16.0	< 1

Table 5.4: *Surface and top of atmosphere direct radiative effect [Wm^{-2}] for the series of model runs described in the text. Averaged regional (ΔF_{reg}), land (ΔF_{land}), and oceanic (ΔF_{sea}) values for September are presented. The percentage change from the base case ($\delta_{reg/land/sea}$) and the range in the regional average (Range$_{reg}$) are also shown.* [a] *base case uses GCM OC+BC aerosol optical depth distribution x 4.4, fresh aerosol properties (ω_0=0.84) where TRMM fire counts> 500, aged aerosol (ω_0=0.89) everywhere else, MODIS spatial distribution of water cloud optical depth, effective radius and cloud fraction, MODIS broadband surface albedo, cloud and aerosol vertical profile measured onboard the C-130 aircraft over land and ocean.*

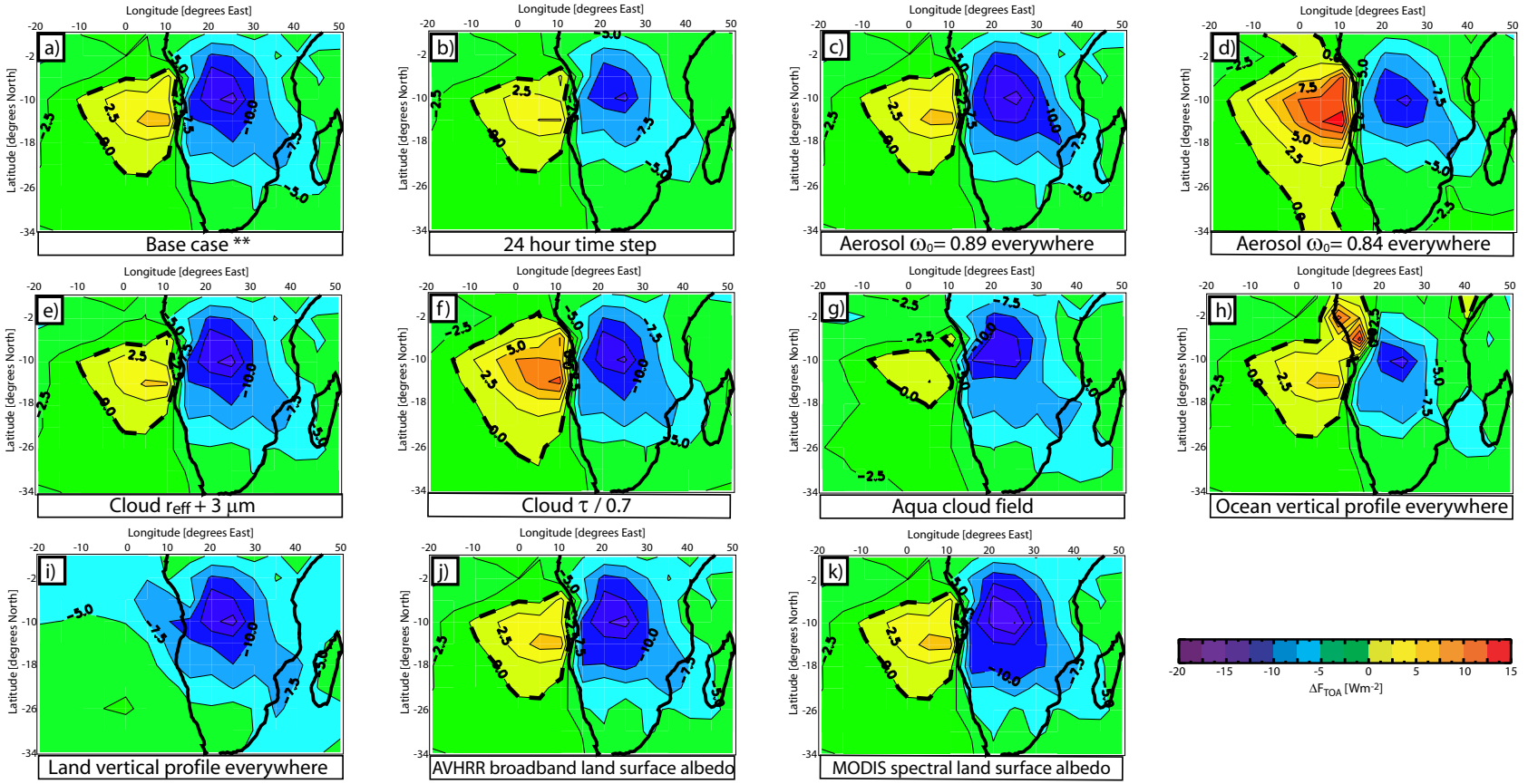

Figure 5.12: *The direct radiative forcing at the top of atmosphere (TOA) for a series of model runs using the spatial distribution of biomass burning aerosol derived from the MODIS satellite whilst perturbing other model inputs. Indicated in the individual panels are the run numbers described in the text and in table 5.3.*

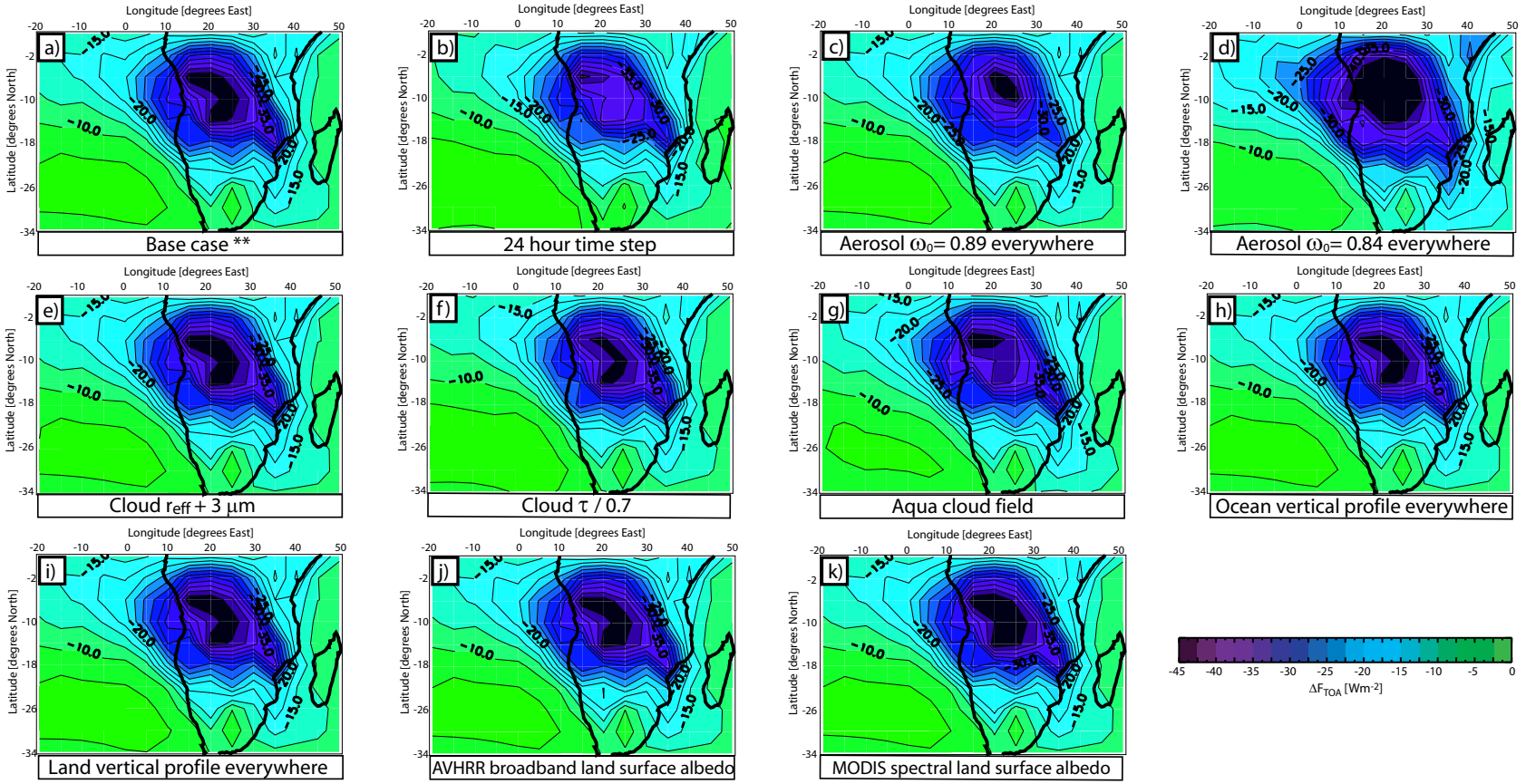

Figure 5.13: *The direct radiative forcing at the surface for a series of model runs using the spatial distribution of biomass burning aerosol derived from the MODIS satellite whilst perturbing other model inputs. Indicated in the individual panels are the run numbers described in the text and in table 5.3.*

5.4 Summary and discussion

In this study a multi-column radiation code is used to model the direct radiative effect of biomass burning aerosols over the southern African region during September (peak of burning season). The input parameters included in the model are constrained by a variety of measurements, and the effect of perturbing these determined in order to quantify the most important parameters that more detailed GCMs need to capture in order to accurately assess the direct aerosol effect.

The spatial distribution of biomass burning aerosols were estimated from the GCM model results of Tegen *et al.* (1997) and from a four year data set of observations from the MODIS satellite. The GCM distribution was found to severely under estimate the column integrated aerosol optical depth when compared to ground based and satellite observations, especially in the dry burning season. Correction factors were derived to compensate for the low bias in the model data and back-out the biomass smoke component. A recent inter-comparison highlighted that there were significant differences in the aerosol mass and τ distribution produced by seven current global aerosol models, with the largest discrepancies found in regions dominated by biomass burning or dust aerosols (Kinne *et al.*, 2003). This highlights the fact that quantification of the spatial distribution of aerosol by type is highly uncertain and leads to large difficulties in constraining the magnitude of any aerosol effect on climate when using aerosol models in GCMs. By placing constraints on the spatial distribution of aerosol included in the modelling work in this study that are based on observations, the aerosol distribution is likely to be less uncertain than in previous GCM studies of the radiative impact of biomass burning aerosols (e.g. Penner *et al.* (1998), Myhre *et al.* (2003)).

The base case model runs included both the satellite and model estimated horizontal distributions of biomass smoke for September. Fresh aerosol optical properties were included in regions of persistent burning and aged aerosol properties elsewhere. The water cloud fraction, optical depth, and droplet effective radius were taken from a four year average from the MODIS Terra satellite. The vertical structure of aerosol and cloud was taken from the C-130 aircraft measurements during SAFARI 2000, with the aerosol existing in an elevated polluted layer above low level cloud over oceanic regions, and the cloud layer at the top of the biomass smoke over land regions. A single broadband surface albedo (0.3 - 5 μm)

derived from MODIS was included over land, and a wavelength independent value of 4% over ocean. The SZA dependence of surface albedo was neglected. A monthly time-step was set in the model runs, thus a monthly mean SZA and insolation at the TOA was calculated for each model grid-box and the radiation code called once. The effect of the day to day variation in SZA and insolation (30 calls to the radiation code) was found to result in negligible changes ($< 1\%$) in the radiative forcing, whilst the impact of accounting for the daily variation in SZA (24 calls to the radiation code) resulted in a reduction in the radiative impact of the smoke by 14% at the TOA and 9% at the surface.

The base case modelled regional average clear-sky ΔF_{TOA} ranged from -9.0 to -10.8 Wm^{-2}, and the $\Delta F_{surface}$ from -20.5 to -24.3 Wm^{-2} with the two aerosol distributions. A stronger radiative impact of the biomass burning aerosol was evident over the oceanic regions, particularly off the eastern coast of Africa using the GCM distribution, as it contained higher aerosol loadings than the MODIS distribution. Over land, the results from the MODIS and GCM runs were in excellent agreement. The ocean only average ΔF_{TOA} ranged from -8.5 to -11.3 Wm^{-2}, and the $\Delta F_{surface}$ from -16.9 to -22.6 Wm^{-2}, which compares favourably with the results of Ichoku *et al.* (2003) (ΔF_{TOA}=-10 Wm^{-2}, $\Delta F_{surface}$=-26 Wm^{-2}), who use the MODIS aerosol optical depth data for September 2000 to determine the clear-sky forcing due to southern African biomass smoke over the Atlantic Ocean.

The inclusion of clouds in the model reduced the radiative impact of the biomass smoke by a factor of 2.5 at the TOA, resulting in an average regional ΔF_{TOA} of -3.5 to -4.2 Wm^{-2} for the MODIS and GCM derived aerosol fields. This is significantly larger than the modelled results from the Oslo GCM (Myhre *et al.*, 2003) for September 2000 (ΔF_{TOA}=-1.7 Wm^{-2}) and is likely dominated by differences in the column burden of aerosol used in the two studies. Whereas the work in this study uses satellite and ground based observations to constrain the aerosol distribution, the Oslo GCM results rely on output from a chemical transport model (CTM) with prescribed emissions and driven by meteorological data to transport the biomass smoke from source regions. Myhre *et al.* (2003) compare the CTM data to that at AERONET stations and from the C-130 aircraft, and find that whilst the pattern of the day to day variability observed at the AERONET sites is fairly well reproduced, there are significant under estimations in the magnitude of the aerosol optical depth. This would lead to a low estimation in the radiative impact of the biomass smoke.

The base case model runs also showed an average whole-sky $\Delta F_{surface}$ of -15.7 to -18.6 Wm^{-2} across the region depending on the aerosol distribution used, with values reaching -55 Wm^{-2} with the MODIS 1x1° degree aerosol data. This strong reduction in the surface solar radiation during the dry season must be compensated by a decrease in either the surface to atmosphere latent heat fluxes due to evaporation or to the sensible heat fluxes (Ramanathan *et al.*, 2001a). A significant reduction in the latent heat flux may occur over the oceanic regions, perhaps resulting in a decrease in precipitation and a general weakening of the hydrological cycle over the southern African region. Due to the dry conditions over land in September the reduction in solar radiation is more likely to be compensated by changes in the sensible heat flux. The absorption by the aerosol layer will also act to stabilise the boundary layer, perhaps suppressing convective activity and altering the local circulation patterns. The inclusion of realistic aerosol and cloud fields as used in this study into more detailed GCMs would be needed to ascertain if these processes are likely to occur, and if so, assess the subsequent effect on regional climate.

By perturbing the model inputs from the base case it was found that models can adequately represent the radiative forcing of biomass burning aerosols on a regional scale by including the optical properties of smoke in the aged regional haze. The added complexity of including fresh smoke properties at regions where biomass burning is prevalent resulted in small differences of 3 to 5$\%$ in the regional averaged ΔF_{TOA}. This is because the evolution of the optical properties with age are likely to occur on time-scales of $<$ day (see chapter 2) and so the inclusion of fresh smoke in the modelling work in this study covered $< 10\%$ of the surface area in the southern African region. However, if models use aerosol properties measured near source regions and prescribe them to every model grid-box, the error in the ΔF_{TOA} becomes large. For example, the work in this study found a 46 to 50$\%$ weakening in the magnitude of the regional ΔF_{TOA} when compared to the base case with the inclusion of the fresh aerosol everywhere. The strength of this weakening increased to $\backsim 100\%$ when considering only the ocean, where fresh aerosol is unlikely to be found in significant quantities.

It has also been shown that an underestimation in τ_{cloud} of 30$\%$ and in the r_e of 3μm leads to errors in the regional averaged ΔF_{TOA} as large as -24$\%$ and +4$\%$ respectively. The effect is stronger over the oceanic regions (-60$\%$ and +10$\%$ respectively) where the amount

of cloud is much greater than over land during the dry season. The potential low bias in the MODIS retrieval of τ_{cloud} due to the presence of overlying biomass burning aerosols could lead to a significant overestimation of the direct effect over southern Africa in this study. It also shows that cloud amount needs to be well represented in GCMs when assessing the direct aerosol effect.

The effect of the diurnal cycle of cloud on the radiative forcing was examined by replacing the MODIS Terra (morning overpass) with the MODIS Aqua (afternoon overpass) cloud fields. The Namibian cloud sheet decreased in optical thickness and amount during the day due to solar heating. This decreased the extent of the positive area of ΔF_{TOA} (net warming of the atmosphere) over the Atlantic Ocean, resulting in a change in the sea averaged ΔF_{TOA} of $\backsim 42\%$. The radiative impact of the biomass smoke over land was only slightly reduced (-2$\%$) as a result of the increase in cloud amount at the top of the aerosol layer. The net effect was to strengthen the average ΔF_{TOA} across the region by 13 to 15$\%$. To constrain the direct aerosol effect in GCMs the cloud diurnal cycle must be well represented, particularly in regions where partially absorbing aerosol overlies cloud.

The ΔF_{TOA} was found to be extremely sensitive to whether the oceanic (aerosol above cloud) or land (aerosol in and below cloud) was prescribed to the whole region, with differences from the base case ranging from -45 $\%$ over land to +160 $\%$ over the sea. It is interesting to note that the only way the modelling work in this study could obtain a spatial distribution of negative radiative forcing similar to the GCM calculations of Penner *et al.* (1998) (see figure 1.4), Grant *et al.* (1999), and Iacobellis *et al.* (1999) over the whole southern African region was in the model run with an unrealistic vertical structure of aerosol and cloud over oceanic regions. This highlights the importance of accurately representing both aerosol and cloud fields in models when assessing the magnitude and sign of the direct aerosol effect at the TOA.

Current methods to measure the vertical structure of aerosols rely on in-situ and remotely sensed aircraft or ground based instrumentation. The spatial distribution of such measurements is therefore poor. Future spaceborne instruments such as the Cloud-Aerosol Lidar and Infrared Pathfinder Satellite Observations (CALIPSO) instrument will play an important role in assessing the vertical structure of aerosols on much greater spatial and temporal scales than is possible with current methods (Winker *et al.*, 2003), allowing the possibil-

ity of comparisons and improvements to the vertical profile in global aerosol models to be made.

Both the AVHRR and MODIS broadband retrievals of surface albedo were included in the model. The difference between the two retrieval algorithms and the time periods where the measurements were taken resulted in a small difference of 4% in the land averaged ΔF_{TOA}. Changes to the $\Delta F_{surface}$ were 1%. Application of a more detailed spectral albedo from the MODIS data strengthened the land averaged TOA radiative effect of the biomass burning aerosols by 13 to 14% due to the high spectral dependence of the optical properties of the biomass burning aerosol. This shows that the wavelength dependence of surface albedo plays an important role in determining the radiative impact of aerosols. It was found that the inclusion of a visible and near infra-red (NIR) broadband albedo resulted in small differences of $<3\%$ in the ΔF_{TOA} compare to using a more detailed spectrally varying albedo (220 bands), suggesting that the simple inclusion of a visible and NIR broadband albedo in GCMs will improve the assessment of any direct aerosol radiative effect when compared to using a single broadband albedo.

An important conclusion from this work is that in order to address the current uncertainties in the radiative impact of aerosols, future modelling studies should make a concerted effort to constrain the model inputs by detailed in-situ and remotely sensed observations. In particular, the important parameters that need to be modelled well in GCMs in order to accurately simulate the direct aerosol effect of biomass smoke over southern Africa region are prioritised as follows:

i) Accurate representation of the horizontal distribution of biomass smoke.

ii) Aerosol and cloud vertical structure, especially in the area of the Namibian cloud sheet.

iii) Absorption properties of the aerosol. The use of aged aerosol optical properties is sufficient.

iv) Well simulated cloud fields, including cloud optical properties and diurnal cycle.

v) Spectral dependence of land surface albedo. Incorporating a visible and NIR band is sufficient.

Chapter 6

Conclusions

6.1 Overview

Aerosols are believed to offset the enhanced anthropogenic greenhouse warming through the direct scattering and absorption of solar radiation, in which biomass burning aerosols are thought to play a major role (IPCC, 2001). Estimates of the direct radiative effect of biomass burning aerosols and their resulting impacts on the climate system are primarily drawn from studies that utilise GCMs and/or CTMs. Large uncertainties in the model simulations exist due to a poor knowledge of the emission sources, transport processes, and the spatial and temporal distribution of the burden and optical properties of the smoke.

The primary goal of this thesis was to advance the understanding of the direct radiative effect of southern African biomass burning aerosols. To achieve this aim, the microphysical and optical properties of fresh and aged biomass smoke were characterised from detailed in-situ aircraft measurements taken during the SAFARI 2000 field campaign. Radiative closure studies were then performed to determine the optical depth and to assess the direct radiative effect of the biomass smoke on local scales under clear sky conditions. The direct radiative effect of biomass burning aerosols above cloud was then explored, with an emphasis on the impact that the aerosol has on satellite retrievals of cloud optical properties. Finally, through a combination of observations and modelling, the regional direct radiative effect of the smoke is determined and the sensitivity to the model inputs investigated.

6.2 Conclusions and suggestions for future research

This thesis presents the first temporal measurements of changes in the single scattering albedo within a fresh smoke plume as the aerosol is advected away from the fire. A rapid increase in the single scattering albedo from 0.84 to 0.88 was observed in the first few hours subsequent to emission, indicating that the aerosol is becoming less absorbing with age in the atmosphere. The rapid change suggests that measurements of the optical properties of biomass smoke taken near emission sources are of limited use when assessing the large-scale radiative effects of biomass smoke. It is inferred from the optical measurements that the increase in the single scattering albedo is likely to be dominated by the condensation of volatile species from the gaseous phase, and that changes in the aerosol size distribution and the morphology of black carbon are of secondary importance. Future sampling over and downwind of biomass fires that utilise aerosol mass spectrometers will be able to detect changes in the amount of volatile organic and inorganic material within fresh smoke plumes and therefore test this hypothesis, something that is not possible with current filter based methods. Measuring black carbon mass in-situ would also be advantageous, and the development of instruments for this purpose should be the focus of future research. Further, observations in smoke plumes that cover a wide range of source characteristics, such as fuel type, fire intensity, and combustion phase should be performed to determine whether the results presented in this thesis are representative of the large number of fires that occur in southern Africa on an annual basis.

Measurements in the regional haze show that a single scattering albedo of 0.89 was typical for the aged smoke, in agreement with other studies (Haywood *et al.*, 2003a, Magi *et al.*, 2003). The aerosol size distribution showed a shift to larger particle sizes in the accumulation mode when compared to the fresh smoke, suggesting that particle growth due to coagulation is significant once the plume has dispersed into the background haze. Characterising the aging processes of biomass burning aerosols from fresh smoke plumes to the background haze should be a focus of further research in order to improve the representation of the transport of biomass burning aerosols away from source regions in CTMs. The size distribution and optical properties of the coarse mode particles in the biomass smoke were not well constrained due to the poor performance of the FFSSP instrument, the uncertainty in the refractive index and density of the particles, and the potential effects

of non-spherical aerosols. Although the coarse particles are relatively inactive in an optical sense in comparison to the accumulation mode particles, the large amount of mass that resides in the larger particles means that future observations should aim to accurately measure the coarse fraction for validation of the spatial and temporal distribution of aerosol mass produced by CTMs.

A comparison of the various methods that have been used in several field campaigns to determine the aerosol optical depth in clear skies from onboard the C-130 aircraft was performed. The techniques ranged from the integration of the in-situ measurements of the aerosol extinction in vertical profiles to sophisticated radiative transfer modelling of the measured spectral radiances. There was reasonable consistency between the different methods once the sources of error and the spatial variability of the aerosol burden were considered, with a mean optical depth of 0.41 for the biomass smoke. The effects of aircraft shadow contamination, the under-sampling of the PCASP instrument in profile ascents, and the possible coating of the BBRs with biomass smoke were identified as sources that can produce erroneous results. The shape of the measured sky-radiance distribution below the biomass plume was well simulated with the inclusion of the observed biomass and sea salt aerosols, lending a degree of confidence to the in-situ aerosol optical and microphysical measurements. The retrieval algorithm of Dubovik *et al.* (2000), developed to determine the columnar optical properties and size distribution from the global network of AERONET Sun-sky scanning photometer measurements of the down-welling spectral radiance, was shown to be in reasonable agreement with the aircraft data. Future measurement campaigns should aim at measuring the spectral sky-radiance distribution as this is thought to be the most accurate method in determining the optical depth, and continue to validate the AERONET retrieval under a variety of atmospheric conditions and aerosol types.

The biomass burning aerosol was observed to be typically well mixed in the continental boundary layer over land regions. As it is advected off the Namibian and Angolan coast, the polluted haze tended to exist in an elevated layer that was separated by a clean air slot from the MBL, which was often capped by a stratocumulus cloud deck. Temperature inversions associated with the clean air slot are likely to inhibit aerosol-cloud interactions, thereby minimising any aerosol indirect effects. The presence of the partially absorbing biomass smoke above low-level stratocumulus clouds leads to a reduction in the outgoing

flux at the TOA through the direct absorption of solar radiation. This is not accounted for in the current operational AVHRR and MODIS satellite retrievals of cloud optical depth and effective radius, that employ a look-up table approach whereby modelled cloud parameters are fitted to give agreement with the measured radiation. The theoretical calculations of Haywood *et al.* (2004) simulate the effect of the biomass smoke on the satellite retrievals, and predict a low bias in the cloud effective radius retrieval that uses the 1.63 μm waveband. The MODIS pixel level cloud product was examined in this thesis for six cases from SAFARI 2000, and a modal bias in the cloud effective radius retrieval using the 1.63 μm waveband of up to -2.78 μm was evident. Further, spatial distributions of the low bias in cloud effective radius appear to be correlated with the spatial distribution of biomass smoke as identified with the TOMS AI. Similar biases in cloud optical properties may be apparent in other regions of the world where partially absorbing aerosol layers exist above low-level clouds. This effect should be borne in mind when attempting to evaluate the indirect aerosol effect from satellite based remote sensing.

Calculations of the regional direct radiative effect of southern African biomass smoke during September were performed with a multi-column radiation code. The monthly mean radiative forcing at the TOA ranged from -3.5 to -4.2 Wm^{-2}, and at the surface from -15.7 to -18.6 Wm^{-2} for the burden of smoke derived from the MODIS satellite and from the corrected GCM results of Tegen *et al.* (1997) respectively. This translates to a monthly average absorption of solar radiation in the intervening atmosphere of 12.1 to 14.4 Wm^{-2}. The strong reduction in the solar irradiance at the surface may be compensated by a spin down of the hydrological cycle, and the perturbation to the atmospheric heating rate through the direct scattering and absorption of solar radiation could alter the atmospheric circulation patterns (Ramanathan *et al.*, 2001a) and cloud amount (Johnson *et al.*, 2004). The work in this thesis could be extended to explore these aspects by including realistic burdens, vertical profiles, and optical properties of biomass smoke into a more complex GCM.

Experiments were performed to test the sensitivity of the radiative forcing to changes in the model inputs, with the aim of determining the most important parameters that need to be constrained by future observations and included in GCMs. As a result of the rapid evolution in the aerosol optical properties downwind from the emission sources, it was found that models can adequately simulate the regional mean direct radiative effect of the

biomass smoke when the optical properties of aged aerosols are prescribed throughout the southern African region, whereas model simulations that included the optical properties of fresh smoke everywhere resulted in an underestimation in the TOA radiative forcing of up to 50%. Therefore, measurements of biomass smoke taken at source should not be used exclusively when determining the net regional or global scale direct radiative effect.

The role of the land surface characteristics were examined by including the AVHRR and MODIS satellite retrievals of land surface albedo into the model at various spectral resolutions. The wavelength dependence of the surface reflectance was shown to play an important role in simulating the direct aerosol effect, and that the inclusion of a visible and near infrared broadband albedo improved the representation of the surface when compared to including a single broadband retrieval. Future measurement campaigns should therefore examine the spectral dependency of surface albedo in order to both validate satellite based retrievals and to provide constraints for local column radiative closure studies.

An example of in-situ aircraft measurements of surface albedo that can be made for this purpose is given in figure 6.1. Figure 6.1 (a) shows the broadband surface albedo derived from the measured up and down welling BBR irradiances from low-level runs made in the vicinity of the large anthropogenic biomass burning episode studied in chapter 2. An increase in the surface albedo from approximately 10 to 20 % is evident as the aircraft flew from an area containing a burn scar into an area that had not been affected by biomass burning. The gradual interchange between the two in the measurements is due to the wide field of view of the BBR instruments. In reality, the transition between the non-burned and burned area is immediate as shown by the sharp change in the spectral dependency of the up-welling radiances between the two land surface types in figure 6.1 (b). The reduction in the magnitude of the albedo and the change in the spectral shape of the reflectance in the burned region provides an opportunity for the validation of current satellite based retrievals.

The vertical structure of biomass burning aerosols and clouds was critical in determining the sign of the radiative forcing at the TOA. Using realistic vertical profiles, sharp contrasts between regions of strong positive and negative radiative forcing were apparent. A large region of positive radiative forcing over the southern Atlantic Ocean was calculated in this work where the biomass smoke is advected above low level clouds, which is in contrast with the previous GCM studies that were considered by IPCC (2001), indicating that the

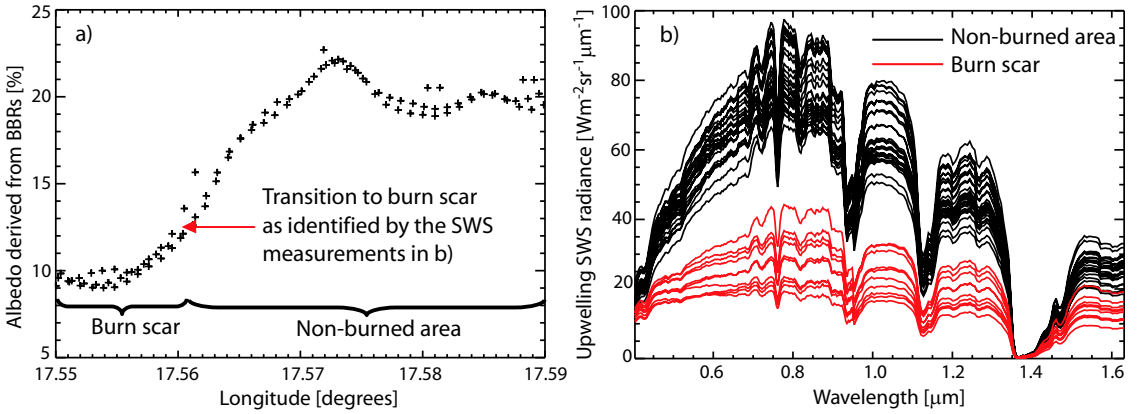

Figure 6.1: *a) Land surface albedo derived from the ratio of the up and down-welling irradiance (0.3-3.0 μm) measured onboard the C-130 aircraft during flight a790. The area containing the burn scar (as identified from the SWS measurements and the lower albedo) is indicated. b) An example of the up-welling SWS radiances measured over the burned and non-burned areas.*

vertical structure and/or cloud fields were not simulated well in those models. Unfortunately, current measurements of the vertical structure of aerosols and clouds are limited to aircraft and ground based measurements, and are therefore both spatially and temporally data sparse. As a result, it is often difficult to validate vertical profiles generated by global aerosol models. With the advent of spaceborne lidars such as the CALIPSO satellite, due to launch in 2005, vertical distributions of tropospheric aerosols and clouds will be characterised on a global scale, providing a means of improving model simulations.

The degree of positive radiative forcing at the TOA over the Atlantic Ocean was shown to be sensitive to the diurnal cycle of clouds, which therefore needs to be well represented in GCMs when assessing the direct effect, particularly in regions where partially absorbing aerosols exist in elevated layers. The recent measurements from the polar orbiting MODIS Aqua satellite (afternoon overpass) will complement the data from the MODIS Terra satellite (morning overpass) in building up a global picture of the diurnal cycle of clouds, albeit are limited to two measurements over an individual scene each day. Data from geostationary satellites, such as Meteosat 7, can provide high temporal information of clouds that are likely to be more useful in validating the diurnal cycle in GCMs (e.g. Slingo *et al.* (2004)).

Assimilation of satellite based aerosol products into models is now coming to the fore, and has been shown to improve the representation of aerosol optical depth in current models (Collins *et al.*, 2001). As data assimilation techniques become more advanced, and future

satellites observe the atmosphere in more detail, the technique could be used to improve the representations of the burden, vertical distribution, and optical properties of aerosols and clouds in both climate simulations and numerical weather prediction models, thereby reducing many of the large uncertainties in the radiative effects of aerosols and the resulting changes in the meteorology and climate. However, the potential uncertainties in spaceborne retrievals of atmospheric constituents must be borne in mind. For example, the potential low bias in cloud optical depth retrievals from the MODIS satellite due to the 'missing aerosol effect' (Haywood *et al.*, 2004) is shown to lead to an overestimation of the radiative forcing at the TOA in the model calculations presented in this thesis. Detailed in-situ aircraft and ground based measurements are therefore required to validate the operational satellite based retrievals under a wide range of atmospheric conditions.

6.3 Final summary

This thesis represents a comprehensive investigation into the direct interaction of biomass burning aerosols with solar radiation in the southern African region, and shows that the smoke can exert a significant positive or negative TOA radiative forcing on the climate system depending on the local meteorology, and a large reduction in the solar irradiance at the surface under present day conditions. With an increase in the population and industrialisation of developing countries in the tropics, where biomass burning is common, predicting future trends in anthropogenic burning activities is problematic. Furthermore, if global temperatures continue to rise and longer or more frequent droughts occur, the number of natural fires is likely to increase. Therefore, identifying long term patterns in the distribution of emissions, atmospheric burden, and optical properties of biomass burning aerosols is critical in the assessment of any future climatic response to biomass smoke. The advances in ground based, in-situ, and spaceborne measurements of atmospheric constituents that have occured in the past decade and in future years will enable the direct and indirect aerosol effects of biomass smoke to be determined with a greater degree of confidence, and any long term trends to be identified. The potential to improve weather forecasting through the integration of these observations into numerical weather prediction models should be studied, particularly in regions such as southern Africa where the impact of biomass burn-

ing aerosols leads to significant changes in the tropospheric and surface energy budgets, and may therefore influence the hydrological cycle and atmospheric circulation patterns.

Appendix A

C-130 instrumentation

A.1 Instruments

A list of the relevant instrumentation used in this thesis is given in table A.1. Also included is the variable measured, range, and accuracy of each of the instruments.

Aerosol particles were sized in 15 bins covering the range 0.1 to 3.0 μm diameter with a Passive Cavity Aerosol Spectrometer Probe 100X (PCASP). In addition, a Fast Forward Scattering Spectrometer Probe (FFSSP) sized aerosol and/or cloud particles with diameters ranging from 2 to 47 μm. A TSI 3563 integrating nephelometer was used to measure the aerosol scattering coefficient at three wavelengths (0.45, 0.55, and 0.70 μm), and a Particle Soot Absorption Photometer 100X (PSAP) to measure the aerosol absorption coefficient at a wavelength of 0.567 μm. An overview of the assumptions and standard corrctions applied to the PCASP, FFSSP, nephelometer, and PSAP data in this thesis are given in section A.2.

The C-130 aircraft was fitted with several instruments to measure the radiative influence of the biomass smoke. Upward and downward mounted clear domed Eppley broadband radiometers (BBRs) measured the hemispherical irradiances in the solar spectrum (0.3 - 3.0 μm). Down-welling radiances at wavelengths of 0.55, 0.62, 0.87, 1.04, 1.25, 1.61, and 2.01 μm were measured with the Scanning Airborne Filter Radiometer (SAFIRE) instrument, which was mounted on the top of the aircraft and fixed in a zenith viewing mode. The up-welling radiances were measured with the Short Wave Spectrometer (SWS) instrument

Instrument	Variable measured	Range	Accuracy
GPS receiver	Latitude and longitude	global	± 50m
Radar altimeter	Altitude	0-1525 m	±3%
Internal navigation unit (INU)	Aircraft pitch	0-90°	0.07° r.m.s.
Pilot static system, INU, gust probes, and GPS	Wind speed and direction		±0.5 ms^{-1}
Rosemount 1201F variable capacitance	Static pressure	1030-100 mb	±3 mb
Rosemount 102BL platinum resistance	Temperature	-80 to +40°C	±0.3°C
Thermoelectric hygrometer	Dew point temperature	-60 to +50°C	±0.25°C >0°C ±1.0°C <0°C
TECO 49 UV photometric	Ozone concentration	0-1000 ppbv	±2 ppbv
Passive Cavity Aerosol Spectrometer Probe (PCASP)	Aerosol size distribution	0.05-1.5 μm radius	Size calibration for spherical latex particles [a]
Fast Forward Scattering Spectrometer Probe (FFSSP)	Aerosol size distribution	1-23.5 μm radius	Size calibration for spherical glass beads [a]
TS3I 3563 nephelometer	Aerosol scattering	λ=0.45,0.55,0.70 μm	±10%
Particle Soot Absorption Photometer (PSAP)	Aerosol absorption	λ=0.567 μm	±10%
Broad Band Radiometer (BBR); clear dome	Solar irradiance	λ=0.3-3.0 μm	±2 Wm^{-2} for diffuse ±3 Wm^{-2} for direct
Short Wave Spectrometer (SWS)	Radiance	λ=0.3-1.7 μm	Resolution: 0.010 (λ=0.3-0.95μm) and 0.018 (λ=0.95-1.7μm) Absolute accuracy: ± 4 $Wm^2sr^{-1}\mu m^{-1}$ [b]
Scanning Airborne Filter Radiometer (SAFIRE)	Radiance	λ=0.55,0.62,0.87,1.04, 1.25,1.61,2.01 μm	±5-8 % [c]

Table A.1: *A summary of the instrumentation installed on the Met Office C-130 aircraft during SAFARI 2000 that is used in this thesis. The accuracy of the instrumentation is taken from Anderson (1997), except for;* [a] *see appendix A.2 for details,* [b] *J. Haywood, personal communication (2004), and* [c] *Francis* et al. *(1999).*

with a spectral resolution of approximately 0.010 μm in the spectral range 0.30-0.95 μm, and of 0.018 μm in the range 0.95-1.70 μm (Haywood *et al.*, 2003a). The SWS was located beneath the aircraft and was fixed in a nadir view (half angle = 0.75°).

A.2 Standard corrections and uncertainties

An outline of the standard corrections applied to the aerosol size distribution and optical properties measured during SAFARI 2000 is presented. A discussion of the uncertainties in the measurements is also given.

Passive Cavity Aerosol Spectrometer Probe 100X (PCASP)

The PCASP measures the aerosol size distribution in 15 bins over the size range 0.05 to 1.5μm radius, by illuminating aerosol particles with a helium-neon laser. The aerosols act to scatter the incident radiation, which is detected by a photodetector module over scattering angles of 35 to 120°. The fraction of scattered radiation is dependent on the particle size, refractive index, and morphology, through the Mie scattering phase function. The PCASP is calibrated using spherical latex particles ($n = 1.585 - 0i$) of known sizes. Therefore, any departure in the refractive index or shape of the biomass smoke particles will result in a misclassification of particle size.

Uncertainty in the refractive index, n; The response of the PCASP instrument to biomass burning aerosols with refractive indices representative of fresh (n=1.54-0.025i, Abel *et al.* (2003)) and aged (n=1.54-0.018i, Haywood *et al.* (2003a)) smoke were determined with Mie theory. Table A.2 shows that the fractional error in the sizing of particles is as large as 77% for bin 15 with a refractive index representative of fresh smoke. However, Haywood *et al.* (2003a) show that >90% of particle scattering and absorption of biomass smoke occurs for particles sizes in the PCASP bins 4 to 10. In bins 4 to 10 the fractional error in the particle sizing is 5-10% for aged biomass burning aerosols and 6-14% for fresh biomass smoke. Errors in sizing through the refractive index will therefore not significantly affect the derived single scattering albedo or asymmetry parameter.

A correction can be made to the measured PCASP size distributions using the calculated

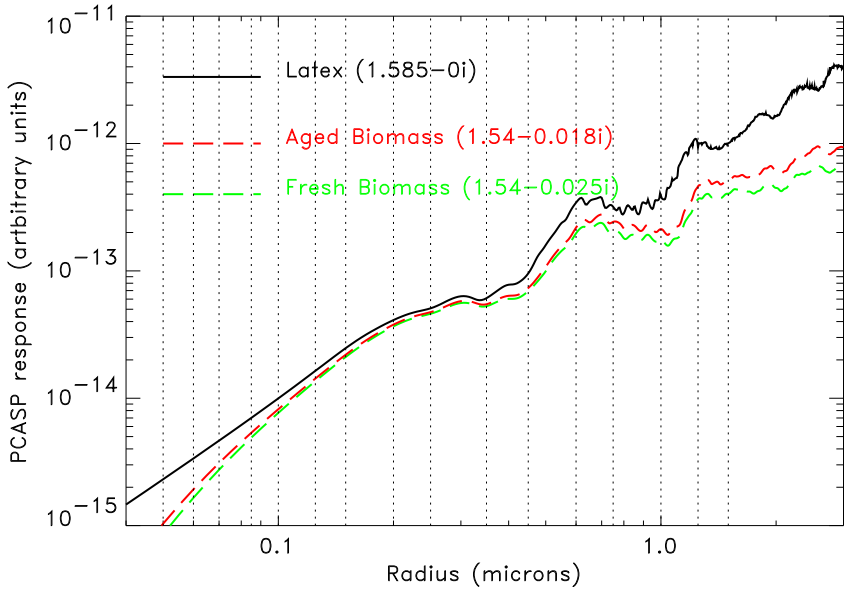

Figure A.1: *The PCASP-100X response to calibration latex spheres and to aged and fresh biomass burning aerosols at a wavelength of 0.635μm.*

Mie phase function shown in figure A.1. It should be noted that the refractive index used for biomass burning aerosols in this study is primarily constrained by obtaining agreement between the independent PSAP and nephelometer measurements of aerosols scattering and absorption with those determined from Mie theory, using the measured size distribution. The refractive index is therefore representative of the most optically active particles in bins 4-10, where the error in sizing is small. As such, no correction for refractive index is made in the work in this thesis.

Uncertainty in the morphology of particles: A departure from spherical particles will lead to errors in the sizing of particles. It is difficult to quantify the magnitude of this effect as a knowledge of the distribution of particle shapes is required, and the relevant effective phase function modelled. However, the majority of particles over the PCASP size range in biomass smoke are spherical (Haywood *et al.*, 2003a) and the effect is neglected in this thesis.

Evaporation of volatile compounds in the PCASP; On sampling the aerosol, volatile compounds may be evaporated due to drying processes within the instrument, leading to an underestimate in the size of particles. The internal de-icing heaters in the probe were turned off throughout the SAFARI 2000 campaign to minimise this effect.

PCASP bin number	Midpoint $(n = 1.585 - 0i)$ μm	Midpoint $(n = 1.54 - 0.018i)$ μm	$r_{aerosol}/r_{latex}$	Midpoint $(n = 1.54 - 0.025i)$ μm	$r_{aerosol}/r_{latex}$
1	0.0550	0.0674	0.81	0.0705	0.78
2	0.0650	0.0763	0.85	0.0791	0.85
3	0.0775	0.0874	0.89	0.0900	0.86
4	0.0925	0.1011	0.91	0.1036	0.89
5	0.1125	0.1202	0.94	0.1227	0.94
6	0.1375	0.1454	0.95	0.1480	0.93
7	0.1750	0.1855	0.94	0.1897	0.92
8	0.2250	0.2397	0.94	0.2454	0.92
9	0.3000	0.3235	0.93	0.3471	0.86
10	0.4000	0.4327	0.92	0.4583	0.87
11	0.5250	0.8370	0.63	0.8629	0.61
12	0.6750	1.1794	0.57	1.2244	0.55
13	0.8750	1.1927	0.73	1.2587	0.70
14	1.1250	1.8784	0.60	2.7133	0.41
15	1.3750	2.8425	0.48	4.1690	0.33

Table A.2: *The midpoint radius of the PCASP bins when calibrated with spherical latex spheres ($n = 1.585 - 0i$) and that computed using Mie scattering theory for aged biomass smoke ($n = 1.54 - 0.018i$) and fresh biomass smoke ($n = 1.54 - 0.025i$). Also shown is the fractional error $r_{aerosol}/r_{latex}$ in the sizing of the smoke particles.*

Fast Forward Scattering Spectrometer Probe (FFSSP)

The FFSSP measures the aerosol (and cloud droplet) size distribution in 15 bins over the size range 0.1 to 23.5μm radius, by illuminating aerosol particles with a focussed helium-neon laser. The amount of forward scattered light (scattering angle $\backsim$ 4 to 15°) is measured. The FFSSP is calibrated using glass beads of known sizes and refractive indices. The refractive index of the glass beads is similar to that of water. Similar uncertainties with those from the PCASP measurements arise from differences between the measured aerosol particles and the calibration spheres.

The FFSSP instrument was unable to measure the size distribution of aerosol particles with sufficient accuracy in biomass smoke during SAFARI 2000. This may be the result of non-sphericity effects and/or dissimilar refractive indices in the coarse particles compared to the calibration beads. Low laser power and hardware rejection from the instrument may have also contributed. Determination of the optical properties of the biomass burning aerosols from the measured size distribution and Mie scattering theory in this thesis do not use the FFSSP data.

Nephelometer scattering

The TSI 3563 integrating nephelometer measures the the aerosol scattering coefficient, σ_{sca} (m^{-1}), at wavelengths of 0.45, 0.55, and 0.70μm. The aerosol inlet and plumbing on the C-130 aircraft led to a very low efficiency of super micron aerosols being sampled. The corrections of Haywood and Osborne (2000) which are based on those of Anderson and Ogren (1998) for sub-micron particles are therefore used in this thesis.

Correction for the missed forward scattering (C_{ts}); The nephelometer does not measure radiation scattered at angles $<7^{\circ}$ and a correction to total scattering needs to be applied. The correction factor, C_{ts}, is linearly related to the $\dot{A}$ngstrom coefficient, $\dot{A}(\lambda_1/\lambda_2)$, given by

$$\dot{A}(\lambda_1/\lambda_2) = -\frac{log(\sigma_{sca}^{\lambda_1}/\sigma_{sca}^{\lambda_2})}{log(\lambda_1/\lambda_2)}. \tag{A.1}$$

$\dot{A}(\lambda_1/\lambda_2)$ is determined using λ_1=0.45μm and λ_2=0.70μm for λ=0.55μm; λ_1=0.45μm and λ_2=0.55μm for λ=0.45μm; λ_1=0.55μm and λ_2=0.70μm for λ=0.70μm. The correction factor is then calculated with the equation

$$C_{ts}^{\lambda} = -0.044\dot{A} + 1.152, \tag{A.2}$$

and typically increases the scattering coefficient by 5 to 40$\%$ depending on the value of $\dot{A}(\lambda_1/\lambda_2)$.

Correction to standard temperature and pressure; The nephelometer is calibrated to STP. To account for variations in both T and P the following equation is used,

$$\sigma_{scacorr}^{\lambda} = C_{ts}^{\lambda}\sigma_{sca}^{\lambda}\left(\frac{T}{273.2}\frac{1013.2}{P}\right), \tag{A.3}$$

where $\sigma_{scacorr}$ is the measured scattering coefficient corrected for both forward scattering and STP.

Correction for relative humidity; On sampling the aerosol, the nephelometer dries the aerosol to a degree. A growth factor needs to be applied to correct the scattering to the ambient RH. No such correction is made in this thesis when calculating the optical properties of biomass smoke because growth factors measured during SAFARI 2000 show that the effect is negligible (Magi and Hobbs, 2003).

PSAP absorption

The Radiance Research Particle Soot Absorption Photometer (PSAP) instrument measures the aerosol absorption coefficient, σ_{abs} (m^{-1}), at a wavelength of $0.567\mu m$. The instrument works by monitoring changes in the transmittance across a loaded filter, and can be calculated using the equation

$$\sigma_{abs} = \frac{A}{V} ln \left(\frac{I_0}{I} \right), \tag{A.4}$$

where A is the spot size on the filter, V is the volume of air drawn through the filter in an integration time period ($\backsim$ 30 seconds), and I_0 and I are the average filter transmittances in the current and previous time period respectively. The suggested corrections of Haywood and Osborne (2000) are applied to the data used in this thesis, and take the form of:

$$\sigma_{abscorr} = \frac{C_{ss} C_{flow} \sigma_{abs} - K_1 \sigma_{sca}}{K_2}, \tag{A.5}$$

where $\sigma_{abscorr}$ is the corrected absorption, σ_{sca} is the measured nephelometer scattering coefficient at λ=0.55μm, and C_{ss}, C_{flow}, K_1, and K_2 are correction factors outlined below.

Corrections for variations in spot size (C_{ss}); The reported spot size diameter from the manufacturer, A is 4.765 mm, whereas that measured on typical PSAP instruments, A_{meas}, is closer to 5.2 mm. Correcting σ_{abs} for the difference in the spot area $(A/A_{meas})^2$ gives C_{ss} = 0.84 $\pm$ 0.02.

Corrections for flow rate (C_{flow}); The flow rate measured by the PSAP installed on the C-130 underestimates V when compared with that measured with a more accurate bubble flow meter by $\backsim 19\%$, resulting in the correction C_{flow} = 1.19 $\pm$ 0.03.

Correction due to misinterpreted absorption (K_1); An artifact absorption is measured by the PSAP because transmission through the filter is reduced due to particle scattering. The measurements of Bond *et al.* (1999) found that $\backsim 2\%$ of scattering was interpreted as absorption, leading to a value of K_1 = 0.02 $\pm$ 0.02.

Correction due to multiple scattering (K_2); If the aerosol particles have a chance to absorb a photon on multiple occasions, the absorption inferred with the PSAP will be enhanced. Laboratory measurements of Bond *et al.* (1999) suggest that the absorption is overestimated by 22 $\pm$ 20 $\%$ for atmospheric aerosols after the above corrections have been made, such that K_2 = 1.22 $\pm$ 0.20.

The corrections outlined above suggest that the PSAP overestimates the aerosol absorption by $\backsim 20\%$.

Appendix B

AERONET climatology data

AERONET station	Jan	Feb	Mar	Apr	May	Jun	Jul	Aug	Sep	Oct	Nov	Dec
Ascension Island	0.17	0.19	0.15	0.12	0.10	0.12	0.21	0.24	0.18	0.12	0.10	0.11
Bethlehem	0.11	0.08	0.07	0.06	0.04	0.06	0.10	0.18	0.18	0.26	0.07	0.09
Etosha Pan	0.11	0.10	0.10	0.07	0.07	0.06		0.19	0.33	0.41	0.07	0.08
Inhaca	0.15	0.25	0.07	0.13	0.17	0.18	0.14	0.35	0.35	0.39	0.21	0.16
Joberg		0.20	0.17						0.27	0.26		
Kaloma						0.09	0.16	0.56				
Kaoma								0.22	0.87			
Kasama					0.04	0.15	0.21	0.25				
Maun Tower									0.35	0.50		
Mfuwe						0.08	0.13	0.25	0.48	0.29	0.31	0.31
Mongu	0.12	0.12	0.09	0.07	0.10	0.15	0.17	0.29	0.54	0.43	0.25	0.13
Mwinilumga								0.62	0.95			
Ndola								0.37	0.67			
Senanga						0.11	0.22	0.31	0.65	0.39	0.21	0.08
Sesheke						0.14		0.35	0.40	0.47		
Skukuza	0.12	0.14	0.10	0.20	0.12	0.15	0.13	0.26	0.35	0.31	0.20	0.18
Skukuza Aeroport									0.20	0.55		
Solwezi								0.52	0.85			
Sua Pan								0.17	0.56			
Swakopmund									0.13			
Witts University	0.16	0.19			0.12	0.10	0.10	0.41	0.19		0.13	
Zambezi						0.15	0.40	0.47	0.65	0.35	0.33	0.34

Table B.1: *Level 2.0 monthly mean aerosol optical depth for southern African AERONET sites interpolated to 0.55μm using a quadratic fit of the form $y=a+bx+cx^2+dx^3$ to measurements at λ=0.34,0.38,0.44,0.50,0.67,0.87, and 1.02μm. The monthly mean is calculated from daily mean values where at least three observations were made. The observation period of the data ranges from June 1995 - September 2003, and the observation statistics for the individual sites are given in table B.2.*

AERONET	Jan		Feb		Mar		Apr		May		Jun		Jul		Aug		Sep		Oct		Nov		Dec		**Year**	
station	N	M	N	M	N	M	N	M	N	M	N	M	N	M	N	M	N	M	N	M	N	M	N	M	**N**	**M**
Ascension Island	89	4	89	5	88	5	85	4	77	3	55	3	39	2	41	2	35	2	32	3	72	4	76	4	**778**	**41**
Bethlehem	27	1	20	1	14	1	22	2	36	2	28	1	28	1	15	1	25	1	29	1	18	1	26	1	**288**	**14**
Etosha Pan	29	1	17	1	28	1	21	1	31	1	6	1			23	1	28	1	31	1	29	1	26	1	**269**	**11**
Inhaca	1	1	1	1	1	1	24	1	43	2	25	1	23	1	41	2	43	2	20	1	23	2	4	1	**249**	**16**
Joberg			10	1	14	1											19	1	10	1					**53**	**4**
Kaloma											17	1	6	1	8	1									**31**	**3**
Kaoma															6	1	7	1							**13**	**2**
Kasama									8	1	27	1	26	1	24	1									**85**	**4**
Maun Tower																	17	1	6	1					**23**	**2**
Mfuwe											10	1	25	1	31	1	27	1	9	1	6	1	9	1	**117**	**7**
Mongu	60	4	62	4	61	4	98	4	114	4	143	7	197	8	216	8	197	8	185	8	121	8	85	5	**1539**	**72**
Mwinilumga															21	1	20	1							**41**	**2**
Ndola															26	1	20	1							**46**	**2**
Senanga											16	1	6	1	29	3	49	3	14	2	9	1	7	1	**130**	**12**
Sesheke											14	1			4	1	16	1	6	1					**40**	**4**
Skukuza	72	4	49	4	54	4	37	2	59	3	85	3	77	4	105	4	80	4	69	4	53	4	65	4	**805**	**44**
Skukuza Aeroport																	12	1	2	1					**14**	**2**
Solwezi															18	1	21	1							**39**	**2**
Sua Pan															9	1	4	1							**13**	**2**
Swakopmund																	7	1							**7**	**1**
Witts University	3	1	10	1					5	1	11	1	2	1	1	1	2	1			19	1			**53**	**8**
Zambezi											8	1	6	1	67	3	77	3	48	2	17	2	1	1	**224**	**13**
Total	**281**	**16**	**258**	**18**	**260**	**17**	**287**	**14**	**373**	**17**	**445**	**23**	**435**	**22**	**685**	**34**	**706**	**36**	**461**	**27**	**367**	**25**	**299**	**19**	**4857**	**268**

Table B.2: *Summary of the number of days (N) and months (M) in the observation period June 1995 - September 2003 where the aerosol τ was measured at the AERONET stations in southern Africa. Only days where at least three individual measurements are available are included.*

Appendix C

Geophysical Research Letters Paper

GEOPHYSICAL RESEARCH LETTERS, VOL. 30, NO. 15, 1783, doi:10.1029/2003GL017342, 2003

Evolution of biomass burning aerosol properties from an agricultural fire in southern Africa

Steven J. Abel
Department of Meteorology, University of Reading, UK

Jim M. Haywood
Met Office, UK

Eleanor J. Highwood
Department of Meteorology, University of Reading, UK

Jia Li
Department of Chemistry and Biochemistry, Arizona State University, USA

Peter R. Buseck
Department of Geological Sciences, Arizona State University, USA
Department of Chemistry and Biochemistry, Arizona State University, USA

Received 17 March 2003; revised 23 May 2003; accepted 1 July 2003; published 1 August 2003.

[1] Measurements on the UK Met Office C-130 within a distinct biomass burning plume during the Southern AFricAn Regional science Initiative (SAFARI 2000) show an increase in the single scattering albedo as the aerosol ages, from 0.84 at source to 0.90 in the aged regional haze in 5 hours. Condensation of scattering material from the gas phase appears to be the dominant mechanism; the change in black carbon morphology, from a chain to clump like structure, does not significantly affect the bulk aerosol single scattering albedo. *INDEX TERMS:* 0305 Atmospheric Composition and Structure: Aerosols and particles (0345, 4801); 0315 Atmospheric Composition and Structure: Biosphere/atmosphere interactions; 0345 Atmospheric Composition and Structure: Pollution—urban and regional (0305); 3359 Meteorology and Atmospheric Dynamics: Radiative processes; 9305 Information Related to Geographic Region: Africa. **Citation:** Abel, S. J., J. M. Haywood, E. J. Highwood, J. Li, and P. R. Buseck, Evolution of biomass burning aerosol properties from an agricultural fire in southern Africa, *Geophys. Res. Lett.*, *30*(15), 1783, doi:10.1029/2003GL017342, 2003.

1. Introduction

[2] Biomass burning aerosol has a large, but poorly quantified radiative effect on climate. The uncertainty in this effect is the result of temporal and spatial variability of the smoke, along with uncertainties in the optical properties of the aerosol itself [*IPCC*, 2001]. *Reid et al.* [1998] found that the aerosol from biomass burning emitted at source had a significantly lower single scattering albedo than the aerosol within the aged regional haze. Quantifying this change in aerosol properties with age is vital if we are to model the climatic effect accurately. This is the first study to analyze measurements of the temporal evolution of biomass burning aerosol single scattering albedo as the smoke is advected downwind from the source.

0094-8276/03/2003GL017342$05.00

2. Instrumentation and Flight Pattern

[3] This study focuses on measurements made by the U.K. Met Office C-130 aircraft during the Southern AFricAn Regional science Initiative (SAFARI 2000) campaign on 13 September 2000 at Otavi in Namibia (flight a790). Sampling was performed over and progressively downwind of a large anthropogenic biomass burning event on agricultural land. The burning had also spread to the surrounding hillsides. The fire consisted of both agricultural and savanna/scrubland fuel sources, with flaming and smoldering combustion occurring.

[4] The C-130 was fitted with the instrumentation detailed in *Haywood et al.* [2003a]. In brief, a Passive Cavity Aerosol Spectrometer Probe (PCASP) was used to measure the aerosol particle distribution from 0.05–1.5 μm radius. A TSI 3563 nephelometer was used to measure the aerosol scattering at 0.45, 0.55, and 0.70 μm. A Radiance Research Particle Soot Absorption Photometer (PSAP) was used to measure the aerosol absorption at 0.567 μm.

[5] The flight consisted of a series of straight and level runs over the source at altitudes ranging from 210–1,233 m above ground level (AGL). This series was followed by a raster pattern of cross plume transits at 1,233 m (standard deviation = 17 m) AGL to 73 km downwind as shown in Figure 1, as is the aerosol number concentration measured with the PCASP. Concentrations up to 100,000 cm^{-3} were observed over the source region, marked with a cross. The two peaks in aerosol number concentration on each side of the cross indicate the areas of most intense burning. The number concentration is shown to spread out and decrease in magnitude as the plume becomes more dilute downwind.

3. Results

3.1. PSAP and Nephelometer Measurements

[6] The single scattering albedo at a wavelength of 0.55 μm, ($\omega_{0\lambda=0.55\ \mu m}$), was calculated along each cross plume transit where the nephelometer scattering coefficient,

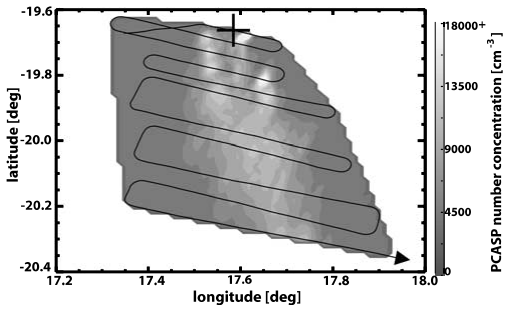

Figure 1. Flight track over and downwind of the fire at Otavi. Measured PCASP number concentration (cm^{-3}) is shown. Source region is marked with a cross.

$\sigma_{s\lambda=0.55\ \mu m}$, exceeded 1×10^{-4} m^{-1}. This limit was the typical background value outside of the influence of the plume, and sharp peaks above this were evident when the aircraft entered the plume itself. The mean atmospheric relative humidity (RH) within the plume where $\omega_{0\lambda=0.55\ \mu m}$ is calculated was 22.1% (standard deviation = 0.7%). The effect of an increase in particle scattering from the nephelometer measurements due to water uptake on the aerosol is negligible as at this low RH [*Magi and Hobbs*, 2003]. The $\omega_{0\lambda=0.55\ \mu m}$ calculation at the source combines measurements from four straight and level runs at various altitudes over the fire (765, 914, 1,057, 1,233 m AGL). Figure 2 shows the evolution of aerosol co-albedo, $(1-\omega_{0\lambda=0.55\ \mu m})$, as the plume moves downwind. The mean and the standard deviation for each cross plume transit are shown. The time subsequent to emission is determined from the measured wind velocity and the aircraft Global Positioning System (GPS). The co-albedo decreases from 0.16 at source to 0.12 two and a half hours downwind, indicating that the aerosol is becoming less absorbing/more scattering as it ages. The standard deviation about the mean is greatest at the source due to the large variability in the smoke plume directly above the fire. *Haywood et al.* [2003a] show that the mean co-albedo of the aged regional haze measured throughout the campaign is 0.10, which suggests that the aerosol measured downwind has not yet fully evolved. An exponential fit suggests it would take approximately 5 hours from emission for the aerosol co-albedo to decrease to 0.10, which is typical of aged regional haze.

3.2. Model Simulations

[7] The observed change in aerosol optical properties subsequent to emission may be the result of changes in the aerosol size distribution, black carbon morphology, chemical composition and the mixing state of the aerosol. These mechanisms are investigated further in 3.2.1 and 3.2.2.

3.2.1. Changes in the Aerosol Size Distribution

[8] $\omega_{0\lambda=0.55\ \mu m}$ was also calculated using the mean PCASP size distributions along each cross plume transit combined with Mie scattering calculations. A refractive index of 1.54−0.018 *i* is used. This is the campaign mean refractive index for the aged regional haze [*Haywood et al.*, 2003a] and is in excellent agreement with AERONET retrieved values on the same day at Etosha Pan [*Haywood et al.*, 2003b]. Etosha Pan is approximately 220 km West from the Otavi fire. The PCASP derived values of co-albedo in Figure 2 are lower than those derived using the PSAP and nephelometer measurements, especially at the source of the aerosol. There is little variation in the modeled co-albedo as the aerosol ages, with a mean value of 0.12 and standard deviation of 0.004. This constancy implies that the aged aerosol effective refractive index is not representative of the refractive index within the plume. Increasing the imaginary part of the refractive index to 0.025 *i* increases the co-albedo at source to 0.16, which is consistent with the independent PSAP and nephelometer result. This result suggests that in this case, it is more important to constrain changes in the effective refractive index than the variation in the size distribution when determining $\omega_{0\lambda=0.55\ \mu m}$ within the plume. However, the Mie scattering calculations assume that the aerosol particles are spherical. *Martins et al.* [1998b] suggest that only smoke particles residing in the atmosphere for more than 1 hour have collapsed sufficiently to be considered spherical. Further investigation into the effect of the variation in particle morphology with age on the aerosol optical properties is made in 3.2.2.

3.2.2. Changes in the Mixing State of the Aerosol and Black Carbon Morphology

[9] Fresh biomass burning aerosol exists as an external mixture in the plume, consisting of quasi-spherical scattering components (organic and inorganic matter) and chain aggregates of black carbon (BC) [*Pósfai et al.*, 2003; *Li et al.*, 2003]. Post combustion BC exists in open chain-like structures of individual spherules. Figure 3 shows a transmission electron microscopy (TEM) image of BC collected in a biomass burning plume by the University of Washington's (UW) CV-580 aircraft in the Timbavati Game Reserve during SAFARI 2000 at a distance between 8–37 km downwind. The exact age of the soot chains are

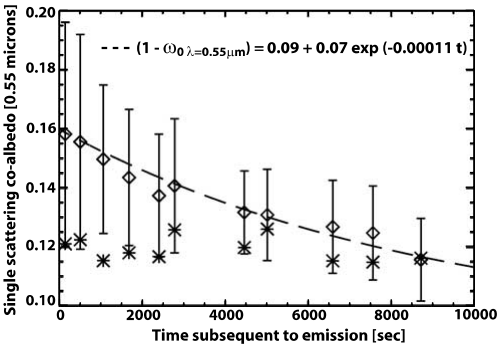

Figure 2. Evolution of the aerosol co-albedo downwind of the fire. Diamonds represent the mean value for each cross plume transit measured with the PSAP and nephelometer. Error bars are the standard deviation from this mean. Values using the PCASP size distribution for each transit and Mie calculations (n = 1.54 − 0.018i) are shown with an asterisk. The exponential fit suggests that it will take 5 hours for the co-albedo to reach 0.10, which is representative of the aged regional haze.

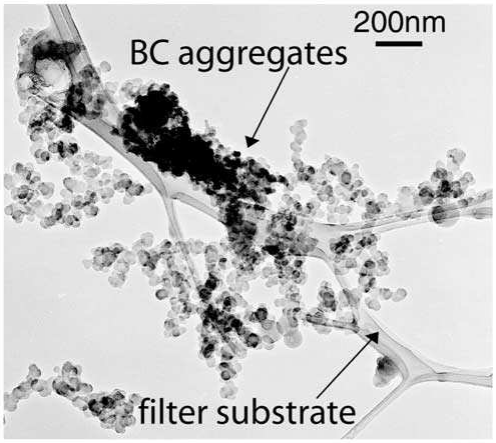

Figure 3. TEM image of BC aggregates in the Timbavati Game Reserve. The age is estimated to be between 12 and 55 minutes subsequent to emission.

difficult to determine owing to the flight pattern performed but the aerosol is estimated to be between 12 and 55 minutes old. As the aerosol ages the chain-like aggregates collapse into densely packed soot clusters [*Martins et al.*, 1998a; *Johnson et al.*, 1991], and the individual components of biomass burning aerosol become internally mixed [*Pósfai et al.*, 2003]. The mass of BC to total aerosol (M_{BC}/M_{tot}) required to match the measurements of the aerosol co-albedo at source and in the aged regional haze was modeled.

[10] The aerosol emitted at source was modeled using an external mixture of the highly absorbing BC with the primarily scattering components. The BC was modeled with the Mie code of *Mishchenko and Travis* [1998], which determines the scattering properties of non-overlapping clusters of spheres. Individual BC spherules were assumed to have a radius of 0.0118 μm and a refractive index of 1.75−0.44 *i* [*WCP*, 1986]. Aggregates consisting of 65 individual BC spheres, with shapes ranging from the chain-like structure associated with fresh aerosol, to the more densely packed clusters associated with the regional haze, were randomly oriented with respect to the incident radiation and their scattering properties modeled. Figure 4 shows the modeled co-albedo at 0.55 μm decreases as the chain-like structure collapses, with a value of 0.97 for the open chain and 0.90 for the packed cluster. This decrease is primarily the result of the particle scattering increasing as the chain collapses. The co-albedo values are much higher than the measurements because only the highly absorbing BC component of the aerosol is modeled. The BC structures in Figure 4 were externally mixed with the scattering component. The scattering component was modeled using Mie calculations with a bi-modal log normal fit to the PCASP size distribution measured in the fresh aerosol and a refractive index of 1.53−0.00 *i* [*Haywood et al.*, 2003a], which results in a $\omega_{0\lambda=0.55\mu m}$ of 1.0. The co-albedo of the composite external mixture of scattering and absorbing aerosol was found to be relatively insensitive to the BC shape (varied by <0.01 with a constant M_{BC}/M_{tot}). Therefore, the changing morphology is unlikely to explain the measured variation in the co-albedo between the fresh and aged aerosol. A M_{BC}/M_{tot} of approximately 12% is required to match the measured co-albedo of 0.16 at source.

[11] The Maxwell-Garnet mixing rule was used to model the M_{BC}/M_{tot} in aged regional haze ($n = 1.54 - 0.018\ i$). The rule adequately represents the internal mixing of BC spheres coated with scattering material, typical of particle structures observed in an aged regional haze in Brazil [*Martins et al.*, 1998a]. The absorbing component was assumed to be BC, with a refractive index of 1.75−0.44 *i* at 0.55 μm [*WCP*, 1986] and a density of 1.7 g cm^{-3} [*Haywood et al.*, 2003a]. The scattering component was assumed to have a refractive index of 1.53−0.00 *i* at 0.55 μm [*Haywood et al.*, 2003a]. By constraining the composite aerosol to have a density of 1.35 g cm^{-3} [*Reid and Hobbs*, 1998], the M_{BC}/M_{tot} is 5.4% for the aged regional haze, which is consistent with measurements using filter mass loadings collected onboard the C-130 aircraft from aged regional haze [*Haywood et al.*, 2003a].

4. Discussion and Conclusions

[12] Airborne measurements over and downwind of an agricultural fire show an increase in $\omega_{0\lambda=0.55\mu m}$ from 0.84 at source to 0.90 in the aged regional haze in 5 hours. *Reid et al.* [1998] find a similar increase of 0.06 in $\omega_{0\lambda=0.55\ \mu m}$ with age from measurements in fresh aerosol and aged regional haze in Brazil. This increase has fundamental implications for climate modeling and could be combined with modeling efforts to better constrain the radiative effect of biomass burning aerosol on regional/global scales. However, the results presented use observations from a single biomass burning fire that may not be representative of the very large number of fires annually in southern Africa.

[13] An attempt was made to obtain closure between the measured $\omega_{0\lambda=0.55\ \mu m}$ and Mie calculations using the varying PCASP size distribution downwind with the fixed refractive index of aged regional haze. The changing size distribution alone cannot account for the increase in $\omega_{0\lambda=0.55\mu m}$. Increasing the imaginary part of the refractive index at the source is required to get consistency. This suggests that it is more important to constrain changes in the effective

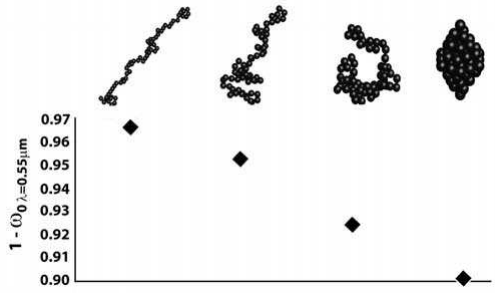

Figure 4. Co-albedo for a variety of BC aggregates, each containing 65 individual spherules.

refractive index than the variation of the size distribution within the plume.

[14] Model results suggest that for $\omega_{0\lambda=0.55\mu m}$ to be consistent with observations the M_{BC}/M_{tot} decreases from approximately 12% at source to 5.4% in the aged haze. The effect of BC morphology on the bulk aerosol absorption is found to be of secondary importance. Therefore, the change in $\omega_{0\lambda=0.55\mu m}$ is likely the result of an increase in the amount of scattering material as the aerosol ages. *Hobbs et al.* [2003] find that subsequent to removing the effect of plume dilution from a separate fire in southern Africa, the number of particles began to increase 10 minutes after emission. This production of new particles can occur by organic carbon (OC) condensing from the gas phase. TEM derived number concentrations of different particle types within a plume during SAFARI 2000 indicate a large increase in the number of tar balls (primarily OC) as the aerosol ages [*Pósfai et al.*, 2003]. *Reid et al.* [1998] observe an increase of 20–45% in aerosol mass concentration from fresh to aged biomass burning aerosol and estimate that between 50–75% of this increase is the result of condensation of volatile organics. However, thermal optical transmission measurements from quartz filters collected onboard the C-130 suggest that the mass of elemental carbon to OC (M_{EC}/M_{OC}) is smaller for fresh aerosol [*Formenti et al.*, 2003], but uncertain due to poor sampling statistics. *Kirchstetter et al.* [2003] also find an increase in M_{BC}/M_{OC} with age but attribute this increase to the biomass burning aerosol mixing with air masses that are characterized by a higher M_{BC}/M_{OC} ratio (e.g., fossil fuel burning). The time scale for this large-scale mixing is likely to be significantly larger than measured/modeled here. Furthermore our model simulations assume that BC is the only significant absorbing component, whereas biomass burning aerosol is likely to contain amounts of absorbing colored organic matter [*Formenti et al.*, 2003]. The apparent discrepancy between our results and those from filter measurements may be elucidated in future measurement campaigns utilising aerosol mass spectrometers.

[15] **Acknowledgments.** We would like to thank the MRF aircrew and support staff for their efforts during SAFARI 2000. The TEM image was collected on board the UW CV-580 under the direction of Peter Hobbs. The ASU research was funded by a grant from the NASA Radiation Science Program and is part of the SAFARI 2000 Southern African Regional Science Initiative. S. Abel is funded by a NERC CASE studentship with the UK Met. Office.

References

Formenti, P., W. Elbert, W. Maenhaut, J. Haywood, S. Osborne, and M. O. Andreae, Inorganic and carbonaceous aerosols during Southern African Regional Science Initiative (SAFARI 2000) experiment: Chemical characteristics, physical properties, and emission data for smoke from African biomass burning, *J. Geophys. Res.*, *108*(D13), 8448, doi:10.1029/2002JD002408, 2003.

Haywood, J. M., S. R. Osborne, P. N. Francis, A. Keil, P. Formenti, M. O. Andreae, and P. H. Kaye, The mean physical and optical properties of regional haze dominated by biomass burning aerosol measured from the C-130 aircraft during SAFARI 2000, *J. Geophys. Res.*, *108*(D13), 8473, doi:10.1029/2002JD002226, 2003a.

Haywood, J. M., P. Francis, O. Dubovik, M. Glew, and B. Holben, Comparison of aerosol size distributions, radiative properties, and optical depths determined by aircraft observations and Sun photometers during SAFARI 2000, *J. Geophys. Res.*, *108*(D13), 8471, doi:10.1029/2002JD002250, 2003b.

Hobbs, P. V., S. Parikhit, R. J. Yokelson, T. J. Christian, D. R. Blake, S. Gao, T. W. Kirchstetter, T. Novakov, and P. Pilewskie, Evolution of gases and particles from a savanna fire in South Africa, *J. Geophys. Res.*, *108*(D13), 8485, doi:10.1029/2002JD002352, 2003.

IPCC (Intergovernmental Panel on Climate Change), *Climate Change 2001: The Scientific Basis*, edited by J. T. Houghton, Y. Ding, D. J. Griggs, M. Noguer, P. J. van der Linden, X. Dai, K. Maskell, and C. A. Johnson, Cambridge Univ. Press, Cambridge, United Kingdom and New York, NY, USA, 2001.

Johnson, D. W., C. G. Kilsby, D. S. McKenna, R. W. Saunders, G. J. Jenkins, F. B. Smith, and J. S. Foot, Airborne observations of the physical and chemical characteristics of the Kuwait oil smoke plume, *Nature*, *353*, 617–621, 1991.

Kirchstetter, T. W., T. Novakov, P. V. Hobbs, and B. Magi, Airborne measurements of carbonaceous aerosols in southern Africa during the dry biomass burning season, *J. Geophys. Res.*, *108*(D13), 8476, doi:10.1029/2002JD002171, 2003.

Li, J., M. Pósfai, P. V. Hobbs, and P. R. Buseck, Individual aerosol particles from biomass burning in southern Africa: 2. Compositions and aging of inorganic particles, *J. Geophys. Res.*, *108*(D13), 8484, doi:10.1029/2002JD002310, 2003.

Magi, B. I., and P. V. Hobbs, Effects of humidity on aerosols in southern Africa during the dry biomass burning season, *J. Geophys. Res.*, *108*(D13), 8495, doi:10.1029/2002JD002144, 2003.

Martins, J. V., P. Artaxo, C. Liousse, J. S. Reid, P. V. Hobbs, and Y. J. Kaufman, Effects of black carbon content, particle size, and mixing on light absorption by aerosols from biomass burning in Brazil, *J. Geophys. Res.*, *103*, 32,041–32,050, 1998a.

Martins, J. V., P. V. Hobbs, R. E. Weiss, and P. Artaxo, Sphericity and morphology of smoke particles from biomass burning in Brazil, *J. Geophys. Res.*, *103*, 32,051–32,057, 1998b.

Mishchenko, M. I., and L. D. Travis, Capabilities and limitations of a current Fortran implementation of the T-Matrix method for randomly oriented, rotationally symmetric scatterers, *J. Quant. Spectrosc. Radiat. Transfer*, *60*, 309–324, 1998.

Pósfai, M., R. Simonics, J. Li, P. V. Hobbs, and P. R. Buseck, Individual aerosol particles from biomass burning in southern Africa: 1. Compositions and size distributions of carbonaceous particles, *J. Geophys. Res.*, *108*(D13), 8483, doi:10.1029/2002JD002291, 2003.

Reid, J. S., and P. V. Hobbs, Physical and optical properties of young smoke from individual biomass fires in Brazil, *J. Geophys. Res.*, *103*, 32,013–32,030, 1998.

Reid, J. S., P. V. Hobbs, R. J. Ferek, D. R. Blake, J. V. Martins, M. R. Dunlap, and C. Liousse, Physical, chemical, and optical properties of regional hazes dominated by smoke in Brazil, *J. Geophys. Res.*, *103*, 32,059–32,080, 1998.

World Climate Program (WCP), A Preliminary Cloudless Standard Atmosphere for Radiation Computation, World Meteorol. Organ., Geneva, 1986.

S. J. Abel and E. J. Highwood, Department of Meteorology, The University of Reading, Reading, RG6 6BB, UK. (s.j.abel@reading.ac.uk)

J. M. Haywood, Met Office, Y46 Bldg, Cody Technology Park, Farnborough, Hants, GU14 OLX, UK.

P. R. Buseck and J. Li, Department of Chemistry and Biochemistry, Arizona State University, Tempe, AZ 85287-1604, USA.

Appendix D

Quarterly Journal of the Royal Meteorological Society Paper

Q. J. R. Meteorol. Soc. (2004), **130**, pp. 779–800 doi: 10.1256/qj.03.100

The effect of overlying absorbing aerosol layers on remote sensing retrievals of cloud effective radius and cloud optical depth

By JIM M. HAYWOOD[1]*, SIMON R. OSBORNE[1] and STEVEN J. ABEL[2]
[1]*Met Office, Exeter, UK*
[2]*Department of Meteorology, University of Reading, UK*

(Received 13 June 2003; revised 8 December 2003)

SUMMARY

Two types of partially absorbing aerosol are included in calculations that are based on intensive aircraft observations: biomass burning aerosol characterized during the Southern AFricAn Regional science Initiative (SAFARI 2000) and mineral dust aerosol characterized during the SaHAran Dust Experiment (SHADE). Measurements during SAFARI 2000 reveal that the biomass burning aerosol layer is advected over the South Atlantic ocean at elevated altitudes above the marine boundary layer which is capped by semi-permanent stratocumulus cloud sheets. Similarly, the mineral dust is measured at elevated altitudes during SHADE resulting in transport above cloud for distances of several thousands of kilometres. We perform theoretical calculations of the effect of these partially absorbing aerosol layers on satellite retrievals of cloud effective radius and cloud optical depth, and show that, in these cases, retrievals of cloud optical depth or liquid water path are likely to be subject to systematic low biases. The theoretical calculations suggest that the cloud effective radius may be subject to a significant low bias for Moderate resolution Imaging Spectrometer (MODIS) retrievals that rely on the 0.86 and 1.63 μm radiance pair for an overlying aerosol layer of either biomass burning aerosol or mineral dust. Conversely, the cloud effective radius may be subject to a significant high bias for Advanced Very High Resolution Radiometer or MODIS retrievals that rely on the 0.63 and 3.7 μm radiance pair for an overlying aerosol layer of mineral dust. Analysis of 1 km resolution MODIS data for the SAFARI 2000 period suggests that the effective radius derived from the 0.86 and 1.63 μm radiance pair is, indeed, subject to a low bias in the presence of overlying biomass burning aerosol. These results show the difficulties associated with remote sensing retrievals, which must be kept in mind when attempting to assess any potential indirect effect.

KEYWORDS: Biomass burning Indirect effects Microphysics Radiation

1. INTRODUCTION

Aerosols affect the radiative balance of the earth–atmosphere system via the direct effect whereby they scatter and absorb solar and terrestrial radiation, and via the indirect effect whereby they modify the microphysical properties of clouds thereby affecting their radiative properties and lifetimes. When a partially absorbing aerosol, such as biomass burning aerosol or mineral dust, exists over a dark/bright surface the direct radiative effect is negative/positive; i.e. the local planetary albedo is increased/decreased (e.g. Haywood and Boucher 2000; Keil and Haywood 2003, Hsu *et al*. 2003). Thus, the presence of a partially absorbing aerosol above bright underlying stratocumulus may reduce the spectral irradiances at the top of the atmosphere (TOA).

Retrievals of cloud effective radius, r_e, and optical depth, δ_{cloud}, from satellite instruments, such as the Advanced Very High Resolution Radiometer (AVHRR) or the Moderate resolution Imaging Spectrometer (MODIS), use the fact that upwelling radiances at wavelengths of less than $\sim$1 μm provide information primarily on δ_{cloud}, intermediate wavelengths around 1–2.5 μm provide information on both δ_{cloud} and r_e, while those at wavelengths greater than $\sim$2.5 μm provide information primarily on r_e (e.g. Han *et al*. 1994, 1998; King *et al*. 2003, Platnick *et al*. 2003). These retrievals use look-up tables built up from theoretical radiative transfer models including clouds for different solar zenith angles and viewing-geometry combinations. However, while these theoretical models include gaseous absorption and Rayleigh scattering, they do not include the scattering and absorption by aerosol, because the aerosol optical depth,

* Corresponding author: Observational Research, Met Office, FitzRoy Road, Exeter, Devon EX1 3PB, UK.
e-mail: jim.haywood@metoffice.com

δ_{aerosol}, the optical parameters and the vertical profile of the aerosol are all essentially unknown. In addition δ_{aerosol} is likely very much smaller than δ_{cloud}, and therefore it might be assumed that including aerosol should not significantly affect the radiances or the retrievals of δ_{cloud} or r_{e}.

We investigate two cases here: the case of a biomass burning aerosol layer overlying stratocumulus off the coast of Namibia/Angola during SAFARI 2000, and the case based on measurements made during the SaHAran Dust Experiment (SHADE) when mineral dust from a Saharan dust outbreak overlies low-level cloud. Both case-studies use *in situ* measurements of the aerosol physical and optical properties. Details of the optical properties of these aerosols are given in section 2, section 3 reports the typical vertical profiles of the aerosol layer and cloud during the measurement campaign, and section 4 provides details of the radiative transfer calculations. Section 5 analyses the theoretical results and section 6 uses MODIS level-2 data products (assigned as MOD06 products; Platnick *et al*. (2003)) to assess whether the theoretical biases are present in the MODIS data. Section 7 presents a discussion and conclusions.

2. Aerosol optical properties

The single scattering albedos, ω_{o}, at a wavelength, λ, of 0.55 μm for biomass burning aerosol and Saharan dust are both derived from *in situ* measurements of scattering measured by a TSI 3563 nephelometer and absorption measured by a Radiance Research Particle Soot Absorption Photometer. The wavelength-dependence of the optical parameters are obtained using log–normal fits to mean aerosol size distributions measured using a Passive Cavity Aerosol Spectrometer Probe (PCASP-100X) combined with suitable refractive indices and Mie scattering theory (Haywood *et al*. 2003a,b). The imaginary part of the refractive index at 0.55 μm is assumed to be 0.018i for biomass burning aerosol and 0.0015i for Saharan dust aerosol (Haywood *et al*. 2003a,b).

For biomass burning aerosol measured during the SAFARI 2000 campaign, three log–normal distributions are used to fit the size distribution representative of aged regional haze as in Haywood *et al*. (2003a). The campaign mean for aged regional haze suggest a $\omega_{\text{o}\lambda=0.55}$ of 0.91 ± 0.04, a specific extinction coefficient, $k_{\text{e}\lambda=0.55}$, of 5.0 m^2g^{-1} and an asymmetry factor, $g_{\lambda=0.55}$, of 0.59. We show the wavelength-dependence of these parameters in Fig. 1(a), and report the values of the optical parameters at specific AVHRR and MODIS wavelengths in Table 1. When optical parameters determined in this way are included in radiative transfer calculations, the modelled angular distribution of the sky radiance has been shown to be in excellent agreement with independent measurements (Haywood *et al*. 2003c) at wavelengths in the range 0.55–2.01 μm. This suggests that the optical parameters for biomass burning aerosol are sufficiently accurate in representing the transfer of atmospheric radiation.

For Saharan dust measured during the SHADE campaign, five log–normal distributions are used to fit the size distribution measured during the dust outbreak off the coast of Senegal on 25 September 2000 as in Haywood *et al*. (2003b). While the PCASP enables determination of the aerosol size distribution for particle radii <1.5 μm, there is a significant contribution to scattering and absorption at solar and near infrared wavelengths from super-micron particles. This necessitates the use of surface-based sunphotometers in determining the super-micron aerosol size distribution (Haywood *et al*. 2003b). Mineral dust may have a significant effect on radiation at terrestrial wavelengths >3 μm (Highwood *et al*. 2003), although there is considerable uncertainty in the real and imaginary refractive index at these wavelengths (Sokolik *et al*. 1998). Although Highwood *et al*. (2003) showed that the refractive indices of Fouquart *et al*. (1987)

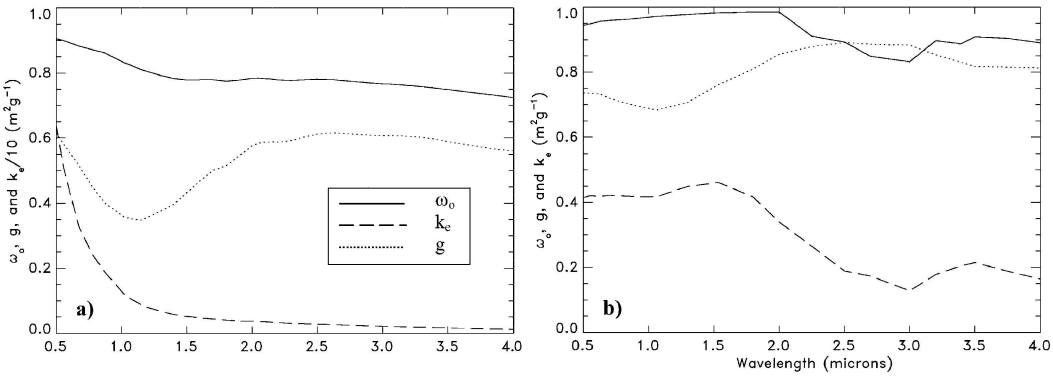

Figure 1. Graph showing the optical properties of: (a) the biomass burning aerosol, and (b) the Saharan dust aerosol used in the calculations. Here ω_o is the single scattering albedo; g is an asymmetry factor and k_e the specific extinction coefficient. In (a) k_e, has been divided by a factor of ten for ease of graphical representation.

TABLE 1. THE OPTICAL PARAMETERS FOR BIOMASS BURNING AEROSOL (BB), AND SAHARAN DUST AT WAVELENGTHS, λ, USED IN THE RADIATIVE TRANSFER CALCULATIONS

	$\lambda = 0.55$			$\lambda = 0.63$			$\lambda = 0.87$			$\lambda = 1.63$			$\lambda = 2.13$			$\lambda = 3.7$		
	ω_o	g	k_e	ω_o	g	k_e	ω_o	g	k_e	ω_o	g	k_e	ω_o	g	k_e	ω_o	g	k_e
BB	0.91	0.59	5.00	0.88	0.52	3.90	0.86	0.40	3.50	0.78	0.48	0.50	0.78	0.79	0.40	0.75	0.57	0.20
Dust	0.95	0.74	0.42	0.96	0.73	0.42	0.96	0.70	0.42	0.98	0.78	0.44	0.94	0.86	0.30	0.90	0.82	0.24

The specific extinction coefficient, k_e, is given in m^2g^{-1}. In the calculations, the aerosol optical depth, $\delta_{aerosol}$, is set to 0.5 at a wavelength of 0.55 μm; thus $\delta_{aerosol\lambda}$ can be approximated as $0.1k_{e\lambda}$ for biomass burning aerosol, and $1.2k_{e\lambda}$ for Saharan dust aerosol.

better represent the absorption and scattering of Saharan dust in the 8–12 μm atmospheric window; these refractive indices are only available for wavelengths >4.5 μm. Therefore the refractive indices of dust from WMO (1986) are assumed for radiative calculations performed at 3.7 μm. The modelled aerosol optical parameters suggest a $\omega_{o\lambda=0.55}$ of 0.95 ± 0.04, $k_{e\lambda=0.55}$ of 0.42 m^2g^{-1} and g_λ of 0.74 at $\lambda = 0.55$ μm. We show the wavelength dependence of these parameters in Fig. 1(b), and report the values of the optical parameters at specific AVHRR and MODIS wavelengths in Table 1. It is interesting to note that ω_o increases at wavelengths between 0.55 and 2.0 μm, reaching a value of 0.98 at 2.0 μm. Note here that spherical particles are assumed in determining the radiative properties and radiative effects; the effects of non-sphericity are beyond the scope of the present work.

For Saharan dust $\omega_{o\lambda=0.55}$ is greater than for biomass burning, indicating that Saharan dust is less absorbing because it does not contain black carbon which is the major absorbing component of atmospheric aerosol (e.g. Haywood and Boucher 2000). One of the most notable differences between Figs. 1(a) and (b) is that k_e is a strong function of wavelength for biomass burning aerosol (Fig. 1(a)), while for mineral dust it shows much less variation across the range of wavelengths (Fig. 1(b)). This difference is due to the fact that the Saharan dust size distribution contains proportionally more large particles, and this is important when interpreting the results presented in section 5.

3. VERTICAL DISTRIBUTION OF AEROSOLS AND CLOUDS

The Met Office C-130 aircraft flew a total of six dedicated flights off the coasts of Namibia and Angola during the SAFARI 2000 measurement campaign (flight numbers

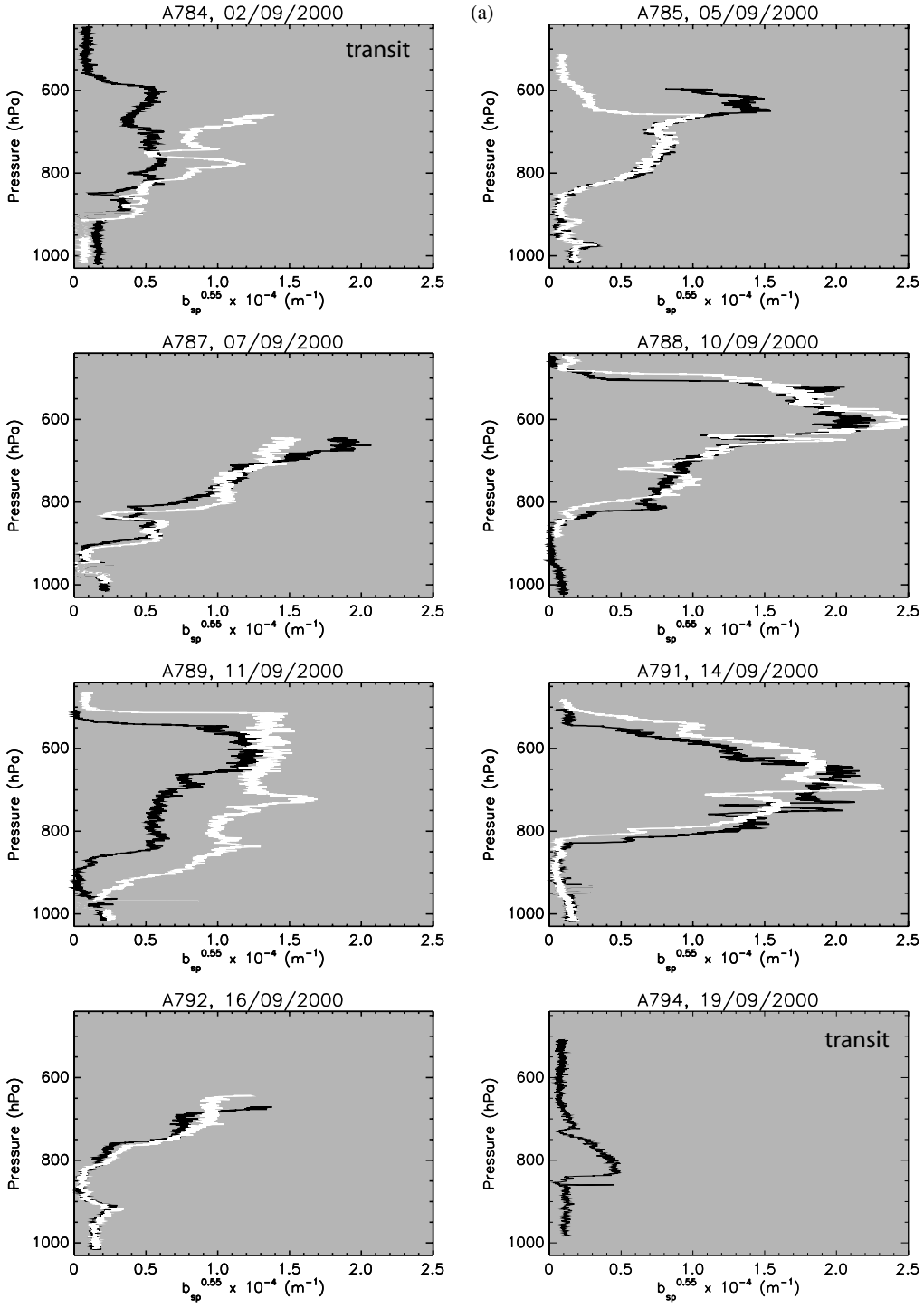

Figure 2. The aerosol scattering coefficient at 0.55 μm, $b_{sp}^{0.55}$, measured by the nephelometer on the C-130 aircraft. Each profile is shown by a separate colour, and in the interests of clarity a maximum of two profiles are shown for each flight. (a) Biomass burning aerosol measured during SAFARI 2000, for eight transit flights as indicated above each frame; (b) Saharan dust aerosol measured during SHADE for six flights. The absolute error in $b_{sp}^{0.55}$ is estimated as $\pm 0.3 \times 10^{-4}$ m^{-1} for biomass burning aerosol (Haywood and Osborne 2000), but $\pm 0.5 \times 10^{-4}$ m^{-1} for Saharan dust owing to super-micron sampling losses (Haywood *et al*. 2003c). See text for details.

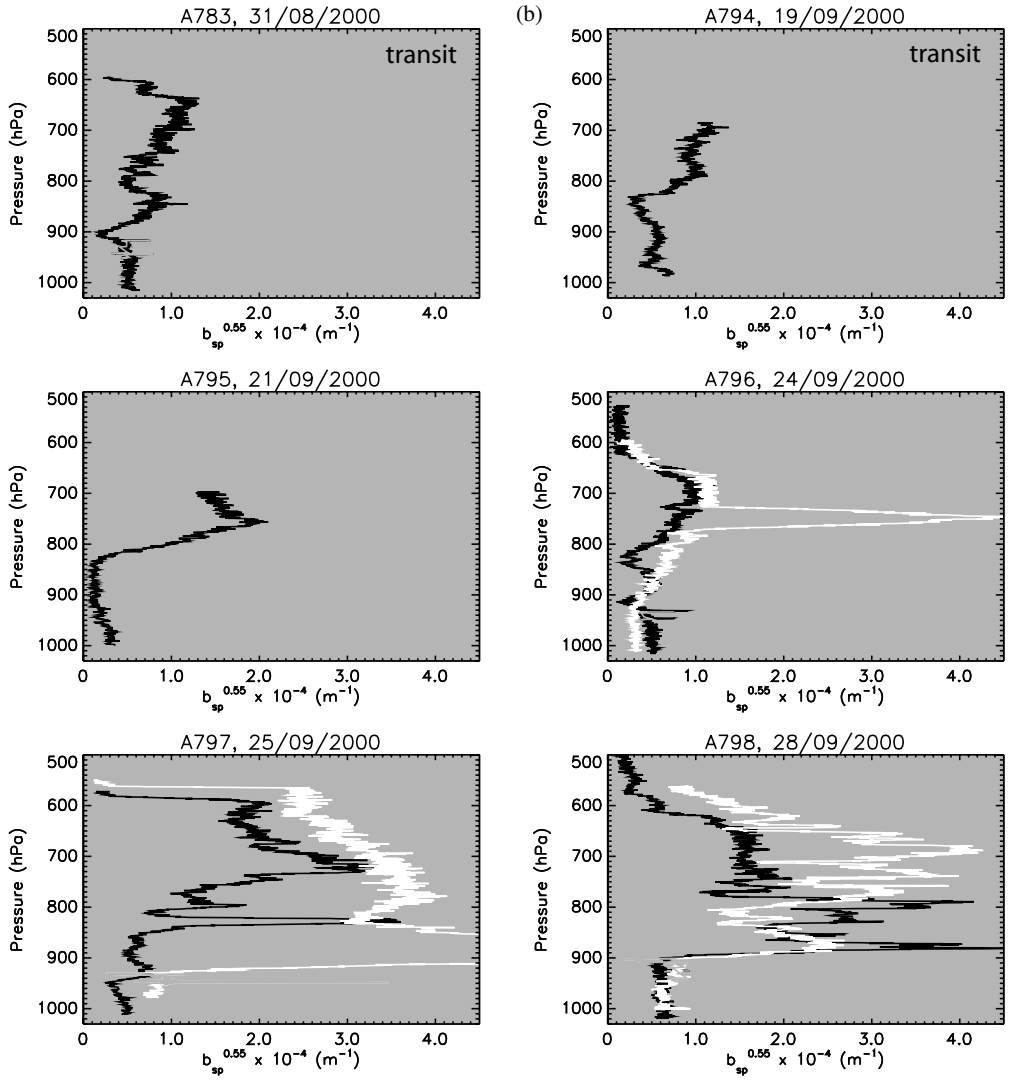

Figure 2. Continued.

a785, a787, a788, a789, a791 and a792). In addition, biomass burning aerosol and stratocumulus cloud were investigated in transit flights to and from Namibia via Ascension Island (a784 and a794). Even at Ascension Island, some 2500 km from the coast of southern Africa, the presence of the biomass burning aerosol layer at elevated altitudes above the marine boundary layer was clear (a794). Figure 2(a) shows a composite of the aerosol volume scattering coefficient at 0.55 μm, $b_{\mathrm{sp}}^{0.55}$, in units of m^{-1}, measured by the nephelometer as a function of pressure during profiles flown by the C-130 over ocean. Although the estimated absolute error in $b_{\mathrm{sp}}^{0.55}$ is $\pm 0.3 \times 10^{-4}$ m^{-1}, this error is likely to be systematic and therefore the variability in the profiles is likely to be real. This variability is also revealed in independent measurements on the Convair-580 aircraft and remotely sensed lidar retrievals from the ER-2 aircraft (Kaufman *et al*. 2003). The top of the biomass burning aerosol layer is typically at approximately 500–600 hPa (5120 ± 550 m), and the bottom of the layer is typically at approximately 800–900 hPa

(1520 ± 660 m). Analysis of the vertical location of stratocumulus clouds reveals that the stratocumulus tops were at around 950 hPa, often separated from the overlying biomass burning plume by a 'clear-slot' (Hobbs 2002; Haywood *et al.* 2003a).

The C-130 performed a total of four dedicated flights from Sal, Cape Verde Islands, during the SHADE campaign (Tanré *et al*. 2003) during the period 21–28 September 2000 (flights a795 to a798). In addition, dust was encountered during profiles on 31 August (a783) and 19 September 2000 (a794) in the vicinity of Sal when the C-130 was travelling to/from Sal–Ascension Island. During the SHADE campaign a large dust storm was advected off the coast of Senegal during the period 24–28 September as shown in Fig. 2(b). The top of the Saharan dust layer was typically 500–600 hPa, which is similar to the situation for biomass burning aerosols shown in Fig. 2(a), while the bottom of the aerosol layer shows considerable variability but is again frequently between 800–900 hPa. Cloud layers were observed at a variety of different levels during SHADE, ranging from small low- to mid-level cumulus to more extensive cloud systems associated with mesoscale systems linked to the intertropical convergence zone (ITCZ). Because of this variability, it is not possible to characterize the typical vertical distribution of clouds in this case.

4. Radiative transfer calculations

Radiative transfer calculations were performed using a radiance version of the radiation code of Edwards and Slingo (1996). Typical vertical profiles of humidity, ozone and temperature from the C-130 during SAFARI 2000 were used in the calculations from the surface to approximately 450 hPa; above this level tropical profiles for humidity and temperature from McClatchey *et al*. (1972) were assumed. The exact choice of vertical profiles makes negligible difference to the results. The surface was modelled as a Lambertian surface with constant surface reflectance of 0.05. The use of a more realistic surface parametrization of Glew *et al*. (2004) makes negligible difference to the results. All of the calculations are for nadir views with a solar zenith angle of 30°. Calculations for a solar zenith angle of 60° suggest that the nature of the results in terms of biases is unchanged. Radiative transfer calculations were performed at five wavelengths that are commonly used in retrievals of δ_{cloud} and r_{e}, these are: 0.63, 0.86, 1.63, 2.13 and 3.7 μm. The first and last of these wavelengths are used in AVHRR retrievals (e.g. Han *et al*. 1994), while the last four are used in MODIS retrievals (King *et al*. 2003, Platnick *et al*. 2003). For wavelengths of 0.63–2.13 μm the contribution to the TOA upwelling radiances from thermal emission is negligible. For the radiative transfer calculations at 3.7 μm, a realistic sea-surface temperature (SST) of 287 K and a cloud-top temperature of 300 K from aircraft measurements during SAFARI 2000 were assumed; the total TOA upwelling radiance was obtained by summing the solar and terrestrial radiances.

(*a*) *Biomass burning aerosol*

Having identified that the biomass burning aerosol generally exists above stratocumulus in the region of investigation during the burning season, the effect of biomass burning aerosol overlying stratocumulus on upwelling radiances at TOA was investigated as follows. The stratocumulus cloud droplet distribution was simulated using a log–normal distribution with a fixed geometric standard deviation, σ, of 1.42 ($\ln \sigma 0.35$) which is typical of that found in stratocumulus cloud. The cloud was modelled between 950 and 980 hPa by varying the liquid water content so that δ_{cloud} ranged from 4–20, and by varying r_{e} from 4–20 μm. These ranges of δ_{cloud} and r_{e} encompass those found off the coast during the measurement campaign in practical terms. Keil and Haywood

(2003) report cloud-top values of r_e of 7.4 ± 3.6, 7.4 ± 3.1 and 7.8 ± 1.1 μm, and liquid water paths of 58 ± 16, 13 ± 8 and 7 ± 12 g m^{-2}, for flights a787, a789, and a793, respectively, suggesting values of δ_{cloud} ranging from 1 to 12. The radiative transfer calculations were repeated including biomass burning aerosol with δ_{aerosol} of 0.5 at 0.55 μm inserted between 900 and 500 hPa (Fig. 2(a)) using the spectrally dependent optical properties shown in Fig. 1(a). Analysis of monthly mean MODIS data (Myhre *et al*. 2003) suggests that a δ_{aerosol} of 0.5 is typical of regions off the coast of Namibia and Angola during September 2000.

(*b*) *Saharan dust aerosol*

Stratocumulus cloud was the dominant cloud type encountered during the SAFARI 2000 mission, and the variability in the vertical profile was relatively modest compared to that encountered during SHADE. It is not possible to characterize typical cloud conditions associated with the presence of Saharan dust events. However, Saharan dust was detected at altitudes above the marine boundary layer, and may be transported over large areas leading to frequent detection in North, Central and South America. In this study, we make the assumption that the underlying cloud consists of stratocumulus with the same characteristics as those modelled in subsection 4(a), and we use the same atmospheric profiles of temperature and humidity and the same SSTs. While these conditions may not be typical, it facilitates a direct comparison of the results from radiative transfer calculations including biomass burning aerosol with those including Saharan dust aerosol. The calculations including Saharan dust aerosol assume a δ_{aerosol} of 0.5 at 0.55 μm inserted between 900 and 500 hPa (Fig. 2(b)) using the spectrally dependent optical properties shown in Fig. 1(b). The δ_{aerosol} value of 0.5 at 0.55 μm is the same as that used for the biomass burning aerosol calculations, which again facilitates comparison. Haywood *et al*. (2003b) show a δ_{aerosol} at 0.55 μm ranging from 0.52 to approximately 1.5 between Sal and Dakar. The highest values of δ_{aerosol} are likely to decrease as the aerosol plume dilutes on moving away from the source regions. It is likely that the size distribution of Saharan dust will evolve during the transport across the Atlantic, with large particles dropping out as a result of sedimentation; this effect is not investigated here.

5. Results

We present results both for AVHRR and MODIS retrievals for biomass burning aerosol in subsection (a), and for mineral dust aerosol in subsection (b).

(*a*) *Biomass burning aerosol*

(i) *AVHRR retrievals.* Figure 3(a) shows the TOA 0.63 μm radiance plotted against that for 3.7 μm for the ranges of δ_{cloud} and r_e discussed in the text. The black lines show the radiances excluding the overlying aerosol; these lines represent those associated with the retrieval algorithms. The white lines show the radiances including the overlying aerosol. The effect of the aerosol upon the 0.63 μm radiance is significant, while there is very little effect upon the 3.7 μm radiance. This can be explained by considering the wavelength-dependence of k_e (or equivalently δ_{aerosol}) shown in Fig. 1. While δ_{aerosol} is equal to 0.5 at 0.55 μm, and a still significant 0.39 at 0.63 μm, it is only 0.02 at 3.7 μm. The effect of including aerosol in the calculations is to reduce the 0.63 μm radiance, making the cloud appear less bright. The reduction of the 0.63 μm radiance has important consequences. Consider the point marked A on Fig. 3(a): the retrieval

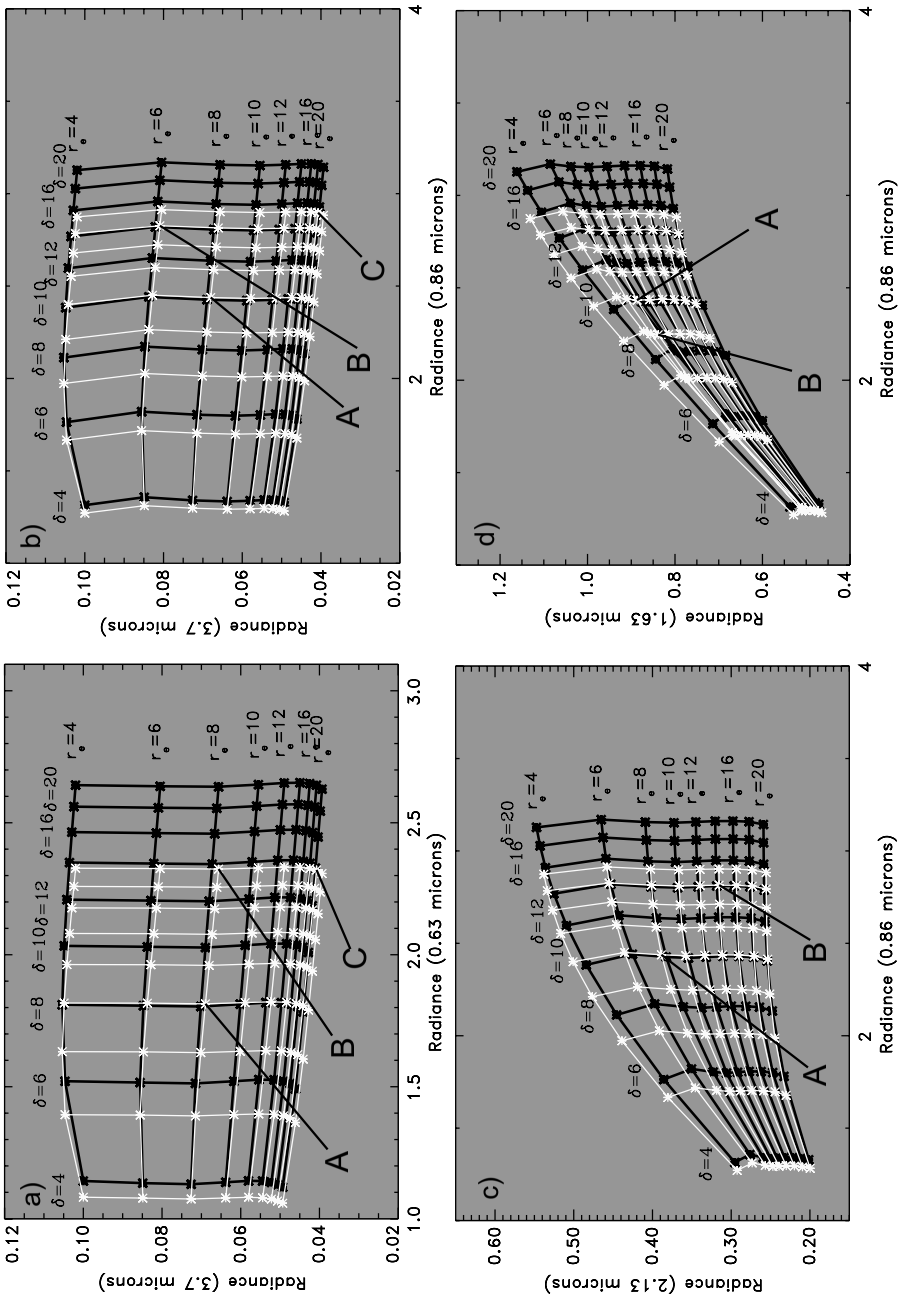

Figure 3. The radiances used in: (a) AVHRR, (b) MODIS retrievals of r_e, (c) the default $r_{2.13}$ which is used in obtaining the level-3 MOD08 product, (d) MODIS retrievals of δ_{cloud} (δ in the figures). The black (white) lines shows results excluding (including) the overlying biomass burning aerosol. The calculations assume a solar zenith angle of 30°, and a Lambertian surface reflectance of 0.05. Letters mark points discussed in section 5. See text for details.

would suggest an apparent δ_{cloud} value of 8, while the actual δ_{cloud} is 10, leading to a 20% bias on the low side. Point B on Fig. 3(a) reveals a low bias larger than 30%, with an apparent δ_{cloud} of <14 while the correct δ_{cloud} is 20. The effect is most pronounced when the aerosol overlies bright clouds with large δ_{cloud}. This effect has been previously documented for TOA irradiances, and radiances for a layer of overlying partially absorbing aerosol (Liao and Seinfeld 1998; Kaufman *et al*. 2001; Hsu *et al*. 2003).

The effects of including overlying partially absorbing aerosols in the retrievals of r_{e} are relatively modest, leading to a systematic overestimation of r_{e} by less than 1 μm for $4 < r_{\text{e}} < 12$ μm. However, when r_{e} is 18 μm, an apparent r_{e} of 20 μm would be returned by the retrieval as shown by point C on Fig. 3(a).

(ii) *MODIS retrievals.* King *et al*. (2003) and Platnick *et al*. (2003) describe the current operational MODIS retrievals in full, but a brief overview is given here. Over ocean regions, the non-absorbing band of 0.86 μm is used to minimize the effects of Rayleigh scattering. The default retrievals over ocean use the 0.86 μm reflectance in combination with the 2.13 μm reflectance to determine δ_{cloud} and r_{e}. In addition, two other retrieval combinations using the 0.86/1.63 and the 0.86/3.7 μm reflectance pairs are performed. We adopt the nomenclature of $r_{\text{e1.63}}$, $r_{\text{e2.13}}$, and $r_{\text{e3.7}}$ to represent r_{e} determined from the 0.86/1.63, 0.86/2.13 and 0.86/3.7 μm reflectance pairs.

In the level-2 MOD06 cloud product, $r_{\text{e1.63}}$–$r_{\text{e2.13}}$ and $r_{\text{e3.7}}$–$r_{\text{e2.13}}$ are also reported (Platnick *et al*. 2003). The level-3 MOD08 global-gridded (1 degree) cloud product reports daily, 8-day and monthly mean δ_{cloud} and r_{e} from aggregations of the default 2.13 μm band retrievals. As the MOD06 products are derived from individual reflectance pairs, we present results from each of the sets of retrievals. We also choose radiances rather than reflectances; reflectances would show identical features.

The results from the 0.86/3.7 μm radiance pair shown in Fig. 3(b) suggest that, as for AVHRR retrievals, there is a significant underestimation of δ_{cloud}. Once again, the effect is greatest for larger δ_{cloud}. Point A highlighted on Fig. 3(b) shows an apparent δ_{cloud} of 10 for a real δ_{cloud} of 12, while the point B shows an apparent δ_{cloud} of 14 for a real δ_{cloud} of 18. The underestimation of δ_{cloud} is therefore not as severe as for AVHRR, because the δ_{aerosol} is 0.39 at 0.63 μm but reduces to 0.20 at 0.86 μm and, therefore, the effect of including the overlying partially absorbing aerosol is not so significant. The effect of including the overlying biomass burning aerosol upon retrievals of r_{e} is an underestimate of less than 2 μm (point C) in the parameter space tested here.

The results from the 0.86/2.13 μm radiance pair shown in Fig. 3(c) show similar biases in δ_{cloud} to those shown in Fig. 3(b), with point A showing an apparent δ_{cloud} of 10 for a real δ_{cloud} of 12, while point B shows an apparent δ_{cloud} of 14 for a real δ_{cloud} of 18. The effect of including the overlying aerosol upon retrievals of r_{e} is small using these two wavelengths, and does not exceed 1 μm in the parameter space tested here.

The results from the 0.86/1.63 μm radiance pair shown in Fig. 3(d) are perhaps the most interesting. In this case, retrievals of δ_{cloud} are similar to those shown in Figs. 3(b) and (c) when 0.86 and 2.13 μm are used, and suggest an apparent δ_{cloud} of 14 for a real δ_{cloud} of 18. However, point A suggests an apparent r_{e} of $\sim$7 μm for a real r_{e} of 10 μm; thus the presence of overlying biomass burning aerosol can lead to an underestimate of r_{e} that might be interpreted as an 'apparent indirect effect', whereby r_{e} appears lower than it actually is. The reason that r_{e} is affected to a larger degree in the 0.86/1.63 μm radiance pair combination, is that the lines of constant effective radius shown on Fig. 3(d) are less parallel to the 0.86 μm radiance abscissa axis than in the other two cases shown in Figs. 3(b) and (c). Thus a reduction in the 0.86 μm radiance

caused by inclusion of the aerosol moves all the points to the left, while the reduction in the 1.63 μm radiance is fairly small. The white lines of constant real r_e cross the black lines of constant apparent r_e. Point B shows an apparent r_e of $\sim$5 μm for a real r_e of up to 10 μm, which could lead to serious misinterpretation of r_e, and consequent differences in the r_e obtained using the 0.86/1.63 and the default 0.86/2.13 μm radiance pairs.

(*b*) *Saharan dust aerosol*

(i) *AVHRR retrievals.* Figure 4(a) shows the results from the 0.63/3.7 μm radiance pair. The effect on the 0.63 μm radiance, and hence on the retrieval of δ_{cloud}, is still significant, but not as great as in the case for an overlying biomass burning layer. This is because $\omega_{o\lambda=0.63}$ and $g_{\lambda=0.63}$ are higher for Saharan dust than for biomass burning aerosol, resulting in less absorption and more forward scattering by the aerosol. Again, the underestimate is largest for larger δ_{cloud}. The effect of including mineral dust aerosol on the 3.7 μm radiance is much more significant than when biomass burning aerosol is included, because the specific extinction coefficient is still significant at 3.7 μm owing to the presence of large particles (Table 1). The radiance is reduced due to absorption of solar radiation, and also due to absorption and re-emission of terrestrial radiation, where in effect the aerosol is behaving in a similar manner to greenhouse gases (e.g. Highwood *et al*. 2003). This reduction in 3.7 μm radiances has an important consequence: in this case r_e is overestimated. Point A shows that an apparent r_e of 18 μm would be retrieved for a real r_e of 12 μm. Thus the biases in retrievals of r_e may be either positive (i.e. dust overlying clouds in the AVHRR $r_{e3.7}$ retrieval) or negative (i.e. biomass burning aerosol overlying clouds in the MODIS $r_{e1.63}$ retrieval) which further complicates reconciliation of r_e retrievals using different wavelengths.

(ii) *MODIS retrievals.* Figure 4(b) shows the results from the 0.86/3.7 μm radiance pair; they are similar to those shown in Fig. 4(a) for the AVHRR retrieval. Once again an apparent r_e of 18 μm would be retrieved for a real r_e of 12 μm (point A) thus showing that r_e is overestimated in this case.

Figure 4(c) shows the results from the 0.86/2.13 μm radiance pair. As for biomass burning aerosol, the effect on the 0.86 μm radiance is significant, which leads to the apparent δ_{cloud} being less than the real δ_{cloud}, with a real δ_{cloud} of 20 being interpreted as approximately 16 (e.g. point A). The effect of including Saharan dust above cloud reduces the 0.86 μm radiance less than for biomass burning, despite the fact that $\delta_{\text{aerosol}\lambda=0.86}$ is 0.50 for Saharan dust and 0.20 for biomass aerosol. This is because $\omega_{o\lambda=0.86}$ is higher for Saharan dust (less absorption), and because $g_{\lambda=0.86}$ is higher (less scattering in the backward direction). The underestimate of δ_{cloud} turns into a very small (insignificant) overestimate for a δ_{cloud} value of 4. The mechanism for this changeover from a decrease to an increase in reflectance has been documented for irradiances (e.g. Haywood and Shine 1995, Haywood and Boucher 2000), and is due to the effective surface reflectance decreasing so that the partially absorbing aerosol increases the local planetary albedo. Liao and Seinfeld (1998) document this effect for broadband irradiances for the specific case of mineral dust aerosol above cloud. This mechanism has been suggested to be a plausible method for determining ω_o above bright surfaces (Kaufman *et al*. 2001). Figure 4(c) shows that the radiances at 2.13 μm are decreased to a larger extent than the comparable case for biomass burning aerosols (Fig. 3(c)); this is because the wavelength-dependence of k_e is much less significant for Saharan dust, and thus $\delta_{\text{aerosol}\lambda=2.13}$ is 0.36 for Saharan dust but only 0.04 for biomass

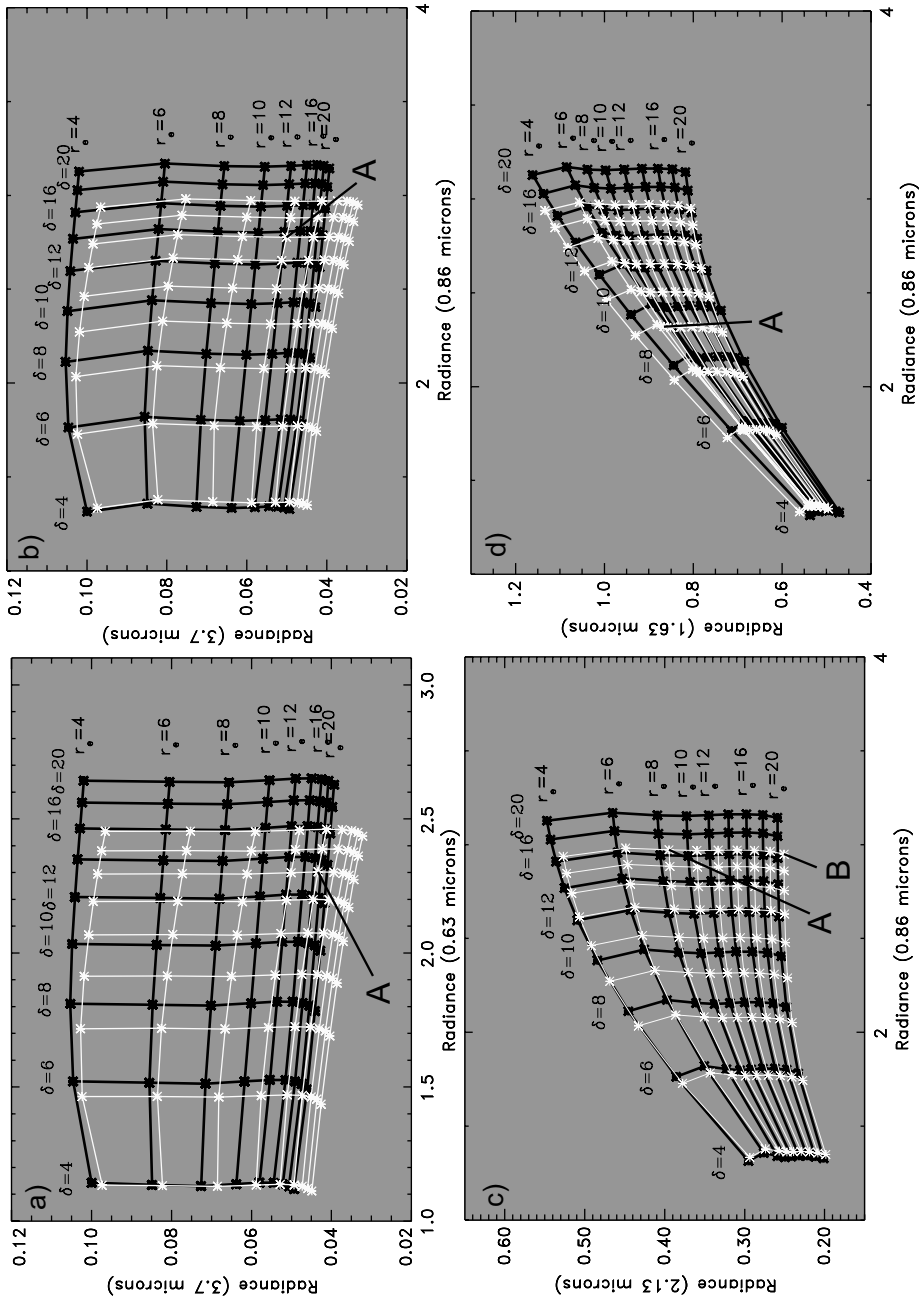

Figure 4. As for Fig. 3 but for Saharan dust aerosol.

burning aerosol. This may lead to a small overestimate of r_e by up to 1 μm (e.g. point B) for large values of r_e.

Figure 4(d) shows the results from the 0.86/1.63 μm radiance pair. These results are in many ways similar to those presented for biomass burning aerosol in Fig. 3(d). Once again there is evidence that $\omega_{o\lambda=1.63}$ is close to the critical value at which the presence of aerosol increases the radiance at low δ_{cloud} but decreases the radiance at high δ_{cloud}. Again an underestimate of δ_{cloud} occurs, and again an underestimation of r_e occurs whereby an apparent r_e of $\sim$5 μm is returned for a real r_e of up to 10 μm (point A), with consequences for remote sensing of the indirect effect.

6. Evidence of the effect upon r_e in MODIS retrievals

While section 5 has presented the theoretical basis for possible biases in δ_{cloud} and r_e, no evidence has so far been presented of these biases being present in the actual retrievals. Because δ_{cloud} is essentially determined by just a single radiance (0.63 μm for AVHRR, and 0.86 μm for MODIS), it is not possible to judge whether there are any differences/biases in δ_{cloud} by analysing the self-consistency of the data; further wavelength-dependent radiance information would be needed and/or analyses of *in situ* aircraft data, which is beyond the scope of this paper. However, as shown in section 5, differences in r_e derived from the 0.86/1.63, 0.86/2.13 and 0.86/3.7 μm radiance pairs should be evident, and this information is reported in the MOD06 level-2 atmospheric product (subsection 5(a)(ii)). Here we use MODIS data gathered from the Terra platform concurrent with the C-130 aircraft measurements during the SAFARI 2000 period. Stratocumulus clouds were not the prevailing cloud type during the SHADE period, with significant cumulus, cirrus and convective cells associated with the ITCZ all being present in and around the area of investigation. Additionally, while the well-aged biomass burning aerosol showed physical and optical characteristics that did not vary a great deal during the SAFARI 2000 measurement period (Haywood *et al*. 2003a), the aerosol physical and optical properties during SHADE showed significant spatial and temporal variability (Haywood *et al*. 2003b). Therefore, in this investigation we limit ourselves to analysis of the relatively better constrained data from SAFARI 2000.

It is important to realize that in real clouds, where the particle droplet size distribution is a function of geometric height within the cloud, radiances at 1.63 μm are less affected by droplet absorption than those at 2.13 and 3.7 μm, and consequently $r_{e1.63} < r_{e2.13} < r_{e3.7}$. This is because, in effect, the shorter wavelength radiances are made up of photons scattered from further down in the cloud where the droplet size is typically smaller (e.g. Garrett and Hobbs 1995; Platnick 2000). Keil and Haywood (2003) show the liquid water content and r_e determined from *in situ* instrumentation during two C-130 profiles on flight a787 on 7 September 2000, and show that the stratocumulus clouds are close to adiabatic in nature with r_e values of $\sim$5–6 μm at cloud base and $\sim$9 μm at cloud top. Platnick (2000) performs theoretical calculations investigating differences in $r_{e1.63}$, $r_{e2.13}$, and $r_{e3.7}$ for a range of different vertical profiles of cloud particle size distribution. In all cases for $5 < \delta_{cloud} < 15$, $|r_{e1.63}-r_{e2.13}| < |r_{e3.7}-r_{e2.13}|$; i.e. the positive difference between $r_{e3.7}$ and $r_{e2.13}$ is greater in magnitude than the negative difference between $r_{e1.63}$ and $r_{e2.13}$. In these theoretical calculations, $|r_{e1.63}-r_{e2.13}|$ and $|r_{e3.7}-r_{e2.13}|$ are less than 1 μm for the modelled adiabatic cloud, and less than 1.5 μm when the cloud is modelled as sub-adiabatic at mid levels. When MOD06 level-2 data off the coast of South America are analysed by Platnick *et al*. (2003) $|r_{e3.7}-r_{e2.13}|$ is generally less than 1 μm. However, significant regions exist where $|r_{e1.63}-r_{e2.13}| > 1$,

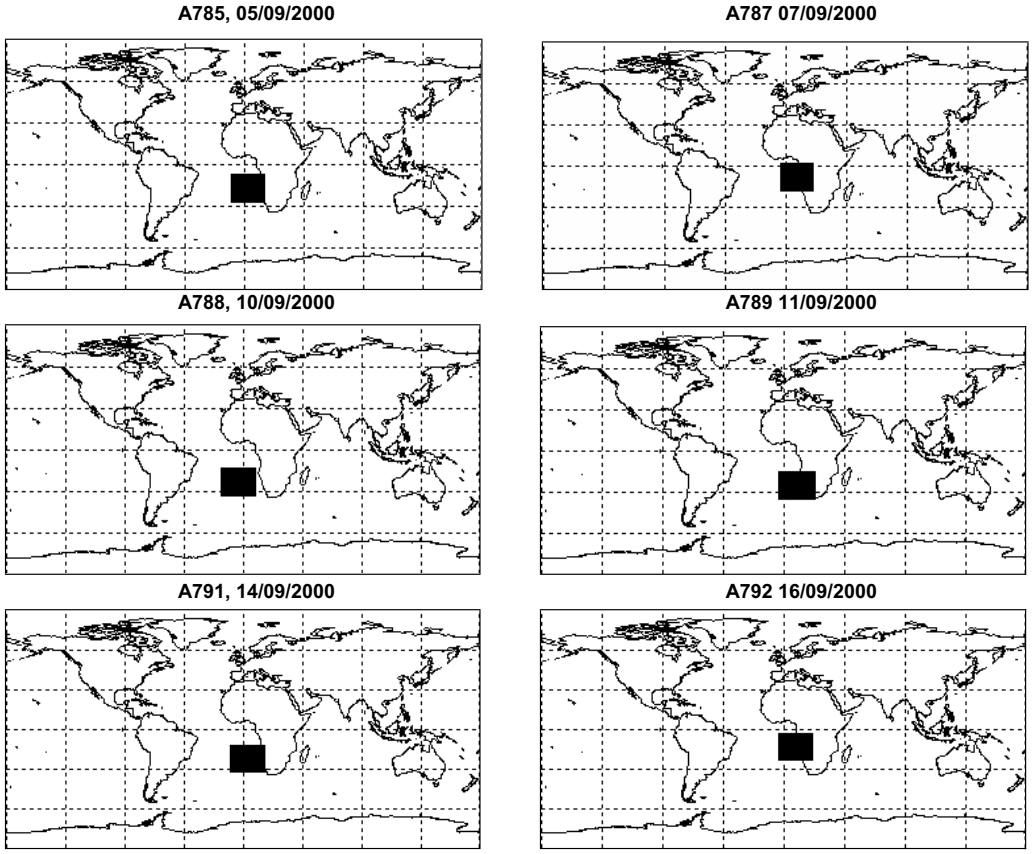

Figure 5. The locations of the granules (see text) of MODIS data shown in the quick-look data in Fig. 6 and satellite retrievals in Fig. 7 for flights as indicated.

and sometimes $|r_{e1.63}-r_{e2.13}| > 2.5$, despite the fact that this region should not be influenced by overlying absorbing aerosol. Thus any influence of absorbing aerosol above cloud in the Namibian/Angolan coastal regions on $r_{e1.63}$ is likely to be in addition to that due to vertical photon transport, which will complicate detection of the theoretical aerosol effect.

The granules* that are analysed here are available from http://daac.gsfc.nasa.gov/MODIS/, and are collocated temporally and geographically with the dedicated aircraft flights (see Fig. 1 in Haywood *et al*. 2003a). The geographic locations of the areas examined here are shown in Fig. 5, and quick-look, real-colour imagery of the scenes that are investigated in detail (September 7 and September 10) are shown in Fig. 6. A cursory examination of Fig. 6 shows the presence of biomass burning smoke aerosol over land regions. An approximate north–south gradient can clearly be seen in Total Ozone Mapping Spectrometer (TOMS) Aerosol Index (AI) data during this period (e.g. Haywood *et al*. 2003a). Smoke is more difficult to distinguish over the ocean regions because of the presence of clouds and areas of sun-glint in some of the data. The areas where smoke aerosol or sun-glint are obviously visually apparent are marked on Fig. 6. Visually, it is difficult to distinguish which cloudy areas are affected by smoke from

* 'Granules' is the technical National Aeronautics and Space Administration term for the data that are analysed, not the results of the analysis.

the MODIS quick-look images, and a more detailed quantitative knowledge of the areas affected by high concentrations of aerosols is required. Here we use the TOMS AI data (http://toms.gsfc.nasa.gov/aerosols/aerosols.html) from the same day as that on which the MODIS data were collected. The TOMS and the MODIS instruments are on different satellite platforms, and therefore the aerosol will not be in exactly the same locations due to advection. However, we make the reasonable assumption that the advection rate is relatively small. It would theoretically be possible to determine the regions affected by aerosol by analysing the MODIS MOD04 aerosol products, but δ_{aerosol} may only be determined in cloud-free conditions and thus calculations of δ_{aerosol} and δ_{cloud} are mutually exclusive. We prefer to use the TOMS AI data in this analysis because the statistics for δ_{aerosol} from MODIS are comparatively extremely sparse. The TOMS AI does not translate to δ_{aerosol} via a universal linear relationship, but is dependent on the aerosol absorption properties and the altitude of the aerosol. Hsu *et al.* (1999) compared sun-photometer data to aerosol optical depth both for African biomass burning sites and for Saharan dust (Dakar and Cape Verde) sites, and reported an aerosol-type-dependent linear relationship for both cases. For biomass burning the relationship $\delta_{\text{aerosol}\lambda=0.38} \sim 0.80(\text{TOMS AI})$ was found, while for Saharan dust the relationship $\delta_{\text{aerosol}\lambda=0.38} \sim 0.35(\text{TOMS AI})$ was found. We convert $\delta_{\text{aerosol}\lambda=0.38}$ to $\delta_{\text{aerosol}\lambda=0.55}$ by using the modelled wavelength-dependence of k_{e}. The approximate relationships $\delta_{\text{aerosol}\lambda=0.55} = 0.40(\text{TOMS AI})$ for biomass burning aerosol and $\delta_{\text{aerosol}\lambda=0.55} \sim 0.36(\text{TOMS AI})$ for Saharan dust are deduced.

The quick-look images of Fig. 6 are shown in detail for 7 and 10 September. These represent two cases where the δ_{aerosol} and the TOMS AI were high, and the area showed significant quantities of cloud in the range $5 < \delta_{\text{cloud}} < 25$, values that are consistent with the theoretical analyses. There is a significant difference between the two cases. For 7 September we shall see that the TOMS AIs indicate that there is significant aerosol loading throughout the region (subsection 6(a)); for 10 September there is a significant gradient in TOMS AI indicating the presence of aerosol to the north of the region, but clean, aerosol-free areas to the south (subsection 6(b)). The other four cases are less ideal for a variety of reasons including: lack of stratocumulus cloud, the effects of other types of cloud in the region, lack of aerosol, and/or the effects of sun-glint in the MODIS retrievals; consequently we chose not to present a detailed analysis here. However, we do present statistics that summarize the results from these cases (subsection 6(c)).

(*a*) *7 September 2000*

Figure 7(a) shows the TOMS AI over the region. Highest TOMS AIs are evident close to the coast of Angola where the AI exceeds 3.5 ($\delta_{\text{aerosol}\lambda=0.55}$ exceeds $\sim$1.4). It is evident that the majority of the region under investigation is influenced by aerosol. Figure 7(b) shows the default $r_{\text{e}2.13}$ for 7 September. The majority of the regions of stratocumulus show $12 > r_{\text{e}2.13} > 5$ μm. *In situ* measurements of the near-cloud-top r_{e}, by instruments on the C-130 between 15 and 17°S off the coast of Angola, reveal $r_{\text{e}} = 7.4 \pm 3.6$ μm (Keil and Haywood 2003) and are thus in general agreement with the MODIS data in that area. Figure 7(b) shows the area affected by sun-glint; in this region r_{e} is only derived for clouds that are optically thick enough to make the effects of sun-glint negligible. Figure 7(c) shows the difference in effective radius between $r_{\text{e}3.7}$ and the default $r_{\text{e}2.13}$, $r_{\text{e}3.7}$–$r_{\text{e}2.13}$, obtained for 7 September. The theoretical calculations presented in subsection 5(a)(ii) suggest that there should be little influence of overlying aerosol at these wavelengths, and therefore one would expect $r_{\text{e}3.7}$–$r_{\text{e}2.13}$ to be close to zero or slightly positive from parcel theory (Platnick 2000; Platnick *et al.* 2003). This is indeed the case (see Fig. 7(c)), with the majority of areas showing differences of less

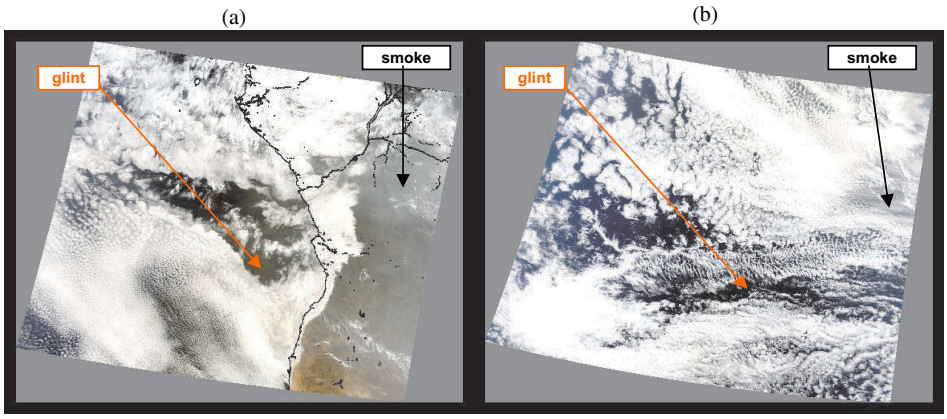

Figure 6. Quick-look data from the MODIS website (http://daac.gsfc.nasa.gov/MODIS/) of the areas shown in Fig. 5 for (a) 7 and (b) 10 September 2000. Discernible cloud-free areas with significant aerosol loading and areas of sun-glint are marked as 'smoke' and 'glint'.

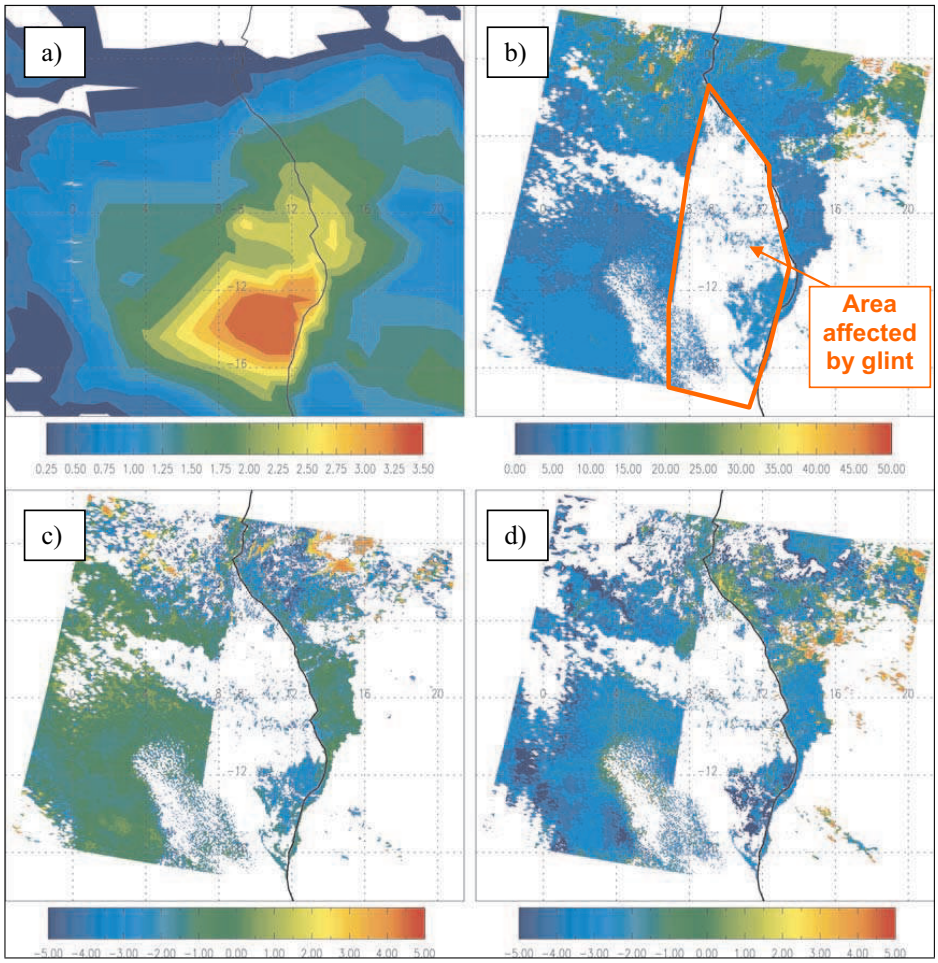

Figure 7. Satellite retrievals for 7 September 2000, over the regions shown in Figs. 5 and 6. (a) TOMS data showing the Aerosol Index (http://toms.gsfc.nasa.gov/aerosols/aerosols.html); the data are interpolated in regions outside the TOMS swath; the approximate relationship $\delta_{\mathrm{aerosol}\lambda=0.55} \sim 0.40\mathrm{TOMS\ AI}$ applies. (b) The MODIS MOD06 level-2 default $r_{\mathrm{e}2.13}$, showing the area affected by sun-glint. (c) $r_{\mathrm{e}3.7}-r_{\mathrm{e}2.13}$ and (d) $r_{\mathrm{e}1.63}-r_{\mathrm{e}2.13}$. See text for details.

than $\sim$1 μm in magnitude. Some of the northern regions in Fig. 7(c) show yellow and red colours, i.e. $r_{e3.7}$–$r_{e2.13} > 2$ μm; these are likely to be associated with deep convection and, while important, are not relevant in this study. The blue colours shown in Fig. 7(d) indicate a significant negative difference in $r_{e1.63}$–$r_{e2.13}$. Mid-blue colours represent $r_{e1.63}$–$r_{e2.13}$ values of approximately -2 to -4 μm, and the dark blues represent values ranging from -4 to -7 μm (the scale ranges to a maximum of -5 μm). The theoretical analysis of Platnick (2000) suggests that $|r_{e3.7}$–$r_{e2.13}| > |r_{e3.7}$–$r_{e1.63}|$, but this is not the case here, which might be an indication that overlying absorbing aerosols are influencing the retrievals. However, the analysis by Platnick *et al*. (2003) of MODIS data off the coast of S. America suggests that $|r_{e3.7}$–$r_{e2.13}| < |r_{e3.7}$–$r_{e1.63}|$, so we cannot infer that overlying biomass burning aerosol is influencing the retrievals from this feature alone. Indeed, the lack of a spatial gradient in aerosol loading in this case makes it difficult to reach a definite conclusion that overlying biomass burning aerosol is affecting the retrievals. Such a case is provided by 10 September. A more detailed statistical analysis of $r_{e3.7}$–$r_{e2.13}$ and $r_{e3.7}$–$r_{e1.63}$ in the form of probability density functions (pdfs) is given in subsection 6(c).

(*b*) *10 September 2000*

Figure 8(a) shows the TOMS AI over the region. In this case a strong spatial contrast is evident, with aerosol affecting the north and particularly the north-east of the region with maximum AIs exceeding 2 ($\delta_{\text{aerosol}\lambda=0.55} >\sim 0.8$). To the south of the region the AI is close to zero. Figure 8(b) shows the default $r_{e2.13}$ for 10 September; once again the area affected by sun-glint is evident. Typically, $12 < r_{e2.13} < 5$ μm, which is similar to the $r_{e2.13}$ retrievals on 7 September. There is evidence of ice cloud present in the lower left-hand side of the image, shown by $r_{e2.13}$ reaching 15–30 μm. Figure 8(c) once again shows that the $r_{e3.7}$ retrieval is not greatly affected by overlying aerosol, with the majority of regions showing green colours indicating that $|r_{e3.7}$–$r_{e2.13}|$ is less than 1–2 μm. Figure 8(d) shows $r_{e1.63}$–$r_{e2.13}$. To the south of the region there is little difference between the $r_{e1.63}$ and $r_{e2.13}$, and therefore the majority of the south shows green colours associated with $|r_{e1.63}$–$r_{e2.13}|$ of less than 1–2 μm. To the north of the region differences between $r_{e1.63}$ and $r_{e2.13}$ become greater in magnitude and hence blue colours become evident. It is clear that the geographic north–south split in $r_{e1.63}$–$r_{e2.13}$ appears well correlated with the TOMS AI shown in Fig. 8(a). This piece of evidence supports the theoretical calculations that are presented in section 5, which suggest that $r_{e1.63}$ is biased to smaller values by the presence of overlying absorbing biomass burning aerosol. Again, a statistical analysis of $r_{e3.7}$–$r_{e2.13}$ and $r_{e3.7}$–$r_{e1.63}$ is given in subsection 6(c).

(*c*) *Statistical analysis of the results*

An analysis of the MODIS data for 7 and 10 September is given in the form of pdfs in Fig. 9 and Table 2. In determining the data in the pdfs three criteria are applied.

(i) $5 < \delta_{\text{cloud}} < 25$. This removes clouds with large optical thicknesses such as convective cloud, and the results should be consistent with the theoretical calculations performed in sections 4 and 5.

(ii) *Cloud over land areas is screened out.* This is because over land areas the aerosol tends to be well-mixed throughout the boundary layer (Haywood *et al*. 2003a), and the relative vertical position of aerosol and cloud cannot be assured.

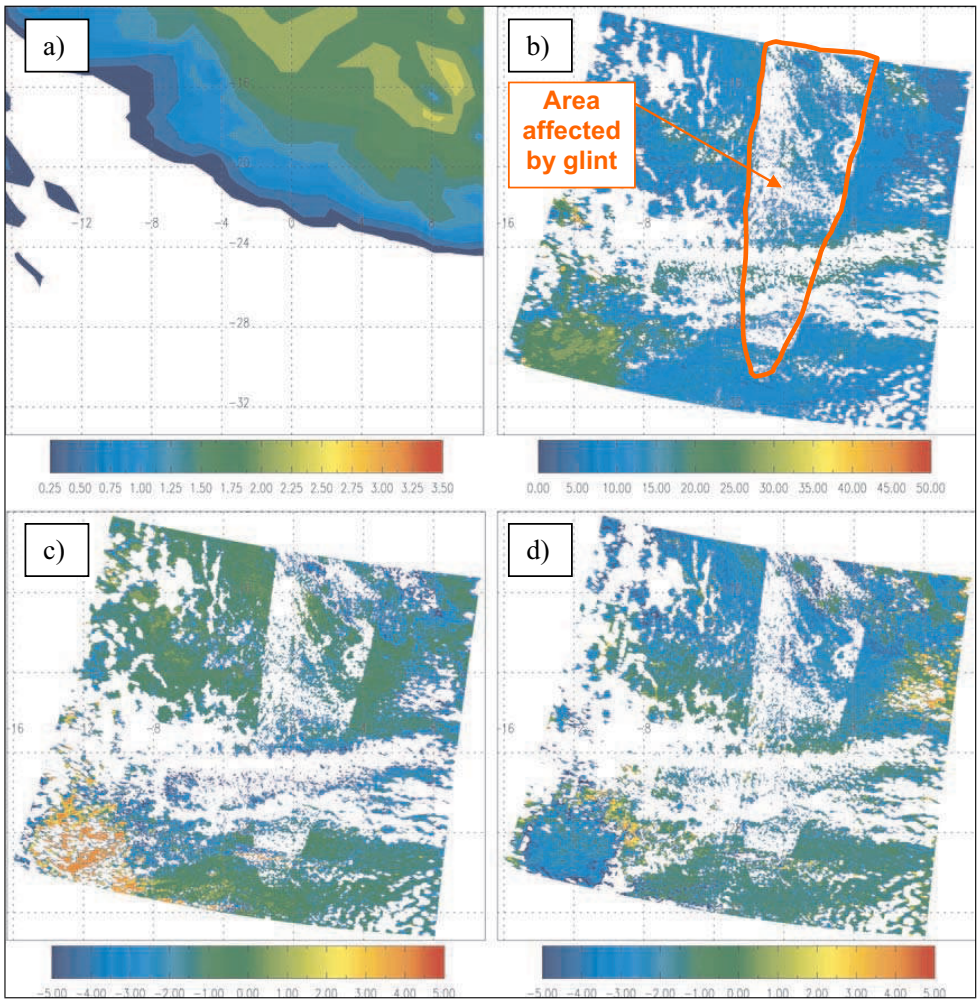

Figure 8. As for Fig. 7 but for 10 September 2000.

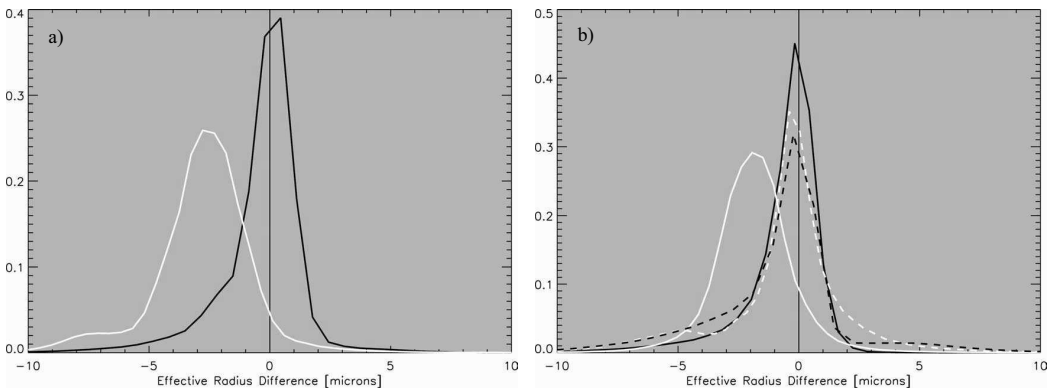

Figure 9. Probability density functions (pdfs) of $r_{e1.63}$–$r_{e2.13}$ (white lines) and $r_{e3.7}$–$r_{e2.13}$ (black lines) for: (a) 7 September, and (b) 10 September 2000. Solid lines represent the pdfs from aerosol-influenced pixels, and the dashed lines represent the pdfs from non-aerosol-influenced pixels.

TABLE 2. STATISTICS SHOWING THE MODAL EFFECTIVE RADIUS OF THE PDFS FOR AEROSOL- AND NON-AEROSOL-INFLUENCED PIXELS BOTH FOR $r_{e1.63}$–$r_{e2.13}$ AND $r_{e3.7}$–$r_{e2.13}$

		Mode of pdf (μm)						
		aerosol		non-aerosol		Approximate number of pixels × 1000		
Flight	Date	$r_{e1.63}$–$r_{e2.13}$	$r_{e3.7}$–$r_{e2.13}$	$r_{e1.63}$–$r_{e2.13}$	$r_{e3.7}$–$r_{e2.13}$	aerosol	Indeterminate	non-aerosol
A785	5 Sept	−1.14	−0.15	−0.58	−0.31	425	450	460
A787	7 Sept	−2.78	+0.45	n/a	n/a	735	20	0
A788	10 Sept	−1.93	−0.17	−0.40	−0.22	705	115	490
A789	11 Sept	−1.02	−1.04	−0.04	−0.62	130	55	295
A791	14 Sept	−1.68	−1.40	+0.74	−0.86	185	85	330
A792	16 Sept	−1.32	+0.25	−0.10	−0.32	380	180	140

See text for details.

(iii) *TOMS AI.* A pixel is assigned as being 'aerosol-influenced' when the TOMS AI $\geqslant 0.25$, 'non-aerosol-influenced' when the TOMS AI $\leqslant 0$, and 'indeterminate' when $0 <$ TOMS AI < 0.25.

We introduce the indeterminate classification to reduce misclassification of aerosol-influenced and non-aerosol-influenced pixels around the edges of the biomass burning aerosol plume, because the data from MODIS and TOMS are not exactly temporally collocated and a small amount of advection may have taken place. It would theoretically be possible to correlate $r_{e1.63}$–$r_{e2.13}$ to TOMS AI, but inferences from such a correlation are made difficult by the variability in: δ_{cloud}, cloud geometric height, aerosol above cloud, solar geometry, and satellite viewing geometry. Therefore we stick to our system of three classifications: aerosol-influenced, non-aerosol-influenced, and indeterminate pixels.

For 7 September, all of the area is affected by aerosol as shown by the statistics presented in Table 2; there are approximately 735 000 aerosol-influenced MODIS pixels and 20 000 indeterminate pixels, and zero non-aerosol-influenced pixels in the pdfs. Figure 9(a), therefore, shows only two pdfs associated with aerosol-influenced $r_{e3.7}$–$r_{e2.13}$ and aerosol-influenced $r_{e1.63}$–$r_{e2.13}$. The modal value of $r_{e3.7}$–$r_{e2.13}$ is slightly positive at $+0.45$ μm as expected from parcel theory. However, a value of $r_{e1.63}$–$r_{e2.13}$ of -2.78 μm is greater in magnitude than any of the theoretical calculations of Platnick (2000) for clouds of similar optical depths, and appears significantly greater than the analysis of real MODIS data shown in Platnick *et al.* (2003), although no statistical analysis is shown in that work, which is again suggestive of the influence of overlying absorbing aerosol on the retrievals. Approximately 11% of aerosol-influenced pixels show a negative bias of $|r_{e1.63}$–$r_{e2.13}|$ of more than 5 μm, results that are difficult to explain unless overlying absorbing aerosol is affecting $r_{e1.63}$.

For 10 September, 705 000 pixels are assigned as being aerosol-influenced, 490 000 pixels are non-aerosol-influenced, and 115 000 indeterminate. Figure 9(b), therefore, shows four pdfs associated with $r_{e3.7}$–$r_{e2.13}$ and $r_{e1.63}$–$r_{e2.13}$ both for aerosol-influenced and for non-aerosol-influenced cases. Considering first $r_{e3.7}$–$r_{e2.13}$, the non-aerosol-influenced case shows a modal value of -0.22 μm and the aerosol-influenced case shows a modal value of -0.17 μm; statistically there is no difference between these two values. The modal $r_{e1.63}$–$r_{e2.13}$ for the non-aerosol-influenced pixels is relatively modest at -0.40 μm, which is consistent with the small negative bias associated with parcel theory, while the aerosol-influenced case shows a modal value of -1.93 μm. The mean bias for the aerosol-influenced pixels is -1.85 μm with a standard deviation of 1.78 μm and therefore the mean bias is significant to 1σ. Thus, by using TOMS AI to discriminate between aerosol-influenced and non-aerosol-influenced pixels, a bias in

$r_{e1.63}$ is revealed. The magnitude of this bias is somewhat less than the statistics suggest for aerosol-influenced pixels for 7 September; this might be expected because the TOMS AI and $\delta_{aerosol}$ for 10 September is somewhat smaller than for 7 September.

The results of the statistical analysis for the rest of the cases examined here (5, 11, 14 and 16 September) are summarized in Table 2. The results for $r_{e3.7}$–$r_{e2.13}$ show a slightly negative bias for the non-aerosol-influenced pixels, but when aerosol-influenced pixels are considered $r_{e3.7}$–$r_{e2.13}$ can be either more positive or more negative. The results for $r_{e1.63}$–$r_{e2.13}$ are quite different; in all cases the non-aerosol-influenced pixels show more positive values than the aerosol-influenced pixels. This provides further evidence that overlying aerosol is influencing the retrieval of $r_{e1.63}$.

7. Discussion and conclusions

Using realistic aerosol properties and reasonable relative positions of aerosol and cloud, we perform model radiative transfer calculations that show that satellite retrievals of δ_{cloud} are likely to be underestimated in regions that are affected by overlying partially absorbing aerosol. This result is despite the fact that an additional $\delta_{aerosol}$ of 0.5 at 0.55 μm is included in the calculations, leading to a larger δ_{total}.

We also show that the combination of 0.86/1.63 μm radiances/reflectances used in MODIS retrievals is theoretically susceptible to producing an underestimate in $r_{e1.63}$ in regions of overlying partially absorbing aerosol. These results are backed up by a practical analysis of the MODIS data for six cases (two cases presented in detail) where overlying biomass aerosol exists above stratocumulus clouds. Platnick *et al.* (2003), investigating an example of stratocumulus off the western coast of Chile and Peru, show that $|r_{e1.63}–r_{e2.13}|$ is often within 1 μm although some significant differences exist of around ~ -2.5 μm. It is suggested that these differences are associated with parcel theory (Platnick *et al.* 2003), whereby the 1.63 μm reflectance is less affected by water droplet absorption than the 2.13 μm reflectance, and therefore probes deeper in the cloud where cloud droplets tend to be smaller. The theoretical calculations using cloud droplet distributions with an r_e that does not vary in the vertical, suggest systematic biases in $|r_{e2.13}–r_{e1.63}|$ of as much as 5 μm, which generally exceeds the differences that might be expected from parcel theory. By using the TOMS AI to delineate regions that are/are not affected by aerosols, we show: firstly a modal bias in $r_{e1.63}$–$r_{e2.13}$ of as much as -2.78 μm; secondly statistical analyses suggesting that $|r_{e2.13}–r_{e1.63}|$ is greater than -5 μm for as much as 11% of aerosol-influenced pixels; and thirdly spatial structures in the biases of $r_{e2.13}$–$r_{e1.63}$ that appear correlated to the presence of overlying aerosol. These results support the theoretical calculations, suggesting that not only the vertical distribution of cloud droplet size but also overlying partially absorbing aerosol are responsible for the smaller value of $r_{e1.63}$ compared to $r_{e2.13}$ and $r_{e3.7}$. It might be argued that the presence of the overlying absorbing aerosol might change the dynamical evolution of stratocumulus, thereby affecting the cloud geometric height and r_e (Johnson *et al.* 2004). However, both this semi-direct and the indirect effect should not lead to significant *wavelength-dependent* differences in r_e, and are thus unlikely to explain the result that $r_{e1.63}$ has a low bias in regions affected by aerosol.

Our results for biomass burning aerosol are somewhat better constrained than the results for mineral dust aerosol, because we have reasonable statistics for determining the aerosol and underlying stratocumulus cloud properties, while in the regions where Saharan dust outbreaks are frequent the cloud is much more variable in nature. Because of this variability, we do not present an analysis of MODIS data for the SHADE period. However, the assumptions made in determining the radiances for Saharan dust aerosol

appear reasonable. While our results are applicable to the Namibian/Angolan stratocumulus regions and regions affected by Saharan dust outbreaks, absorbing aerosol above low cloud is experienced in a number of other regions, such as the pollution advected from eastern Asia studied during the Aerosol Characterisation Experiment (ACE-Asia, Hsu *et al*. 2003). The CALIPSO (Cloud–Aerosol Lidar and Infrared Pathfinder Satellite Observations) instrument may have an important role in clarifying the effects of different types of overlying aerosol upon cloud physical parameter retrievals (Winker *et al*. 2003).

One of the largest sources of uncertainty in determining the direct radiative impact of aerosols stems from the lack of knowledge of the aerosol $\omega_{o\lambda}$, which determines whether an aerosol heats or cools the atmosphere (e.g. Haywood and Boucher 2000). For example, considerable uncertainty has recently been highlighted in the absorption properties of mineral dust, with recent *in situ* and remote sensing methods suggesting a much lower degree of absorption than previously thought (e.g. Kaufman *et al*. 2001; Haywood *et al*. 2003b). It might be possible to determine $\omega_{o\lambda}$ by performing retrievals where the 1.63 μm reflectance is combined with reflectances from other MODIS bands in the spectral range 0.4–0.75 μm (MODIS has 11 bands in this range), and consistency of the modelled optical properties including $\omega_{o\lambda}$ could be assessed. A low bias in the retrieved r_e will only be evident if the aerosol is significantly absorbing. Variability in cloud and aerosol optical properties and vertical profiles may make this sort of analysis difficult in practice.

An important conclusion from this study is that those wishing to investigate the indirect effect of aerosols upon cloud in these regions via remote sensing techniques should be aware of this 'apparent indirect effect', whereby anomalously low values of $r_{e1.63}$ are retrieved due to the presence of *overlying* absorbing aerosols, rather than the influence of aerosols upon the cloud microphysics.

ACKNOWLEDGEMENTS

We would like to thank the Meteorological Research Flight aircrew and support staff for their efforts during SAFARI 2000. Peter Francis is thanked for his input to this work, and for reading an earlier version of the manuscript. John Edwards is thanked for development and maintenance of the radiative transfer code. Steve Platnick is thanked for his extremely valuable comments regarding the MODIS retrieval algorithms and MODIS products. Steven Abel would like to thank NERC and the Met Office for providing the CASE studentship under which this research was undertaken.

REFERENCES

Edwards, J. M. and Slingo, A. 1996 Studies with a flexible new radiation code. I: Choosing a configuration for a large-scale model. *Q. J. R. Meteorol. Soc*., **122,** 689–720

Fouquart, Y., Bonnel, B., Brogniez, G., Buriez, J. C., Smith, L. and Morcrette, J. J. 1987 Observations of Saharan aerosols: Results of ECLATS field experiment. Part II: Broadband radiative characteristics of aerosols and vertical flux divergence. *J. Clim. Appl. Meteorol*., **26,** 38–52

Garrett, T. J. and Hobbs, P. V. 1995 Long-range transport of continental aerosols over the Atlantic Ocean and their effects on cloud structure. *J. Atmos. Sci.*, **52,** 2977–2984

Glew, M. D., Hignett, P. and Taylor J. P. 2004 Aircraft measurements of sea surface albedo. *J. Atmos. Sci*., in press

Han, Q., Rossow, W. B. and Lacis, A. A. 1994 Near-global survey of effective droplet radii in liquid water clouds using ISCCP data. *J. Climate*, **7,** 465–497

Han, Q., Rossow, W. B., Chou, J. and Welch, R. M. 1998 Global variation of column droplet concentration in low-level clouds. *Geophys. Res. Lett*., **25,** 1419–1422

Haywood, J. M. and Boucher, O. 2000 Estimates of the direct and indirect radiative forcing due to tropospheric aerosols: A review. *Revs Geophys*., **38,** 513–543

Haywood, J. M. and Osborne, S. R. 2000 'Corrections to be applied to the PSAP and nephelometer for accurate determination of the absorption coefficient, scattering coefficient and single scattering albedo'. MRF Technical Note No 31. Available from: Met Office, Y46 Bldg, Cody Technology Park, Farnborough, Hants, GU14 0LX, UK

Haywood, J. M. and Shine, K. P. 1995 The effect of anthropogenic sulfate and soot aerosol on the clear sky planetary radiation budget. *Geophys. Res. Lett*., **22,** 603–606

Haywood, J. M., Osborne, S. R., Francis, P. N., Keil, A., Formenti, P., Andreae, M. O. and Kaye, P. H. 2003a The mean physical and optical properties of regional haze dominated by biomass burning aerosol measured from the C-130 aircraft during SAFARI 2000. *J. Geophys. Res.*, **108**(D13)**,** 8473, doi:10.1029/2002JD002226

Haywood, J. M., Osborne, S. R., Francis, P., Glew, M., Highwood, E., Formenti, P. and Andreae, M. 2003b Radiative properties and direct radiative effect of Saharan dust measured by the C-130 aircraft during SHADE: 1. Solar spectrum. *J. Geophys. Res.*, **108**(D13)**,** 8577, doi:10.1029/2002JD002687

Haywood, J. M., Francis, P. N., Glew, M. D., Dubovik, O. and Holben, B. N. 2003c Comparison of aerosol size distributions, radiative properties, and optical depths determined by aircraft observations and sun photometers during SAFARI-2000 *J. Geophys. Res.*, **108**(D13)**,** 8471, doi:10.1029/2002JD002250

Highwood, E. J., Haywood, J. M., Silverstone, M. D., Newman, S. M. and Taylor, J. P. 2003 Radiative properties and direct effect of Saharan dust measured by the C-130 aircraft during SHADE. 2: Terrestrial spectrum. *J. Geophys. Res.*, **108**(D18)**,** 8578, doi:10.1029/2002JD002552

Hobbs, P. V. 2002 Clean air slots amid atmospheric pollution. *Nature*, **415,** 861

Hsu, N. C., Herman, J. R., Torres, O., Holben, B. N., Tanré, D., Eck, T. F., Smirnov, A., Chatenet, B. and Lavenu, F. 1999 Comparison of the TOMS aerosol index with sun-photometer aerosol optical thickness: Results and applications. *J. Geophys. Res*., **104,** 6269–6279

Hsu, N. C., Herman, J. R. and Chen, S.-C. 2003 Radiative impacts from biomass burning in the presence of clouds during boreal spring in southeast Asia. *Geophys. Res. Lett.,* **30**(5)**,** 1224, doi:10.1029/2002GL016485

Johnson, B. T., Shine, K. P. and Forster, P. M. 2004 The semi-direct aerosol effect: Impact of absorbing aerosols on marine stratocumulus. *Q. J. R. Meteorol. Soc*., in press

Kaufman, Y., Tanré, D., Dubovik, O., Karnieli, A. and Remer, L. A. 2001 Absorption of sunlight by dust as inferred from satellite and ground-based remote sensing. *Geophys. Res. Lett*., **28,** 1479–1483

Kaufman, Y., Haywood, J. M., Hobbs, P. V., Hart, W., Kleidman, R. and Schmid, B. 2003 Remote sensing of vertical distribution of smoke aerosol off the coast of Africa during SAFARI 2000. *Geophys. Res. Lett.*, **30,** 1831, doi:10.1029/2003GL017068

Keil, A. and Haywood, J. M. 2003 Solar radiative forcing by biomass aerosol particles over marine clouds during SAFARI-2000. *J. Geophys. Res.*, **108**(D13)**,** 8467, doi:10.1029/2002JD002315

King, M. D., Menzel, W. P., Kaufman, Y. J., Tanré, D., Gao, B.-C., Platnick, S., Ackerman, S. A., Remer, L. A., Pincus, R. and Hubanks, P. A. 2003 Cloud and aerosol properties, precipitable water and profiles of temperature and water vapor from MODIS. *IEEE Trans. Geosci. Remote Sensing*, **41,** 442–458, doi:10.1109/TGRS.2002.808226

Liao, H. and Seinfeld, J. H. 1998 Radiative forcing by mineral dust aerosol: Sensitivity to key variables *J. Geophys. Res.*, **103,** 31637–31646

McClatchey, R. A., Fenn, R. W., Selby, J. E. A., Volz, P. E. and Garing, J. S. 1972 'Optical properties of the atmosphere (third edition)'. Research paper 411, Air Force Cambridge, MA, USA

Myhre, G., Berntsen, T. K., Haywood, J. M., Sundet, J. K., Holben, B. N., Johnsrud, M. and Stordal, F. 2003 Modelling the radiative impact of aerosols from biomass burning during SAFARI-2000. *J. Geophys. Res.*, **108**(D13)**,** 8501, doi:10.1029/2002JD002313

Platnick, S. 2000 Vertical photon transport in cloud remote sensing problems. *J. Geophys. Res*., **105**(D18)**,** 22919–22935

Platnick, S., King, M. D., Ackerman, S. A., Menzel, W. P., Baum, B. A., Riédi, J. C. and Frey, R. A. 2003 The MODIS cloud products: algorithms and examples from Terra. *IEEE Trans. Geosci. Remote Sensing*, **41,** 459–473, doi:10.1109/TGRS.2002.808301

Sokolik, I. N., Toon, O. B. and Bergstrom, R. W. 1998 Modelling the radiative characteristics of airborne mineral aerosols at infrared wavelengths. *J. Geophys. Res.*, **103,** 8813–8826

Tanré, D., Haywood, J. M., Pelon, J., Léon, J. F., Chatenet, B., Formenti, P., Francis, P., Goloub, P., Highwood, E. J. and Myhre, G. 2003 Measurement and modeling of the Saharan dust radiative impact: Overview of the SaHAran Dust Experiment (SHADE). *J. Geophys. Res.*, **108**(D13)**,** 8574, doi:10.1029/2002JD003273

Winker, D. M., Pelon, J. and McCormick, M. P. 2003 The CALIPSO mission: Spaceborne lidar for observation of aerosols and clouds. *Proc. SPIE*, **4893,** 1–11

WMO 1986 'A preliminary cloudless standard atmosphere for radiation computation'. World Climate Program of the World Meteorological Organization, Geneva, Switzerland

Glossary of Abbreviations

AERONET	Aerosol Robotic Network
AGL	Above ground level
AI	Aerosol Index
AVHRR	Advanced Very High Resolution Radiometer
BBR	Broad band radiometer
BC	Black carbon
BDRF	Bidirectional reflectance function
CALIPSO	Cloud-aerosol Lidar and Infrared Pathfinder Satellite Observations
CCN	Cloud condensation nuclei
CTM	Chemical Transport Model
FFSSP	Fast forward scattering spectrometer probe
GCM	General Circulation Model
IPCC	Intergovernmental Panel on Climate Change
ISCCP	International Satellite Cloud Climatology Project
LWM	Liquid water mass
LWP	Liquid water path
MBL	Marine boundary layer
MODIS	Moderate Resolution Imaging Spectroradiometer
NIR	Near infrared

OC	Organic carbon
PCASP	Passive cavity aerosol spectrometer probe 100X
PSAP	Particle soot absorption photometer
RH	Relative humidity
SAFARI 2000	Southern African Regional Science Initiative
SAFIRE	Scanning airborne filter radiometer
SLR	Straight and level run
SWS	Short wave spectrometer
SZA	Solar zenith angle
TEM	Transmission electron microscopy
TOA	Top of the atmosphere
TOMS	Total Ozone Mapping Spectrometer
TRMM	Tropical Rainfall Measuring Mission
VIRS	Visible and Infrared Scanning instrument
WCP	World Climate Program

References

Abel, S. J., Haywood, J. M., Highwood, E. J., Li, J., and Buseck, P. R. (2003). Evolution of biomass burning aerosol properties from an agricultural fire in southern Africa. *Geophys. Res. Lett.*, **30**, 1783, doi:10.1029/2002GL017342.

Albrecht, B. (1989). Aerosols, cloud microphysics and fractional cloudiness. *Science*, **245**, 1227 – 1230.

Anderson, B. E., Grant, W. B., Gregory, G. L., Browell, E. V., Collins Jr, J. E., Sachse, G. W., Bagwell, D. R., Hudgins, C. H., Blake, D. R., and Blake, N. J. (1996). Aerosols from biomass burning over the tropical South Atlantic region: Distributions and impacts. *J. Geophys. Res.*, **101**, 24,117 – 24,137.

Anderson, D. (1997). Mk.2 Hercules. Summary of capability, MRF Tech. Note No. 21, (Available from Met. Off., Exeter, UK).

Anderson, T. L. and Ogren, J. A. (1998). Determining aerosol radiative properties using the TSI 3563 integrating nephelometer. *Aerosol. Sci. and Technol.*, **29**, 57 – 69.

Andreae, M. O., Rosenfeld, D., Artaxo, P., Costa, A. A., Frank, G. P., Longo, K. M., and Silva-Dias, M. A. F. (2004). Smoking rain clouds over the Amazon. *Science*, **303**, 1337 – 1342.

Bates, T. S., Huebert, B. J., Gras, J. L., Griffiths, F. B., and Durkee, P. A. (1998). International Global Atmospheric Chemistry (IGAC) project's first Aerosol Characterization Experiment (ACE 1): Overview. *J. Geophys. Res.*, **103**, 16,297–16,318.

Bergstrom, R. W., Pilewskie, P., Schmid, B., and Russell, P. B. (2003). Estimates of the spectral aerosol single scattering albedo and aerosol radiative effects during SAFARI 2000. *J. Geophys. Res.*, **108**, 8474, doi:10.1029/2002JD002435.

Bond, T. C., Anderson, T. L., and Campbell, D. (1999). Calibration and intercomparison of filter-based measurements of visible light absorption by aerosols. *Aerosol. Sci. and Technol.*, **30**, 582 – 600.

Campbell, J. R., Welton, E. J., Spinhirne, J. D., Ji, Q., Tsay, S. -C., Piketh, S. J., Barenbrug, M., and Hoben, B. N. (2003). Micropulse lidar observations of tropospheric aerosols over northeastern South Africa during the ARREX and SAFARI 2000 dry season experiments. *J. Geophys. Res.*, **108**, 8497, doi:10.1029/2002JD002563.

Chin, M., Jacob, D. J., Gardner, G. M., Spiro, P. A., Foreman-Fowler, M., and Savoie, D. L. (1996). A global three-dimensional model of tropospheric sulfate. *J. Geophys. Res.*, **101**, 18,677–18,690.

Chu, D. A., Kaufman, Y. J., Ichoku, C., Remer, L. A., Tanré, D., and Holben, B. N. (2002). Validation of MODIS aerosol optical depth retrieval over land. *Geophys. Res. Lett.*, **29**, doi:10.1029/2001GL013205.

Chuang, C. C., Penner, J. E., Prospero, J. M., Grant, K. E., and Rau, G. H. (2000). Effects of anthropogenic aerosols on cloud susceptibility: a sensitivity study of radiative forcing to aerosol characteristics and global concentration, Lawrence Livermore National Laboratory Internal Report, No. UCRL-JC-139097 Rev 1., Lawrence Livermore National Laboratory, CA, USA.

Chylek, P. and Wong, J. (1995). Effect of absorbing aerosols on global radiation budget. *Geophys. Res. Lett.*, **22**, 929 – 931.

Chylek, P., Videen, G., Ngo, D., Pinnick, R. G., and Klett, J. D. (1995). Effect of black carbon on the optical properties and climate forcing of sulfate aerosols. *J. Geophys. Res.*, **100**, 16,325 – 16,332.

Cofer, W. R., III., Levine, J. S., Winstead, E. L., Cahoon, D. R., Sebacher, D. I., Pinto, J. P., and Stocks, B. J. (1996). Source compositions of trace gases released during African savanna fires. *J. Geophys. Res.*, **101**, 23,597 – 23,602.

Collins, W. D., Rasch, P. J., Eaton, B. E., Khattatov, B. V., Lamarque, J. -F., and Zender, C. S. (2001). Simulating aerosols using a chemical transport model with assimilation of satellite aerosol retrievals: Methodology for INDOEX. *J. Geophys. Res.*, **106**, 7313 – 7336.

Cook, J. and Highwood, E. J. (2004). Climate response to tropospheric absorbing aerosols in an Intermediate General-Circulation Model. *Quart. J. Roy. Met. Soc.*, **130**, 175 – 191.

Crutzen, P. J. and Andreae, M. O. (1990). Biomass burning in the tropics: impact on atmospheric chemistry and biogeochemical cycles. *Science*, **250**, 1669 – 1678.

Csiszar, I. and Gutman, G. (1999). Mapping global land surface albedo from NOAA AVHRR. *J. Geophys. Res.*, **104**, 6215 – 6228.

Dubovik, O. and King, M. D. (2000). A flexible inversion algorithm for retrieval of aerosol optical properties from Sun and sky radiance measurements. *J. Geophys. Res.*, **105**, 20,673 – 20,696.

Dubovik, O., Smirnov, A., Holben, B. N., King, M. D., Kaufman, Y. J., Eck, T. F., and Slutsker, I. (2000). Accuracy assessments of aerosol optical properties retrieved from Aerosol Robotic Network (AERONET) Sun and sky radiance measurements. *J. Geophys. Res.*, **105**, 9791 – 9806.

Dubovik, O., Holben, B., Eck, T. F., Smirnov, A., Kaufman, Y. J., King, M. D., Tanré, D., and Slutsker, I. (2002). Variability of absorption and optical properties of key aerosol types observed in worldwide locations. *J. Atmos. Sci*, **59**, 590 – 608.

Duncan, B. N., Martin, R. V., Staudt, A. C., Yevich, R., and Logan, J. A. (2003). Interannual and seasonal variability of biomass burning emissions constrained by satellite observations. *J. Geophys. Res.*, **108**, 4100, doi:10.1029/2002JD002378.

Eatough, D. J., Eatough, N. L., Pang, Y., Sizemore, S., Kirchstetter, T. W., Novakov, T., and Hobbs, P. V. (2003). Semivolatile particulate organic material in southern Africa during SAFARI 2000. *J. Geophys. Res.*, **108**, 8479, doi:10.1029/2002JD002296.

Eck, T. F., Holben, B. N., Ward, D. E., Mukelabai, M. M., Dubovik, O., Smirnov, A., Schafer, J. S., Hsu, N. C., Piketh, S. J., Queface, A., Le Roux, J., Swap, R. J., and Slutsker, I. (2003). Variability of biomass burning aerosol optical characteristics in southern Africa during the SAFARI 2000 dry season campaign and a comparison of single scattering albedo estimates from radiometric measurements. *J. Geophys. Res.*, **108**, 8477, doi:10.1029/2002JD002321.

Edwards, J. M. and Slingo, A. (1996). Studies with a flexible new radiation code. Part 1. Choosing a configuration for a large-scale model. *Quart. J. Roy. Met. Soc.*, **122**, 689–719.

Ferek, R. J., Reid, J. S., Hobbs, P. V., Blake, D. R., and Liousse, C. (1998). Emission factors of hydrocarbons, halocarbons, trace gases and particles from biomass burning in Brazil. *J. Geophys. Res.*, **103**, 32,107 – 32,118.

Formenti, P., Elbert, W., Maenhaut, W., Haywood, J., Osborne, S., and Andreae, M. O. (2003). Inorganic and carbonaceous aerosols during the Southern African Regional Science Initiative (SAFARI 2000) experiment: Chemical characteristics, physical properties, and emission data for smoke from African biomass burning. *J. Geophys. Res.*, **108**, 8448, doi:10.1029/2002JD002408.

Francis, P. N., Hignett, P., and Taylor, J. P. (1999). Aircraft observations and modeling of sky radiance distributions from aerosol during TARFOX. *J. Geophys. Res.*, **104**, 2309–2319.

Fuller, K. A., Malm, W. C., and Kreidenweis, S. M. (1999). Effects of mixing on extinction by carbonaceous particles. *J. Geophys. Res.*, **104**, 15,941 – 15,954.

Gao, S., Hegg, D. A., Hobbs, P. V., Kirchstetter, T. W., Magi, B. I., and Sadilek, M. (2003). Water-soluble organic components in aerosols associated with savanna fires in southern Africa: Identification, evolution, and distribution. *J. Geophys. Res.*, **108**, 8491, doi:10.1029/2002JD002324.

Garrett, T. J. and Hobbs, P. V. (1995). Long-range transport of continental aerosols over the Atlantic Ocean and their effects on cloud structures. *J. Atmos. Sci*, **52**, 2977 – 2984.

Garstang, M., Tyson, P. D., Swap, R., Edwards, M., Kållberg, P., and Lindesay, J. A. (1996). Horizontal and vertical transport of air over southern Africa. *J. Geophys. Res.*, **101**, 23,721 – 23,736.

Gatebe, C. K., King, M. D., Lyapustin, A. I., Arnold, G. T., and Redemann, J. (2004). Airborne spectral measurements of ocean directional reflectance, In press. *J. Atmos. Sci*.

Giglio, L., Kendall, J. D., and Mack, R. (2003). A multi-year active fire dataset for the tropics derived from the TRMM VIRS. *Int. J. Remote Sensing*, **24**, 4505 – 4525.

Glew, M. D., Hignett, P., and Taylor, J. P. (2004). Aircraft measurements of sea surface albedo, Submitted to. *J. Atmos. Sci*.

Grant, K. E., Chuang, C. C., Grossman, A. S., and Penner, J. E. (1999). Modeling the spectral optical properties of ammonium sulfate and biomass burning aerosols: parameterization of relative humidity effects and model results. *Atmos. Environ.*, **33**, 2603 – 2620.

Gutman, G., Tarpley, D., Ignatov, A., and Olson, S. (1995). The enhanced NOAA global land dataset from the Advanced Very High Resolution Radiometer. *Bull. Amer. Meteorol. Soc.*, **76**, 1141 – 1156.

Guyon, P., Graham, B., Beck, J., Boucher, O., Gerasopoulos, E., Mayol-Bracero, O. L., Roberts, G. C., Artaxo, P., and Andreae, M. O. (2003). Physical properties and concentration of aerosol particles over the Amazon tropical forest during background and biomass burning conditions. *Atmos. Chem. Phys.*, **3**, 951 – 967.

Hale, G. M. and Querry, M. R. (1973). Optical constants of water in the 200nm to 200μm wavelength region. *Appl. Opt.*, **12**, 555 – 563.

Hallett, J., Hudson, J. G., and Rogers, C. F. (1989). Characterization of combustion aerosols for haze and cloud formation. *Aerosol. Sci. and Technol.*, **10**, 70 – 83.

Han, Q., Rossow, W. B., and Lacis, A. A. (1994). Near-global survey of effective droplet radii in liquid water clouds using ISCCP data. *J. Climate*, **7**, 465 – 497.

Hansen, J. E., Sato, M., and Reudy, R. (1997). Radiative forcing and climate response. *J. Geophys. Res.*, **102**, 6831 – 6864.

Haywood, J. and Boucher, O. (2000). Estimates of the direct and indirect radiative forcing due to tropospheric aerosols: a review. *Revs. Geophys.*, **38**, 513 – 543.

Haywood, J. M. and Osborne, S. R. (2000). Corrections to be applied to the PSAP and nephelometer for accurate determination of the absorption coefficient, scattering coefficient and single scattering albedo, MRF Tech. Note No. 31, (Available from Met. Off., Exeter, UK).

Haywood, J. M. and Shine, K. P. (1995). The effect of anthropogenic sulfate and soot aerosol on the clear sky planetary radiation budget. *Geophys. Res. Lett.*, **22**, 603 – 606.

Haywood, J. M. and Shine, K. P. (1997). Multi-spectral calculations of the radiative forcing of tropospheric sulphate and soot aerosols using a column model. *Quart. J. Roy. Met. Soc.*, **123**, 1907 – 1930.

Haywood, J. M., Roberts, D. L., Slingo, A., Edwards, J. M., and Shine, K. P. (1997). General Circulation Model calculations of the direct radiative forcing by anthropogenic sulfate and fossil-fuel soot aerosol. *J. Climate*, **10**, 1562 – 1577.

Haywood, J. M., Osborne, S. R., Francis, P. N., Keil, A., Formenti, P., Andreae, M. O., and Kaye, P. H. (2003a). The mean physical and optical properties of regional haze dominated by biomass burning aerosol measured from the C-130 aircraft during SAFARI 2000. *J. Geophys. Res.*, **108**, 8473, doi:10.1029/2002JD002226.

Haywood, J. M., Francis, P., Dubovik, O., Glew, M., and Holben, B. (2003b). Comparison of aerosol size distributions, radiative properties, and optical depths determined by aircraft observations and sun photometers during SAFARI 2000. *J. Geophys. Res.*, **108**, 8471, doi:10.1029/2002JD002250.

Haywood, J. M., Francis, P., Osborne, S., Glew, M., Loeb, N., Highwood, E., Tanré, D., Myhre, G., Formenti, P., and Hirst, E. (2003c). Radiative properties and direct radiative effect of Saharan dust measured by the C-130 aircraft during SHADE: 1. Solar spectrum. *J. Geophys. Res.*, **108**, 8577, doi:10.1029/2002JD002687.

Haywood, J. M., Osborne, S. R., and Abel, S. J. (2004). The effect of overlying absorbing aerosol layers on remote sensing retrievals of cloud effective radius and cloud optical depth. *Quart. J. Roy. Met. Soc.*, **130**, 779 – 800.

Herman, J. R., Bhartia, P. K., Torres, O., Hsu, C., Seftor, C., and Celarier, E. (1997). Global distribution of UV-absorbing aerosols from Nimbus7/TOMS data. *J. Geophys. Res.*, **102**, 16,911 – 16,922.

Highwood, E. J., Haywood, J. M., Silverstone, M. D., Newman, S. M., and Taylor, J. P. (2003). Radiative properties and direct effect of Saharan dust measured by the C-130 aircraft during Saharan Dust Experiment (SHADE): 2. Terrestrial spectrum. *J. Geophys. Res.*, **108**, 8578, doi:10.1029/2002JD002552.

Hignett, P., Taylor, J. P., Francis, P. N., and Glew, M. D. (1999). Comparison of observed and modeled direct aerosol forcing during TARFOX. *J. Geophys. Res.*, **104**, 2279 – 2287.

Hobbs, P. V. (2003). Clean air slots amid dense atmospheric pollution in southern Africa. *J. Geophys. Res.*, **108**, 8490, doi:10.1029/2002JD002156.

Hobbs, P. V., Reid, J. S., Kotchenruther, R. A., Ferek, R. J., and Weiss, R. (1997). Direct radiative forcing by smoke from biomass burning. *Science*, **275**, 1776 – 1778.

Hobbs, P. V., Sinha, P., Yokelson, R. J., Christian, T. J., Blake, D. R., Gao, S., Kirchstetter, T. W., Novakov, T., and Pilewskie, P. (2003). Evolution of gases and particles from a savanna fire in South Africa. *J. Geophys. Res.*, **108**, 8485, doi:10.1029/2002JD002352.

Holben, B. N., Eck, T. F., Slutsker, I., Tanré, D., Buis, J. P., Setzer, A., Vermote, E., Reagan, J. A., Kaufman, Y. J., Nakajima, T., Lavenu, F., Jankowiak, I., and Smirnov, A. (1998). AERONET - A federated instrument network and data archive for aerosol characterization. *Remote Sens. Environ*, **66**, 1 – 16.

Hsu, N. C., Herman, J. R., Bhartia, P. K., Seftor, C. J., Torres, O., Thompson, A. M., Gleason, J. F., Eck, T. F., and Holben, B. N. (1996). Detection of biomass burning smoke from TOMS measurements. *Geophys. Res. Lett.*, **23**, 745 – 748.

Hsu, N. C., Herman, J. R., Torres, O., Holben, B. N., Tanre, D., Eck, T. F., Smirnov, A., Chatenet, B., and Lavenu, F. (1999). Comparisons of the TOMS aerosol index with Sun-photometer aerosol optical thickness: Results and applications. *J. Geophys. Res.*, **104**, 6269 – 6279.

Hsu, N. C., Herman, J. R., and Tsay, S. -C. (2003). Radiative impacts from biomass burning in the presence of clouds during boreal spring in southeast Asia. *Geophys. Res. Lett.*, **30**, 1224, doi:10.1029/2002GL016485.

Huebert, B. J., Bates, T., Russell, P. B., Shi, G., Kim, Y. J., Kawamura, K., Carmichael, G., and Nakajima, T. (2003). An overview of ACE-Asia: Strategies for quantifying the relationships between Asian aerosols and their climatic impacts. *J. Geophys. Res.*, **108**, 8633, doi:10.1029/2003JD003550.

Iacobellis, S. F., Frouin, R., and Somerville, R. C. J. (1999). Direct climate forcing by biomass-burning aerosols: Impact of correlations between controlling variables. *J. Geophys. Res.*, **104**, 12,031 – 12,045.

Ichoku, C., Remer, L. A., Kaufman, Y. J., Levy, R. Chu, D. A., Tanré, D., and Holben, N. N. (2003). MODIS observations of aerosols and estimation of aerosol radiative forcing over southern Africa during SAFARI 2000. *J. Geophys. Res.*, **108**, 8499, doi:10.1029/2002JD002366.

Ingram, W. J., Woodward, S., and Edwards, J. (1997). Unified Model documentation paper no 23: Radiation, (Available from Met. Off., Exeter, UK).

IPCC (2001). *Climate change 2001: The scientific basis. Third assessment of the Intergovernmental Panel on Climate Change (IPCC)*, edited by Houghton, J. T., Ding, Y., Griggs, D. J., Noguer, M., van der Linden, P. J., Dai, X., Maskell, K. and Johnson, C. A. Cambridge Univ. Press, New York, USA.

Iziomon, M. and Lohmann, U. (2003). Optical and meteorological properties of smoke-dominated haze at the ARM Southern Great Plains Central Facility. *Geophys. Res. Lett.*, **30**, 1123, doi:10.1029/2002GL016606.

Jin, Y. F., Schaaf, C. B., Gao, F., Li, X. W., Strahler, A. H., Lucht, W., and Liang, S. L. (2003a). Consistency of MODIS surface bidirectional reflectance function and albedo retrievals: 1.Algorithm performance. *J. Geophys. Res.*, **108**, 4158, doi:10.1029/2002JD002803.

Jin, Y. F., Schaaf, C. B., Woodcock, C. E., Gao, F., Li, X. W., Strahler, A. H., Lucht, W., and Liang, S. L. (2003b). Consistency of MODIS surface bidirectional reflectance function and albedo retrievals: 2.Validation. *J. Geophys. Res.*, **108**, 4159, doi:10.1029/2002JD002804.

Johnson, B. T., Shine, K. P., and Forster, P. M. (2004). The semi-direct aerosol effect: Impact of absorbing aerosols on marine stratocumulus. *Quart. J. Roy. Met. Soc.*, **130**, 1407 – 1422.

Johnson, D. W., Kilsby, C. G., McKenna, D. S., Saunders, R. W., Jenkins, G. J., Smith,

F. B., and Foot, J. S. (1991). Airborne observations of the physical and chemical characteristics of the Kuwait oil smoke plume. *Nature*, **353**, 617 – 621.

Joshi, M., Shine, K., Ponater, M., Stuber, N., Sausen, R., and Li, L. (2003). A comparison of climate response to different radiative forcings in three general circulation models: towards an improved metric for climate change. *Clim. Dyn.*, **20**, 843 – 854.

Jost, C., Trentmann, J., Sprung, D., Andreae, M. O., McQuaid, J. B., and Barjat, H. (2003). Trace gas chemistry in a young biomass burning plume over Namibia: Observations and model simulations. *J. Geophys. Res.*, **108**, 8482, doi:10.1029/2002JD02431.

Kaufman, Y. J. and Fraser, R. S. (1997). The effect of smoke particles on clouds and climate forcing. *Science*, **277**, 1636 – 1639.

Kaufman, Y. J., Tanré, D., Remer, L. A., Vermote, E. F., Chu, A., and Holben, B. N. (1997). Operational remote sensing of tropospheric aerosol over land from EOS moderate resolution imaging spectroradiometer. *J. Geophys. Res.*, **102**, 17,051 – 17,067.

Kaufman, Y. J., Hobbs, P. V., Kirchoff, V. W. J. H., Artaxo, P., Remer, L. A., Holben, B. N., King, M. D., Ward, D. E., Prins, E. M., Longo, K. M., Mattos, L. F., Nobre, C. A., Spinhirne, J. D., Ji, Q., Thompson, A. M., Gleason, J. F., Christopher, S. A., and Tsay, S. -C. (1998). Smoke, Clouds, and Radiation-Brazil (SCAR-B) experiment. *J. Geophys. Res.*, **103**, 31,783 – 31,808.

Kaufman, Y. J., Smirnov, A., Holben, B. N., and Dubovik, O. (2001). Baseline maritime aerosol: methodology to derive the optical thickness and scattering properties. *Geophys. Res. Lett.*, **28**, 3251 – 3254.

Kaufman, Y. J., Haywood, J. M., Hobbs, P. V., Hart, W., Kleidman, R., and Schmid, B. (2003). Remote sensing of vertical distributions of smoke aerosol off the coast of Africa. *Geophys. Res. Lett.*, **30**, 1831, doi:10.1029/2003GL017068.

Keil, A. and Haywood, J. M. (2003). Solar radiative forcing by biomass burning aerosol particles during SAFARI 2000: A case study based on measured aerosol and cloud properties. *J. Geophys. Res.*, **108**, 8467, doi:10.1029/2002JD002315.

King, M. D., Tsay, S., -C., Platnick, S. E., Wang, M., and Liou, K., -N. (1998). Cloud retrieval algorithms for MODIS: optical thickness, effective particle radius, and thermodynamic phase. Technical report, Products: 06_L2, 08_D3, 08_E3, 08_M3, ATBD reference number: ATBD-MOD-05.

King, M. D., Menzel, W. P., Kaufman, Y. J., Tanré, D., Gao, B.-C., Platnick, S., Ackerman, S. A., Remer, L. A., Pincus, R., and Hubanks, P. A. (2003). Cloud and aerosol properties, precipitable water, and profiles of temperature and water vapour from MODIS. *IEEE Trans. Geosci. Remote Sensing*, **41**, 442 – 458.

Kinne, S., Lohmann, U., Feichter, J., Schulz, M., Timmreck, C., Ghan, S., Easter, R., Chin, M., Ginoux, P., Takemura, T., Tegen, I., Koch, D., Herzog, M., Penner, J., Pitari, G., Holben, B., Eck, T., Smirnov, A., Dubovik, O., Slutsker, I., Tanre, D., Torres, O., Mishchenko, M., Geogdzhayev, I., Chu, D. A., and Kaufman, Y. (2003). Monthly averages of aerosol properties: A global comparison among models, satellite data, and AERONET data. *J. Geophys. Res.*, **108**, 4634, doi:10.1029/2001JD001253.

Kirchstetter, T. W., Novakov, T., Hobbs, P. V., and Magi, B. (2003). Airborne measurements of carbonaceous aerosols in southern Africa during the dry biomass burning season. *J. Geophys. Res.*, **108**, 8476, doi:10.1029/2002JD002171.

Koren, I., Kaufman, Y. J., Remer, L. A., and Martins, J. V. (2004). Measurement of the effect of Amazon smoke on inhibition of cloud formation. *Science*, **303**, 1342 – 1345.

Kotchenruther, R. A. and Hobbs, P. V. (1998). Humidification factors of aerosols from biomass burning in Brazil. *J. Geophys. Res.*, **103**, 32,081–32,089.

Le Canut, P., Andreae, M. O., Harris, G. W., Wienhold, F. G., and Zenker, T. (1996). Airborne studies of emissions from savanna fires in southern Africa 1. Aerosol emissions measured with a laser optical particle counter. *J. Geophys. Res.*, **101**, 23,615 – 23,630.

Li, J., Pósfai, M., Hobbs, P. V., and Buseck, P. R. (2003). Individual aerosol particles from biomass burning in southern Africa: 2. Compositions and aging of inorganic particles. *J. Geophys. Res.*, **108**, 8484, doi:10.1029/2002JD002310.

Liousse, C., Penner, J. E., Chuang, C., Walton, J. J., Eddleman, H., and Cachier, H. (1996).

A global three-dimensional model study of carbonaceous aerosols. *J. Geophys. Res.*, **101**, 19,411 – 19,432.

Lohmann, U. and Feichter, J. (2001). Can the direct and semi-direct aerosol effect compete with the indirect effect on a global scale? *Geophys. Res. Lett.*, **28**, 159 – 161.

Lohmann, U., Feichter, J., Penner, J., and Leaitch, R. (2000). Indirect effect of sulfate and carbonaceous aerosols: A mechanistic treatment. *J. Geophys. Res.*, **105**, 12,193 – 12,206.

Magi, B. I. and Hobbs, P. V. (2003). Effects of humidity on aerosols in southern Africa during the biomass burning season. *J. Geophys. Res.*, **108**, 8495, doi:10.1029/2002JD002144.

Magi, B. I., Hobbs, P. V., Schmid, B., and Redemann, J. (2003). Vertical profiles of light scattering, light absorption, and single scattering albedo during the dry, biomass burning season in southern Africa and comparisons of in situ and remote senesing measurements of aerosol optical depths. *J. Geophys. Res.*, **108**, 8504, doi:10.1029/2002JD002361.

Martin, G. M., Johnson, D. W., and Spice, A. (1994). The measurement and parameterization of effective radius of droplets in warm stratocumulus clouds. *J. Atmos. Sci*, **51**, 1823 – 1842.

Martins, J. V., Artaxo, P., Liousse, J. S., Reid, J. S., Hobbs, P. V., and Kaufman, Y. J. (1998a). Effects of black carbon content, particle size, and mixing on light absorption by aerosols from biomass burning in Brazil. *J. Geophys. Res.*, **103**, 32,041 – 32,050.

Martins, J. V., Hobbs, P. V., Weiss, R. E., and Artaxo, P. (1998b). Sphericity and morphology of smoke particles from biomass burning in Brazil. *J. Geophys. Res.*, **103**, 32,051 – 32,057.

McClatchey, R. A., Fenn, R. W., Selby, J. E. A., Volz, P. E., and Garing, J. S. (1972). Optical properties of the atmosphere (3rd Edition). *Air Force Cambridge Research Papers*, page 411.

Mishchenko, M. I. and Travis, L. D. (1998). Capabilities and limitations of a current Fortran implementation of the T-Matrix method for randomly oriented, rotationally symmetric scatterers. *J. Quant. Spectrosc. Radiat. Transfer*, **60**, 309 – 324.

Myhre, G., Bernsten, T. K., Haywood, J. M., Sundet, J. K., Holben, B. N., Johnsrud, M., and Stordal, F. (2003). Modeling the solar radiative impact of aerosols from biomass burning during the Southern African Regional Science Initiative (SAFARI-2000) experiment. *J. Geophys. Res.*, **108**, 8501, doi:10.1029/2002JD002313.

Osborne, S. R., Haywood, J. M., Francis, P. N., and Dubovik, O. (2004). Short-wave radiative effects of biomass burning aerosol during SAFARI 2000. *Quart. J. Roy. Met. Soc.*, **130**, 1423 – 1447.

Palmer, K. F. and Williams, D. (1974). Optical properties of water in the near infrared. *J. Opt. Soc. Am.*, **64**, 1107 – 1110.

Penner, J. E., Dickinson, R. E., and O'Neill, C. A. (1992). Effects of aerosol from biomass burning on the global radiation budget. *Science*, **256**, 1432 – 1433.

Penner, J. E., Chuang, C. C., and Grant, K. (1998). Climate forcing by carbonaceous and sulfate aerosols. *Clim. Dyn.*, **14**, 839 – 851.

Platnick, S. (2000). Vertical photon transport in clooud remote sensing problems. *J. Geophys. Res.*, **105**, 22,919 – 22,935.

Platnick, S. and Valero, F. P. J. (1995). A validation of a satellite cloud retrieval during ASTEX. *J. Atmos. Sci*, **52**, 2985 – 3001.

Platnick, S., King, M. D., Ackerman, S. A., Menzel, W. P., Baum, B. A., Riédi, J. C., and Frey, R. A. (2003). The MODIS cloud products: algorithms and examples from Terra. *IEEE Trans. Geosci. Remote Sensing*, **41**, 459 – 473.

Pósfai, M., Simonics, R., Li, J., Hobbs, P. V., and Buseck, P. R. (2003). Individual aerosol particles from biomass burning in southern Africa: 1. Compositions and size distributions of carbonaceous particles. *J. Geophys. Res.*, **108**, 8483, doi:10.1029/2002JD002291.

Pósfai, M., Gelencsér, A., Simonics, R., Arató, K., Li, J., Hobbs, P. V., and Buseck, P. R. (2004). Atmospheric tar balls: Particles from biomass and biofuel burning. *J. Geophys. Res.*, **109**, D06213, doi:10.1029/2003JD004169.

Quaas, J., Boucher, O., and Bréon, F. -M. (2004). Aerosol indirect effects in POLDER satellite data and the Laboratoire de Météorologie Dynamique-Zoom (LMDZ) general circulation model. *J. Geophys. Res.*, **109**, DO8205, doi:10.1029/2003JD004317.

Raes, F., Bates, T., McGovern, F., and Van Liedekerke, M. (2000). The 2nd Aerosol Characterization Experiment (ACE-2): general overview and main results. *Tellus*, **52B**, 111 – 125.

Ramanathan, V., Crutzen, P. J., Kiehl, J. T., and Rosenfeld, D. (2001a). Aerosols, climate, and the hydrological cycle. *Science*, **294**, 2119 – 2124.

Ramanathan, V., Crutzen, P. J., Lelieveld, J., Mitra, A. P., Althausen, D., Anderon, J., Andreae, M. O., Cantrell, W., Cass, G. R., Chung, C. E., Clarke, D., Coakley, J. A., Collins, W. D., Conant, W. C., Dulac, F., Heintzenberg, J., Heymsfield, A. J., Holben, B., Howell, S., Hudson, J., Jayaraman, A., Kiehl, J. T., Krishnamurti, T. N., Lubin, D., McFarquhar, G., Novakov, T., Ogren, J. A., Podgorny, I. A., Prather, K., Priestley, K., Prospero, M., Quinn, P. K., Rajeev, K., Rasch, P., Rupert, S., Sadourny, R., Satheesh, S. K., Shaw, G. E., Sheridan, P., and Valero, F. P. J. (2001b). Indian Ocean Experiment: An integrated analysis of the climate forcing and effects of the great Indo-Asian haze. *J. Geophys. Res.*, **106**, 28,371 – 28,398.

Reid, J. S. and Hobbs, P. V. (1998). Physical and optical properties of young smoke from individual biomass fires in Brazil. *J. Geophys. Res.*, **103**, 32,013–32,030.

Reid, J. S., Hobbs, P. V., Ferek, R. J., Blake, D. R., Martins, J. V., Dunlap, M. R., and Liousse, C. (1998). Physical, chemical, and optical properties of regional hazes dominated by smoke in Brazil. *J. Geophys. Res.*, **103**, 32,059 – 32,080.

Reid, J. S., Koppmann, R., Eck, T. F., and Eleuterio, D. P. (2005). A review of biomass burning emissions part II:intensive physical properties of biomass burning particles. *Atmos. Chem. Phys.*, **5**, 799 – 825.

Remer, L. A., Kaufman, Y. J., Levin, Z., and Ghan, S. (2002a). Model assessment of the ability of MODIS top-of-atmosphere direct radiative forcing from smoke aerosols. *J. Atmos. Sci*, **59**, 657 – 667.

Remer, L. A., Tanré, D., Kaufman, Y. J., Ichoku, C., Mattoo, S., Levy, R., Chu, D. A., Holben, B., Dubovik, O., Smirnov, A., Martins, J. V., Li, R. -R., and Ahmad, Z. (2002b). Validation of MODIS aerosol retrieval over ocean. *Geophys. Res. Lett.*, **29**, doi:10.1029/2001GL013204.

Roeckner, E., Bengtsson, L., Feichter, J., Lelieveld, J., and Rodhe, H. (1999). Transient climate change simulations with a coupled atmosphere-ocean GCM including the tropospheric sulfur cycle. *J. Climate*, **12**, 3004 – 3032.

Ross, J. L., Hobbs, P. V., and Holben, B. (1998). Radiative characteristics of regional hazes dominated by smoke from biomass burning in Brazil: closure tests and direct radiative forcing. *J. Geophys. Res.*, **103**, 31,925 – 31,941.

Rossow, W. B. and Schiffer, R. A. (1991). ISCCP cloud data products. *Bull. Amer. Meteor. Soc.*, **72**, 2 – 20.

Rozendaal, M. A., Leovy, C. B., and Klein, S. A. (1995). An observational study of diurnal variations of marine stratiform cloud. *J. Climate*, **8**, 1795 – 1809.

Russell, P. B., Hobbs, P. V., and Stowe, L. L. (1999). Aerosol properties and radiative effects in the United States East Coast haze plume: An overview of the Tropospheric Aerosol Radiative Forcing Experiment (TARFOX). *J. Geophys. Res.*, **104**, 2213 – 2222.

Satheesh, S. K. and Ramanathan, V. (2000). Large differences in tropical aerosol forcing at the top of the atmosphere and Earth's surface. *Nature*, **405**, 60 – 63.

Sato, M., Hansen, J., Koch, D., Lacis, A., Ruedy, R., Dubovik, O., Holben, B., Chin, M., and Novakov, T. (2003). Global atmospheric black carbon inferred from AERONET. *P. Natl. Acad. Sci. USA*, **100**, 6319 – 6324.

Schmid, B., Redemann, J., Russell, P. B., Hobbs, P. V., Hlavka, D. L., McGill, M. J., Holben, B. N., Welton, E. J., Campbell, J. R., Torres, O., Kahn, R. A., Diner, D. J., Helmlinger, M. C., Chu, D. A., Robles-Gonzalez, C., and de Leeuw, G. (2003). Coordinated airborne, spaceborne, and ground-based measurements of massive thick aerosol layers during the dry season in southern Africa. *J. Geophys. Res.*, **108**, 8496, doi:10.1029/2002JD002297.

Scholes, M. and Andreae, M. O. (2000). Biogenic and pyrogenic emissions from Africa and their impact on the global atmosphere. *Ambio.*, **29**, 23 – 29.

Sekiguchi, M., Nakajima, T., Suzuki, K., Kawamoto, K., Higurashi, A., Rosenfeld, D., Sano, I., and Mukai, S. (2003). A study of the direct and indirect effects of aerosols using global satellite data sets of aerosol and cloud parameters. *J. Geophys. Res.*, **108**, 4699, doi:10.1029/2002JD003359.

Sellers, P. J., Randall, D. A., Collatz, G. J. ans Berry, J. A., Field, C. B., Dazlich, D. A., Zhang, C., Collelo, G. D., and Bounoua, L. (1996). A revised land surface parameterization (SiB2) for atmospheric GCMs. Part I: Model formulation. *J. Climate*, **9**, 676 – 705.

Sinha, P., Hobbs, P. V., Yokelson, R. J., Bertschi, I. T., Blake, D. R., Simpson, I. J., Gao, S., Kirchdtetter, T. W., and Novakov, T. (2003). Emissions of trace gases and particles from savanna fires in southern Africa. *J. Geophys. Res.*, **108**, 8487, doi:10.1029/2002JD002325.

Slingo, A. (1989). A GCM parameterization for the shortwave radiative properties of water clouds. *J. Atmos. Sci*, **46**, 1419 – 1427.

Slingo, A. and Schrecker, H. M. (1982). On the shortwave radiative properties of stratiform water clouds. *Quart. J. Roy. Met. Soc.*, **108**, 407 – 426.

Slingo, A., Nicholls, S., and Schmetz, J. (1982). Aircraft observations of marine stratocumulus during JASIN. *Quart. J. Roy. Met. Soc.*, **108**, 833 – 856.

Slingo, A., Hodges, K. I., and Robinson, G. J. (2004). Simulation of the diurnal cycle in a climate model and its evaluation using data from Meteosat 7. *Quart. J. Roy. Met. Soc.*, **130**, 1449 – 1467.

Swap, R. J., Garstang, M., Macko, S. A., Tyson, P. D., Maenhaut, W., Artaxo, P., Kållberg, P., and Talbot, R. (1996). The long-range transport of southern African aerosols to the tropical South Atlantic. *J. Geophys. Res.*, **101**, 23,777 – 23,791.

Swap, R. J., Annegarn, H. J., Suttles, J. T., Haywood, J., Helmlinger, M. C., Hely, C., Hobbs, P. V., Holben, B. N., Ji, J., King, M. D., Landmann, T., Maenhaut, W., Otter,

L., Pak, B., Piketh, S. J., Platnick, S., Privette, J., Roy, D., Thompson, A. M., Ward, D., and Yokelson, R. (2002a). The Southern African Regional Science Initiative (SAFARI 2000): overview of the dry season campaign. *S. Afr. J. Sci.*, **98**, 125 – 130.

Swap, R. J., Annegarn, H. J., and Otter, L. (2002b). Southern African Regional Science Initiative (SAFARI 2000): summary of science plan. *S. Afr. J. Sci.*, **98**, 119 – 124.

Takemura, T., Nakajima, T., Dubovik, O., Holben, B. N., and Kinne, S. (2002). Single-scattering albedo and radiative forcing of various aerosol species with a global three-dimensional model. *J. Climate*, **15**, 333 – 352.

Tanré, D., Kaufman, Y. J., Herman, M., and Mattoo, S. (1997). Remote sensing of aerosol properties over oceans using the MODIS/EOS spectral radiances. *J. Geophys. Res.*, **102**, 16,971 – 16,988.

Tanré, D., Haywood, J. M., Pelon, J., Léon, J. F., Chatenet, B., Formenti, P., Francis, P., Goloub, P., Highwood, E. J., and Myhre, G. (2003). Measurement and modelling of the Saharan dust radiative impact: Overview of the Saharan Dust Experiment (SHADE). *J. Geophys. Res.*, **108**, 8574, doi10:1029/2002JD003273.

Tegen, I. and Fung, I. (1995). Modeling of mineral dust in the atmosphere: Sources, transport, and optical thickness. *J. Geophys. Res.*, **100**, 18,707 – 18,726.

Tegen, I., Hollrig, P., Chin, M., Fung, I., Jacob, D., and Penner, J. (1997). Contribution of different aerosol species to the global aerosol extinction optical thickness: Estimates from model results. *J. Geophys. Res.*, **102**, 23,895 – 23,915.

Ten Brink, H. M., Khlystov, A., Kos, G. P. A., Tuch, T., Roth, C., and Kreyling, W. (2000). A high-flow humidograph for testing water uptake by ambient aerosol. *Atmos. Environ.*, **34**, 4291–4300.

Thomas, G. E. and Stamnes, K. (1999). Radiative transfer in the atmosphere and ocean. Cambridge Univ. Press, New York.

Twomey, S. (1974). Pollution and the planetary albedo. *Atmos. Environ.*, **8**, 1251 – 1256.

Tyson, P. D. and D'Abreton, P. C. (1998). Transport and recirculation of aerosols off southern Africa - Macroscale plume structure. *Atmos. Environ.*, **32**, 1511 – 1524.

WCP (1986). World Climate Program (WCP), A preliminary cloudless standard atmosphere for radiation computation. World Meteorol. Organ., Geneva.

Winker, D. M., Pelon, J., and McCormick, M. P. (2003). The CALIPSO mission: Spaceborne lidar for observation of aerosols and clouds. *Proc. SPIE*, **4893**, 1 – 11.

Yokelson, R. J., Bertschi, I. T., Christian, T. J., Hobbs, P. V., Ward, D. E., and Hao, W. M. (2003). Trace gas measurements in nascent, aged, and cloud-processed smoke from African savanna fires by airborne Fourier transform infrared spectroscopy (AFTIR). *J. Geophys. Res.*, **108**, 8478, doi:10.1029/2002JD002322.